Sapienza
Università di Roma

Calibration and commissioning results of the NUCLEUS experiment

Facoltà di Scienze Matematiche, Fisiche e Naturali
PhD in Physics (XXXVII cycle)

Giorgio Del Castello
ID number 1755135

Advisor
Marco Vignati

Academic Year 2024

Thesis defended on 08/01/2025
in front of a Board of Examiners composed by:

Prof. Roberto Bonciani (chairman)
Prof.ssa Ilaria Rinaldi
Dott.ssa Claudia Tomei

Calibration and commissioning results of the NUCLEUS experiment
PhDthesis. Sapienza University of Rome

This thesis has been typeset by LaTeX and the Sapthesis class.

Version: January 9, 2025

Author's email: giorgio.delcastello@uniroma1.it

Abstract

Neutrinos, despite outnumbering every other particle in the entire universe, have eluded discovery for more than 25 years after being postulated and still pose a challenge both to theorists and experimentalists.

There are diverse neutrino-matter interactions which span a broad range of energies, with a common denominator: the smallness of the cross-section. For MeV neutrinos, this cross-section is below 10^{-40} cm^2 and makes the observation of these particles in laboratory experiments extremely challenging, as years of dedicated neutrino oscillation experiments have demonstrated. One notable exception to this rule is the Coherent Elastic Neutrino-Nucleus Scattering (CEνNS). This weak neutral current interaction stands out by having a large, by neutrino standards, Standard Model cross-section, which is more than 2 orders of magnitude higher than other neutrino processes. This is a game changer in the experimental landscape, as it allows the study of neutrinos using relatively small detectors (with masses ranging from 10 g to 1 kg), as opposed to ton or multitone experiments such as Borexino or Juno. On the other hand, the only CEνNS observable is the energy of the induced nuclear recoil, which is at the 100 eV scale, meaning that this process is renown to be difficult to measure because detectors with an energy threshold as low as O(10 eV) are needed.

Among the many physics motivations to study CEνNS, a precision measurement of its cross-section would provide the means to unveil new physics beyond the Standard Model, like non-standard interactions or an unforeseen scaling of the weak mixing angle. Moreover, the detector miniaturization, allowed by the high cross-section, will give rise to new branches of neutrino applications for both civilian and military purposes.

This thesis develops in the context of the NUCLEUS experiment, which aims to detect CEνNS using the high anti-neutrino flux from the two 4.25 GW$_{\mathrm{th}}$ reactors cores of the Chooz-B nuclear power plant in France. NUCLEUS will exploit an innovative detection system that consists of a 10 g array of cubic $CaWO_4$ and Al_2O_3 crystals as target detectors. The energy deposited in the crystals is read with superconductive Transition-Edge Sensors deposited on the material surface. This technique allowed the NUCLEUS collaboration to develop detectors that reach the low energy thresholds required for a successful CEνNS observation.

At the start of this Ph.D. research, the NUCLEUS experiment was in its preliminary stage and only the basic setup for detector development was present. Over recent years, substantial improvements have been made to both the experimental setup

and data analysis.

A crucial issue facing cryogenic calorimeters, designed to measure energy depositions as low as O(10 eV), is the characterization of their response. To tackle this, NUCLEUS adopted a novel calibration technique based on the use of optical photons shining on the target calorimeter. The LANTERN project was developed in the context of this work to provide a highly scalable and cost-effective hardware setup to perform this calibration. LANTERN proved to be an elegant and simple solution that can be employed to achieve a full characterization of the detector response, both in terms of calibration and non-linearity evaluation, and will be deployed in the NUCLEUS setup in its final configuration.

The NUCLEUS target detectors are expected to respond equally to both electron and nuclear recoils. To validate this, the NUCLEUS collaboration conducted a calibration campaign using the absorption of thermal neutrons from the nuclei present in the target detectors. The absorption produces an excited nuclear state that, by decaying to its ground state, generates a high energetic photon, that escapes detection, and a nuclear recoil of 100 eV, exactly in the region of interest of the NUCLEUS experiment. Detecting an interaction at 100 eV with a noise level of 10 eV (as for the NUCLEUS detectors) is difficult due to the low signal-to-noise ratio. Therefore, a suitable data analysis procedure was developed and used to observe the first direct detection of nuclear recoils with the NUCLEUS target detectors, achieving a 3σ significance. Since neutrinos interacting via CEνNS produce nuclear recoils in the same 100 eV energy range, this data was the perfect test-bed to define the fundamental analysis aspects that need to be followed for a fruitful neutrino detection. Due to the importance of the developed data analysis, a thorough description is presented in this work along with the results of the nuclear recoil calibration.

At the time of completing this thesis, the NUCLEUS collaboration commissioned its experimental setup and performed a long background characterization campaign. The interplay between the main subsystems, including LANTERN, was demonstrated and stable operation of the NUCLEUS detectors over an extended period of time (a few weeks) was achieved. The analysis of the data taken during this period is defined and presented in this work, with focus on the development of the first combined use of the active muon veto and target detectors as devised for the final configuration of NUCLEUS setup. At the end of this thesis, a discussion over the achieved background results is conducted.

In summary, this thesis presents an overview of the CEνNS interaction and the status of its searches with focus on the NUCLEUS experiment, which is the experimental context of this work. The central theme of this dissertation is the characterization and use of the cryogenic calorimeters employed for the detection of nuclear recoils at the few hundreds of electron volt scale. This topic is addressed from both the experimental and the analysis points of view, with the development of an optical calibration, as well as assessing the accuracy of these new procedures with the observation of calibrated nuclear recoils induced by neutron absorption. Finally, the results of the background characterization campaign and the setup commissioning are shown.

Contents

Acronyms used in this work

Al_2O_3	Sapphire
BSM	Beyond Standard Model
$CaWO_4$	Calcium Tungstate
CCD	Charge-Coupled Device
CEνNS	Coherent Elastic Neutrino-Nucleus Scattering
COV	Cryogenic Outer Veto
CRAB	Calibrated nuclear Recoils for Accurate Bolometry
DAQ	Data Aquisition
DC	Direct Coupling
DFT	Discrete Fourier Transform
dru	Dark Matter Rate units (counts/keV kg day)
ESS	European Spallation Source
FWHM	Full Width at Half Maximum
HEMT	High Electron Mobility Transistor
HPA	Heater Pulse Amplitude
HPGe	High Purity Germanium
IAEA	International Atomic Energy Agency
IBD	Inverse Beta Decay
LANSCE	Los Alamos Neutron Science Center
LANTERN	LED Array for Non-Intrusive Tuning of the Energy Range with Nimbleness
LAr	Liquid Argon
LEE	Low Energy Excess
LMA	standard Large Mixing Angle
MOSFET	Metal-Oxide-Semiconductor Field-Effect Transistor
MV	Muon Veto
m.w.e.	Meter Water Equivalent
NEP	Noise Equivalent Power
NIN	Neutrino Induced Neutrons
NPSD	Noise Power Spectral Density
NSI	Non-Standard Interactions
PE	Polyethylene
PMT	PhotoMultiplier Tube
ROI	Region-Of-Interest
RMS	Root Mean Square
SiPM	Silicon PhotoMultiplier

SM	Standard Model
SNF	Spent Nuclear Fuel
SNR	Signal-to-Noise Ratio
SNS	Spallation Neutron Source
SQUID	Superconducting Quantum Interference Device
TES	Transition-Edge Sensor
TPC	Time Projection Chamber
TTL	Transistor Transistor Logic
TUM	Technische Universität München
UGL	Underground Laboratory
VNS	Very Near Site
WIMP	Weakly Interacting Massive Particles
WLS	Wavelength Shifting

Chapter 1

Coherent Elastic Neutrino Nucleus Scattering

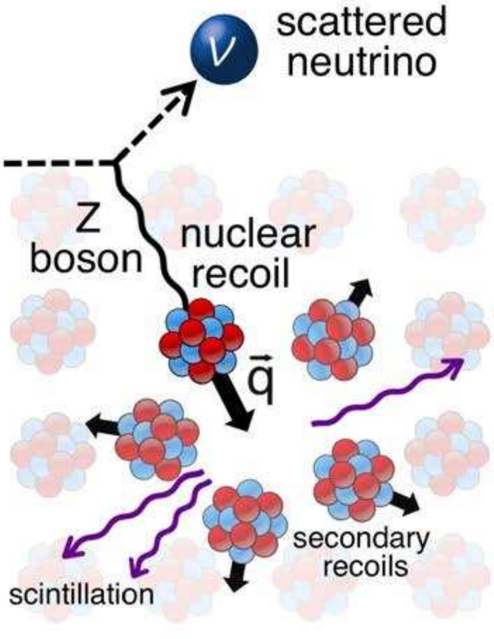

Figure 1.1. Artistic depiction of the coherent elastic neutrino-nucleus scattering presented in [1].

Measurements taken from the Gargamelle neutrino experiment in 1973 suggested the presence of neutral-current interactions between neutrinos and hadronic matter [2]. Based on this observation, Daniel Z. Freedman in 1974 proposed the presence of an elastic scattering process between neutrinos and atomic nuclei with a sharp coherent forward peak [3]. This process, shown in Figure 1.1, is now known as *coherent elastic neutrino-nucleus scattering* (CEνNS) and was measured for the first time in 2017 by the COHERENT experiment [1]. In this process, a neutrino scatters elastically via the exchange of a neutral Z boson with an atomic nucleus producing a recoil of the latter, which is the only physical observable of the process.

The long period, 43 years, elapsed between the initial prediction of the process and the first measurement is due to the important experimental challenges. Already in 1974 Freedman defines his proposal as “an act of hubris” and says that CEνNS experiments would be “very difficult” since the measurements are limited by the interaction rate, with the consequent requirement of low background levels, and the low energy threshold needed to measure the nuclear recoils.

In this chapter, an overview on the main characteristics of this interaction along with some applications and the current experimental status are presented.

1.1 Standard Model Cross-section

CEνNS is a neutrino-matter interaction predicted by the standard model. A derivation from first principles of the differential cross-section is presented in [4, 5] and yields the following equation for a spin 0 nucleus:

$$\frac{d\sigma_{\mathrm{CE}\nu\mathrm{NS}}}{dT} = \frac{G_F^2}{4\pi} M_A Q_W^2 \left(1 - \frac{T}{E_\nu} - \frac{M_A T}{2E_\nu^2}\right) F^2(q^2) \tag{1.1}$$

where G_F is the Fermi constant, E_ν^2 is the energy of the incoming neutrino, T is the nuclear recoil energy, q is the transferred momentum in the interaction, Q_W^2 and M_A are respectively the weak charge and the mass of the target nucleus and $F(q^2)$ is the nuclear form factor.

The term *coherent* in the name of the interaction is given by the fact that the incoming neutrino does not transfer to the nucleus a high enough momentum to distinguish its internal structure, meaning that the contributions from all the nucleons sum up coherently, greatly enhancing the cross-section. In eq. (1.1) this is described by the nuclear form factor $F(q^2)$ which encodes the information of how much the neutrino scattering is affected by the nucleon distribution, this term can be set to $F(q^2) \approx 1$ when the coherency condition is fully satisfied (see section 1.1.2).

The kinematics of a two body elastic scattering yields the following relations between the neutrino energy and the nuclear recoil:

$$q^2 = 2E_\nu^2(1 - \cos(\theta)) \longrightarrow q_{max} = 2E_\nu \tag{1.2}$$

$$T = \frac{q^2}{2M_A} = \frac{E_\nu^2(1 - \cos(\theta))}{M_A} \longrightarrow T_{max} = \frac{2E_\nu^2}{M_A} \qquad \langle T \rangle = \frac{2E_\nu^2}{3M_A} \tag{1.3}$$

where θ is the scattering angle with respect to the direction of the incoming neutrino.

Considering the coherency, i.e. disregarding the form factor in the integration, and the expression for the maximum recoil energy just derived, it is possible to integrate eq. (1.1) from 0 to T_{max} obtaining an approximate for of the total cross-section for low momentum transfer:

$$\sigma_{\text{CE}\nu\text{NS}} = \frac{G_F^2}{4\pi} E_\nu^2 Q_W^2 \left(1 - \frac{2E_\nu}{M_A}\right) F^2(q^2) \tag{1.4}$$

Compared to other neutrino-matter interactions (see Figure 1.2), CEνNS has one of the highest cross-sections for neutrino energies at the MeV scale. Moreover, being an elastic scattering there is no minimum energy requirement, giving the possibility to measure neutrinos down to extremely low energies.

1.1.1 Mass Scaling

In eq. (1.1) and eq. (1.4) the term Q_W is the total weak charged of the nucleus, which for an element with N neutrons and Z protons is given by:

$$Q_W = N - \epsilon Z \qquad \epsilon = 1 - 4\sin^2(\theta_W) \tag{1.5}$$

where θ_W is the weak mixing angle (Weinberg angle). Getting the average value of $\sin^2(\theta_W)$ from [6] one has that $\epsilon \approx 0.075$. Due to the small value of ϵ the main contribution to Q_W is thus given from the neutrons, meaning that cross-section scales like N^2 as visible from the vertical scaling of the CEνNS cross-sections in Figure 1.2. Due to the quadratic scaling of the cross-section with the number of neutrons (i.e. a quadratic scaling with the nuclear mass), it is tempting to choose heavy nuclei as the interaction target, but this goes in conflict with experimental challenges since the detectable nuclear recoil energy scales as M_A^{-1}, as shown in eq. (1.3), meaning that depending on the technologies employed and the neutrino source used there is an optimal target for the interaction.

1.1.2 Coherency and form factor

The nuclear form factor, present in eq. (1.1) and eq. (1.4), describes the weak charge distribution inside the nucleus, meaning that it is related to the nucleon density. In fact, the definition of the weak nuclear form factor for a nucleus with N neutrons and Z protons is:

$$F(q^2) = \frac{1}{Q_W}\Big(N F_N(q^2) - \epsilon Z F_Z(q^2)\Big) \tag{1.6}$$

$$F_i(q^2) = 4\pi \int \rho_i(r) \frac{\sin(qr)}{qr} r^2 dr \qquad i = N, Z \tag{1.7}$$

where $F_N(q^2)$ and $F_Z(q^2)$ are respectively the nuclear neutron and proton form factors and $\rho_N(r)$ and $\rho_Z(N)$ are the normalized nuclear densities for neutrons and protons. From these definitions, it is noticeable that the form factor is the Fourier transform of the nucleon density, where each type of nucleon is weighted with the appropriate weak charge. When the coherency condition $F(q^2) \approx 1$ is imposed, it means that for every r the term $\dfrac{\sin(qr)}{qr}$ is approximately 1. Since r

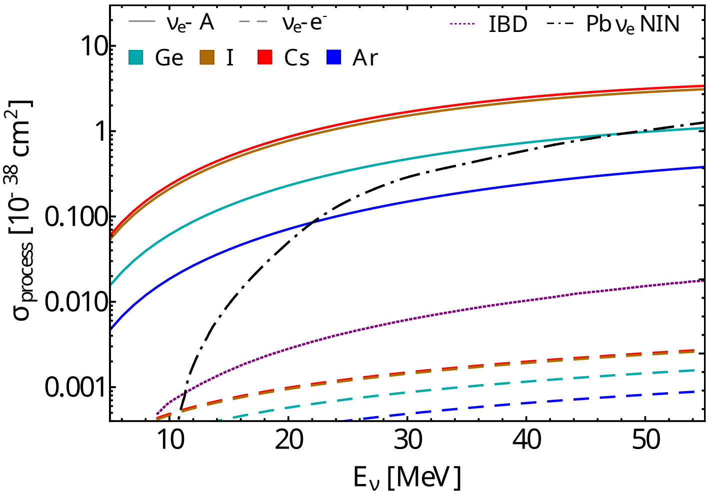

Figure 1.2. CEνNS cross-section compared with other neutrino-matter interactions [7]. The color coding identifies the target materials: argon (blue), cesium (red), iodine (brown), germanium (dark cyan). The line-style indicates the type of interaction: CEνNS (solid), neutrino-electron (dashed). The cross-sections of Inverse Beta Decay (IBD) and Neutrino Induced Neutrons (NIN) on lead are respectively shown as a dotted purple line and a dashed black line.

is the radial integration position inside the nucleus it can at most reach R_A, the nuclear radius, meaning that for $\frac{\sin(qr)}{qr} \leq \frac{\sin(qR_A)}{qR_A} \approx 1$ is equivalent to requiring $qR_A \ll 1$. This is what gives an upper bound to the neutrino energy before the form factor starts majorly influencing the cross-section value. Failing to fulfill the requirement of coherency brings quite a steep decrease of the cross-section, as visible from Figure 1.3. A quantitative estimation for the maximum neutrino energy for targets ranging from helium (He) to uranium (U) is [8]:

$$E_\nu = \frac{q_{max}}{2} \ll \frac{1}{2R_A} \approx 17\text{MeV(U)} \div 60\text{MeV(He)} \tag{1.8}$$

meaning that only neutrinos below the MeV scale can undergo a fully coherent elastic scattering with atomic nuclei. For such neutrino energies the maximum nuclear recoil energy produced is of the order of at most few tens of keV making the detection of this process quite a technological challenge.

1.1.3 Radiative Corrections and Neutrino Flavor Sensibility

The coherent elastic neutrino-nucleus scattering cross-section presented in eqs. (1.1) and (1.4) is flavor independent, this is true only at tree-level. Taking into account the radiative corrections [10] (like neutrino charge radius, WW or ZZ boxes, etc ...) modifies the cross-section coupling parameters, which in turn introduce a neutrino flavor dependence at a few percent level as shown in the bottom panel of Figure 1.4.

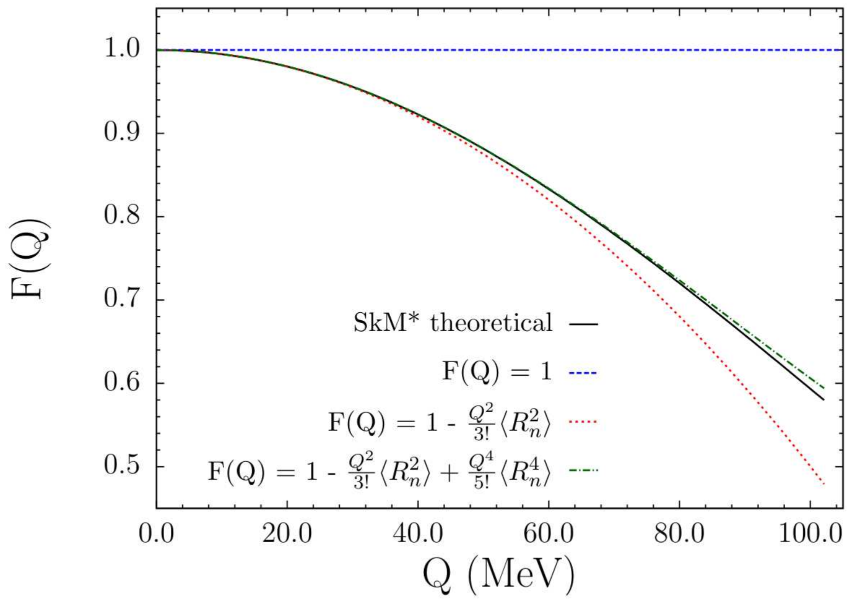

Figure 1.3. Nuclear form factor scaling with respect to transferred momentum Q (figure from [9]).

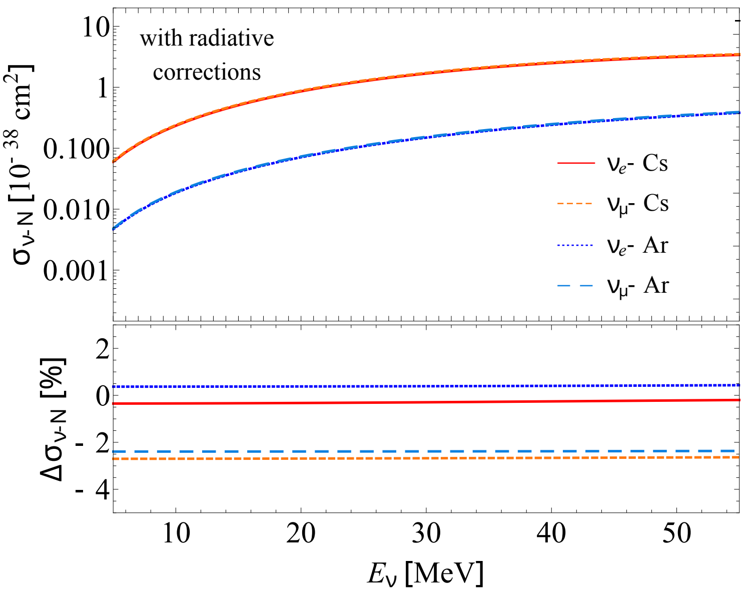

Figure 1.4. CEνNS cross-section radiative corrections based on neutrino flavor [7]. Top: value of the radiative CEνNS cross-section for ν_e and ν_μ neutrinos scattering off Ar and Cs nuclei. Bottom: percentage variation of the radiative CEνNS cross-section from the tree-level one.

1.2 First CEνNS measurement by COHERENT

In this section a brief overview of the first CEνNS detection published in [1] is described in order to later discuss what are the possible scientific reaches of CEνNS both theoretically and experimentally (a more complete review of the discovery can

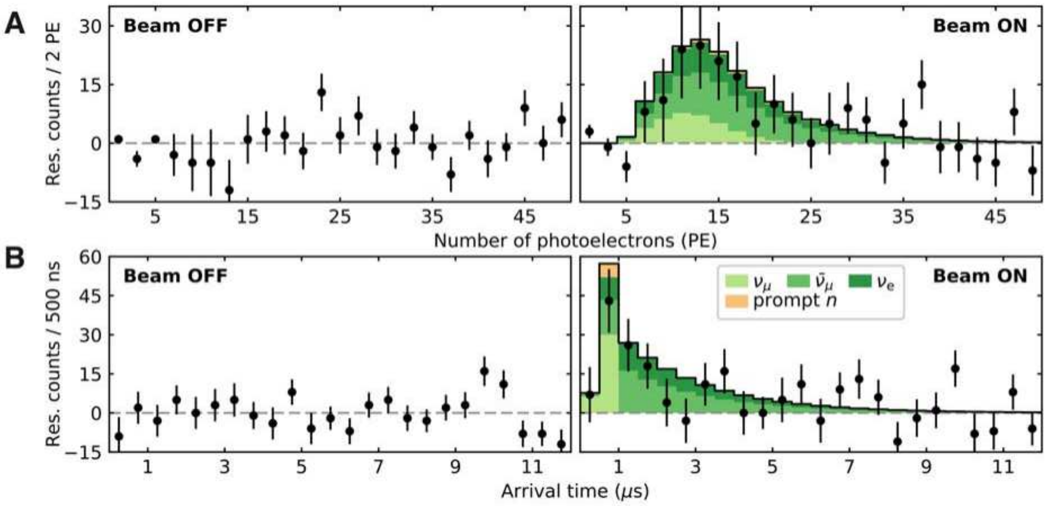

Figure 1.5. Residual difference (data points) between the signals before (left) and after (right) the neutrino production compared with the expected distributions of signal(green) and background (yellow) histograms. Top: Distribution of the nuclear recoil energy spectrum expressed as the number of photoelectrons. Bottom: Distribution of the arrival time of the neutrinos. Figure from [1].

be found in [8]).

In 2017 an article was published on Science presenting the first ever measurement of CEνNS. with a 6.7 σ significance performed by the COHERENT collaboration [1]. The measurement was done at the Spallation Neutron Source (SNS) (Oak Ridge National Laboratory) using a stopped pion neutrino source. The ν_μ, $\overline{\nu_\mu}$ and ν_e neutrinos are produced by the decay of the pions, generated using a proton beam impinging on a mercury target, and have energies of few tens of MeV (at most ~ 50 MeV). Moreover, due to the beam rate and duration and to the different pion decay times, the various neutrino flavors arrive at the detector with a well-defined time profile as visible from the bottom panel in Figure 1.5.

For this first detector, the COHERENT experiment employed a 14.57 kg sodium-doped CsI scintillating crystal readout using a Hamamatsu R877-100 photomultiplier. The detector was surrounded by high-density polyethylene, low background lead, lead, a muon veto and 9 cm of water (see Figure 1.6). To further shield the detector from beam related backgrounds, the CsI[Na] was placed in the *neutrino alley*, which is a corridor separated from the neutrino-production site by 20 to 30 meters (depending on the exact position in the corridor) of concrete and rocks as shown in Figure 1.7.

Apart from the importance of this being the first direct CEνNS measurement, in this paper one can already notice the several problems that experiments in this field have to face, mainly due to background reduction. COHERENT is in the very favorable situation of having an extremely low background, in fact, aside from the shields, muon veto and site overburden, using a beam to produce the neutrinos allows for a strong cut on the arrival time of the neutrinos to effectively select only the interesting events. This, on the other hand, comes at a cost of quite high neutrino

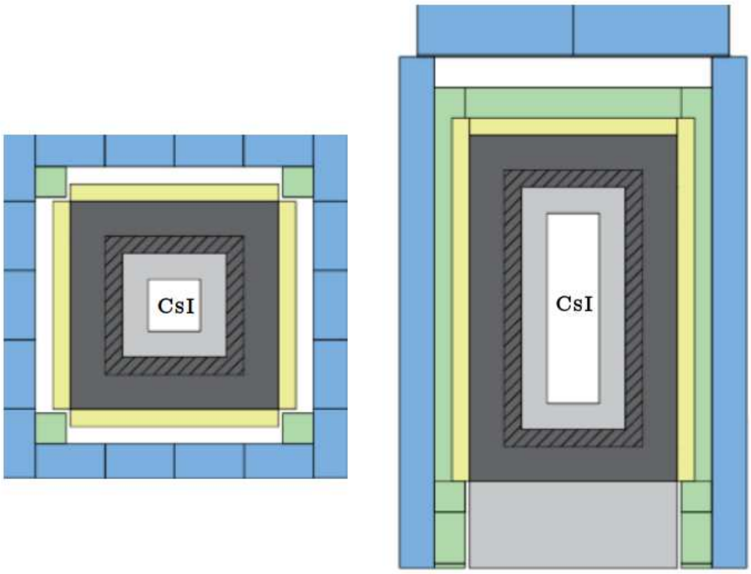

Layer	HDPE	Low Backg. Lead	Lead	Muon Veto	Water
Thickness	7.5cm	5cm	10cm	5cm	9cm
Colour	⬜	▨	⬛	🟨	🟦

Figure 1.6. Schematics of the COHERENT detector used in [1]. Figure from [11].

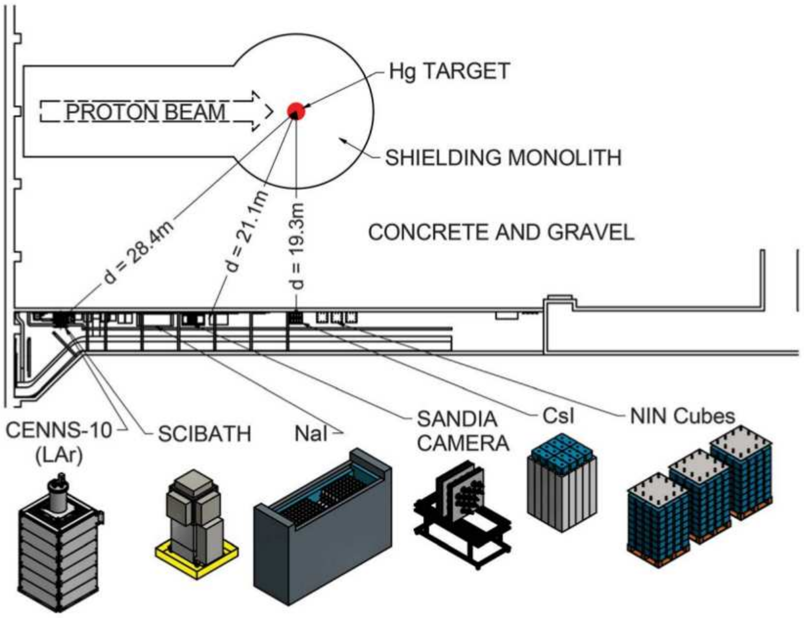

Figure 1.7. Schematic representation of the site used by COHERENT in [1] and in current measurements. The CsI detector is the one used to take the data presented in [1]. Figure from [1].

energies, making the scattering not fully coherent despite the collaboration name (see section 1.1.2).

1.3 Applications

The first detection of CEνNS in 2017 (see section 1.2) was a major incentive in investigating potential applications for this interaction. It has been shown that the coherent elastic neutrino-nucleus scattering can be used to put constraints on several fundamental physics parameters along with being able to test multiple beyond standard model theories. Moreover, due to the dependence from the nuclear form factor (visible when relaxing the coherency requirement) CEνNS can be exploited to measure nuclear form factors putting constraints on nuclear models which are applied in a variety of fields.

Apart from being a useful probe for fundamental physics, CEνNS has other broader applications since it has a relatively high cross-section and no energy threshold. In fact, it has been proposed as a tool for nuclear reactor and nuclear waste monitoring for both civilian and military applications. For the same reasons, it can also be exploited to build a new generation of supernovae telescopes, increasing the tools for multimessenger astronomy.

In this section, these applications are qualitatively described without having the pretense of being an exhaustive or complete review.

1.3.1 Search for Physics in the Standard Model and Beyond

CEνNS is an interesting interaction for the confirmation of several Standard Model (SM) parameters and is consequently sensitive to Beyond Standard Model (BSM) phenomena.

1.3.1.1 Weak angle

Evaluating experimentally the value of the weak mixing angle $\sin^2\theta_W$ provides a direct probe of BSM phenomena and the neutral current nature of CEνNS, along with the low energies at play, make it a precious tool to explore this key parameter. In particular, deviation of $\sin^2\theta_W$ from the SM value can indicate the presence of new bosons, like the dark Z boson [12]. Measurement of this parameter is correlated with the neutron Root Mean Square (RMS) radius of the nuclei considered (see section 1.3.3).

Apart from being a powerful BSM probe, the weak mixing angle is a key parameter describing all weak processes and is therefore of the utmost importance to have precise measurements of its value and scaling. As visible from Figure 1.8, most of the experiments so far can only probe $\sin^2\theta_W$ at high momentum transfer while CEνNS allows to place data points in the still relatively empty low momentum transfer regime.

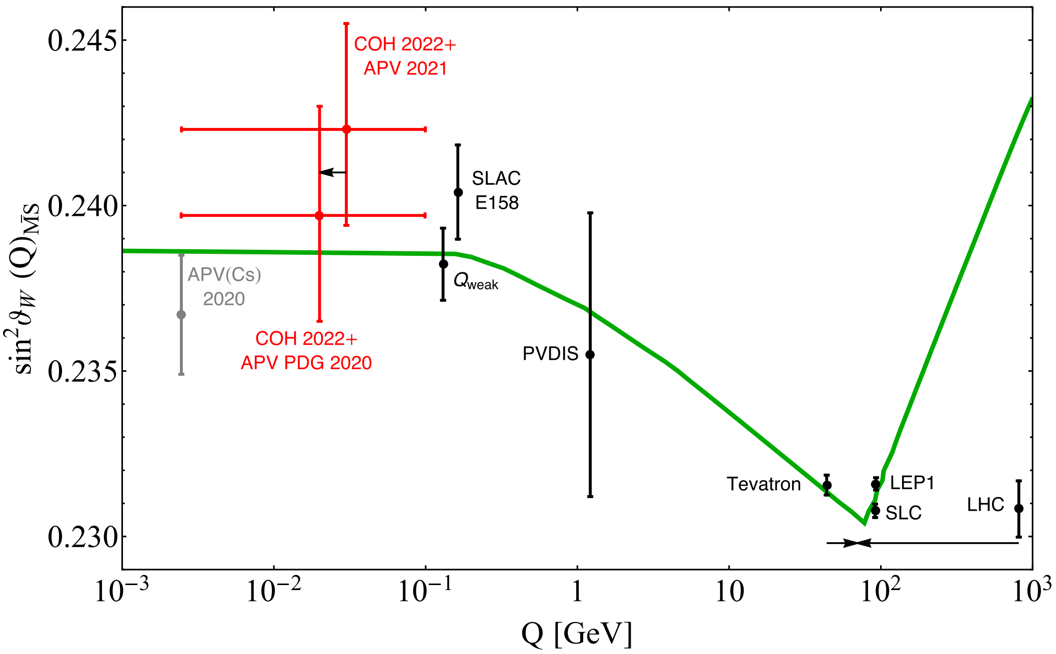

Figure 1.8. Running of the weak mixing angle in the SM (green line) as a function of the transferred momentum Q. The black points represent the status of the art of the measurements, while the red points show the determinations from the combined analysis of APV(Cs) and COHERENT-CsI measurements. Figure from [12]).

1.3.1.2 Non-standard interactions

Already from the first CEνNS measurement, it has been clear that this interaction is a powerful probe of neutrino Non-Standard Interactions (NSI). This class of interactions would be a consequence of a new force feebly coupled to the SM particle and would manifest as anomalous couplings between neutrinos and quarks. As stated in [13], the NSI parameters are not exhaustively tested in neutrino-oscillation experiments, while CEνNS has the ability of breaking the parameter degeneracies. In particular, NSI would affect CEνNS by changing the weak charge and introducing a flavor dependence [13] allowing for studies on standard Large Mixing Angle (LMA) model, initially proposed to solve the solar neutrino problem, and LMA-dark model, which has implications is several exotic neutrino interactions (like Majorana and sterile neutrinos). With the first CEνNS detection by COHERENT (see section 1.2) limits on LMA-dark were placed strongly disproving these NSI parameters.

Additionally, CEνNS is a direct probe for new mediators that may explain the $g-2$ measurement of the muon anomalous magnetic moment [14]. In particular, if NSIs from heavy vector mediators are considered, the coupling between neutrinos and quarks is modified changing the CEνNS rate and spectral shape due to enhanced flavor dependence. Precision measurements of CEνNS, both from reactor and beam neutrinos, coupled with cosmological constraints, can give quite stringent limits on the dark photon which could explain the anomaly of the $g-2$ measurement. Apart from the dark photon, also the existence of light mediators can be tested, such as the Z' light mediator and related models are proposed in [15].

Since CEνNS is a weak neutral current process, it is insensitive to neutrino flavor (at tree-level) and thus allows measurements of the whole SM neutrino spectra. In the case of sterile neutrinos, these would not interact via any weak process causing a sizable reduction of the CEνNS rate. The search for sterile neutrinos via CEνNS is complementary to the one undertaken from oscillation experiments, since it is unaffected by the uncertainty on the oscillation parameters [13].

Finally, CEνNS can also be used to test the BSM neutrino magnetic moment and leptoquark models. The neutrino magnetic moment is one of the most investigated neutrino electromagnetic properties, since it is an observable which is extremely sensitive to BSM physics. Moreover, a precise measurement of the magnetic moment can be an indirect measurement to distinguish Dirac and Majorana neutrinos [16]. Leptoquarks are hypothetical BSM particles that couple to both leptons and baryons, unifying matter within the SM and are predicted by grand unified theories. Since leptoquarks are involved in the neutrino-quark interactions, one can write effective and model independent Lagrangians to study couplings and masses of these exotic type of particles, for more details refer to [17].

More detailed discussions on the CEνNS potential to constrain the various non-standard and beyond standard model interactions can be found in [18].

1.3.2 Non-proliferation and monitor of spent nuclear fuel

The control of fissile materials, both in civil and military denominations, is a central concern since 1946. In 1957 the International Atomic Energy Agency (IAEA) was created with the objective of closely monitoring all stages of fissile material production, from uranium mining to storage of the Spent Nuclear Fuel (SNF), via inspections and accounting measures (which at the moment are the main form of control). For several decades now physicists have entertained the possibility to use neutrinos as a way to ensure nuclear non-proliferation and reactor monitoring, here a discussion about this topic will be presented with particular focus on the CEνNS use-case following the reasoning presented in [19].

There are four main man-made neutrino sources: accelerators, nuclear reactors, atomic bombs and SNF storage; in this section the last three will be analyzed in the context of nuclear monitoring. The neutrinos in these sources are not produced in the fission processes themselves but by the β-decay of the remaining fission fragments, which in a typical decay chain in reactor cores produce averagely 6 electron anti-neutrinos (see Figure 1.9).

At present IBD combined with water Cerenkov detection is the main technology used to detect neutrinos coming from these sources since CEνNS is not mature enough to be employed. IBD is the process in which an electronic anti-neutrino and a proton combine creating a positron and a neutron:

$$\overline{\nu_e} + p \rightarrow e^+ + n \tag{1.9}$$

due to energy conservation, this process has a minimum requirement on the neutrino energy of 1.806 MeV. The detectors that exploit this process have two main observable signals, the first is the prompt energy deposition from positron annihilation, the

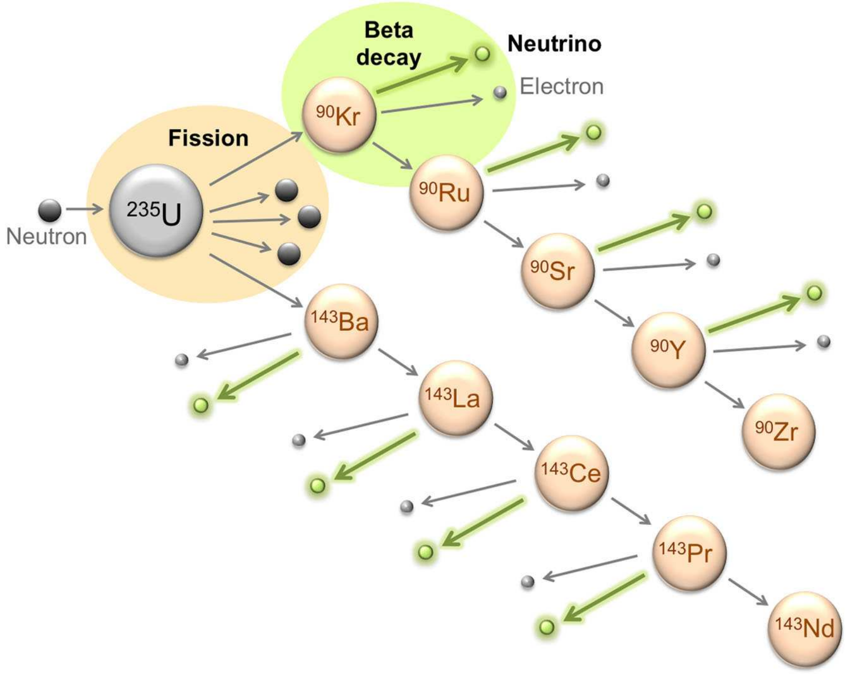

Figure 1.9. Example of the β decay chain of fission fragments, figure from [19].

second is a delayed energy deposition due to the neutron as it undergoes neutron capture. Typically, IBD based detectors are made of scintillating materials and can reach masses of at most few kilotons and, if properly segmented, can give information on the neutrino direction. The combination with water Cerenkov detectors can be achieved via gadolinium-doping and allows for a much easier mass scaling, which could reach a foreseeable $O(100\,\text{ktons})$ due to the reasonably simple and cost-effective instrumentation needed. The main drawbacks of this type of detection are the minimum neutrino energy required and the low cross-section, which demands high neutrino rates or high detector masses.

These, on the other hand, are the strong suits of CEνNS. Here the hypothesis of using this process for the same applications as IBD is entertained.

1.3.2.1 Nuclear Power Plants

The neutrino flux produced from reactor cores depends mainly on the fissile nuclides, meaning that neutrinos can be used for fuel characterization. The dominant neutrino emitters are ^{235}U, ^{238}U, ^{239}Pu and ^{241}Pu, and each is characterized by a different neutrino spectrum and intensity due to their abundance in the reactor core. The spectrum of reactor emitted electron anti-neutrinos spans energies up to ~ 8 MeV and evolves over periods from days to months, which are both ideal situations for a CEνNS measurement.

Due to the high antineutrino energies and flux, non-intrusive monitoring of known reactors is feasible both with IBD and CEνNS detectors (with the caveat that reactor CEνNS remains presently not measured). The possibility to choose and tune, in terms of background, the detector location along with the higher simplicity and technological readiness make IBD detectors an alluring choice for the monitoring and characterization of known reactor cores.

Neutrino detection is a powerful, but complex, technique to discover unknown reactors since it allows to measure the reactor emissions from long baselines. When using IBD based detectors there are several limitations: the smallness of the cross-section, the backgrounds from the rest of the hundreds of civilian reactors worldwide, cosmic-ray induced backgrounds which can be reduced only by underground deployment [19], ambient radioactivity and geoneutrinos. On the other hand, the IBD technology can be tuned to have sensitivity to the incoming direction of the neutrino. Due to the much higher CEνNS cross-section, the neutrino-nucleus elastic scattering based detectors can be much smaller and equipped with active vetoes in order to shield radiation at surface level (as planned for several reactor neutrino experiments currently under commissioning). This means that CEνNS could be a useful tool to determine wide range deviations in the expected neutrino rate.

Apart from power reactors, there are also breeder reactor that are used to produce nuclear fuel, in fact they produce more fissile material than what they consume and are typically based on the use of fast neutrons. Measuring neutrinos from these reactors is challenging because of the low rate due to the low amount of fissions occurring. On the other hand, there is a unique neutrino signature produced [19]:

$$^{238}U + n \rightarrow ^{239}U \overset{\beta^-}{\rightarrow} \ ^{239}Np \overset{\beta^-}{\rightarrow} \ ^{239}Pu \tag{1.10}$$

The two β-decays have short half-lives (24 min and 2.4 days) and end-point energies below the IBD threshold, making CEνNS the best interaction to detect and study such reactors.

Similar to reactor neutrinos, nuclear explosions produce an intense burst of electron anti-neutrinos up to $\sim$ 8 MeV. The main way of detecting such phenomena is via seismic observations which, on the other hand, could be claimed to have been produced by conventional explosions if no radiation is detected, making neutrinos a unique signature for such phenomena. Similar issues with determining the presence of unknown power reactors are with IBD and CEνNS are valid in this case.

1.3.2.2 Spent Nuclear Fuel

Current methods and future plans for long term storage of SNF make use of geological storage sites and dry casts which are difficult to inspect due to the below IBD threshold neutrino production, the lack of surrounding water (used in wet storage facilities) which could be used for water Cerenkov detection and to the heavy shielding and self-shielding effects of any other type of radiation.

As modeled by Sargent's rule, the β-decay neutrinos emitted from SNF have lower energies than the ones emitted from reactors, since most of the high energy β-emitters have half lives of at most few months [19]. The dominant neutrino emission in SNF arises from the ^{90}Sr/^{90}Y decay chain, which, having a half life of 28 years, remains measurable for many decades.

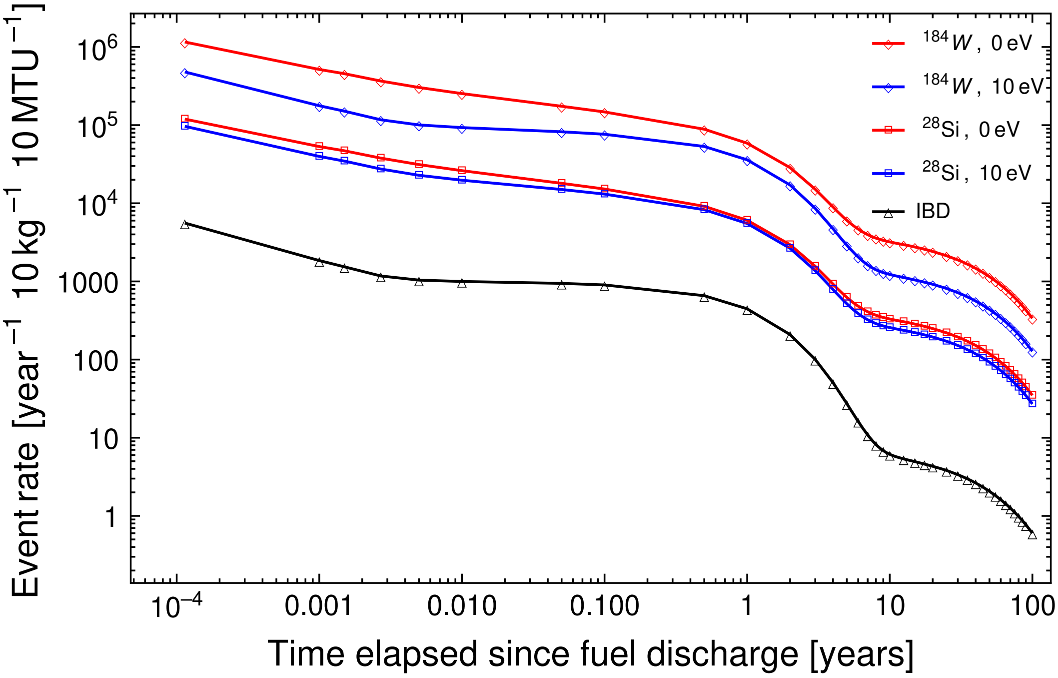

Figure 1.10. Expected event rate for CEνNS in ^{184}W and ^{28}Si detector able to resolve down to 0 eV (red) or 10 eV (blue), compared to IBD rate (black) of a same size detector (10 kg mass). The detectors are placed at a 10 MTU (metric ton of uranium) source with a 3 m standoff (figure from [20]).

The non-intrusive monitoring of SNF is where CEνNS has a decisive advantage on IBD. In fact, the neutrinos emitted by ^{90}Sr/ ^{90}Y decays have an endpoint of 2.28 MeV which translates to a $O(10^{-46}$ cm$^2)$ IBD cross-section due to the threshold [20], on the other hand, as already mentioned in section 1.1.1, CEνNS has already quite a higher cross-section and also no threshold meaning that a measurement of the whole SNF neutrino spectrum is possible (a comparison for this scenario is presented in Figure 1.10). Due to the higher event rate in a CEνNS based detector, the mass required to achieve few percent level accuracy on fuel measurements is of the order of 10 kg (if low enough threshold and background levels are achieved). Moreover, due to the compact nature of CEνNS detectors, they can be placed few meters away from each dry cast allowing for sensitivity to single cast removals, which is unachievable with IBD detectors [20].

1.3.3 Measurement of the nuclear form factors

As already mentioned in section 1.1.2, neutrino-nucleus elastic scattering is affected by the nuclear form factor if the neutrino energy is not low enough. In [21] the potential of using CEνNS to measure the nuclear form factor is analyzed by showcasing a proof of principle by using the data described in section 1.2.

From the weak form factor definition in eq. (1.6) it is visible that weak neutral current processes are mainly sensitive to the neutron nuclear form factor, since the proton one is weighted with ϵ. This feature makes CEνNS a powerful process for

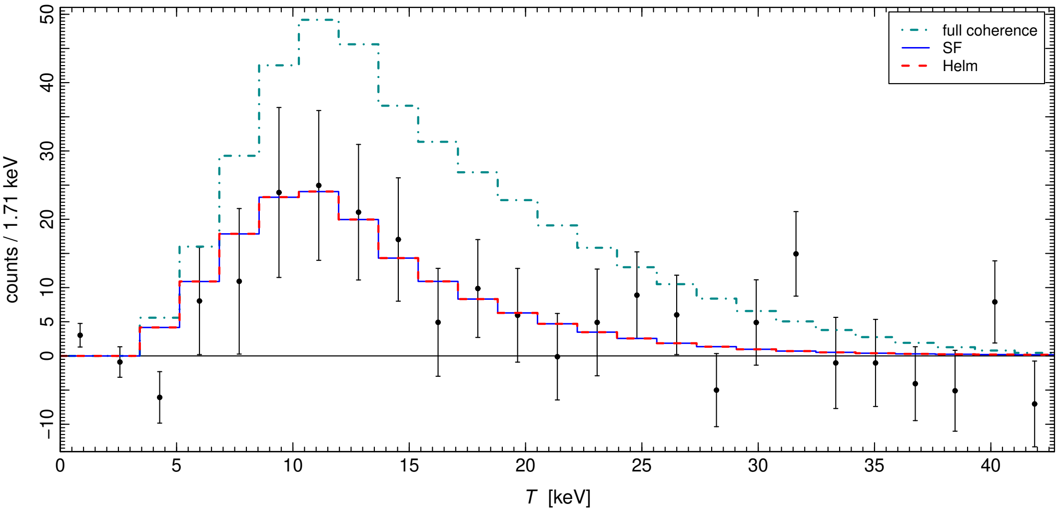

Figure 1.11. Comparison of the CEνNS spectrum measured by the first COHERENT campaign [1] (black data points) with different nuclear form factor models and the fully coherent regime (figure from [21]).

nuclear studies. In fact, while the proton nuclear form factor can be measured using electromagnetic processes [22, 23] (like elastic electron-nucleus scattering, muonic atom spectroscopy, etc...) a measurement of the neutron nuclear form factor is more challenging.

In Figure 1.11 it is shown the effect of the nuclear form factor on the CEνNS rate measured by the COHERENT experiment in [1], the data (after a background subtraction) was fitted with various nuclear density models and compared with the prediction obtained using a fully coherent CEνNS cross-section (i.e. with a unitary form factor). It is evident from Figure 1.11 that the form factor plays an important role in the rate, lowering it by almost a factor two, since, as already mentioned in section 1.2, the experiment was not performed under full coherency. Moreover, it is shown that different form factor models converge to essentially the same results.

Cadeddu, in [21], shows that from the form factor fit presented in Figure 1.11, it is possible to extract the neutron RMS radius of the target nuclei. This quantity represents the average spatial dispersion of neutrons from the center of an atomic nucleus and from the fit it is evaluated to be:

$$R_n = 5.5^{+0.9}_{-1.1}\ \text{fm}$$

which is compatible with expectations on both cesium and iodine, which are considered identical since the uncertainty on the data does not provide such discrimination power. The expectations are computed by projecting previous results obtained on lead and also from ab-initio calculations, both presented in [21].

Having knowledge on the neutron nuclear form factor is relevant in various fields of research aside from purely atomic nuclei characterization. The most direct implication is to lower the background for the direct detection of Weakly Interacting Massive Particles (WIMP), since it allows for a precise determination of the irreducible

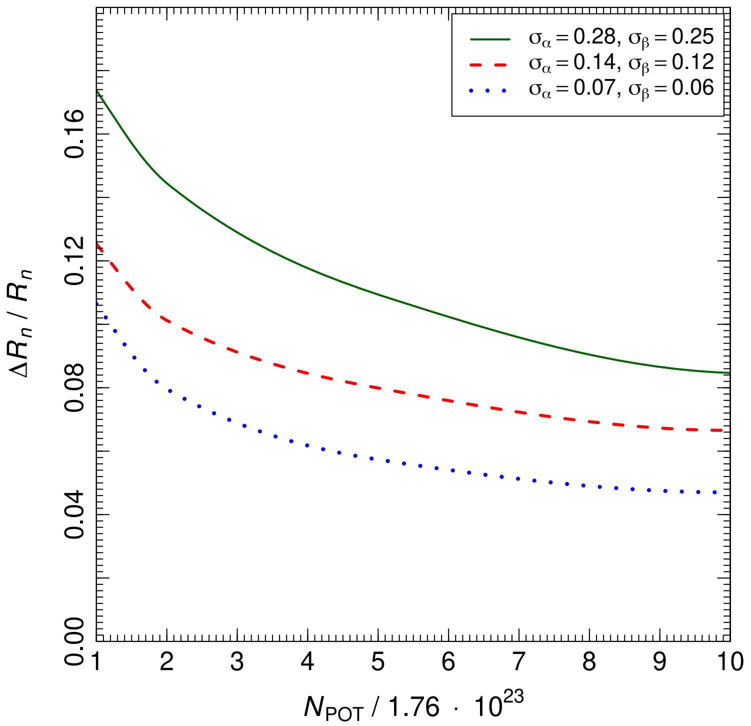

Figure 1.12. Projected relative uncertainty on the neutron RMS radius R_n of cesium and iodine nuclei as a function of the number of neutrinos produced (proportional to the number of protons on target N_{POT}) with data from the COHERENT experiment. The projection is presented for various levels of systematic uncertainties: current (solid green), half of current (dashed red) and one-quarter of current (dotted blue). The figure is taken from the study presented in [21].

CEνNS background. Estimating the neutron RMS radius of nuclei is important to characterized neutron-rich matter as neutron starts, since it impacts their volume and the gravitational signals emitted by these astrophysical systems. By performing further measurements of CEνNS with the COHERENT experimental setup it is possible, increasing the neutrino rate, to reach uncertainties on the neutron RMS radius of cesium and iodine at the 10% level and by reducing the systematical uncertainties it is possible to reach precisions of few percent as shown in Figure 1.12.

This brief discussion showcases the validity of the elastic neutrino-nucleus scattering with relaxed requirements on the coherency as a tool to investigate the internal structure of atomic nuclei.

1.3.4 Supernova neutrino detection

The detection of supernovae neutrino has always been an alluring scientific prospect since they are direct probes of the stellar core, which is not accessible through γ detection. During a supernovae collapse around 10^{58} neutrinos and anti-neutrinos of all flavors are emitted in around 10 s releasing about 99% of the collapse energy. Due to the multiple neutrino types emitted, IBD is not the ideal interaction to use since it is only sensitive to electron neutrinos while CEνNS already greatly increases exposure by simply being sensitive to all neutrinos. Combining this with the large CEνNS cross-section allows to build fairly compact neutrino telescopes to be deployed in underground laboratories. For this type of application, one typically refers to CEνNS glow, since in a short time thousands of isotropically diffused neutrino scatters can be detected. This type of signal can be visible either by a dedicated neutrino telescope [24] or by dark matter detectors (see section 1.4.7). Key requirements for this detection, common to all CEνNS measurements, are low background and low threshold (albeit not as stringent as reactor CEνNS) in order to maximize the measured neutrino event rate.

1.4 Overview of the current experiments

In the panorama of CEνNS experiments, one can distinguish two main research branches: the reactor CEνNS experiments (like the NUCLEUS experiment presented in chapter 2) and the stopped pion neutrino sources experiments (like COHERENT). In this section, a brief description of these two neutrino sources is presented, along with an overview of the status and results of the main CEνNS experiments. Due to the high number of available nuclear power plants in combination with the fact that reactor CEνNS has not been measured yet, most of the experiments in this field are deploying their detectors near reactor cores. In this section, the few but meaningful experiments using a spallation neutron source are presented along with all the several technologies being commissioned at reactors.

1.4.1 Neutrino Sources for CEνNS

The neutrino sources employed for the experiments are essentially two: nuclear reactors (both power and research ones) and the so-called πDAR which stands for pion decay-at-rest.

In πDAR sources, the neutrinos are produced by making a proton beam impinge on a high-Z material. The typical beam has energies ranging from several hundreds of MeV to few GeV and produces a wide range of particles that are used for a multitude of purposes. Among these particles, the pions π_0 and $\pi^{\pm}$ are produced and give rise to neutrinos following the scheme in Figure 1.13. The main decays of these particles are: π^0 decay in two photons, π^- undergoes nuclear capture while π^+ experience a decay at rest (after $\sim$ 26 ns) producing a monochromatic neutrino-antilepton pair with 30 MeV energies each of either muonic flavor (with a $\sim$ 0.9999 branching ratio) or electronic flavor (with a $\sim$ 0.0001 branching ratio making this reaction fairly negligible). After $\sim$ 2200 ns the antimuon produced decays in $\mu^+ \rightarrow \overline{\nu_\mu} + \nu_e + e^+$, where the generated neutrinos have a well-defined energy spectrum. The ν_μ produced from the first pion decay are usually referred to as *prompt neutrinos*, while the $\overline{\nu_\mu}$, ν_e are the *delayed* component. As already mentioned in section 1.2, using this type of source is particularly favorable from a background point of view, since one can set stringent requirements on the neutrino arrival time. On the other hand, the relatively high neutrino energy usually entails a partial loss of the coherency of the measured CEνNS. The πDAR facilities in use or planned for CEνNS measurements are: the European Spallation Source (ESS) [25], the Los Alamos Neutron Science

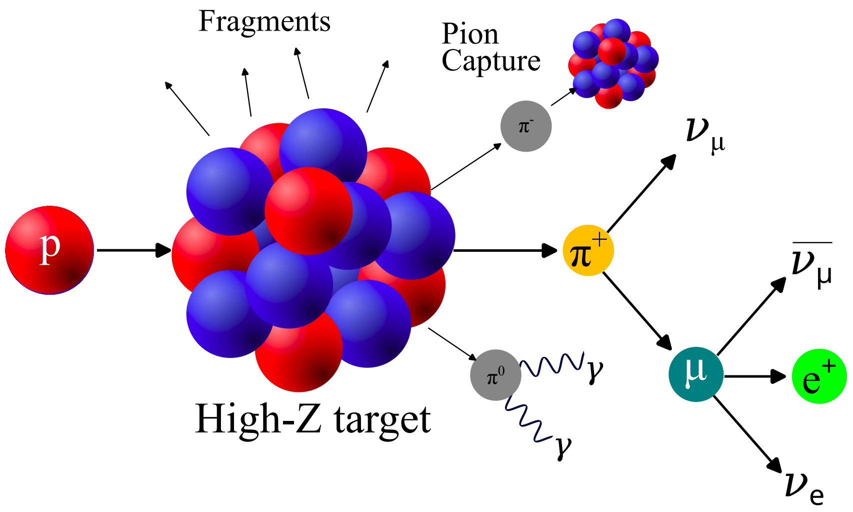

Figure 1.13. Typical process for neutrino production in πDAR neutrino sources.

Center (LANSCE) [26] and the already employed SNS [27]. An additional detail for this kind of source is that experiments usually need to be placed off-axis with respect to the proton beam, since the plethora of neutrons produced mainly propagate in the forward direction.

Reactor neutrinos have already been presented in section 1.3.2.1, a brief summary of the considerations made are presented in the following. Reactors are a pure source of $\overline{\nu_e}$ that have quite lower energies ($\leq$ 8 MeV) than the πDAR ones, meaning that the nuclear scattering happens in a fully coherent regime but also has lower recoil energies associated. Another feature of reactors as neutrino sources is that the neutrinos are not pulsed like the πDAR case but are continuously emitted, making the background reduction much more demanding. Typically, reactor CEνNS experiments employ a complex system of shields and vetoes for background reduction and if they are placed near the reactor core they need to carefully evaluate the background correlating with the reactor activity. To further increment the sensitivity of these experiments, most of them plan to perform, when possible, a comparison with reactor off data in order to directly measure backgrounds. In general, there are two types of nuclear reactors: the power and research reactors. The first ones are the ones used to create electric energy and have usually an extremely high neutrino flux, but the deployment of experiments need to follow the strict reactor security requirements. On the other hand, more simple sites are the research reactors which have lower neutrino rates, but the experimental site can be tuned to the research needs and the nuclear fuel is highly enriched ^{235}U meaning that the neutrino spectrum is known more precisely. A key aspect of reactor CEνNS is that it remains unobserved due to the unavoidable experimental challenges.

Between these two main neutrino sources for CEνNS there is complementarity since reactor neutrinos offer a pure source of electron antineutrinos allowing for more precise limits on NSI parameters as well as the lower momentum transfer which gives a lower contribution to the systematics of the form factors. On the other hand, spallation neutron source neutrinos are of multiple flavors for more broad parameter

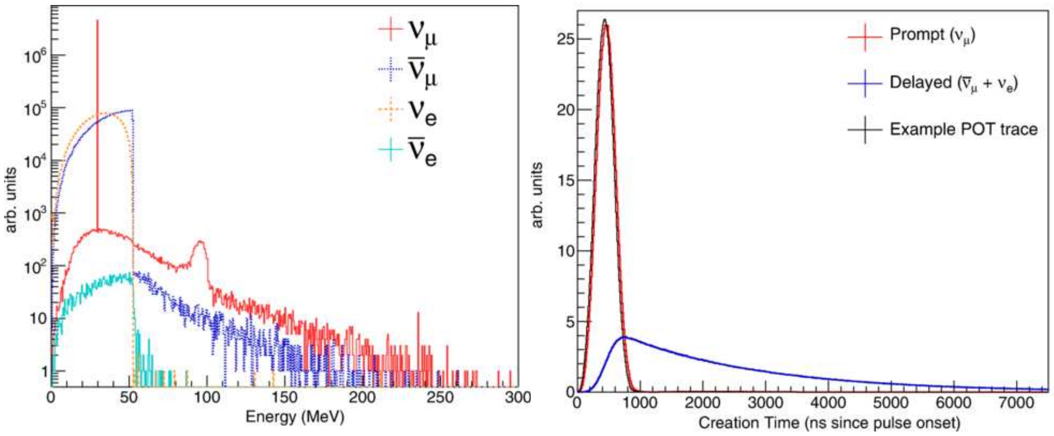

Figure 1.14. SNS neutrino characteristics. Left: neutrino energy spectrum for the various different flavors produced. Right: Spectrum of the arrival times of the different neutrino components produced in the decay chain presented in Figure 1.13 once the protons hit the beam target (POT). Figure from [29].

testing and form factor studies, and due to the easily achievable low background one can perform more systematic campaigns to constraint BSM and NSI parameters.

As shown in section 1.4.7 interesting CEνNS results from solar neutrinos are starting to appear from the realm of dark matter detectors.

1.4.2 πDAR CEνNS

1.4.2.1 COHERENT

As already anticipated in section 1.2 the COHERENT collaboration is currently leading the CEνNS experimental program. The high intensity pulsed neutrinos produced by the SNS (see Figure 1.14) along with the experimental space available allow COHERENT to deploy several detector technologies and materials to study deviations from the expected CEνNS rates. In particular, the collaboration is now conducting a data taking campaign to measure the N^2 dependence of the cross-section. The first detector used by coherent is the same CsI[Na] scintillating crystal as used in first observation (section 1.2) but new data is being taken with improved data-analysis and detector response modeling procedures are being used [28].

The second currently operational detector is a Liquid Argon (LAr) based scintillator [30] which is read out via two Hamamatsu R5912-02MOD PhotoMultiplier Tube (PMT) coupled with a wavelength shifting coating, resulting in an active mass of 24 kg. The LAr is surrounded by a ~ 20 cm layer of polytetrafluoroethylene (PTFE) to shield it from external backgrounds. The scintillation light in LAr is produced from both a fast singlet ($\tau_s \approx 6$ ns) and slow triplet ($\tau_t \approx 1600$ ns) excited molecular states. Electron and nuclear recoils populate these two scintillating states differently, allowing for efficient background discrimination.

The third is a germanium based detector referred to as Ge-Mini [31] which uses 6 high purity germanium ionization detectors. The Ge-Mini detector is not only

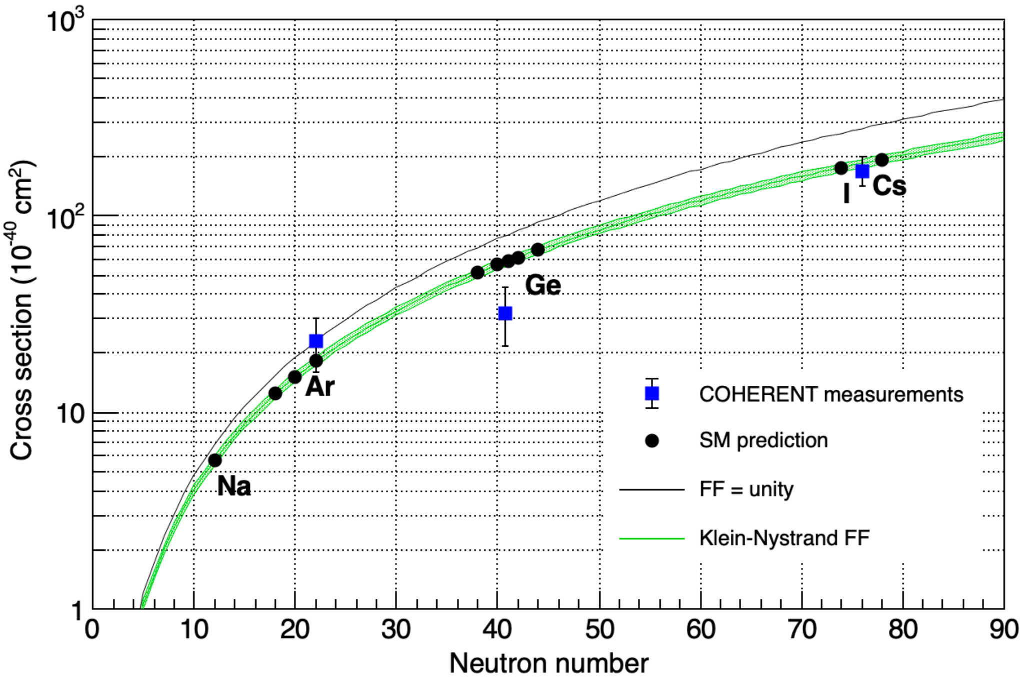

Figure 1.15. N^2 scaling of the CEνNS cross-section as measured by the COHERENT collaboration (blue data points). The black line assumes a form factor of unity, corresponding to no nuclear substructure. The green line corresponds to the cross-section weighted with a Klein-Nystrand form factor, and the width of the green line represents a ±3% uncertainty on the nuclear radius. The predictions for the isotopes relevant for the COHERENT program are shown as black dots. The blue squares with error bars are the flux-averaged COHERENT result. Figure from [33].

equipped with germanium based detectors but also exploits several layers of shields and active vetoes to reduce background contributions. This type of detector is similar to the one used in the experiments described in section 1.4.3.

The previous technologies allowed to measure CEνNS on three different materials, which in order of decreasing mass are cesium, germanium and argon. In Figure 1.15, one can see the measured scaling of the CEνNS rate and its comparison with the expected rates from the SM predictions. As already anticipated in sections 1.2 and 1.4.1, a CEνNS measurement using a πDAR neutrino source is contaminated by the non-negligible form factor, this is visible in Figure 1.15 where the data points are more compatible with the rate given using the form factor approximation described in [32]. This is the currently leading CEνNS results which opens the era for precision coherent elastic neutrino-nucleus elastic scatter measures at πDAR sources.

Aside from the groundbreaking results already achieved by this collaboration, in the near future they will benefit from several upgrades, the main one being that the SNS facility will increase its proton current and proton energy allowing for a higher neutrino flux [29]. Aside from an improvement in the neutrino production, COHERENT plans to deploy several new detectors. The first one is COH-R^{2}D$_2$O

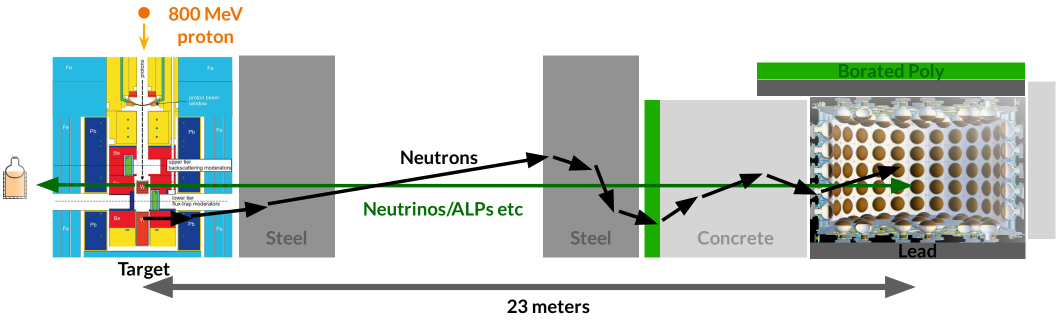

Figure 1.16. Depiction of the CCM experimental setup: left the spallation site where the neutrinos are produced and travel to the detector (right) after passing through several layers of steel and concrete for background reduction (figure from [37]).

which will be used to reduce the uncertainty (current at the 10% level) on the neutrino flux by using the well quantified neutrino capture interaction [34]. Another planned detector is COH-NaIνETe with uses 2425 kg of NaI[Tl] crystals to sense both charge and neutral current neutrino interactions [33]. The Cryo-CsI module [35] uses 10 kg of undoped CsI operated at 77 K, temperature at which the scintillation light yield is more than double the room temperature one, lowering the detection threshold. The LAr technology will be up-scaled to reach 600 kg fiducial volume, with the possibility of using underground argon. Finally, they also plan to deploy the νThor detector [36] which is aimed at studying neutrino-induced nuclear fission using thorium based technology coupled with a NaI scintillating readout for the neutrons produced by the fission.

1.4.2.2 CCM

The Coherent CAPTAIN Mills (CCM) experiment [37] is situated 90° off axis with respect to the proton beam of the LANSCE [26] spallation neutrino source. The detector consists of a 10 ton (5 ton fiducial) liquid argon (LAr) optical detector coupled with 200 PMTs (see Figure 1.16) making the experiment sensitive to energy deposits ranging from 10 keV to 200 MeV. Apart from the usual scintillation signal of LAr detectors, the CCM detector is able to distinguish the Cerenkov light produced via a smart strategy of wavelength shifting coatings on top of some PMTs. Since 2019 the experiment performed some prototype and development runs and is now commissioning the full setup. The scientific goal of the experiment is not only to make a CEνNS measurement, but is also to search for dark matter candidates produced in the hadronic interactions.

1.4.2.3 NuESS

The NuESS program [38] consists of deploying a series of different technologies at the ESS to study measure neutrino properties. Among the detectors planned for deployment there are: cryogenic undoped CsI, a p-type point contact Ge and a high pressure gas Time Projection Chamber (TPC) (see Figure 1.17). This project is still undergoing construction and finalization due also to the fact that the ESS is in the last part of the building phase which is schedule to end in $\sim$ 2025.

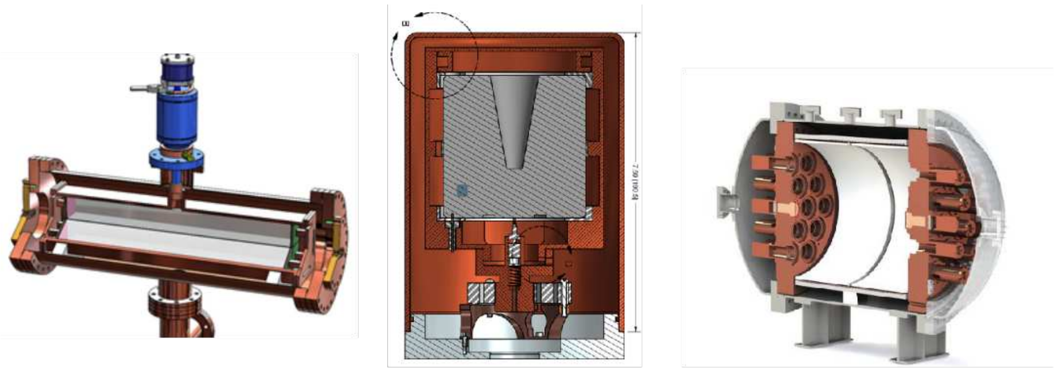

Cryogenic undoped CsI **p-type point contact Ge** **high pressure gas TPC**

Figure 1.17. Detectors planned for the NuESS project (figure from [38]).

1.4.3 Reactor Ge-CEνNS

Another class of experiments are the ones that use High Purity Germanium (HPGe) ionization detectors. These devices are extremely alluring since they are well tested, have very high levels of radio-purity and can be readout with fairly simple electronics. Moreover, the combination of the fairly easy scalability of the detector mass with the quite high atomic number of germanium makes this detector one of the ideal technologies to use for CEνNS. On the other hand, using ionization detectors to study nuclear recoils can be quite challenging due to the presence of the quenching factor (i.e. how much of the nuclear recoil energy is visible in the ionization channel). This is, in fact, one of the main sources of uncertainty, especially in the typical energy range of CEνNS where the community has not fully agreed on the model to use. The usual model used as reference is the Lindhard [39] model, which appears to be compatible with the low energy nuclear recoil measurements done so far.

1.4.3.1 CONUS and CONUS+

The CONUS experiment [40] deployed 4 HPGe crystals (total active mass $\sim$ 16 kg) at the 3.9 GW_{th} commercial nuclear power plant in Brokdorf (Germany) with a 17.1 m baseline. The crystals were deployed in a fully shielded environment, as shown in Figure 1.18, to mitigate the background, which, with a series of dedicated measurement campaigns, is completely described. During the several data taking runs between 2019 and 2022 they managed to optimize their experimental setup while setting stringent limits on reactor CEνNS. In [41] a combined analysis of all the collected data is presented, showing no hints of a direct reactor CEνNS detection, as visible from Figure 1.19. The collaboration set an upper limit (90% confidence interval) stating that the normalization of the CEνNS cross-section can deviate at most of a factor 2 with respect to the SM prediction.

Due to a controversy in the determination of the germanium quenching factor, the CONUS experiment quoted, in [41], the limits on the number of CEνNS events for different quenching factor models. It is shown that the analyzed data favors the

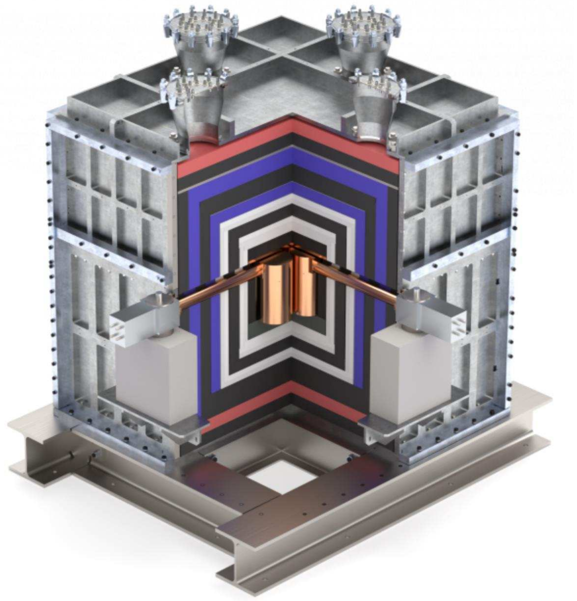

Figure 1.18. Schematic representation of the CONUS detector setup (figure from [42]).

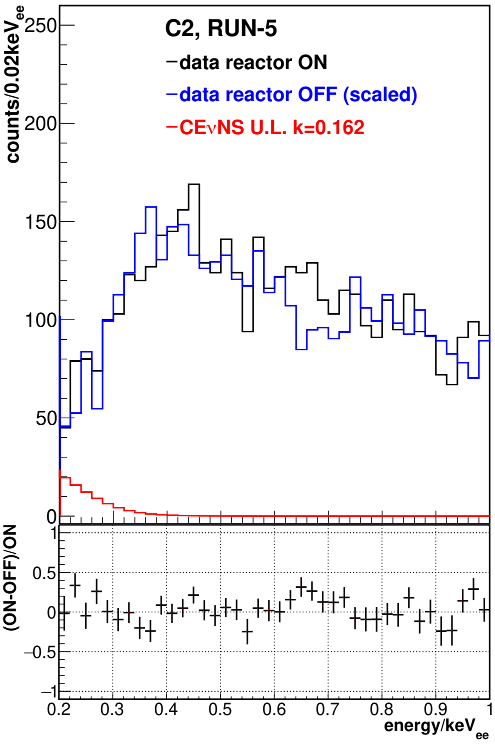

Figure 1.19. Reactor on vs reactor off data taken in Run-5 of the CONUS experiment, including the obtained upper limit of CEνNS events for the C2 detector. Figure from [41].

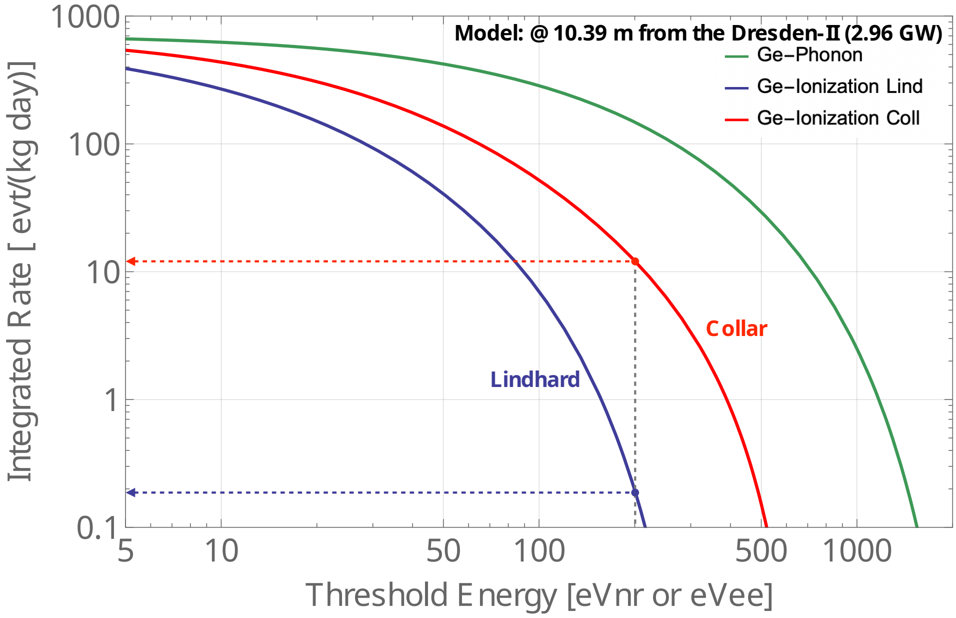

Figure 1.20. Quenching effect on the CEνNS rate measured in a DRESDEN-II like configuration. In blue the usual Lindhard model [39] used, in green the phonon signal (i.e. not affected by quenching) and in red the rate with the quenching presented in [44]. Figure from [45].

Lindhard model with a quenching factor of 0.162, which is the usual model used for germanium ionization detectors.

The experiment is being upgraded to CONUS+ [42] which will be deployed at the Leibstadt 3.6 $\mathrm{GW_{th}}$ Nuclear Power Plant (Switzerland) with a 20.7 m baseline. The upgrade impacts all the previously deployed systems, increasing the sensitivity of the experiment. The CONUS+ setup was deployed in early 2024 and is starting to take the first reactor on data.

1.4.3.2 DRESDEN II

The DRESDEN II collaboration [43] deployed an ultra-low noise germanium ionization detector ($\sim$ 3 kg) at the Dresden-II 3 $\mathrm{GW_{th}}$ nuclear reactor with a $\sim$ 10 m baseline. The experiment took 96.4 days (effective exposure) of reactor on data and 25 days of reactor off data in the first half of 2021. After a thorough measurement of the reactor related backgrounds and a comparison with the reactor off data, the collaboration measured a strong preference for an event excess due to CEνNS.

Claiming a CEνNS detection with HPGe ionization detectors is heavily reliant on the accurate evaluation of the quenching factor of the detector, as visible from Figure 1.20. The Dresden II collaboration conducted a measuring campaign to evaluate the quenching affecting their detectors and from the results presented in [44] a strong deviation from the Lindhard model [39] was measured as shown from Figure 1.21.

This result on the germanium quenching factor and the consequent CEνNS observa-

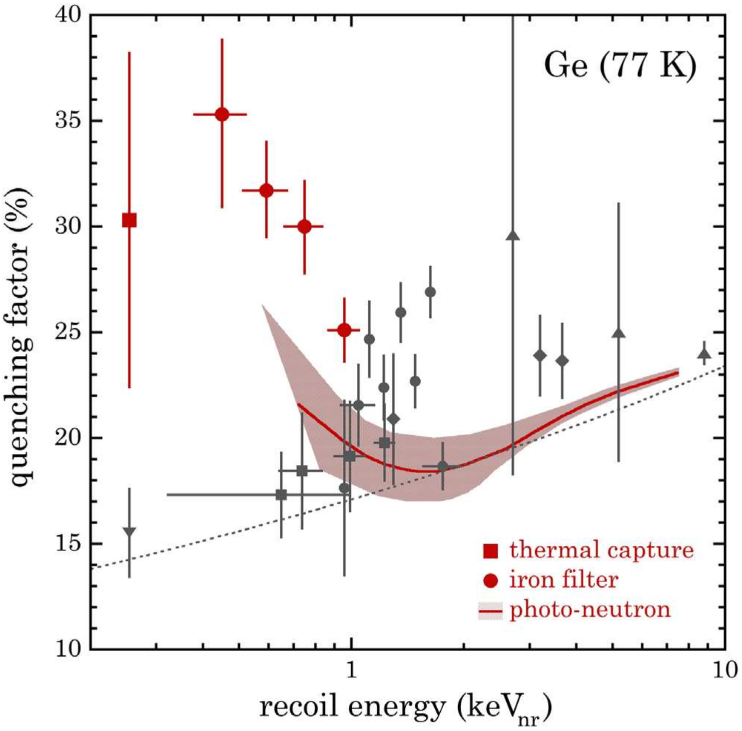

Figure 1.21. Quenching factor on HPGe ionization detectors measured by the Dresden II collaboration (labeled by calibration technique). A red band shows the 95% confidence level region for a model-independent fit of the data points. A dotted line shows the prediction from the Lindhard model. Previous measurements are shown in gray. Figure from [44].

tion have been contested by the community due to the ambiguity on the evaluation of this quantity. Moreover, the CONUS collaboration provided strong evidence that the germanium quenching factor follows indeed the prediction of Lindhard. For these reasons the Dresden II observation was thus reclassified as a wrong parametrization of the detector response model or a wrong evaluation of the background making reactor CEνNS a still unobserved phenomenon.

1.4.3.3 νGEN

The νGEN experiment [46] exploits the intense neutrino flux present at an 11 m baseline from the 3.1 GW_{th} reactor core of the Kalinin Nuclear Power Plant. The detector planned for the CEνNS measurements is made of several HPGe crystals for a total mass of 1.4 kg surrounded by several lead and polyethylene shields that combined with an active muon veto allow for background reduction (see Figure 1.22). The experimental setup was used for a first scientific run lasting 6 months in 2023 where they managed to put limits on reactor CEνNS comparable to the ones of the CONUS experiments. After this first run, the experiment is undergoing an upgrade aimed at background and threshold reduction.

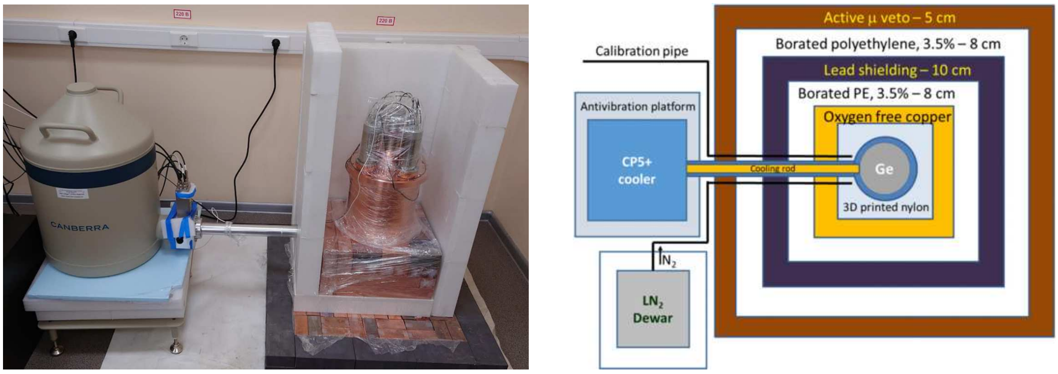

Figure 1.22. Detector setup of the νGEN experiment. Left: picture of the deployed detector. Right: schematic of the setup (figure from [47]).

Figure 1.23. Electrocooled HPGe detector from the TEXONO collaboration (figure from [49]).

1.4.3.4 TEXONO

The TEXONO collaboration [48] has been measuring neutrinos produced by the Kuo-Sheng Nuclear Power Plant -II (2.9 GW$_{\text{th}}$) since 2003 with a 28 m baseline. The collaboration deployed a 500 g HPGe detector with a 200 eV$_{\text{ee}}$ threshold surrounded by lead, polyethylene and a plastic scintillator based muon veto. A peculiarity of these HPGe detectors is that they are electrocooled allowing to reduce the background (see Figure 1.23). After an initial scientific run which demonstrated the potential of their setup, the collaboration is working on upgrading the analysis procedure along with further reducing the background components. Due to the reactor shutdown they are currently moving to the Sandmen Rx plant with 3.4 GW$_{\text{th}}$ reactor core where they have secured a location with a 11 m baseline.

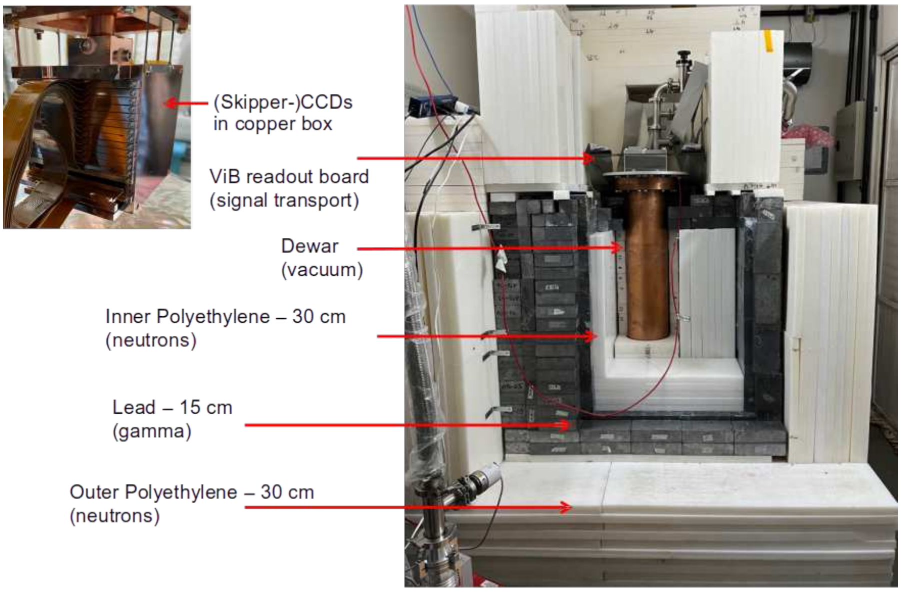

Figure 1.24. CONNIE detector setup. Top Left: Skipper-CCD copper box holder. Right: Shields and vacuum-Dewar. Figure taken from [52].

1.4.4 Reactor CEνNS with skipper CCDs

In this section, the experiments based on skipper Charge-Coupled Device (CCD) technology are presented. The peculiarity of skipper CCDs, when compared to usual CCDs, is that they allow for multiple non-destructive charge readouts, greatly decreasing the noise [50].

1.4.4.1 CONNIE

The Coherent Neutrino-Nucleus Interaction Experiment (CONNIE) deploys scientific skipper CCD made with a thick high-resistivity silicon substrate. The detector is deployed at the Angra 2 reactor (Rio de Janeiro, Brazil) with a 30 m baseline from the $\sim$ 4 $\mathrm{GW_{th}}$ reactor core ($\overline{\nu_e}$ flux of $7.8 \cdot 10^{12} \frac{\overline{\nu}}{\mathrm{s\ cm^2}}$ at detector location). The experiment has a thick layer of lead and polyethylene around the copper box containing the CCDs (see Figure 1.24). The collaboration conducted a first scientific run during 2022 with a 0.25 g sensor, demonstrating a high data quality with a stable 15 eV_{ee} detection threshold [51]. Due to the low detector mass, the collaboration was not able to measure CEνNS or put any competitive limits with the 2022 data, since they were limited by statistical uncertainty. Currently, the experimental setup is being scaled to 8 g and is later planned to reach the kilogram scale in order to lower the statistical limit of the measurements.

1.4.4.2 Skipper CCD@Atucha2

This experiment uses a 2 g high resistivity silicon substrate readout with skipper CCDs. Their sensor is deployed at the Atucha2 $\sim$ 2 $\mathrm{GW_{th}}$ reactor in Argentina with a 12 m baseline. The project has finished the installation of the sensors at the site after a preliminary characterization at Fermilab and is currently taking data and

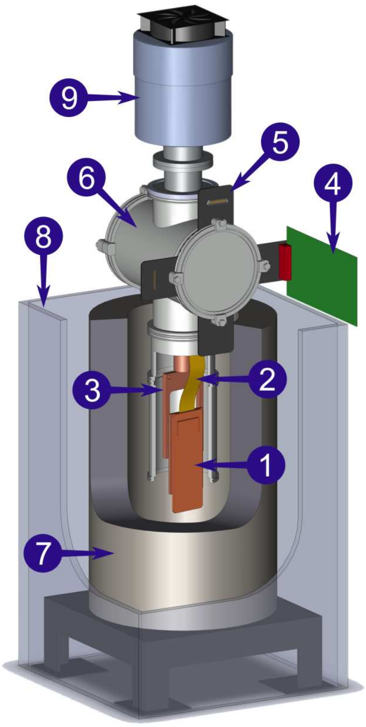

Figure 1.25. Main features of the Skipper CCD@Atucha2 setup: 1. Skipper-CCD inside copper case, 2. Flex cable, 3. Copper tray, 4. Low-threshold Acquisition (LTA) board, 5. VIB readout board, 6. Dewar, 7. Lead shield, 8. Polyethylene shield, 9. Cryocooler (figure from [53]).

tuning their noise conditions to boost sensitivity (currently their analysis threshold is at 45 eV_{ee} [53]). Their detector shielding consists mainly of a layer of polyethylene and another of lead (see Figure 1.25), there are plans to further increase the latter in order to lower background contributions.

1.4.5 Reactor CEνNS with cryogenic calorimeters

A big number of experiments in CEνNS and dark matter detection employ cryogenic calorimeters. These detectors are based on the idea that by detecting the phonons produced by energy depositions in the target material, the detectors reach extremely low detection thresholds (down to few tens of eV) without the presence of quenching factors. This technology comes with some disadvantages, like the need to operate detectors at $O(10\ \text{mK})$ temperatures and typically lower particle identification capabilities. Since the NUCLEUS experiment employs these type of detectors, the technology will be described more in depth in chapter 2 while here a general description of the other experiments is given.

1.4.5.1 RICOCHET

The RICOCHET collaboration [54] has a wide scientific program to measure CEνNS at the ILL 58 MW_{th} research reactor with an 8.8 m baseline. The collaboration

Figure 1.26. Detectors developed by the RICOCHET collaboration. Left: Cryocube detector (figure from [54]). Right: Q-array prototype detector (figure from [55]).

aims to deploy two different core detectors: the *cryocubes* and the *q-array* (see Figure 1.26). The cryocubes consist of germanium crystals with a double readout, heat (or phonons) and ionization, which helps with particle identification since one expects lower ionization signal from nuclear recoils with respect to electron recoils.

One of the main efforts of the collaboration was, in fact, devoted to developing this double readout to be sensitive to the low energy depositions typical of CEνNS, which is particularly difficult for the ionization channel due to the quenching factor. For this reason the collaboration developed an extremely low noise High Electron Mobility Transistor (HEMT) that allows them to perform particle identification at $\sim$ 100 eV which drastically reduces the background. Due to the positive result obtained from the recent characterization measurements, the cryocubes will be commissioned in the upcoming year.

The q-array is composed of cubes made of superconductive crystals (Zn, Al and Sn) as absorbers which are sensed using Transition-Edge Sensor (TES)s coupled with RF-SQUID resonators in order to multiplex the readout and gain a better scalability. The q-array is still in the development phase but is showing promising results. Apart from the target detectors, RICOCHET deploys several layers of polyethylene and lead along with a muon veto with 4π coverage.

1.4.5.2 MINER

The MINER collaboration [56] performs a combined search of reactor induced CEνNS and axion-like particles by deploying cryogenic detectors at a 1 MW TRIGA research reactor with a 2 m baseline. The peculiarity of this TRIGA reactor is that the core has a movement range of several meters, which enables for accurate studies of baseline-dependent neutrino properties (characteristic particularly used in oscillation experiments). One of the detector technologies used by MINER exploit the combined readout of ionization and phonons to distinguish nuclear recoils from other types of energy depositions. The other type of detector deployed instead uses a phonon based readout combined with a high voltage field that further enhances the phonon production via Luke effect, which enables to distinguish nuclear recoils (see Figure 1.27). The experiment terminated a first phase where they demonstrated

Figure 1.27. Detectors employed by the MINER experiment: left: double readout detectors, right: high voltage phonon detector based on the Luke effect. Figure from [57].

the capabilities of their setup and is currently optimizing the signal to background condition.

1.4.6 Other technologies for reactor CEνNS

In the previous sections, the experiments described have been grouped by the basic concept of the technology employed for the detection. Here, on the other hand, there is a collection of experiments with unique technologies for the field.

1.4.6.1 Pico

The Pico collaboration [58] repurposed the bubble chamber technology to make a dark matter and neutrino detector. The main detection concept is that when a particle interacts in a 10 kg LAr bubble chamber, shown in Figure 1.28, it evaporates a small amount of material making a *bubble nucleation* and this process is insensitive to electron recoils. The created bubbles are detected via multiple cameras and piezoelectric acoustic sensors offer means of particle discriminating cuts. The CEνNS branch of this experiment will be deployed at the ININ 1 MW research reactor in Mexico, but is currently still performing detector optimization.

1.4.6.2 NEON

At the Hanbit Nuclear Power Plant Unit 6 (2.8 GW_{th}) the NEON collaboration [60] deployed a 16.7 kg NaI[Ti] scintillator (see Figure 1.29) with a 23.7 m baseline. The detector used by the NEON experiment is surrounded by a liquid scintillator active veto along with multiple layers of polyethylene and lead, which added to the 8 Meter Water Equivalent (m.w.e.) overburden heavily reduce the present background. The NEON collaboration collected 523 days of reactor on data and 143 days of reactor off background measurements. Currently, the collaboration is working on improving the analysis procedure on the taken data and is expected to publish some initial results shortly.

Figure 1.28. Case of the LAr bubble chamber deployed by Pico (figure from [59]).

(b)

Figure 1.29. NaI[Ti] based detector deployed by the NEON collaboration [60].

1.4.6.3 RED-100

The RED-100 experiment [61] exploits a $\sim$ 200 kg liquid xenon dual phase TPC technology shown in Figure 1.30, which is well known in the field of direct dark matter detection. This type of detector is characterized by two different signals for each interaction: the S1 scintillation light flash which arrives promptly when the interaction happen and the S2 electroluminescence flash which is generated when the drifting electrons generated at the interaction point reach the liquid to gas interface where they generate a flash of light. The xy position of the interaction vertex is evaluated using the segmentation of the PMT readout, while the z position can be determined by the time delay between the S1 and S2 signals. Moreover, the ratio between the intensities of the S1 and S2 signals allows to distinguish electron recoils

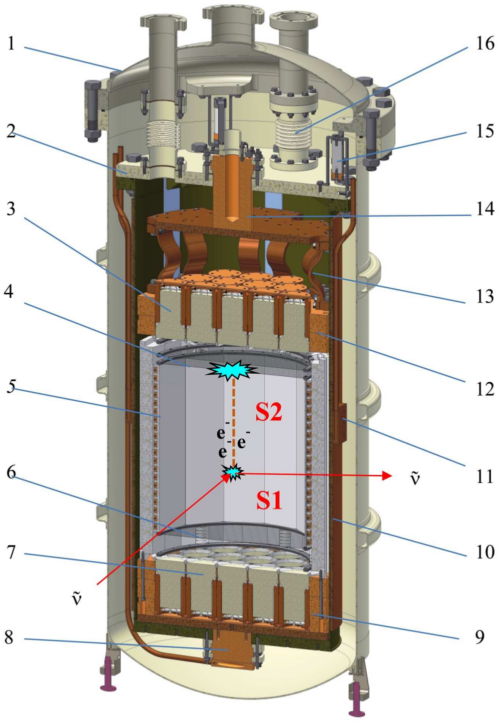

Figure 1.30. Schematic view of the RED-100 detector: 1 – external vessel of the cryostat, 2 – internal vessel of the cryostat, 3 – top array of 19 Hamamatsu R11410-20 photomultipliers, 4 – gridded anode and electron shutter, 5 – drift cage with Teflon reflecting walls, 6 – gridded cathode, 7 – bottom array of 19 Hamamatsu R11410-20 photomultipliers, 8 – cold head of the bottom thermosyphon, 9 – copper housing of the bottom PMT array, 10 – Copper screen of the internal vessel of the cryostat, 11 – cold head of the side thermosyphon, 12 – copper housing of the top PMT array, 13 – flexible heat bridge, 14 – top cold head for xenon condensation, 15 – Vespel made stand supporting cold vessel inside the external vessel of the cryostat, 16 – connection for cable channel; S1 – scintillation flash, S2 – electroluminescence flash. Figure from [61].

from nuclear recoils.

The RED-100 TPC is located at the Kalinin nuclear power plant (3 $\mathrm{GW_{th}}$) at a 19 m baseline. After a thorough campaign of background evaluation, the experiment started acquiring data from 2022. Currently, the first data taking campaign has ended and the data analysis is being finalized and results are expected shortly. Moreover, the collaboration plans to deploy a LAr based dual phase TPC.

1.4.7 Dark Matter experiments as solar neutrino telescopes

The experiments described in this section do not have a CEνNS detection as their main scientific goal, since they are mostly focused on direct dark matter measurements. The experimental signature of CEνNS (the nuclear recoil) is similar to the one searched in direct WIMP [62] detection experiments, this means that dark matter detectors are usually sensitive to CEνNS generated by the environmental neutrinos. In fact, apart from man-made neutrino sources there are several other

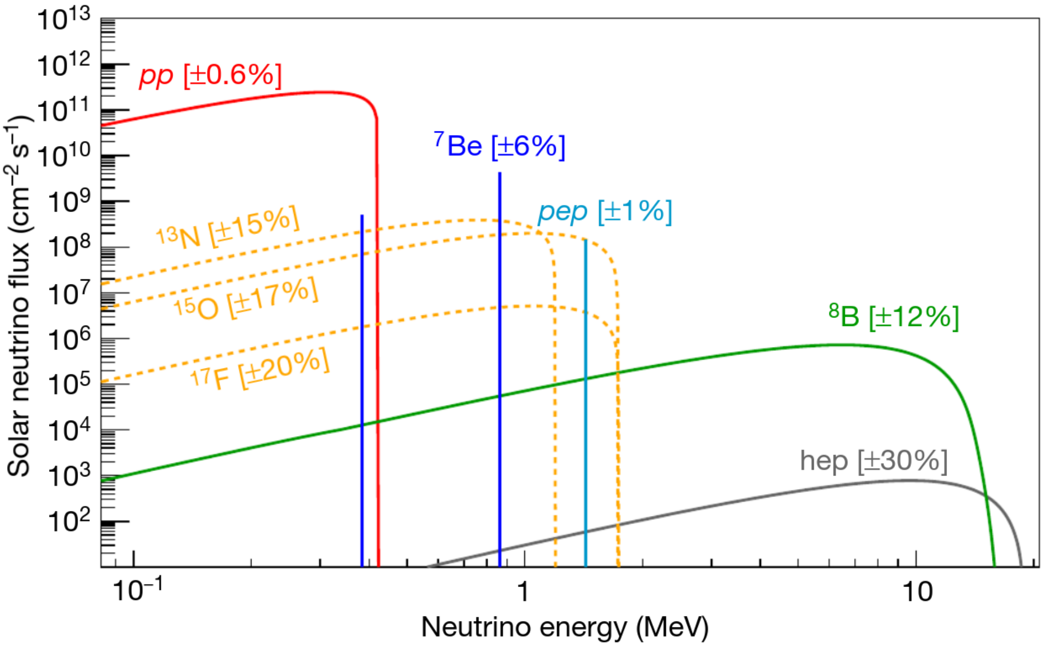

Figure 1.31. Spectrum of the neutrinos produced by the sun separated by the various reaction chains that produce them. Figure from [63].

neutrino emitters in nature, as for example the sun (see Figure 1.31). The current uncertainty on the ambient neutrino flux and on the CEνNS cross-section create the so-called neutrino fog, i.e. a region of the WIMP parameter space where an excess of events could either be due to the detection of dark matter or neutrinos, as described by the exclusion plot in Figure 1.32. In recent years, the name was changed from *neutrino floor* to *neutrino fog* since the spectral features of the CEνNS events and the expected dark matter events are different, making them, in principle, distinguishable.

Direct WIMP detection experiments are starting to be greatly invested in a precise CEνNS characterization, since the systematic uncertainties on this background component poses a severe limit on their sensitivity. On the other hand, due to the similar technological requirements to measure CEνNS and WIMPs the high exposure experiments based on noble liquids are starting to be sensitive to the neutrino-nucleus scattering produced by solar neutrinos (mainly from the ^{8}B chain).

There are two main players for these type of experiments that recently reported positive signals regarding solar CEνNS: PandaX-4T[65] and XENONnT [66]. Both experiments exploit a liquid xenon dual phase TPC with a several ton fiducial volume (5.9 and 3.7 tonnes for respectively XENONnT and PandaX-4T), as shown in Figure 1.33, which use a similar detection principle to the one described for the RED-100 experiment (see section 1.4.6.3), crucial details between experiments might differ but to understand their results they can be disregarded. In order to search for dark matter, these experiments are placed in extremely low background conditions (XENONnT is in the Gran Sasso underground laboratory and PandaX-4T is in the Jinping underground laboratory).

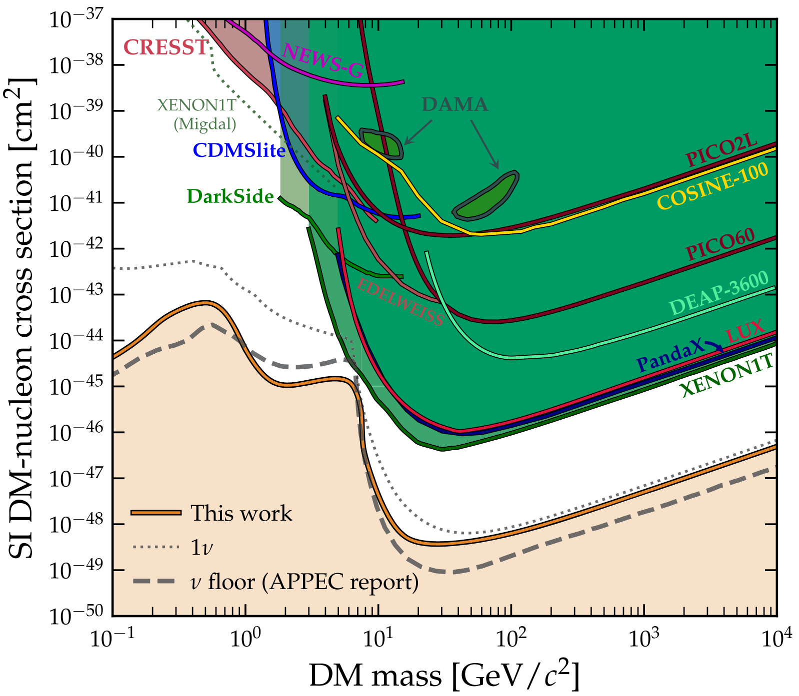

Figure 1.32. Present exclusion limits on the spin-independent dark matter-nucleon cross-section (assuming equal proton/neutron couplings). Beneath these limits, three definitions of the neutrino floor for a xenon target are shown. The dashed line shows a previous state-of-the-art estimation of the neutrino floor. The dotted line shows the region above which 90% C.L. exclusion limits can be placed, allowing for one neutrino event. While in orange, the neutrino fog region is highlighted and the boundary denoted as neutrino floor. Figure extracted from [64].

To proceed in the CEνNS analysis, both collaborations had to place the detection threshold small enough to spot these low energy deposition and carefully evaluate all the sources of background, including the accidental background rate possibly introduced with this new lower limit. The experiments performed a blind analysis of both the S1 and S2 signals recorded in the last few years (2020-2022 for PandaX-4T and 2021-2023 for XENONnT) and reported a positive hint of the presence of solar CEνNS in their data. In particular, when disfavoring the background only hypothesis, the PandaX-4T reported a 2.64 σ significance [65] and XENONnT reported a 2.73 σ significance [67].

While not yet at the 3 or 5 σ significance level, these are the first results for the detection of CEνNS coming from naturally produced neutrinos. Moreover, these observations are complementary to the earlier ^{8}B neutrino measurements (performed by SNO[68], SNO+[69], Super Kamiokande[70], Borexino[71] and KamLAND[72]) and show full compatibility with the SM prediction. Finally, due to the energies at play, these findings are also the first ever hints of a CEνNS measurement in a fully coherent regime.

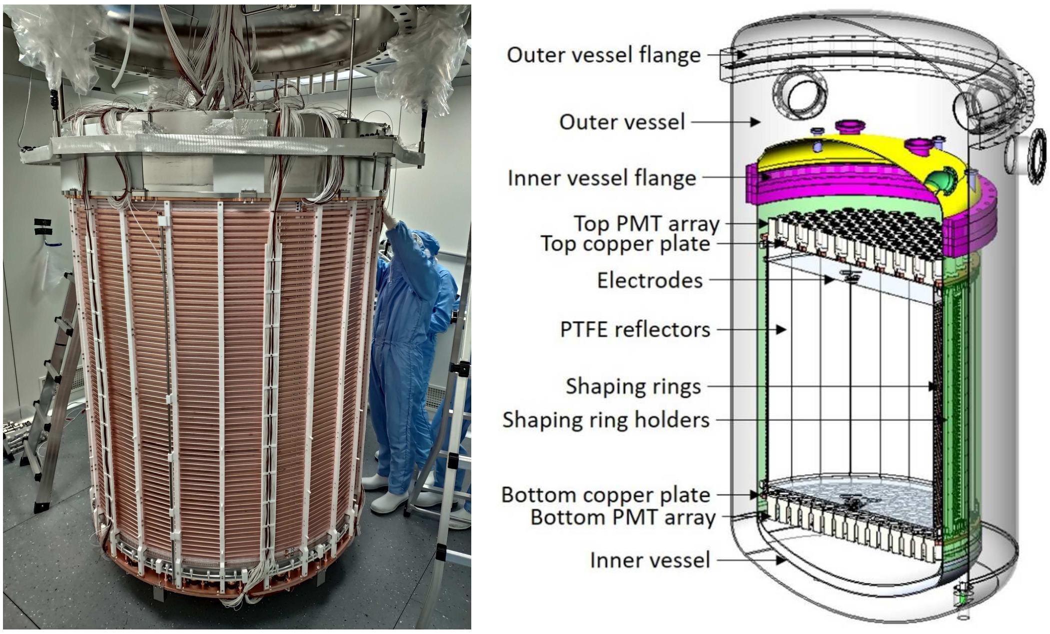

Figure 1.33. Left: XENONnT TPC picture taken during installation at the Gran Sasso Laboratories. Right: Layout of the PandaX-4T detector.

Chapter 2

NUCLEUS experiment

In this chapter, an overview of the NUCLEUS experiment is presented. The chapter starts with a general description of the goals of the experiment, along with some preliminary estimations regarding the expected signal. Then a description of the experimental setup is shown along with the description of the expected background components. Finally, a preliminary evaluation and discussion about the expected sensitivity is presented.

2.1 Scientific goal of the experiment

Figure 2.1. NUCLEUS collaboration members in 2024 (left) and structure (right).

The experiment proposed by the NUCLEUS collaboration (see members and institutions in Figure 2.1) is aimed at measuring CEνNS events produced by reactor antineutrinos in order to measure the cross-section of the process. The experiment aims at exploiting the ultra-low threshold typical of cryogenic calorimeters to measure nuclear recoils with energies around 100 eV.

The precision measurement of the coherent neutrino-nucleus elastic scattering will be carried out in two phases (see Figure 2.2): the first phase consists in deploying a small target (~ 10 g) to measure CEνNS in a relatively short period of time to reach 10% precision, which is dominated by the statistical error, on the neutrino-nucleus

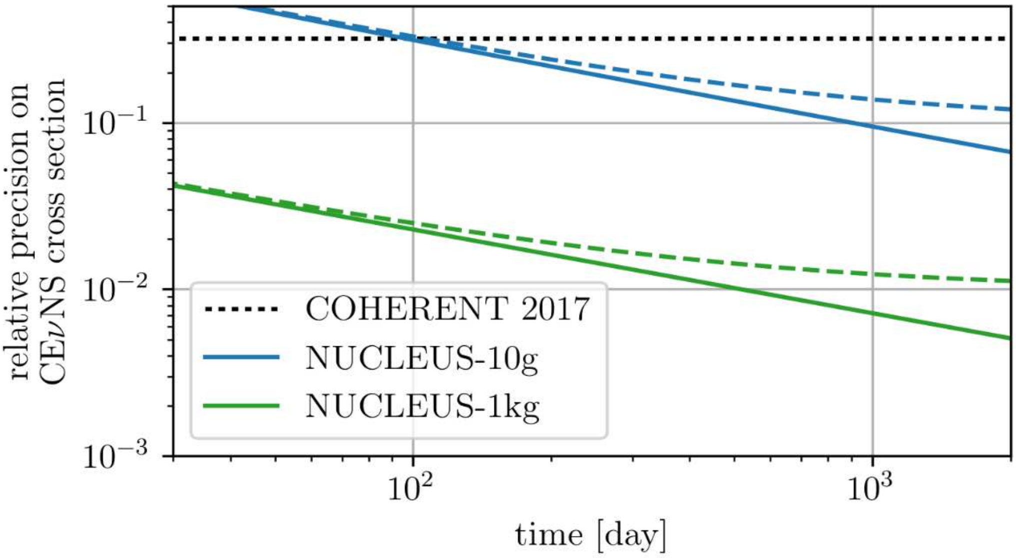

Figure 2.2. The two phases of the NUCLEUS experiment presented in terms of livetime and precision on the cross-section reached for a flat 100counts/(keV kg day) background in comparison with the first COHERENT measurement described in section 1.2. Phase 1: Reaching 10% uncertainty on the CEνNS cross-section (statistical uncertainty dominating), by using a 10 g target detector (blue). Phase 2: Reaching 1% uncertainty on the CEνNS cross-section (systematic uncertainty dominating), by deploying a 1 kg target detector (green). The precision obtained by using the COHERENT data presented in [1] is shown for reference with a black dotted line. Statistical precision is shown as solid lines, for the dashed lines a 10% (1%) systematical uncertainty has been added in quadrature for NUCLEUS-10 g (1 kg).The figure is taken from [73].

scattering cross-section measurement (the collaboration estimated that a ~ 1 year livetime is needed for this measurement, but this number may change based on the experimental background). In a second phase, the exposure of the experiment will be greatly increased by scaling up the target mass to ~ 1 kg, which will allow to reach a 1% precision (limited by the reactor neutrino flux uncertainty) on the cross-section measurement in a similar livetime.

The experimental setup will be installed at the Chooz nuclear power plant in France (see section 2.2) in order to use the intense neutrino flux coming from the two commercial reactor cores present.

2.2 Experimental Site: description and challenges

The NUCLEUS experiment aims at measuring the electron antineutrinos produced by the two 4.25 GW_{th} reactor cores of the Chooz nuclear power plant in the French Ardennes. The apparatus will be deployed in the Very Near Site (VNS) room shown in Figure 2.3, which is a 24 m^2 room in the basement of an administrative building which offers ~ 3 m.w.e. overburden (which translates to a $\sim 30\%$ attenuation for the muon flux and a factor 5 reduction in of the environmental neutrons). The VNS

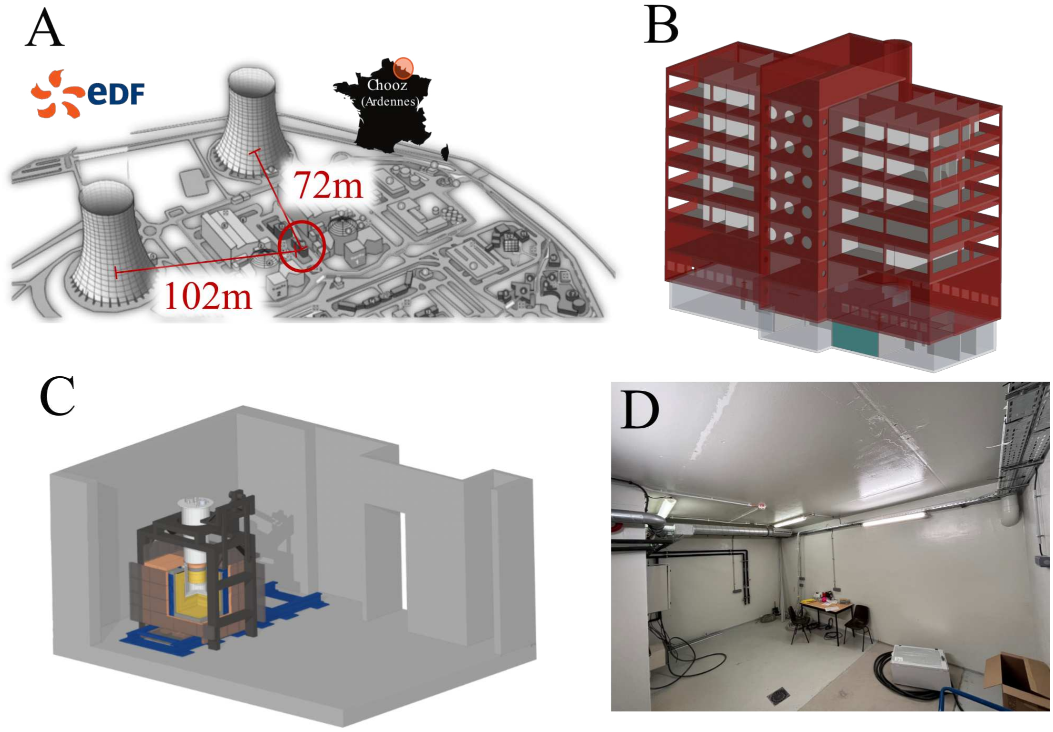

Figure 2.3. Pictures and drawings of the location of the VNS, the NUCLEUS experimental site. Panel A: Aerial drawing of the Chooz nuclear power plant, showing the baselines of 72 m and 102 m. Panel B: 3D rendering of the building in which the NUCLEUS setup will be deployed, the green room in the basement is the VNS. Panel C: 3D rendering of the VNS room with the experimental apparatus deployed. Panel D: Picture of the VNS room as of 2024, the room is ready to host the setup. Figures taken from [74].

is placed at 72 m and 102 m baselines from the two reactor cores. The estimated anti-neutrino flux is $\phi_\nu \approx 1.7 \times 10^{12} \frac{\nu}{\text{s cm}^2}$.

The relatively long baseline with respect to other reactor CEνNS experiments allows NUCLEUS to feature negligible correlation between background and reactor activity, meaning that the only reactor related radiation reaching the detectors are neutrinos. Moreover, the position of the VNS was chosen for practical reasons, since being in an administrative building, the access is relatively simple. The accessibility of the room only appears simple when compared to other nearer reactor sites, which have extreme security and safety access protocols, but the VNS building is still inside the first security perimeter of the power plant, meaning that daily access for a long period of time is not a viable option for the experiment. This is why the experiment is being first commissioned at the Technische Universität München (TUM) and then moved to the experimental site, with particular attention to build a fully remotely controllable setup.

2.2.1 Neutrinos at the VNS

The reactor antineutrino flux expected at the VNS is the blue curve in Figure 2.4. From the figure it is visible that almost all the neutrinos produced have energies below 8 MeV (as described in section 1.4.1) and the bulk of the neutrino flux is present at energies below 2 MeV.

To choose the best target material to measure CEνNS , it is instructive to predict the interaction spectrum in various crystals by folding the incoming neutrino flux with the SM cross-section of the process. The targets here considered are silicon, germanium, Calcium Tungstate ($CaWO_4$) and Sapphire (Al_2O_3) which are typical crystals used in nuclear recoil based experiments. From the curves presented in the panels of Figure 2.4 the typical scaling of the CEνNS interaction rate with the square of the number of neutrons in the target nucleus (N^2 scaling) is visible, as well as the dependence of the induced nuclear recoil with the inverse of the nuclear mass of the target (M_A^{-1} scaling). Considering the kinematics of this two body elastic scattering, the average nuclear recoil energy is given by (see eq. (1.3)):

$$\langle T \rangle = \frac{2}{3} \frac{E_\nu^2}{M_A}$$

this means that for heavy nuclei, like the tungsten in $CaWO_4$, the nuclear recoils have energies of around 100 eV. This is visible in the panels of Figure 2.4 by noticing that the interaction rate on $CaWO_4$, is much more dependent on the minimum detection threshold.

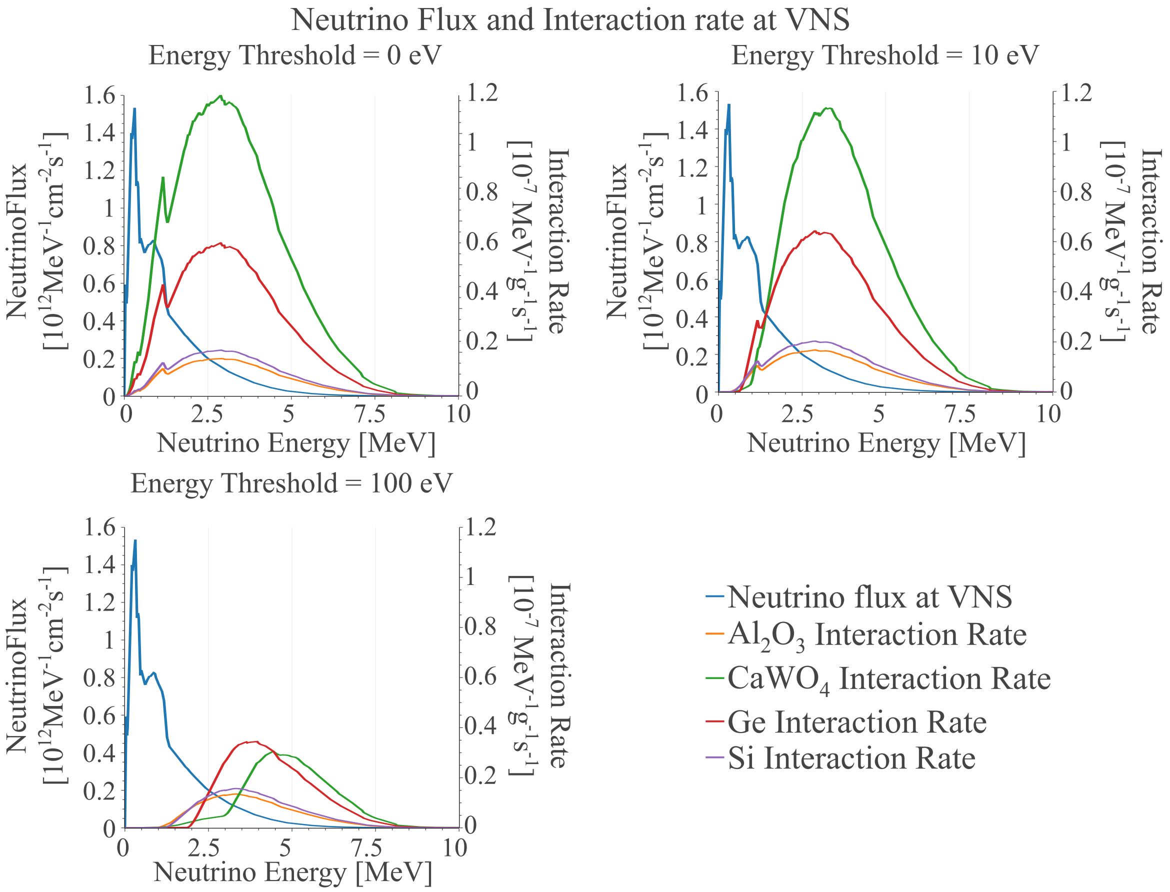

Figure 2.4. Incoming neutrino spectrum at the VNS experimental site (blue) and the expected measurable interaction rates as a function of neutrino energy for Al_2O_3 (orange), $CaWO_4$ (green), Ge (red) and Si (purple). In the various panels, a different minimum energy threshold on the recorded nuclear recoil is applied.

2.3 Apparatus

The NUCLEUS experiment uses a complex experimental apparatus in order to operate ultra-low threshold cryogenic calorimeters (described in section 2.3.1) in stable conditions for long periods of time. The main requirements for the setup of the experiment are: minimal intervention after reaching a stable operating condition, this is required since daily access to the VNS is not a possibility, low noise and background conditions to easily make a statistically significant CEνNS observation.

From the diagram of the setup presented in Figure 2.5 it is visible that the experiment uses several components to reach the goals described above. The 18 target detectors (9 of which made of $CaWO_4$ and the remaining 9 of Al_2O_3) are operated at 10 mK inside a dry dilution cryostat. The detectors are surrounded by several layers of passive shields, made of B_4C, lead and polyethylene, and active vetoes, referred to as the inner veto, the COV and a Muon Veto (MV), in order to reach low background conditions (each of these components is described in the following sections). To reduce the noise present on the detectors, a vibrational decoupling system [75] is

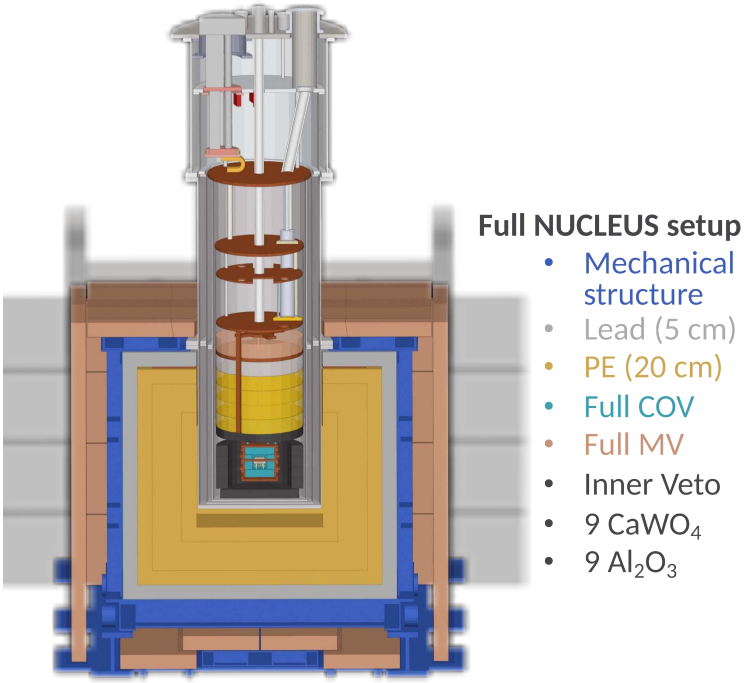

Figure 2.5. Diagram showing all the different components of the NUCLEUS setup (figure from [74]). The various components present in the diagram are: in blue the mechanical structure for holding the shields, in gray the lead shield, in yellow the polyethylene (PE), in orange the muon veto (MV), in light blue the cryogenic outer veto (COV). The inner veto and the target detectors are not discernible from the diagram but are placed inside the Cryogenic Outer Veto (COV).

employed which keeps the COV, the inner veto and the target detectors suspended inside the innermost cryostat vessel.

The collaboration chose to operate detectors in a BlueFors LD400 dry dilution cryostat, shown in Figure 2.6, that reaches base temperatures of under 7 mK. Dry dilution cryostat are closed system refrigerators that keep the base temperature and require no interventions apart from some minor remote monitoring, allowing for a high reliability during operation.

2.3.1 Target Detector

The reactor antineutrinos will be measured by the NUCLEUS collaboration, in the first phase of the experiment, using 2 arrays of made out of 9 crystal cubes of respectively Al_2O_3 and $CaWO_4$. Each calorimeter, also referred to as *cryocube*, has a 5 mm side, as shown in Figure 2.7, and the total target mass is $\sim$ 10 g (6 g of $CaWO_4$ and 4 g of Al_2O_3). The choice of employing two different materials was taken in order to have a differential measurement of the background and CEνNS rates (see section 2.4).

Cryogenic calorimeters exploit a fundamental property deriving directly from the third law of thermodynamics, which in the formulation proposed by Plank states:

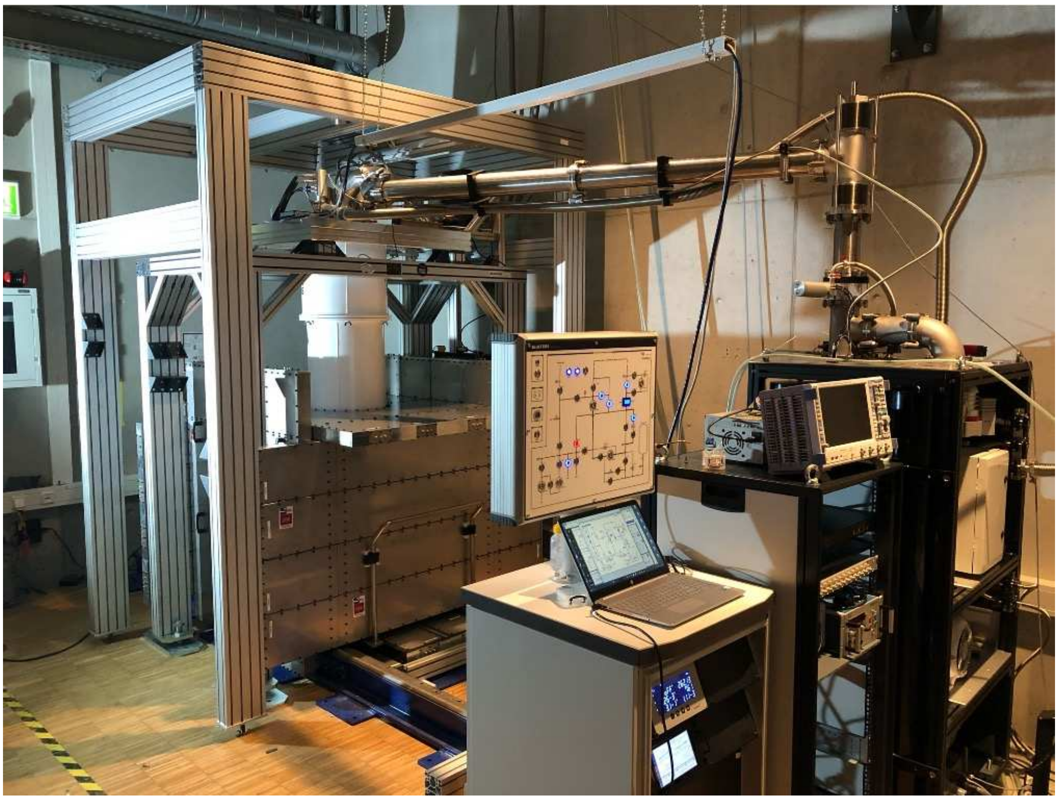

Figure 2.6. Picture of the nucleus cryostat deployed at the Underground Laboratory (UGL) in TUM for the commissioning and background run before the move to the Chooz nuclear power plant. In the picture, the gas handling and cryostat monitor electronics is shown along with the cryostat with its rack surrounded by the room temperature shields and muon veto.

> *As temperature falls to zero, the entropy of any pure crystalline substance tends to a universal constant.*

Since the entropy of an object at a temperature T_1 is given by:

$$S = \int_0^{T_1} \frac{C(T)}{T} dT \tag{2.1}$$

when the temperature approaches zero the fraction inside the integral will diverge, giving a definitely not constant entropy S, unless the heat capacity $C(T)$ goes to zero as fast as T (or more), meaning that at low temperatures the heat capacity is uniformly vanishing. In fact, taking Debye's model for the heat capacity of solids at low temperatures, one has that $C(T) \propto T^3$. Considering that when an energy E is released in a crystal the increase of temperature is given by:

$$\Delta T = \frac{E}{C(T)} \propto \frac{E}{T^3} \tag{2.2}$$

then at temperatures near the absolute zero any small energy deposition is translated into quite a high temperature difference. This is exploited in cryogenic calorimeters, which have a temperature sensing device coupled to these crystals.

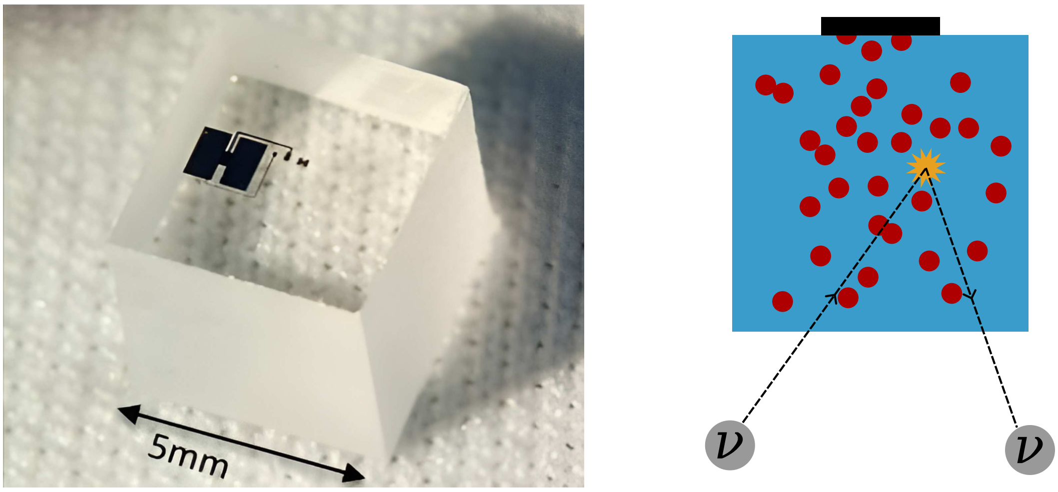

Figure 2.7. Left: Picture of one of Al_2O_3 cryogenic calorimeters used in the NUCLEUS setup (in black the TES lithography is visible). Right: Artistic depiction of a neutrino (gray circle) inducing a nuclear recoil (orange star) in the crystal cube (light blue square) with the following phonon production (red dots) and absorption by the TES (black rectangle).

An energy release in a crystal is quickly converted into phonons, that are quantized vibrations of the crystalline structure and have energies of $O(1\text{ meV})$. The phonons are then absorbed in a sensor coupled to the crystal, this temporarily changes the electrical properties of the device which can be measured and read out as a signal.

In the case of NUCLEUS, the phonons produced are sensed by the use of Transition-Edge Sensors (TESs). The NUCLEUS TESs are made of a thin superconductive tungsten film which is kept at the onset of the transition curve, as shown in Figure 2.8. When a particle interacts in the absorber crystal, the phonons produced break the superconductivity of the coupled TES, by breaking the cooper pairs, and cause an increase in the resistance of the device which can be accurately measured with the readout scheme shown in Figure 2.9.

2.3.1.1 Readout Description

The TES readout circuit translates an increase of the resistance R_T of the sensor in a voltage V_S using a Superconducting Quantum Interference Device (SQUID) [76] which is an extremely sensitive magnetometer. An explanation of the principles behind the inner workings of the SQUID is beyond the scope of this discussion but for all purposes of this thesis it can be regarded as a current to voltage amplifier, meaning that the current I_S passing through the SQUID is translated into a voltage $V_S = g \cdot I_S$ via the gain factor g (a qualitative description on the SQUID working principle is presented in appendix A).

By applying the equations regulating a current divider one has that the voltage V_S measured at the end of the readout chain is:

$$I_S = I_B \frac{R_T}{R_T + R_S} \longrightarrow V_S = g I_B \frac{R_T}{R_T + R_S} \tag{2.3}$$

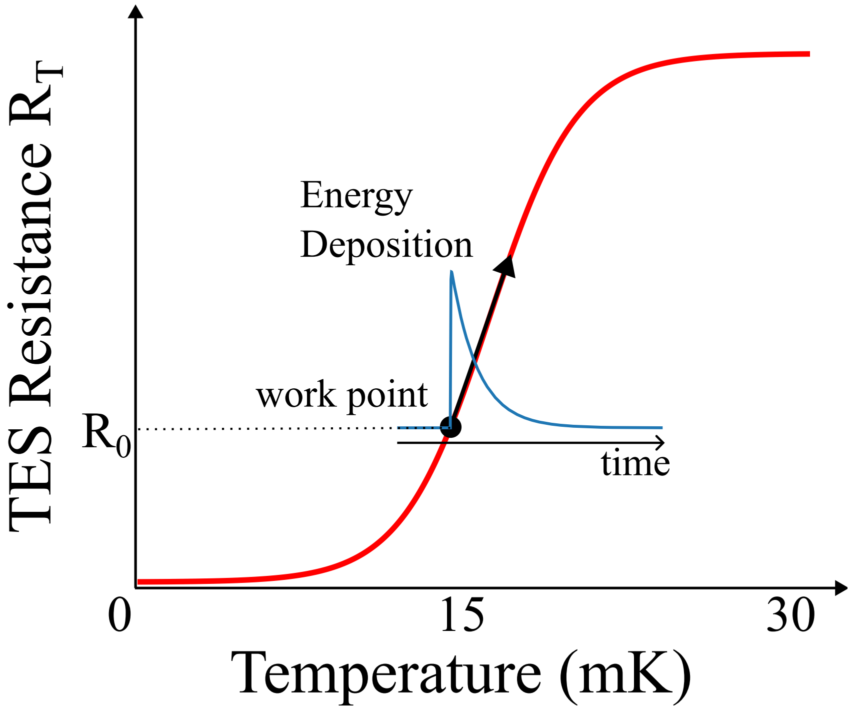

Figure 2.8. Typical depiction of the superconductive transition (red) of the NUCLEUS TES sensors (the temperature scale is present just to give the order of magnitude of the temperature at which the sensors are operated). In blue, the typical shape of a pulse is shown, which roughly corresponds to the time evolution of the TES resistance after an energy deposition occurred.

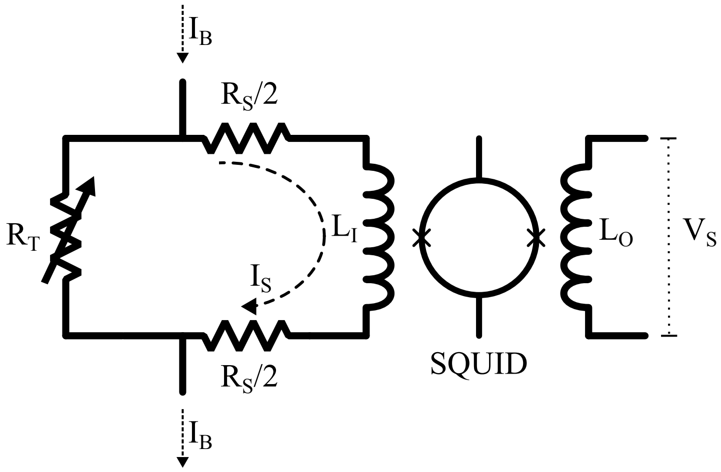

Figure 2.9. TES readout circuit based on the current divider principle. The components in the diagram are: I_B the bias current, $R_S/2$ two shunt resistors, R_T the variable resistance of the TES, L_I and L_O the inductance of the input and output coils of the SQUID and V_S the voltage read out by the system.

where I_B is the bias current of the readout and R_S is the total shunt resistance (which in Figure 2.9 is divided in two different resistors) and the L_I and L_O inductances of the SQUID input and output coils were discarded from this simple calculation since the circuit is operated with a Direct Coupling (DC). Moreover, one is usually interested in the voltage difference from a baseline scenario, so assuming that the TES resistance scales linearly with the energy deposited $R_T = c \cdot E + R_0$ one has:

$$\Delta V_S = gI_B \left[\frac{c \cdot E + R_0}{c \cdot E + R_0 + R_S} - \frac{R_0}{R_0 + R_S} \right] \tag{2.4}$$

where c and R_0 are respectively the responsivity of the TES and its resistance at work point (see Figure 2.8). From eq. (2.4) it is clear that the readout circuit has an intrinsic non-linearity but if $c \cdot E \ll R_0 + R_S$ the linearity is approximately recovered since the read signal is:

$$\Delta V_S \approx gI_B \frac{c \cdot E}{R_0 + R_S} \tag{2.5}$$

To keep the TESs stable in the correct working point, a small resistance, referred to as heater, is lithographed near the sensor. The heater is used to both provide a constant heating in order to keep the TES at the correct working point and also to send “heat” pulses of constant energy used to monitor the possible drift of the TES work-point and to actively correct it by changing the heating power.

2.3.2 Vetoes and shields

As already mentioned, the setup for the NUCLEUS experiment is characterized by several shields and active vetoes, which will be briefly discussed in this section. The shields are presented in order, starting from the inner and coldest layer and ending at the outermost layer of the muon veto.

2.3.2.1 Inner Veto

The active veto placed nearest to the target detectors, which is referred to as *inner veto*, plays two important roles in the setup. Firstly, it acts as the mounting structure directly in contact with the 18 cryocubes deployed, as visible from the diagram in Figure 2.10 and from the picture in Figure 2.11. The second function is to be an active veto with detection thresholds comparable to the target detectors ones. These two features of the *inner veto* allow, during the data analysis, to tag the low energy background component, which can be due to several causes. Some of expected backgrounds to be efficiently removed by the *inner veto* are: signals in the target detector generated by the mechanical stress of the mounting, phonon leakage to the cryocubes coming from other parts of the setup and surface contamination events (i.e. low energy radioactivity present near the target detectors). In particular, this active veto is present in order to mitigate the Low Energy Excess (LEE) background, which is further discussed in section 2.4.3.

In terms of readout, the inner veto is composed of two sets of cryogenic calorimeters consisting of a silicon wafer and a beaker which give a 4π coverage and are readout with glued TESs. This detector is operated at the same temperatures of the target

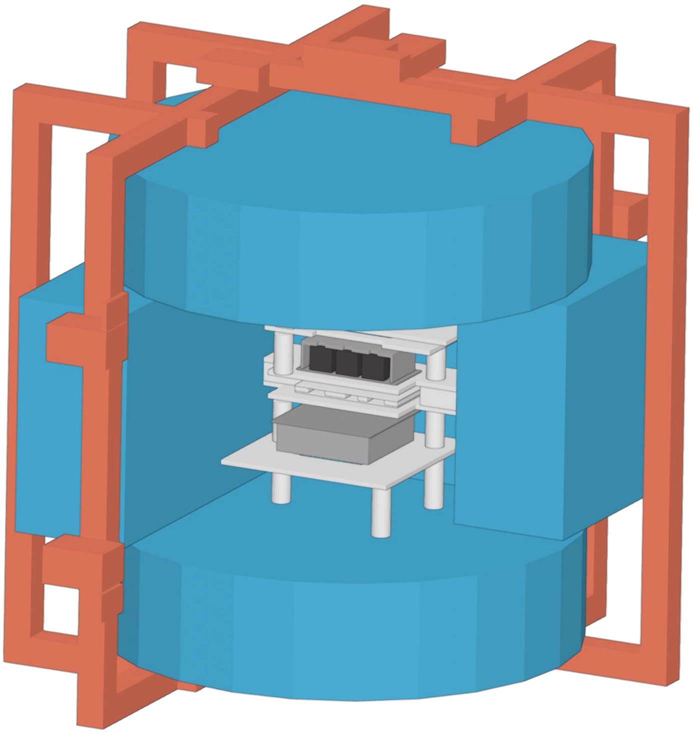

Figure 2.10. Diagram of the foreseen detectors operated at cryogenic temperatures in the NUCLEUS experimental setup. The colors for the various systems are: black for the cryocubes, gray for the inner veto, white for the inactive mounting structure, light blue for the COV and brown for the copper cage holding the setup.

cryocubes, i.e. ∼ 10 mK, and is required to have a detection threshold below 500 eV.

2.3.2.2 Cryogenic Outer Veto

The COV is the second active veto layer that surrounds the inner veto and the cryocubes proving a 4π coverage. It is composed of 6 HPGe crystals, with a total mass of 4 kg and a thickness of 2.5 cm, operated as ionization detectors at ∼ 10 mK. This type of veto is deployed in order to heavily reduce the background due to photons with energies higher than 10 keV (ambient γs). The six crystals are held in place by a copper cage, as shown in Figure 2.12.

2.3.2.3 Passive Shields

Aside from tagging background events, it is also necessary to reduce their number by using passive shielding techniques. NUCLEUS plans to deploy 3 layers of passive shields, each giving a 4π coverage against background components. The first one, completely enclosed in the cryostat and surrounding the COV, is a B_4C Becker that heavily reduces the background given from low energy neutrons. A second layer is made from borated polyethylene and acts as the primary barrier against neutrons and

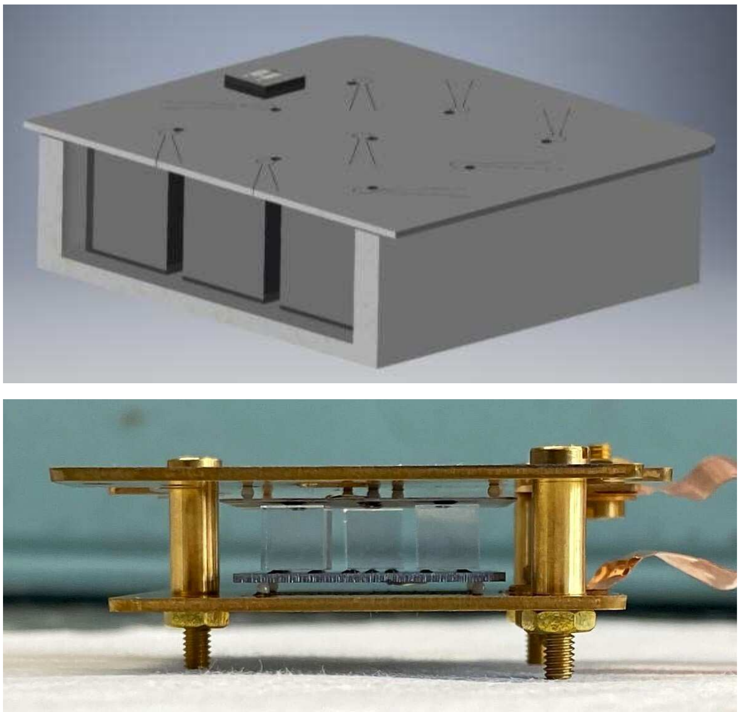

Figure 2.11. In the top panel a 3D rendering of the inner veto conceptual design for a single 3 × 3 cryocube matrix is presented, while in the bottom panel a first assembly of part of the inner veto is shown.

Figure 2.12. COV mockup crystals, made of silicon, installed in the holding copper cage structure for mechanical tests.

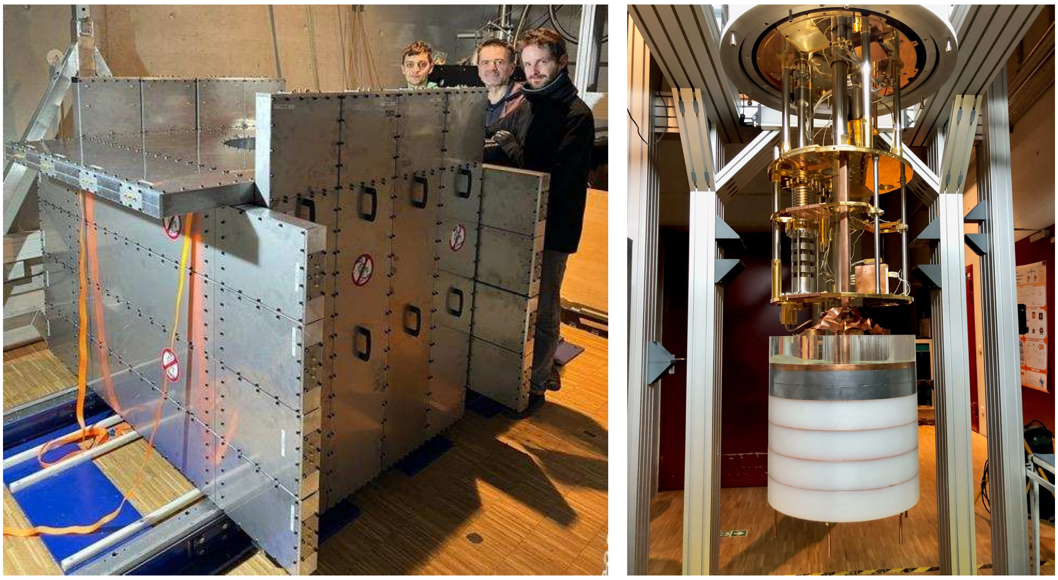

Figure 2.13. Pictures of the NUCLEUS shields and muon veto. In the left panel a picture of the room temperature muon veto and shields being deployed at UGL. On the right, a picture of the mounted cryogenic shields and muon veto is shown.

is placed mostly outside the cryostat vessel with a cryogenic continuation thermalized at 4 K, in order to give a complete coverage. Finally, the last layer present is lead, which is deployed both inside and outside the cryostat vessels. A picture of the cryogenic continuations of the shields is visible in the right panel of Figure 2.13.

2.3.2.4 Muon Veto

As visible in the left picture in Figure 2.13, the outer active veto present is a muon veto. This detector is made of 5 cm thick plastic scintillator plates, each readout with a Silicon PhotoMultiplier (SiPM) and a Wavelength Shifting (WLS) fiber with a detection threshold of about 5 MeV. In order to have a full coverage from muons, the NUCLEUS collaboration developed a cryogenic muon veto based on the same technology of the room-temperature one but thermalized at the 4 K stage, which, considering composed of a bulky plastic material, is a challenging task due to the low thermal conductivity and high mass.

The atmospheric muons detected by this veto deposit energies in the cryocubes that are well above the Region-Of-Interest (ROI) but might also produce neutrons by spallation, especially in the lead shield, which are one of the most dangerous backgrounds for the experiment since they can generate CEνNS-like nuclear recoils.

2.4 Expected signal and backgrounds

In this section, the CEνNS signal and the backgrounds expected in the NUCLEUS measurements at Chooz will be presented in order to discuss the difficulties concerning this reactor neutrino-nucleus scattering experiment. The background present in the experiment will be separated in two main components: the known backgrounds due

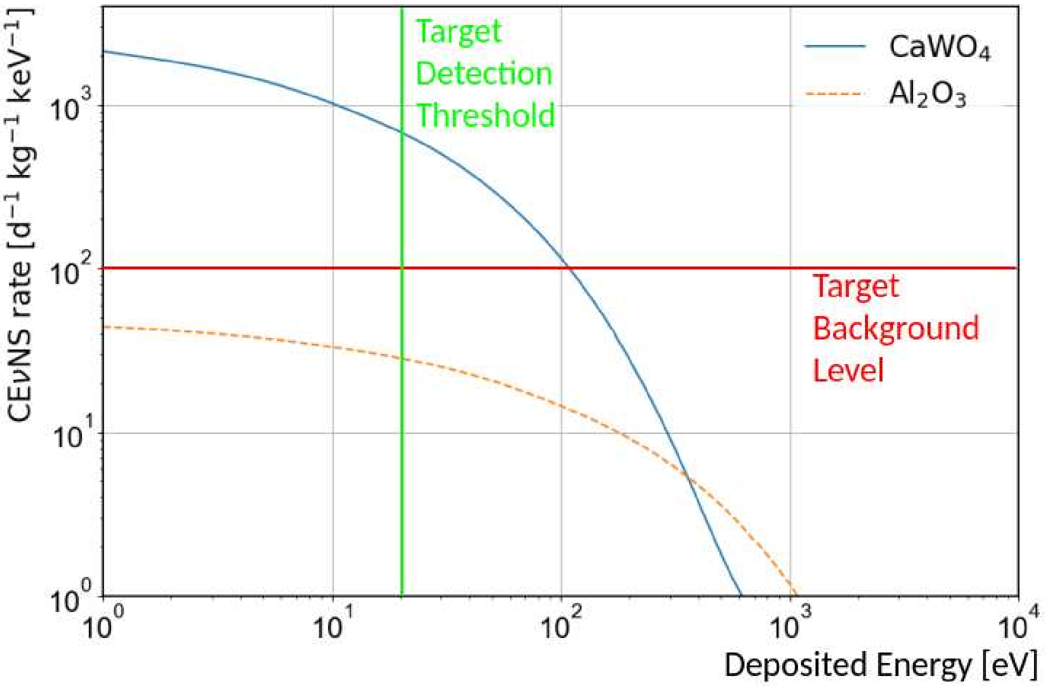

Figure 2.14. CEνNS rate at the VNS for the target materials used by NUCLEUS (figure re-adapted from [74]). Figure with 80% reactor duty cycle (average activity over 1 year).

to ambient or atmospheric radioactivity and an unknown background known as LEE.

2.4.1 Standard Model Signal

The CEνNS signal given from the Chooz reactor and potentially measured by the NUCLEUS experiment can be estimated by folding the neutrino spectrum in Figure 2.4 with the CEνNS differential cross-section in eq. (1.1) for $CaWO_4$ and Al_2O_3, target materials used by NUCLEUS. The neutrino induced nuclear recoil energy spectrum is presented in Figure 2.14 and is characterized by an exponential decrease at low energies. The expected absolute counting rate for the experiment is around $30\frac{\text{counts}}{\text{kg d}}$, meaning that with the targeted background of $\sim 100\left[\text{d}^{-1}\text{kg}^{-1}\text{keV}^{-1}\right]$, the CE$\nu$NS signal can be distinguished only in $CaWO_4$.

The target detectors are, in fact, made of two different absorber crystals in order to allow a combined measurement of the signal (on $CaWO_4$) and the background (on Al_2O_3), decreasing the systematical uncertainties.

2.4.2 Known backgrounds

There are three main known background components that affect the NUCLEUS experiment and that need to be shielded or vetoed: ambient gammas, atmospheric neutrons and muons. As mentioned before, since the NUCLEUS experimental setup will be located at ~100 m from the two reactor cores, no reactor related background is expected to be present.

Operating cryocubes at surface without any vetoes or shields results in a background level of 10^6 Dark Matter Rate units (counts/keV kg day) (dru). When deploying the passive shields and the active vetoes of the NUCLEUS experiment, this background lowers to $O(10^2$ dru) as visible from the panels of Figure 2.15. In the figure the effect of the anti-coincidence cut using the muon veto and the COV is shown while the inner veto is not added in the plot since it does not play a big role in reducing known background but is expected to perform efficient discrimination in the LEE background (see section 2.4.3). A summary of the various background levels and their sources is shown in Figure 2.16 where it is visible that the NUCLEUS experiment will operate in a signal-to-background ratio (S/B) of approximately 1.

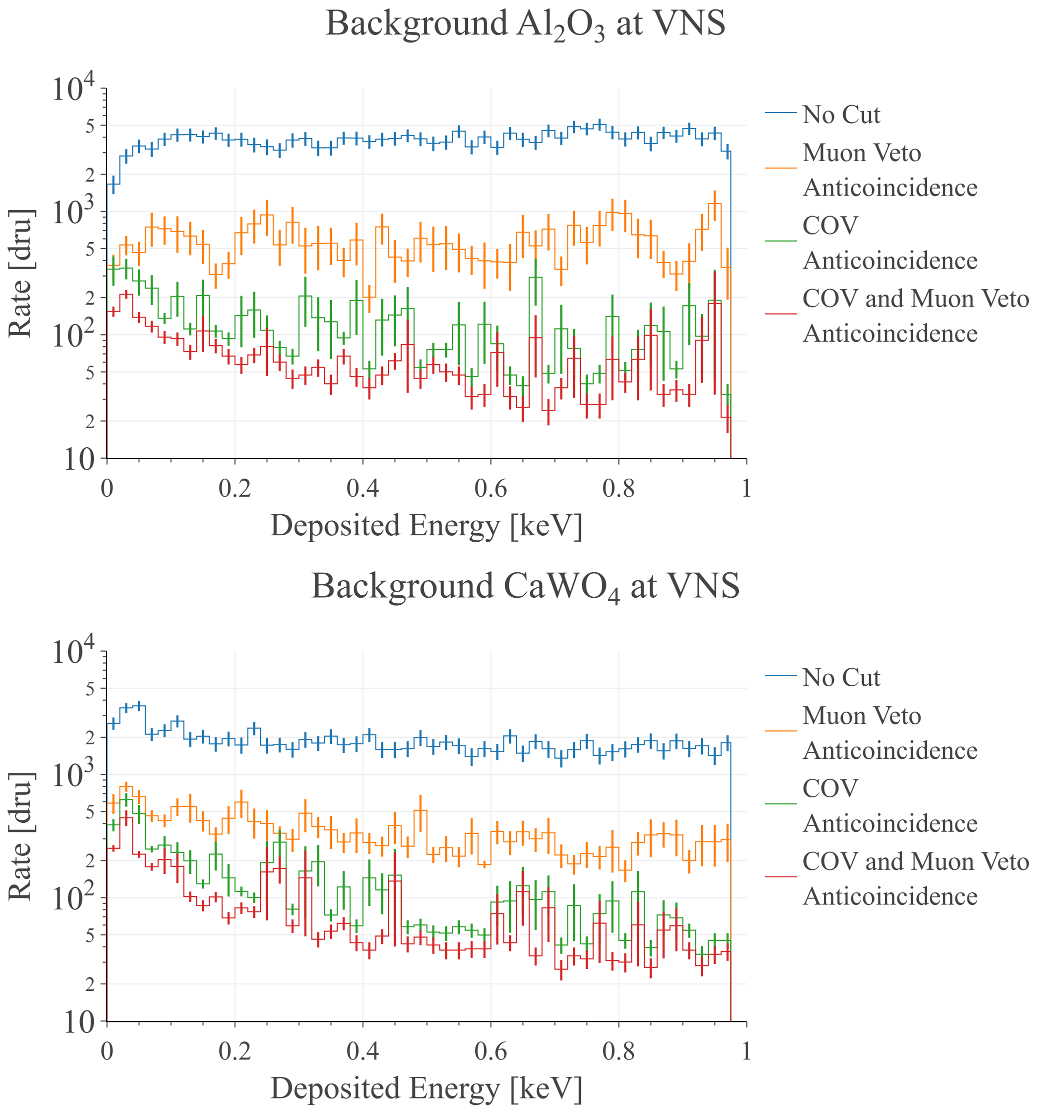

Figure 2.15. Simulated background at the VNS for Al_2O_3 (top) and $CaWO_4$ (bottom). For all spectra, the effect of passive shields of the experiment is already taken into account. The error bar of each bin shows the $\pm 1\sigma$ statistical fluctuation. The spectra shown here are a sum of the ones generated by the different background sources, which have been simulated with non-uniform statistics (more detailed simulations are currently being performed). Figures adapted from [74, 77].

2.4.3 Low Energy EXCESS

Many low-threshold experiments like NUCLEUS observe a sharp rise in the event rate at low energies, which to date remains unexplained. This background, dubbed as Low Energy Excess (LEE) [78], has been measured, in both cryogenic calorimeters and CCDs, to be orders of magnitude larger than expected backgrounds and extending to energies up to a few hundred electronvolts. The LEE is particularly problematic for NUCLEUS since, as visible from Figure 2.17, it shows up as an almost exponential

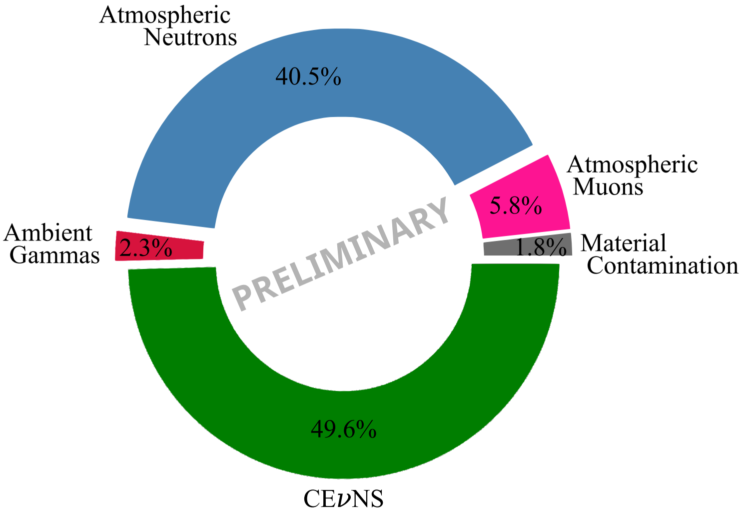

Figure 2.16. Expected contribution from known backgrounds in CEνNS data taken at the VNS (figure from [74]). The ratio between background and CEνNS events is $S/B \sim 1$.

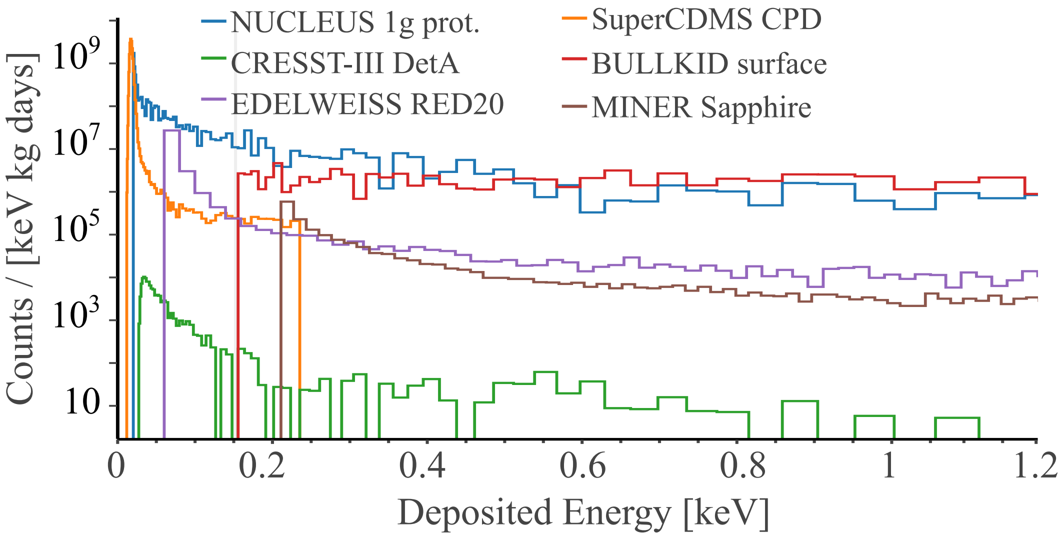

Figure 2.17. Low Energy Excess spectra (LEE) measured by experiments using cryogenic calorimeters (figure re-adapted from [79]).

rise at low energies which both greatly surpasses the CEνNS event rate and has a similar spectral shape which makes a CEνNS excess of events not easily discernible.

The several hypotheses proposed to explain the origins of the LEE in cryodetectors can be divided into 3 main categories. The first category contains explanations regarding stress events due to the mounting and holding of the cryogenic calorimeters. The second type of hypotheses is that there are signals due to crystal lattice defects that slowly anneal, either in the absorber crystal or in the interface between crystal and lithographed sensor (the TES). Finally, the last hypothesis is a leakage to the calorimeters from high energy depositions happened in inactive parts of the setup. All three of these categories are currently being investigated and are most likely all

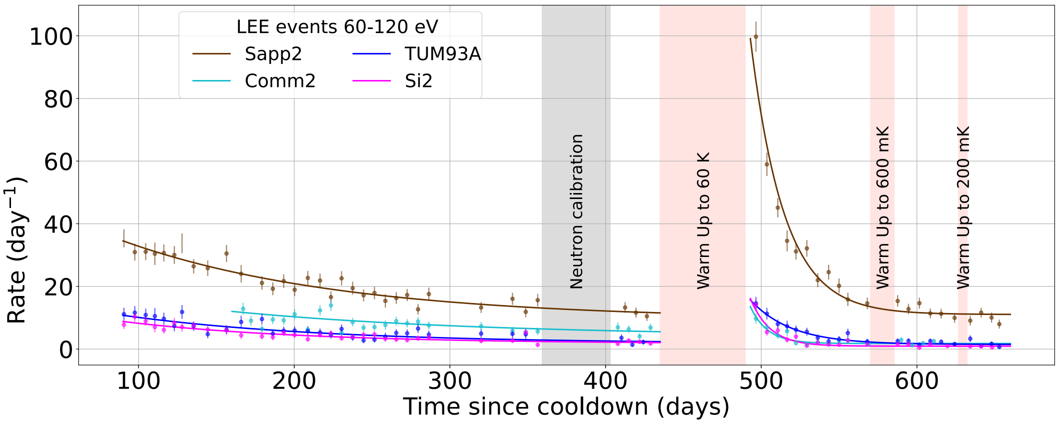

Figure 2.18. Top: Time evolution of LEE rates (60-120 eV) in different detectors of the CRESST experiment for before warm-up (90-380 days) and after warm-up (495-670 days) datasets. Solid lines show the fitted functions ($R(t) = A \cdot exp\left(-\frac{t}{\tau}\right) + C$). Figure from [80].

true, meaning that there is probably more than one cause for the LEE.

Moreover, another characteristic of this background is that it appears to have two major components that decay with time, as visible from Figure 2.18. One component appears to be constantly decreasing with time with a decay constant of almost half a year, while a second component that decays in few tens of days appears to be recharged every time the cryogenic calorimeter goes through a thermal cycle (i.e. is warmed up and cooled again).

In order to attempt a reduction of this background component, two main tools are being deployed by NUCLEUS. The first one is the *inner veto* described in section 2.3.2 which should allow to veto events due to mounting stress or external phonon leakage. The second is the *double TES* which allows for a double readout of the energy deposited in the same crystal. This allows to discriminate events that do not produce the same signal in the two sensors as particles would [81, 82]. The analysis concerning this detector is presented in chapter 5.

2.4.4 Sensitivity

Extracting a sensitivity curve for the NUCLEUS experiment is a challenging task due to the presence of the LEE which, to date, remains fairly unquantified and unconstrained since it appears to have a dependence on time and on the setup used. A brief discussion on the sensitivity of the experiment can still be made in an optimistic scenario in which the LEE is not present.

To build a sensitivity study two main quantities are needed: the neutrino spectrum and a background model. The neutrino spectrum was already shown in Figure 2.4 and the background model can be built by fitting the red curves in the panels of Figure 2.15. The results of the fits are shown in Figure 2.19 and the fitting function used is:

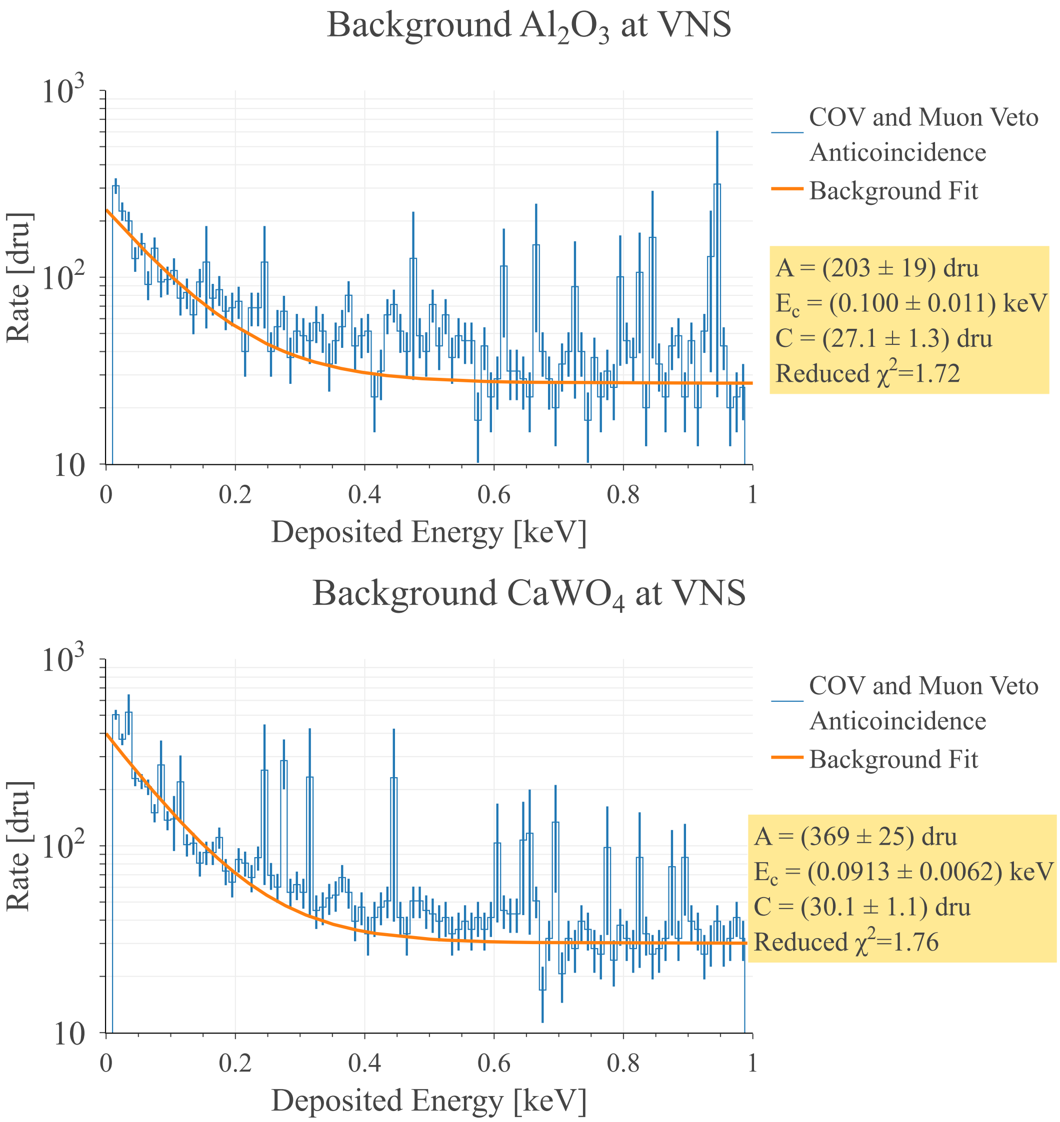

Figure 2.19. Background model obtained by fitting the red curves in the panels of Figure 2.15. In the orange insets of the two panels the best fit parameters are reported. In both panels several peaks are present, but are mostly due to statistical fluctuations (the error bars show the $\pm 1\sigma$ statistical fluctuations). There is one exception which is peak at ~ 0.3 keV in the bottom panel which is due to atmospheric neutrons, investigations on this peak are ongoing to track down the exact physical process that generates it.

$$A \cdot e^{-E/E_c} + C$$

where A is the normalization factor, E_c is the decay constant and C is a constant offset for the flat component of the background.

The probability of observing a certain spectrum is the product of the probability to observe the given number of total events (given by a Poisson distribution) and the probabilities of observing the individual events at their respective energies. With both background and signal models built, it is possible to simulate Monte Carlo experiments by extracting the number of counts, with a Poisson distribution, for each of the two components from their expected behaviors, generating a simulated energy spectrum. With this Monte Carlo experiment, then it is possible to build a *binned likelihood*:

$$-\log\left(\mathcal{L}(\sigma,\beta)\right) = \sum_{t\in\text{targets}} \left[\mu_t(\sigma,\beta) - \sum_{i=0}^{k} \log\left(n_i \cdot \mu_i(\sigma,\beta)\right)\right] \tag{2.6}$$

where β and σ are the background and signal strengths respectively (expected to both be 1 in the presence of CEνNS), $\mu_t(\sigma,\beta)$ is the total expected number of counts due to both background and CEνNS, $\mu_i(\sigma,\beta)$ is the expected number of counts in bin i due to both background and CEνNS, n_i is the number of counts observed in bin i and k is the total number of bins in the spectrum. The likelihood in eq. (2.6) can be maximized (usually the equivalent minimization of the negative logarithm is performed) to extract the β and σ parameters, in particular two maximizations can be made: one for the *background* only hypothesis, in which σ is forced to 0, and one for *background plus signal* hypothesis in which both parameters are free:

$$\mathcal{L}_{\text{bck}}(\beta_0) = \max\nolimits_\beta\left[\mathcal{L}(0,\beta)\right] \qquad \mathcal{L}_{\text{bck+sig}}(\beta_1,\sigma_1) = \max\nolimits_{\beta,\sigma}\left[\mathcal{L}(\sigma,\beta)\right]$$

From the results of these maximizations the statistical significance of the simulated CEνNS measurement can be extracted as:

$$Z = \sqrt{2\log\left(\frac{\mathcal{L}_{\text{bck+sig}}(\beta_1,\sigma_1)}{\mathcal{L}_{\text{bck}}(\beta_0)}\right)} \tag{2.7}$$

By simulating multiple Monte Carlo experiments the average values of Z, β_0, β_1 and σ_1 can be extracted (for more details on the statistical procedure see [4]).

With the simulated background presented in section 2.4.2 and Figure 2.19 and with the $\sim$ 10 g target detector (as foreseen for NUCLEUS) with a 20 eV threshold the sensitivity to a CEνNS detection is shown in Figure 2.20 where it can be seen that in about half a year more than a 5σ significance can be reached on the CEνNS detection. As visible from Figure 2.21 the relative uncertainty reachable on the CEνNS cross-section with this setup is between 10% and 20% in around 1 or 2 years of data taking, while to go beyond this level the livetime needed starts to reach unreasonable numbers. The current cross-section estimation given by COHERENT [28] is $(165^{+30}_{-25}) \times 10^{-40}$ cm^2 ($\sim$ 19% precision).

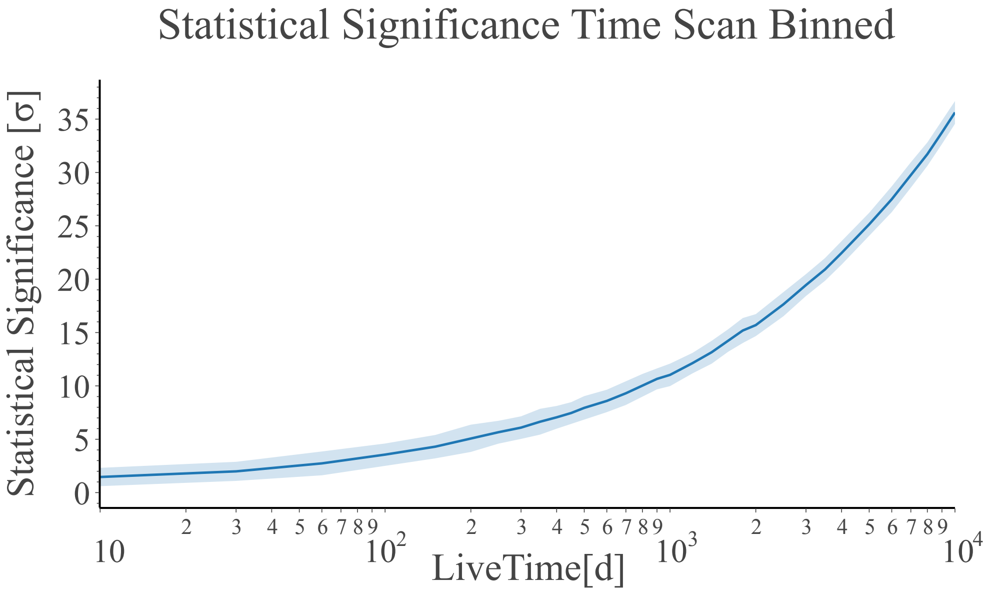

Figure 2.20. Statistical significance expected to be reached by NUCLEUS as a function of the livetime when considering only statistical uncertainties and the background model in Figure 2.19.

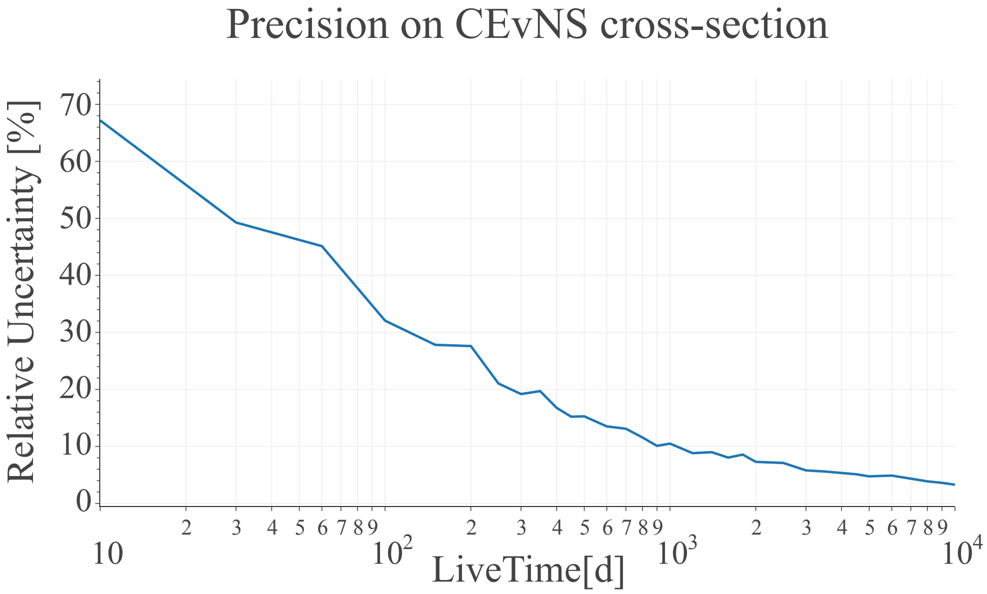

Figure 2.21. Precision on the CEνNS cross-section expected to be reached by NUCLEUS as a function of the livetime when considering only statistical uncertainties and the background model in Figure 2.19.

2.5 Current Status

The NUCLEUS experiment is currently undergoing the commissioning at TUM before deploying the system at the nuclear reactor. All the cold readout electronics has been tested and the shields with the muon veto have been deployed at both cryogenic and room temperature. A single crystal of the COV has been successfully operated with the required performances while the other crystals are being prepared for mounting. Finally, the cryogenic detectors have been repeatedly operated with stable and satisfying performances over weeks of data taking, but not yet deployed with the *inner veto*.

The most recent efforts of the collaboration were aimed at deploying and operating all the different systems simultaneously, while validating the background level with the setup at TUM. A full and stable operation of cryocubes with COV and muon veto has been achieved with optimal detector resolution. Several days of data with these systems have been taken and analyzed, the results are presented in chapter 5. The collaboration is now focused on finalizing all the tested systems and deploying the apparatus at the Chooz power plant in 2025.

Once the setup is moved to Chooz, a preliminary technical run will be performed where the background models will be thoroughly validated along with the performances and stability of all the subsystems. After this last tuning and understanding of the experimental setup, the first phase of the experiment will start.

Chapter 3

Optical Calibration

Experiments using low threshold cryogenic calorimeters, like in the case of NUCLEUS, have always faced the challenge of characterizing and calibrating the detector response in the ROI, which goes from 1 eV to few hundred electronvolts. In fact, it is not trivial to find a radioactive source that deposits energies in this energy range. A typical X-ray source used is ^{55}Fe which produces calibration lines at around 6 keV which, in the case of NUCLEUS, is more than 60 times the typical values of the interesting energies for a reactor CEνNS measurement. To evaluate the response of the detector, then, the characteristic extracted at the radioactive source energy need to be extrapolated down to the ROI but this typically entails an incomplete description of the response and high systematic uncertainties.

Moreover, since cryogenic calorimeters are typically used in low background environments, being able to place and remove the calibration source while keeping the cryostat at base temperature is a requirement. This requisite is difficult to fulfill using keV scale X-ray sources, which need to be placed inside the detector holder due to the low X-ray penetration.

For these reasons, a calibration procedure based on optical photons emitted from a LED has been developed and deployed in both the NUCLEUS and BULLKID experiments. In this chapter, the procedure will be described along with a detailed description of the setup deployed in the context of the NUCLEUS experiment. The commercial setup initially deployed showed some significant limitations which were addressed when building an upgraded custom setup which will be referred to as LANTERN.

3.1 Optical Calibration Procedure

Cryogenic calorimeters are fairly slow devices, with integration times ranging from a few hundred microseconds to several milliseconds. When shining one of these calorimeter with fast light pulses, it is impossible to resolve the arrival time of the single photons. For this reason, the energy depositions of the N_γ photons on the detector are integrated in the same response pulse, whose amplitude follows a Poisson distribution. The mean and variance of this distribution can be expressed

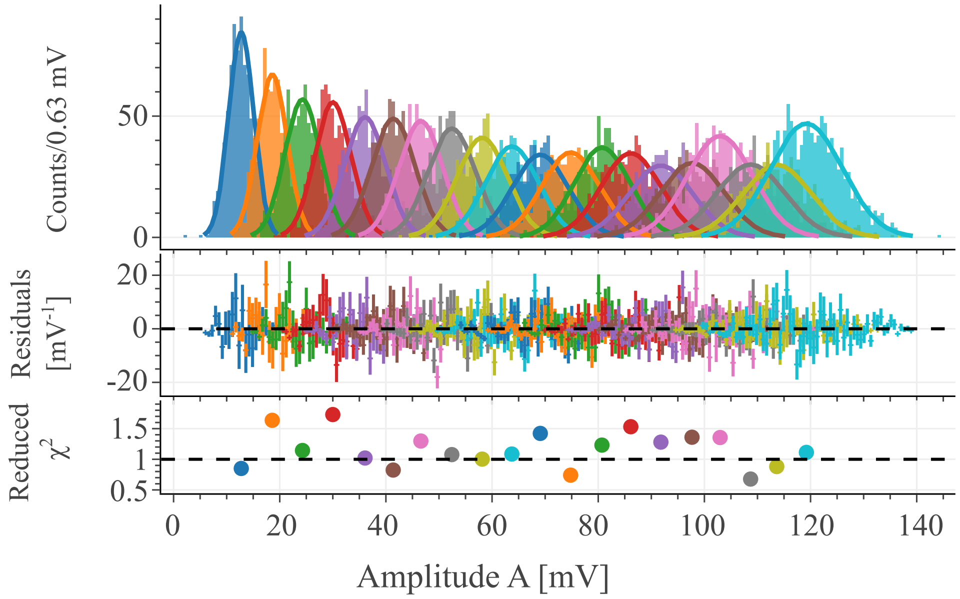

Figure 3.1. Example of Gaussian fitting of the distribution of the amplitudes of the light induced pulses to extract the mean and the variance of the distributions. In the top panel, the histogram of the amplitudes of the LED induced signals are shown. In the middle panel the residuals between the fitting functions and the histogram are shown (the error bars indicate the statistical error of the histogram bin). In the bottom panel the reduced χ^2 of the fit is plotted for each fitted function.

as follows:

$$\mu_\gamma = r < N_\gamma > \epsilon_\gamma \qquad \sigma_\gamma^2 = (r\ \epsilon_\gamma)^2 < N_\gamma >= r\ \epsilon_\gamma\ \mu_\gamma \tag{3.1}$$

where μ_γ and σ_γ^2 are respectively the mean and the variance of amplitude distribution of the generated light pulses, r is the responsivity of the detector (which is the inverse of the calibration constant) and ϵ_γ is the energy of the single photon. The variance can be written in terms of the mean amplitude (as in equation 3.1), and by adding the intrinsic resolution σ_0^2 of the detector one obtains the following relation between the variance and the mean of LED generated distributions and measured with a cryogenic calorimeter with linear response:

$$\sigma^2 = r\ \epsilon_\gamma\ \mu_\gamma + \sigma_0^2 \tag{3.2}$$

As shown in Figure 3.1 one can generate multiple distributions (by varying $< N_\gamma >$) and independently extract σ^2 and μ_γ with a Gaussian fit. By fitting the behavior of σ^2 with respect to μ_γ using equation 3.2 it is possible to extract σ_0^2 and r as shown in Figure 3.2 since ϵ_γ is known and fixed [83]. It is worth to mention that this procedure does not rely on the knowledge of N_γ meaning that it is robust with respect to unquantified light losses or yields.

3.1.1 Beyond the linear approximation

The calibration procedure just presented is only valid under several assumptions which are usually not too constrictive, but not fulfilling them can alter the results.

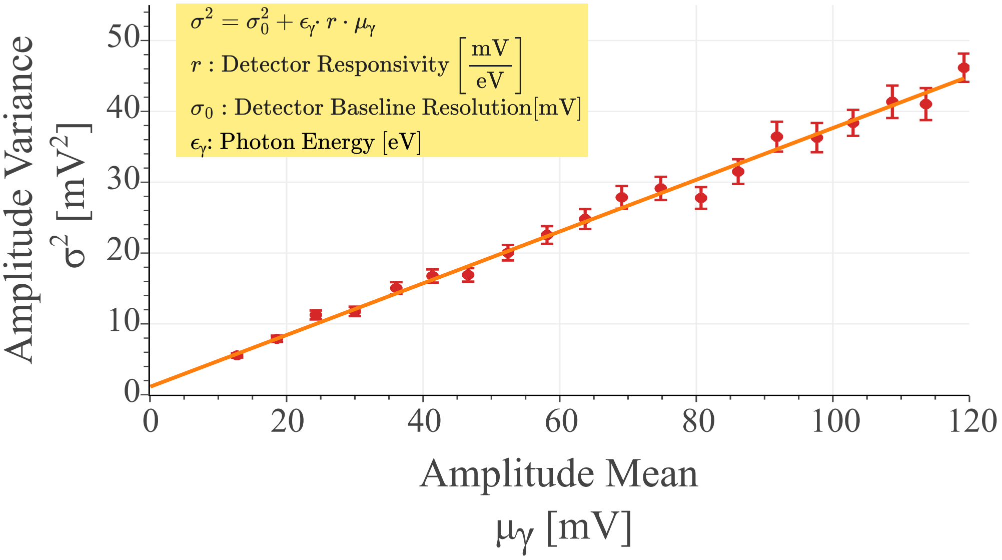

Figure 3.2. Example of the fit of eq. (3.2) to the variance of the light generated amplitude distributions as a function of the mean, in order to extract the responsivity and the baseline resolution of the detector as described in the inset of the figure. The error bars show the statistical error on the points.

The strongest of these assumptions is that the amplitude of the measured detector pulse scales linearly with the deposited energy, which is only true if there are no saturation effects or other non-linearities in the detector response curve.

On the other hand, using the same calibration data, one can evaluate the non-linearities in order to compensate for them. If the calibration setup allows for a linear control on $\langle N_\gamma \rangle$, as it is for the ones described in sections 3.2 and 3.3, then by measuring the behavior of μ_γ with respect to the mean number of detected photons, the level of non-linearity can be extracted. In practice, supposing that from the hardware point of view it is possible to tune a parameter proportional to the light intensity ($n_c \propto \langle N_\gamma \rangle$), one can write a quadratic relation between the mean amplitude of the light induces pulses and n_c as follows:

$$\mu_\gamma = a \cdot n_c \, (1 + b \cdot a \cdot n_c) \tag{3.3}$$

where a is the response of a completely linear detector with respect to a certain value of n_c (meaning that $\langle E_\gamma \rangle = \langle N_\gamma \rangle \, \epsilon_\gamma \propto a \cdot n_c$), and b is the next leading order expressed in units of $\frac{1}{\text{amplitude}}$, meaning that it is the non-linearity affecting a pulse of a given amplitude. These two parameters are the only unknowns from this equation and can be extracted from fitting μ_γ with respect to n_c as shown in Figure 3.3.

For ease of data analysis, it is usually preferred to work in the condition in which the pulse amplitude is linearly proportional to the deposited energy. This means

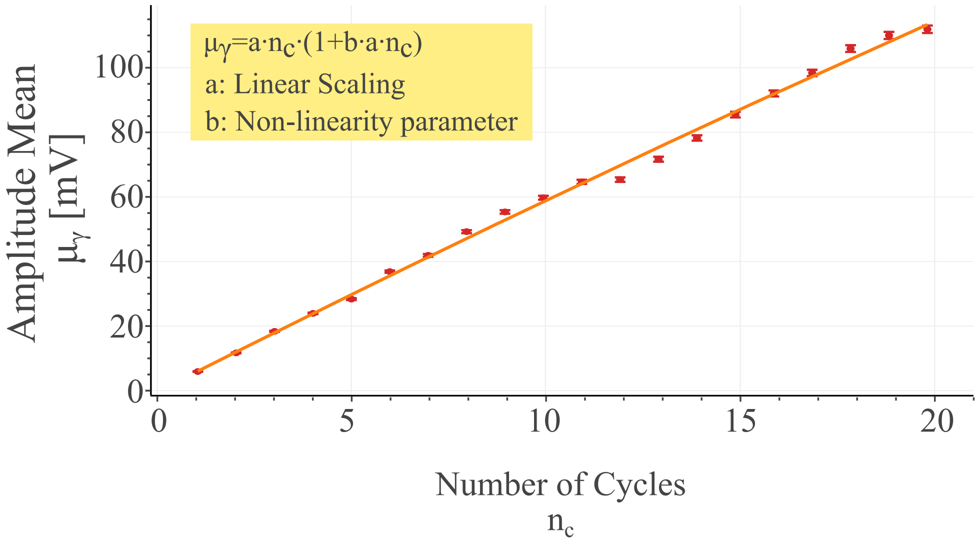

Figure 3.3. Extraction of the detector non-linearity with the parabolic model in eq. (3.3) from the linear scaling of the number of photons absorbed, which is proportional to the parameter n_c (here dubbed as *Number of Cycles* as will be later explained in section 3.2). As visible from the data points, statistically significant deviations from the second degree model (orange line) can be present and can be due to detector instabilities or to a fine structure in the detector response curve that is not taken into account by the model. The error bars on the data points represent the 1σ statistical fluctuations.

that a new *linearized* amplitude can be defined as:

$$A_L := a \cdot n_c = \frac{A}{1 + b \cdot a \cdot n_c} \tag{3.4}$$

where A is the pulse amplitude measured from the detector readout and a and b are the same parameters as eq. (3.3). Since only light induced pulses are characterized by a defined value of n_c it is required to have a way of converting a pulse amplitude A in an effective number of cycles to be used in this definition. Since by fitting eq. (3.3) the average relation between n_c and A is extracted, it is possible to invert this equation in order to convert a pulse amplitude in an effective value of n_c:

$$n_c = \frac{-1 \pm \sqrt{1 + 4b \cdot A}}{2b \cdot a} \tag{3.5}$$

given that n_c is proportional to the average number of detected photons (it is thus defined as a positive value) and that typically A_L is chosen as positive, meaning that $a \geq 0$, the solution with the minus sign needs to be discarded since it would result in nonphysical values and behaviors of n_c. By combining this last equation with the definition of A_L the linearized amplitude can be evaluated from the recorded pulse amplitude as:

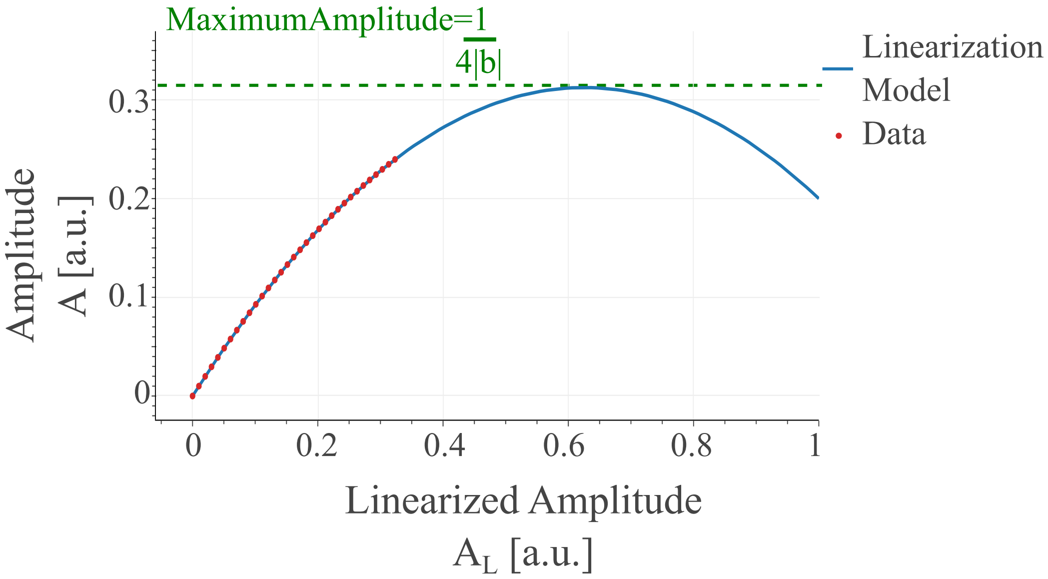

Figure 3.4. Diagram of the maximum range of validity of the LED calibration for negative values of b. The blue line shows the second degree linearization model obtained by fitting the behavior of the average amplitude of the light distributions with respect to the n_c parameter. The red data points show how the average amplitude of the light induced pulses are distributed. The green horizontal dashed line shows the level of the vertex of the parabola.

$$A_L = \frac{-1 + \sqrt{1 + 4b \cdot A}}{2b} \tag{3.6}$$

After this linearization one can perform the calibration procedure described in section 3.1 using A_L as the estimated pulse amplitude.

Since this linearization procedure consists in extracting a 2^{nd} polynomial approximation of the unknown functional of the detector response, the linearization is only valid in the amplitude range in which the data points used for the fit of eq. (3.3) have been generated. This is especially evident when considering the case in which b is negative, in fact, the linearization can be mathematically successful only for amplitude values below the vertex of the parabola described by eq. (3.3). In fact, for a pulse amplitude greater than the parabola's vertex there is no value of n_c for which the parabola reaches such a value as shown in Figure 3.4, making the linearization impossible (in mathematical terms such amplitude values lie outside the domain of the inverse function of the parabola).

TESs are operated with the working point in the linear region of the superconductive transition, and when relatively high energies are deposited in the detector the TES response might get non-linear due to the saturation of the superconductive transition, meaning that negative values of "b" are usually expected.

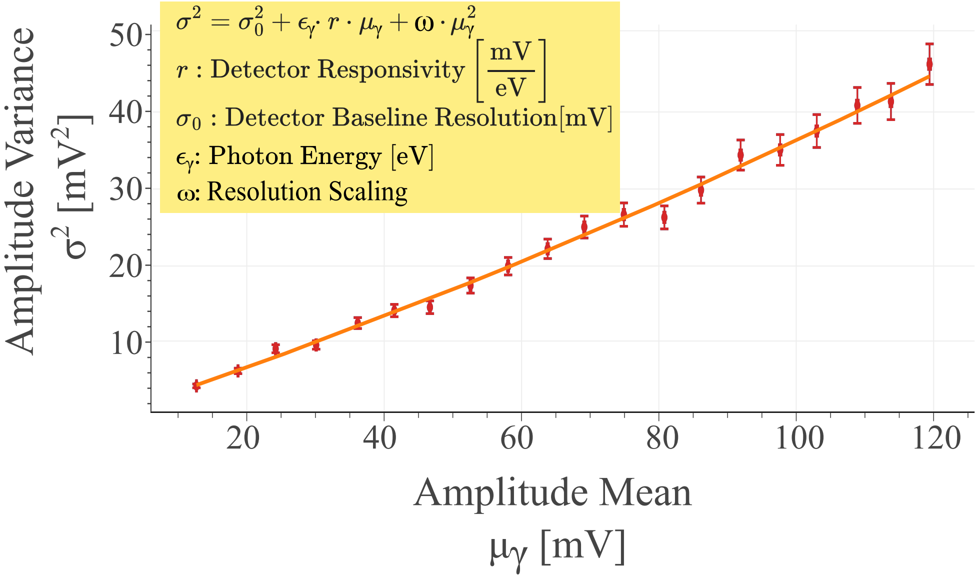

Figure 3.5. Example of an optical calibration using the model in eq. (3.7) to account for non-poissonian increase of the variance of the generated amplitude distributions. The red points are the fitted data extracted from the fit results shown in Figure 3.2, in orange the best fit result is plotted and in the orange inset the names of the fit parameters are shown. The error bars on the points represent the 1σ statistical fluctuations.

3.1.2 Taking detector effects into account

In section 3.1 the scaling of the variance of the light depositions with respect to the mean values due to Poisson statistics was described, but this is not the only effect that contributes to this broadening. One of the typical effects is due, for example, to position dependence of the recorded amplitude which introduces a quadratic scaling:

$$\sigma^2 = \sigma_0^2 + r \cdot \epsilon_\gamma \cdot \mu_\gamma + \omega \cdot \mu_\gamma^2 \tag{3.7}$$

where the ω parameter expresses a broadening of the variance following a quadratic dependence. The value of ω can be extracted by performing a fit of the behavior of σ^2 with respect to μ_γ using the model of eq. (3.7) as shown in Figure 3.5.

Procedurally, it is advisable to perform the fit of eq. (3.7) after the amplitude linearization described above, since they are usually competing effects. In fact, due to the TES saturation the variance of the distributions of the light induced pulse amplitudes at high energies tends to be lower than the Poisson expectation, while the ω term tends to increase the dispersion of the amplitude distribution.

3.2 First optical setup deployed for NUCLEUS

In order to employ the optical calibration effectively, several requirements need to be met. The first one is to have knowledge of the single photon energy ϵ_γ emitted from a

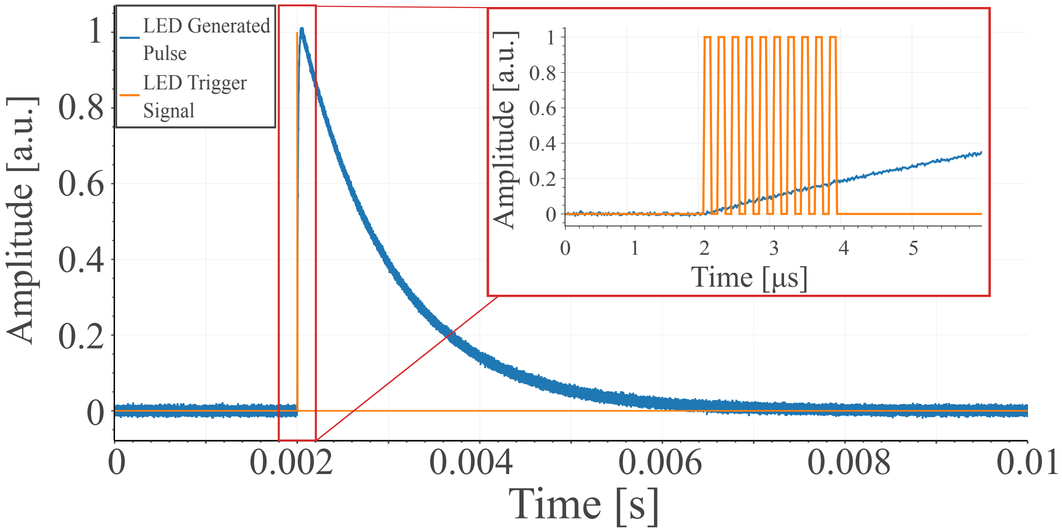

Figure 3.6. Simulated cryogenic detector pulse (blue) generated with an LED triggered with a 5 MHz square wave train made of 10 cycles. In the inset, a zoom on the detector pulse rise time is shown in order to appreciate the time structure of the LED trigger signal.

monochromatic source. For this reason, a LED is used as a controlled photon source since it can be chosen with the desired wavelength and is relatively monochromatic (typically LEDs with less than a 2% spread in the wavelength distribution can be easily found). The photon energy is typically known from the data-sheet of the chosen LED which, on the other hand, reports this value only for operations at room temperature and since the photon wavelength has quite a strong temperature dependence, the LED needs to be operated at $\sim 300\ K$.

To correct the non-linearities of the detector, as explained in section 3.1.1, a linearly tunable average number of photons N_γ is required. This is achieved by exciting the LED with a square wave train (see Figure 3.6), where the numbers of periods, referred to as *cycles*, is then proportional to the number of photons (this is the n_c parameter from the discussion in section 3.1.1). Combining this requirement with the fact that the N_γ photons need to be integrated in the same detector pulse, meaning that the square wave train needs to have a much shorter time duration (typically of an order of magnitude) with respect to the detector rise time τ_r (typically of the order of 100 μs to a few milliseconds), means that the trigger signal for the LED needs to be a square wave with typical frequencies going from hundreds of kilohertz to several megahertz.

3.2.1 Laboratory Calibration Setup

In the first NUCLEUS setup (thoroughly described in [4]), the chosen LED driver to be deployed was the CAEN SP5605, which uses a wavelength $\lambda_\gamma = (248 \pm 8)$ nm and can be operated with a maximum switching frequency of 290 kHz. The choice of the wavelength is due to the fact that both $CaWO_4$ and Al_2O_3 are transparent to visible light, and at cryogenic temperatures it is known that these crystals are opaque to

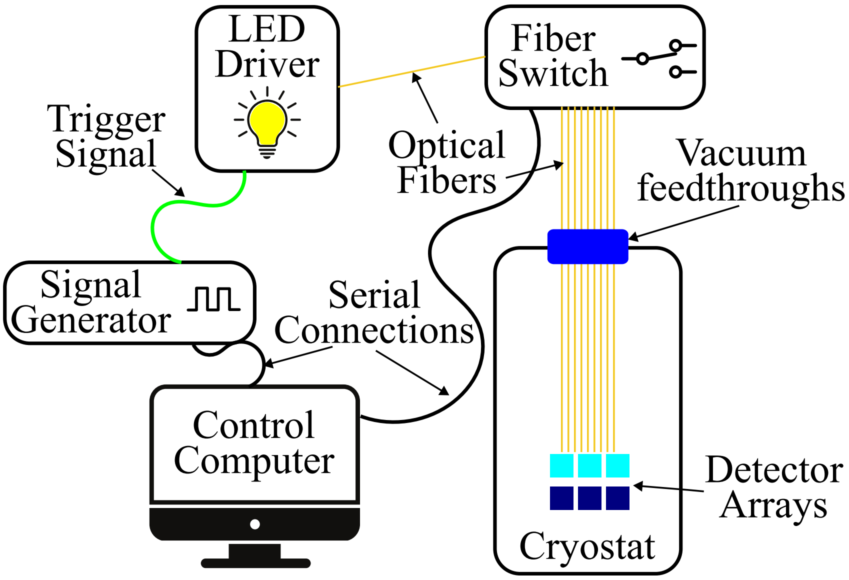

Figure 3.7. Diagram of the main elements of the optical calibration setup in the NUCLEUS experiment. A control computer commands the signal generator to output the trigger signal for the LED driver and commands the Fiber Switch to connect the desired optical output. A single optical fiber brings the light from the LED driver to the Fiber Switch and 9 other optical fibers go to the head of the cryostat and are connected, via vacuum feedthroughs, to other 9 fibers placed inside the cryostat that bring the photons to the detector arrays. More details on this setup can be found in [4].

deep UV light. To generate the LED trigger signal as in Figure 3.6 a commercial signal generator (the Agilent 33250A) is used in order to ensure reliability and repeatability of the generated square wave.

Since NUCLEUS aims to deploy an array of cryogenic calorimeters, the LED light pulses need to be sent to each detector independently. This is achieved by the use of an optical multiplexer, the LEONI Fiber Optical Switch mol 1×16, which takes the LED optical signal as input (via an optical fiber) and transfers it to one of the 16 optical channels it has as output. These outputs are then connected to optical fibers that bring the light to the top of the cryostat as shown in the diagram in Figure 3.7.

3.2.2 Cryogenic Calibration Setup

Once the LED light is at the top of the cryostat it passes through one of the vacuum optical fiber feedthroughs that connect the room temperature fibers to the ones present inside the cryostat. The latter are 120 μm thick and are thermalized with metallic connections throughout the various temperature stages of the cryostat in order not to create an additional heat-load near the detectors.

In order to shine light on the detectors, which are mounted inside the inner veto (see section 2.3.2), a custom device referred to as the *mirror wafer* is used. As shown in Figure 3.8, this device is used to split in two the light coming from the fibers, each fraction is then directed to one of the calorimeters. The mirror wafer then allows to tightly mount the optical fibers near the target detectors and decreases of a factor

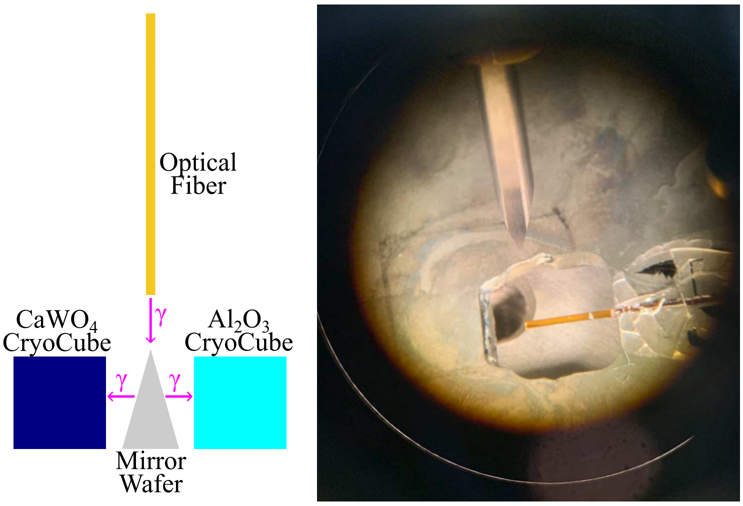

Figure 3.8. Left: Mirror Wafer concept diagram, the light arrives from an optical fiber and is split in two components by the mirror wafer prism and each component is sent to one cryocube of the NUCLEUS target detector array. Right: Picture of one mirror wafer prism under the microscope with a placed optical fiber. More details can be found in [4].

2, with respect to the total number of calorimeters, the amount of optical fibers needed.

3.2.3 Limitations of the Setup

The setup just described presents several limitations. The first one is the use of the optical multiplexer, which is a costly and fragile device: during the three years of operation of this setup, several of the optical channels became unusable due to cross-talk or optical losses because of misalignment. Moreover, even if perfectly functioning, this device introduces a loss of light due to the optical connections it requires.

A second limitation is given by the scalability of the setup that would be needed for NUCLEUS phase 2. Simply increasing the optical channels is not feasible due to cost of the FiberSwitch amounting to 16 k€ and the size of the vacuum feedthroughs. For an increased number of cryogenic detectors, a new solution needs to be implemented.

The last and main limitation is given from the CAEN LED driver, since the maximum signal switching frequency is 290 kHz. Considering that the NUCLEUS detectors have typical rise times ranging from 0.1 ms to 1 ms and that the LED excitation time needs to be at least one order of magnitude shorter, this triggering frequency allows a maximum number of cycles of 3 and 30. This obviously entails a very limited dynamic range and granularity for the calibration.

3.3 The LANTERN project

Due to the severe limitations of the optical calibration setup presented in the last section, a new solution was devised in the context of this work. The LED Array for

Non-Intrusive Tuning of the Energy Range with Nimbleness (LANTERN) project presented here has shown promising results in replacing the old setup and has already been adopted by NUCLEUS since the development of the first prototype.

3.3.1 Project Objectives

The first aim of LANTERN is to have fast switching LED in order to be able to pack several cycles in the detector rise time. This is achieved by the simple yet effective LED driving circuit presented in section 3.3.2. Moreover, the luminosity of the LED was tuned in order to increase the dynamic range of the calibration.

A second aim is to design a system that is relatively easy to scale to the experimental needs. This solution is described in section 3.3.4 and does not only tackle the multiplexing of the light signals but also the cryogenic installation.

Important for LANTERN is also that all the key parameters for the operation need to be fully tunable via a computer interface. This requirement is due to the fact that at the VNS it will not be possible to access the experimental setup daily.

Since none of the limitations or requirements are impacted by using a signal generator to produce the LED triggering signal, the developed setup assumes the presence of an external trigger signal source, which in later stages could be also integrated in the LANTERN electronics.

3.3.2 LANTERN LED Driver Unit

When designing the LED driver unit to be used two main options were considered: a current mirror and a more simple circuit with a transistor acting as a switch. The first option offers greater control on the LED luminosity since it gives direct access to the value of the flowing current, this level of accuracy is not required by the procedure and this solution made scalability a more difficult challenge due to the size of the components and the level of uniformity required from the LED characteristics. Moreover, due to the high current having to flow through the transistors (~ 100 mA) it was not easy to find a suitable component for the mirroring, the current and the switching times. For these reasons, the LED driving circuit presented in Figure 3.9 was chosen.

The driver circuit chosen consists of a voltage divider that is always kept at the DC bias voltage of $\mathrm{V_{CC}}$ (typically $\mathrm{V_{CC}} \approx 10$ V) and goes into conduction only when the Metal-Oxide-Semiconductor Field-Effect Transistor (MOSFET) M is biased with a positive trigger signal T (which has a 50 Ω coupling). Special attention was given to the choice of the MOSFET since it needs to handle quite high impulsed currents (of the order of 100 mA) and fast switching times. In fact, for a 5 MHz square wave triggering signal a typically required rise time is around 10 ns, meaning a signal bandwidth arriving up to ~ 35 MHz which should be less than the bandwidth of the transistor. The combination of high speed and currents is not trivial to have in the same component, which is why several MOSFET models were tested and the one listed in Table 3.1 was chosen.

In order to match the switching speed required for the calibration, a resistor $\mathrm{R_1}$

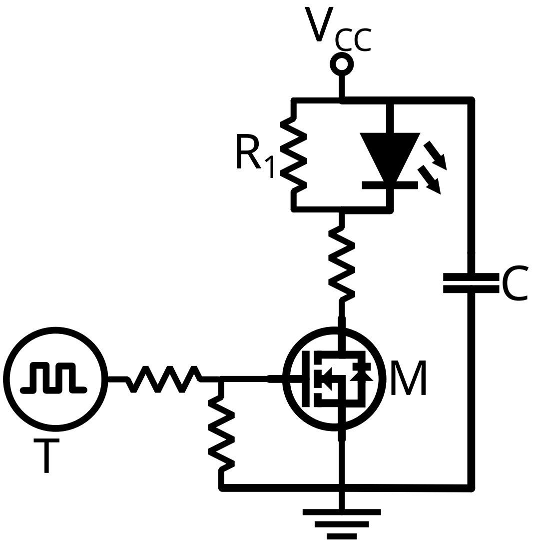

Figure 3.9. LANTERN LED driver unit: the DC bias voltage V_{cc} is applied in parallel to a resistor R_1 and the LED (the resistor is present to guarantee a quick discharge of the LED). The MOSFET M is used to send the circuit into conduction based on the triggering signal T. A capacitor C is added in parallel to the whole circuit as a protection against high frequency fluctuations possibly affecting V_{cc}.

Table 3.1. LANTERN Driver Components

Components	Symbol	Model
MOSFET	M	BSS123
LED 1200 nm		LED1200S-03
LED 400 nm		LLS-UV400
LED 275 nm		N-C35PUDTDU1
LED 250 nm		UVTOP250H-FW-SMD

(typically of few hundred ohms depending on the chosen LED) is placed in parallel to the LED. This allows for faster discharge times of the LED, which is then able to switch states with the required speed. Installing R_1 does come with a drawback, since by being in parallel with the LED it will redirect some current flowing through the device, decreasing its luminosity. This drawback is usually compensated by allowing higher values of V_{CC} and has proven not to be a limiting factor.

Moreover, a capacitor C is put in parallel to the whole driving circuit in order to protect it from potential high frequency noise present in the DC bias V_{CC}. A second resistor is also added right before the MOSFET M in order to protect the LED from burning due to an excessive value of the bias voltage.

This driving circuit design does not require any particular LED. This is a design choice since the LED wavelength must be matched to the crystal used by the cryogenic calorimeters. The LEDs tested with this driver had wavelengths of 255 nm, 275 nm, 400 nm and 1200 nm, ranging from deep UV to far infrared.

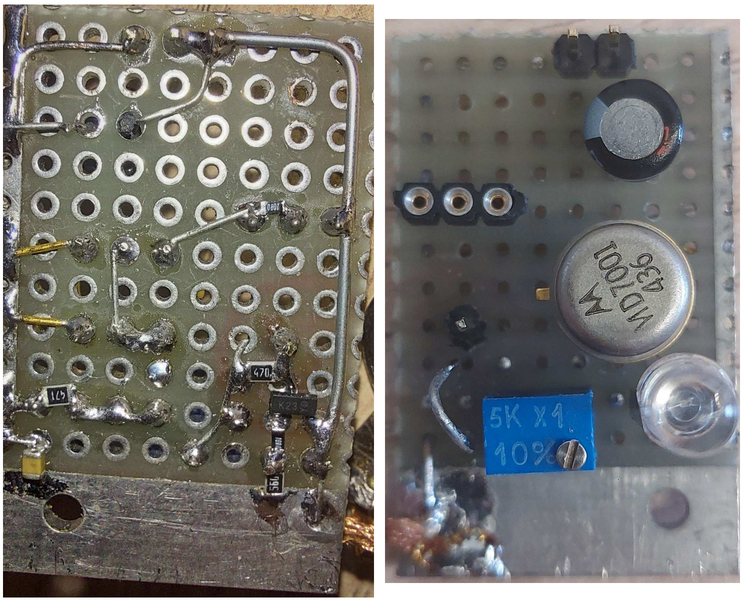

Figure 3.10. Picture of the LANTERN prototype single LED driver (on the left the back side of the board is shown, on the right panel the front of the board with the LED is presented).

3.3.3 Single Pixel Tests

Since the LED driving circuit is the most delicate part of the electronics required for the calibration, several tests have been performed in order to characterize its behavior. The prototype in Figure 3.10 was produce and coupled with a 400 nm LED for most of the tests. This wavelength was chosen since it is easily characterizable with most common optical setups (PMT and spectrometers) and could be compared with the corresponding 400 nm CAEN LED driver available.

The tests made on this prototype involved 3 main instruments: a PMT to measure the time structure of the train of LED bursts, since this sensor has fast response times, a spectrometer to characterize in detail the wavelength spectrum of the device and cryogenic detectors to compare the calibration obtained with the CAEN setup and with the LANTERN prototype.

3.3.3.1 Measurements with PMT

The aim of the measurements done with the Hamamatsu R11065-20 PMT is to characterize the single light cycle produced by LANTERN as a function of all the different parameters. The setup used, shown in Figure 3.11, couples the LANTERN driver of Figure 3.10 to a PMT which is inside the metal box to shield it from ambient light. The driver is also coupled to a Peltier cell with a heat dissipation system in order to regulate the operation temperature of the device which is readout with a digital thermometer placed near the LED, inside the casing. The LED triggering signal and the response from the PMT are read out using a HDO6104A oscilloscope, while the temperature is read and saved by coupling the thermometer to an Arduino Uno board.

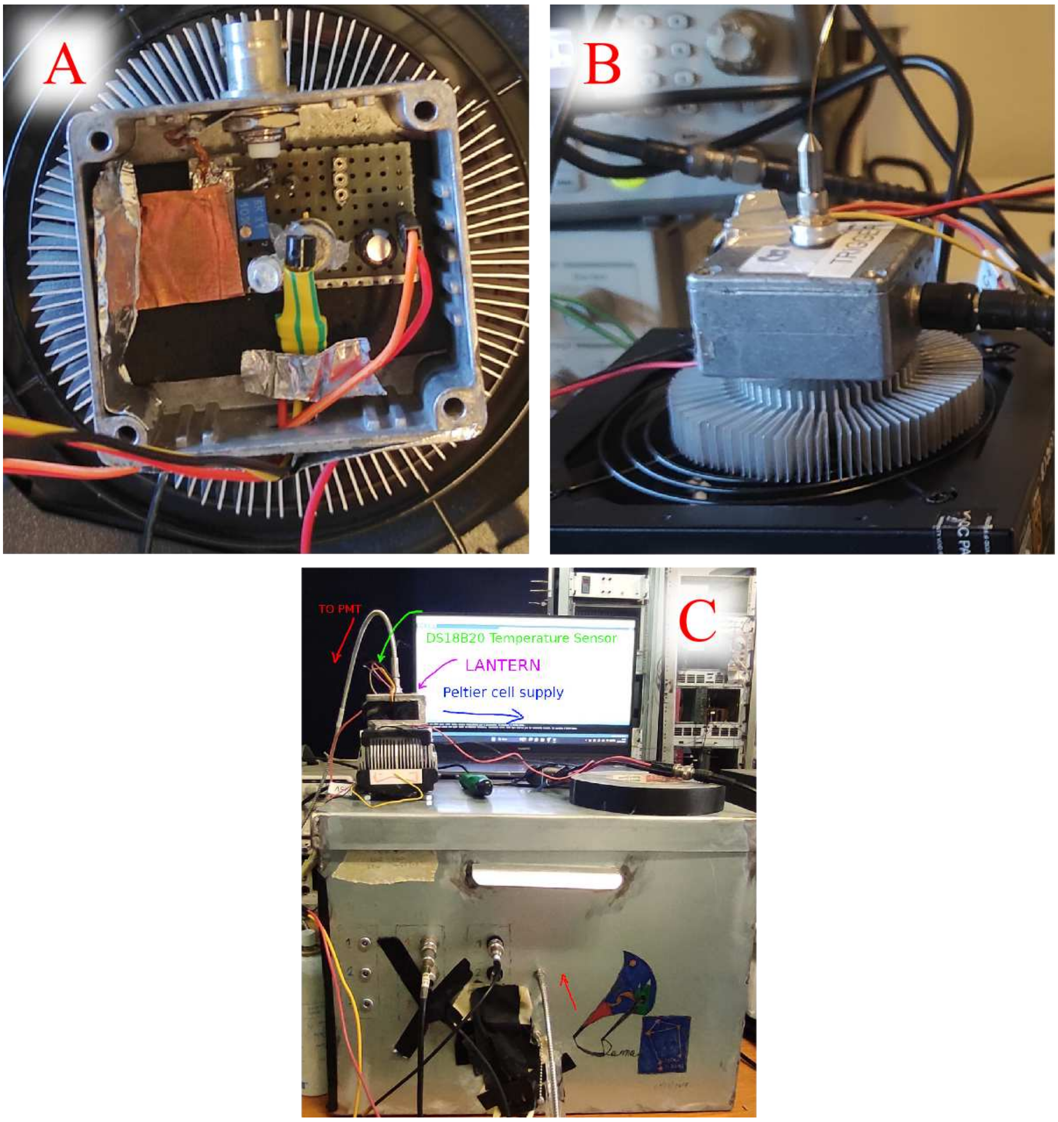

Figure 3.11. Setup used for the PMT characterization of the single LANTERN LED driver unit. In panel A the LED driver in it's casing is shown, a thermometer (device with the yellow and green electrical insulation) is placed inside the casing in contact with the other components to measure the operating temperature of the driver. In panel B the LED driver box coupled to a Peltier cell and a cooling unit is shown. In panel C the coupling of the driver with the PMT box is shown.

The first test being performed was to find the correct parameters in order to have a comparable light pulse with the CAEN driver. After the tuning of the parameters (which are recorded in Table 3.2) the light cycles resulted extremely similar, as shown in Figure 3.12, and for the sake of the optical calibration are essentially identical. The slower decay visible in the signal produced by the LANTERN driver is not worrisome, since the light pulse fulfills the timing requirements. One feature that was immediately noticeable is the much higher luminosity of the LANTERN driver, which will be quantified using the cryogenic calorimeters in section 3.3.3.3.

Table 3.2. Parameters to be used to match the CAEN light pulses with the LANTERN single LED driver prototype.

Trigger Frequency	Duty Cycle	Bias Voltage
5 MHz	14%	6 V

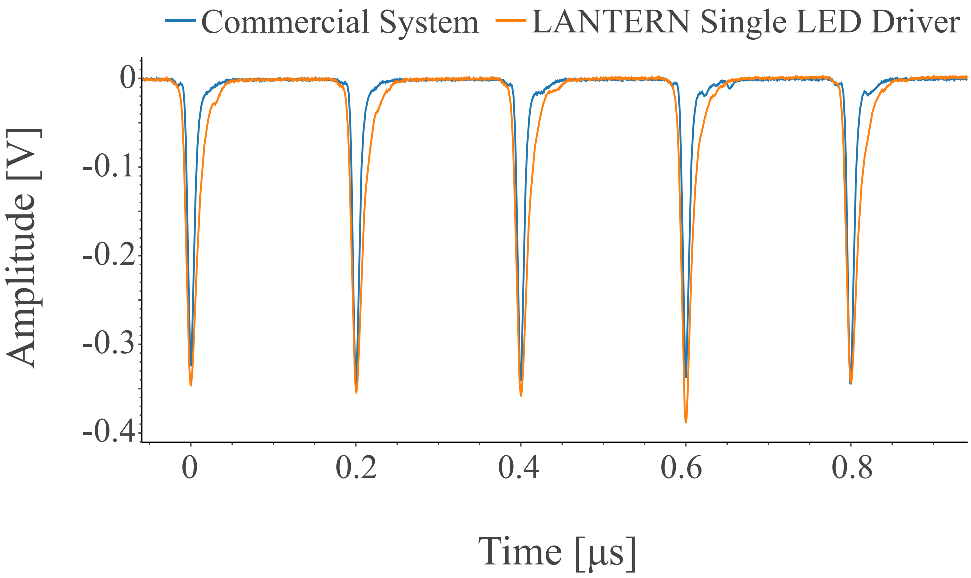

Figure 3.12. Comparison of the PMT signal produced with the commercial CAEN system (blue) and the LANTERN single LED driver prototype (orange).

After having matched the light pulses between the two LED drivers, a measurement of possible unwanted background produced from LANTERN has been done. Two back-to-back measurements were taken of the dark count rate of the PMT with LANTERN. The first one, m_1 with a 16 min duration, with the LED completely unbiased ($\mathrm{V_{CC}} = 0$) and a second one, m_2 lasting 38 min, with a positive applied bias ($\mathrm{V_{CC}} > 0$) but with no trigger signal. The measurements yielded:

$$m_1 = (212 \pm 4)\frac{\text{events}}{\text{min}} \qquad m_2 = (224 \pm 2)\frac{\text{events}}{\text{min}}$$

where the uncertainties given are only statistical, but there are small systematics due to varying luminosity levels in the laboratory and the not complete light tightness of the setup. The two numbers result comparable for the level of precision this measurement allowed, meaning that keeping the LED driver biased but not triggered does not induce any significant increase in the counting rate.

After these two fundamental tests showed the feasibility of using LANTERN to calibrate low background cryogenic experiments, a validation of the luminosity behavior with respect to the bias voltage and the operation temperature was performed. The energy deposited by a fixed train of light pulses was estimated by using the integral

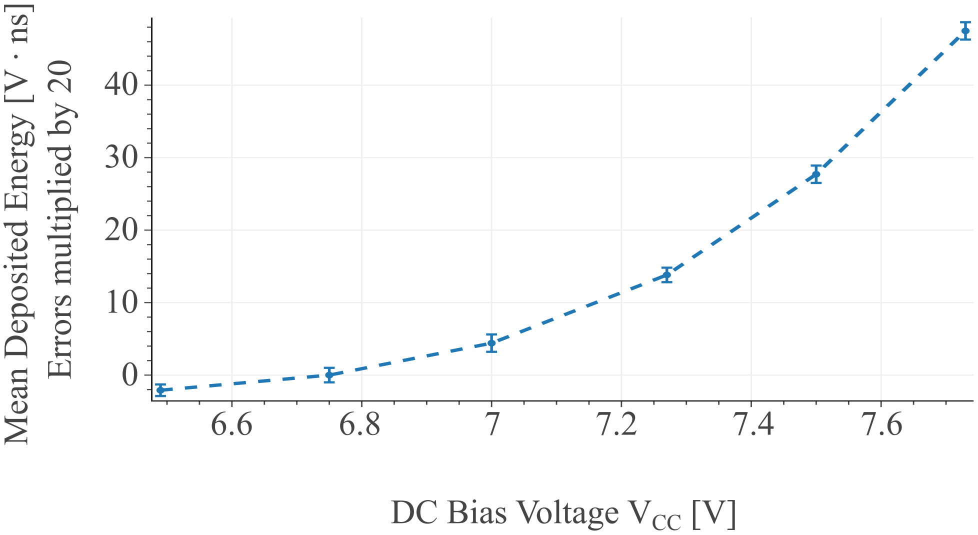

Figure 3.13. Scaling of the energy recorded by a Hamamatsu R11065-20 PMT when LANTERN is shining with 5 cycles as a function of the bias voltage V_{CC}. The error bars represent the 1σ statistical fluctuations (to make the error bars visible a ×20 factor is applied).

of the PMT response to mimic how a cryogenic detector would react to the light depositions. This estimation, which has units of $V \cdot s$, is an uncalibrated energy scale, but since all the characterizations needed require only relative comparisons there is no need to have an absolute energy scale. To extract the average behavior of the luminosity with respect to these parameters, $O(10^3)$ PMT signals have been recorded and their amplitude distribution fitted with a Gaussian. For ease of understanding the scaling of the amplitude, the integral values have their sign switch in order to have the same behavior as they would with in a cryogenic detector measurement (since the calorimeters give a positive response signal, while the PMT gives a negative one).

To measure the scaling of the luminosity with the bias voltage a train of 5 cycles was set and V_{CC} was varied from 6.49 V, which corresponds to no visible pulse, to 7.73 V. The recorded scaling is shown in Figure 3.13, and it goes from noise fluctuations, near $0\ V \cdot ns$ amplitudes, to several tens of $V \cdot ns$ with an almost exponential increase (as expected from the current versus voltage relation of diodes).

For characterizing the scaling of the luminosity with the operating temperature, a train of 10 cycles was set with the parameters in Table 3.2. The temperature was varied from 17°C to 40°C (typical laboratory temperature variations) by changing the voltage on the coupled Peltier cell, which can act both as a heating and a cooling element. The recorded scaling is shown in Figure 3.14, after an initial plateau at around 20°C, which is the data-sheet operating temperature of the LED, the luminosity starts increasing with temperature due to temperature effects of both the

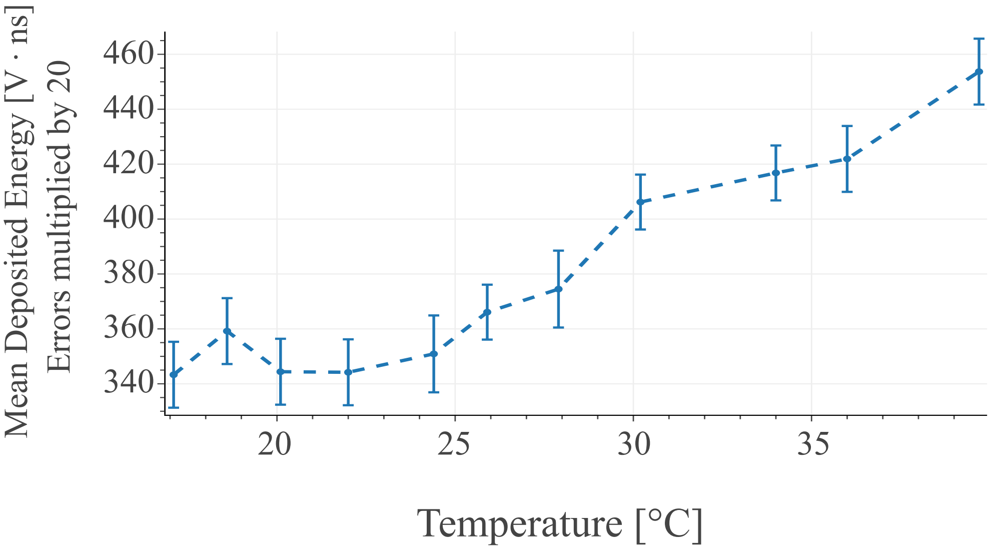

Figure 3.14. Scaling of the energy recorded by a Hamamatsu R11065-20 PMT when LANTERN is shining with 10 cycles as a function of the operating temperature. The error bars represent the 1σ statistical fluctuations (to make the error bars visible a ×20 factor is applied).

solid state elements and the resistors present. The total luminosity increase from 22°C to 40°C is at the 30% level. Since summer to winter reproducibility is not a requirement, albeit it would be a desirable feature, this level of variation is not concerning and since a calibration typically lasts up to a few hours it will not affect the calibration results. Moreover, since the LANTERN electronics is suitable for operation inside the cryostat vessel, it can be operated in a temperature controlled environment.

Finally, the scaling of the recorded light energy with the number of cycles has been evaluated. The measurement was performed by setting the parameters of Table 3.2 and varying the cycles from 1 to 10 (typical values used for an optical calibration). The results show a linear dependence on the number of cycles, apart from 3 outlying points present, as shown from Figure 3.15, this is well in accordance with expectations since the light bursts generated with LANTERN match well the ones generated by the CAEN driver. Moreover, from performing the fit described in section 3.1.1 it is visible that the second degree term “b” is compatible with the absence of any non-linearity.

Overall, the results from the tests done using the Hamamatsu R11065-20 PMT are quite promising and indicated that, while further test are needed for a complete characterization, the LED driver designed for LANTERN is working as required and attention can be shifted to the multiplexing as described in section 3.3.4.

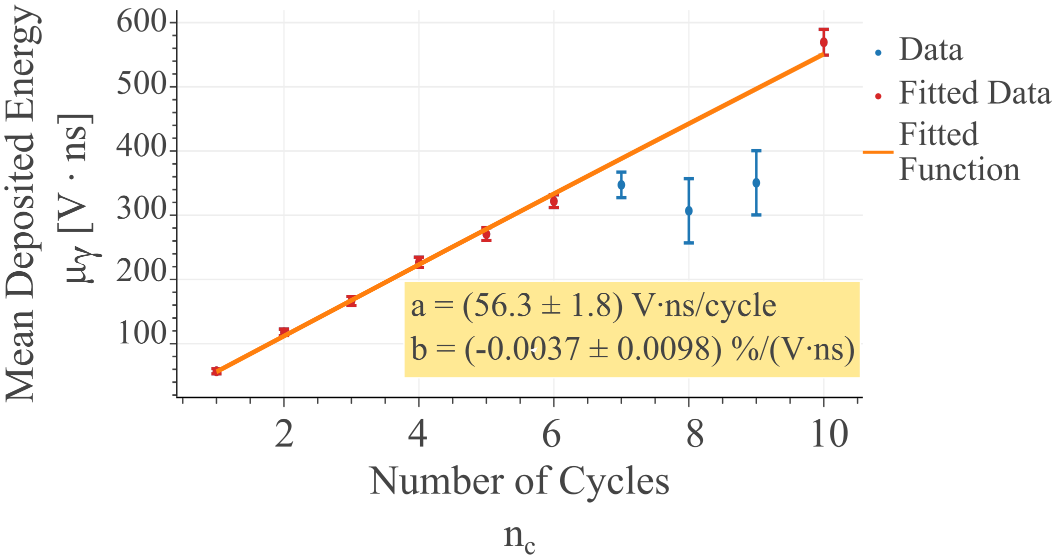

Figure 3.15. Scaling of the energy recorded by a Hamamatsu R11065-20 PMT when LANTERN is shining as a function of the number of cycles used. Three outlying points (blue) are present and were removed from the fitted data (red points). The outlying points are due to a low quality best Gaussian fit of the deposited energy distribution (due to possible changes in the data taking conditions). The error bars represent the 1σ statistical fluctuations of the mean deposited energy as extracted from the Gaussian fitting results.

3.3.3.2 LED Spectrum Validation

An essential measurement to characterize the behavior of the LED drivers is the spectrum of the wavelength of the generated photons. This was done by shining with the LED operated with the typical parameters used for calibrations on a PyLoN:100BR_eXelon CCD [84] which records the incoming wavelength spectrum. By taking the maximum and the Full Width at Half Maximum (FWHM) from the generated spectra, presented in Figure 3.16, the expected wavelengths from the CAEN and LANTERN LED drivers are:

$$\lambda_{\text{CAEN}} = (408.2 \pm 5.9)\text{nm} \qquad \lambda_{\text{LANTERN}} = (398.5 \pm 6.2)\text{nm}$$

where the error is given by converting FWHM in a Gaussian error with the relation $\text{FWHM} = 2\sqrt{2\ln 2}\sigma$. The non-monochromacity of the LED is at the level of few percent, which is satisfying for the calibration procedure. In fact, if the energies of the generated photons have a mean value ϵ_{ph} and a standard deviation $\sigma_{\epsilon_{ph}} \approx \frac{2}{100}\epsilon_{ph}$, then one expects the following term in the variance of the LED generated energy deposition $E_{dep} = \langle \epsilon_{ph} N_{ph} \rangle \approx \langle \epsilon_{ph} \rangle \langle N_{ph} \rangle$ distribution:

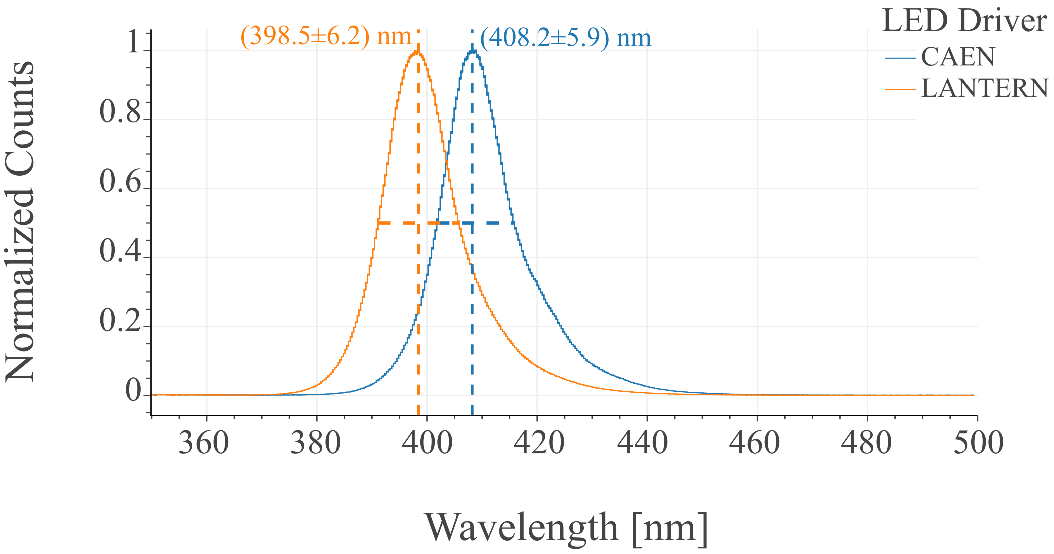

Figure 3.16. Measurement of the LED wavelength spectrum for the CAEN (blue) and the LANTERN (orange) drivers. The spectrum is measured using a PyLoN:100BR_eXelon CCD and renormalized for the quantum efficiency of the device.

$$\sigma^2_{LED} = \sigma^2_{N_{ph}} \langle\epsilon_{ph}\rangle^2 + \sigma^2_{\langle\epsilon_{ph}\rangle} \langle N_{ph}\rangle^2 = \langle N_{ph}\rangle \langle\epsilon_{ph}\rangle^2 + \frac{\sigma^2_{\epsilon_{ph}}}{\langle N_{ph}\rangle} \langle N_{ph}\rangle^2 =$$

$$= \langle N_{ph}\rangle \langle\epsilon_{ph}\rangle^2 \left(1 + \frac{\sigma^2_{\epsilon_{ph}}}{\langle\epsilon_{ph}\rangle^2}\right) = E_{dep} \langle\epsilon_{ph}\rangle \left(1 + \frac{\sigma^2_{\epsilon_{ph}}}{\langle\epsilon_{ph}\rangle^2}\right) \approx E_{dep} \langle\epsilon_{ph}\rangle \left(1 + 10^{-4}\right) \tag{3.8}$$

where $\langle\cdot\rangle$ indicates the mean operation and N_{ph} is the number of absorbed photons. In eq. (3.8) the two term are respectively the Poisson term as described in section 3.1 and a term due to the non-monochromacity of the LED. The presence of the last term slightly increases the variance of the integrated amplitude, by $\sim 10^{-4}$ which results negligible. The eq. (3.8) above has been double-checked with a Monte Carlo simulation done by extracting N_{ph} from a Poisson distribution and for each photon the wavelength was extracted from the sampled distribution in Figure 3.16.

3.3.3.3 Optical calibration comparison

The last test performed is a back-to-back calibration of cryogenic detectors done with both the CAEN and LANTERN drivers in order to check for differences. This test was performed by using one of the $CaWO_4$ NUCLEUS target detectors and the 255 nm wavelength due to the optical properties of the target.

The first test performed was to check for possible pulse shape differences induced by the LED, for this reason the rise time, defined as the time elapsed for the pulse amplitude to increase from 10% to 90%, of each pulse was measured. To make sure no pulse shape effects are present, the LANTERN LED driver was triggered with

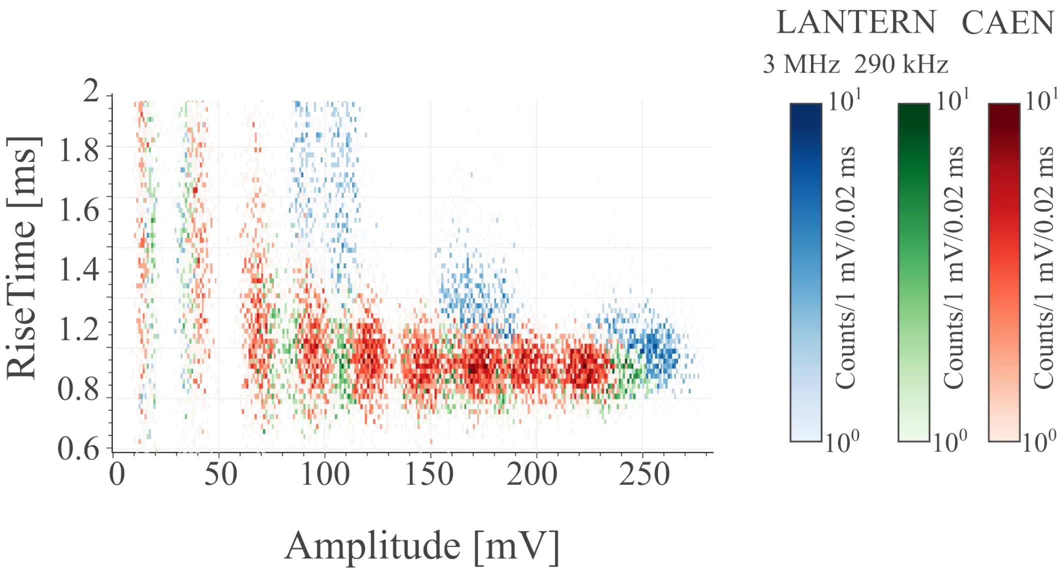

Figure 3.17. Rise time of LED induced cryogenic detector pulses with respect to reconstructed amplitude. In the plot two different triggering frequencies for LANTERN are shown along with the pulses of similar amplitudes generated with the CAEN driver. Different sampling frequency for the 3 MHz data was used in order to match the trigger signal, this causes a different behavior of the rise time at low energies.

both a 3 MHz and 290 kHz square wave. The measured rise times of the produced signals are shown in Figure 3.17.

Below 200 mV, the rise time reconstruction is affected by the Signal-to-Noise Ratio (SNR) of the pulses and by the different sampling frequencies used to save the data (the LANTERN 3 MHz dataset has a higher sampling frequency in order to use the LED trigger as an external trigger for the detector pulses). On the other hand, Figure 3.17 shows the same saturation of the rise time between the two setups for the highest amplitude values, which are the most sensitive to possible pulse shape deformations. In fact, if there were any pulse shape differences one would expect that for amplitude values above 200 mV the rise time would drastically increase due to a wrong integration period of the photons, i.e. the light pulse lasts too much time.

From these three datasets, an optical calibration was also performed, yielding the results presented in Figure 3.18 and Figure 3.19. The calibration constants extrapolated from the fit are compatible with each other in less than one standard deviation, the noise levels are not compatible on the same level but between the CAEN and LANTERN datasets there was an independently measured increase of the noise level and is thus not an artifact of the fit nor of the use of a different LED driver.

With the linearization fit in Figure 3.19 and described in section 3.1.1 it is possible to extrapolate the luminosity “a” of the different drivers in mV, which due to the similar calibration constant extracted can be directly compared. The two LANTERN configurations have similar luminosities, which is expected since the integral of the triggering signal was kept as similar as possible, by changing the trigger parameters accordingly. On the other hand, when comparing to the CAEN driver it is immediately visible that LANTERN has a quite higher luminosity, about a factor 7, showing that this new LED driver prototype has enhanced characteristics with respect to the CAEN one. This consideration is even more true since the CAEN driver was operated at maximum luminosity while LANTERN was not, otherwise it would render the TES normal conducting due to the amount of energy deposited.

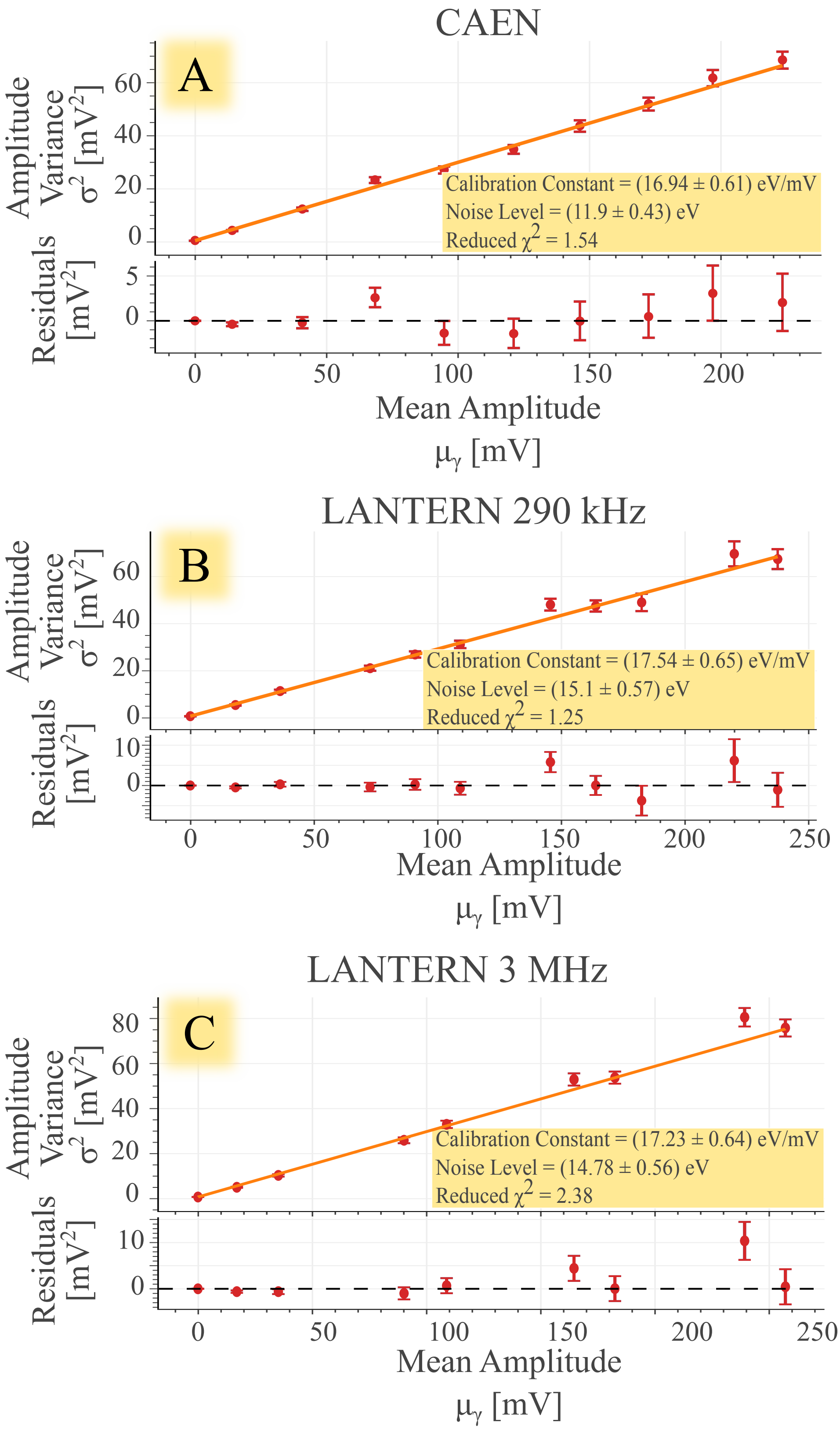

Figure 3.18. Optical calibration of a $CaWO_4$ based cryogenic detector used by the NUCLEUS experiment. The calibration was performed using two different triggering frequencies for LANTERN, 290 kHz in panel B and 3 MHz in panel C and the CAEN LED driver in panel A. For each best fit functions the residuals of the data points from the function are presented in the bottom of the respective panel. The parameters shown in the inset of the plots are derived from the best fit parameters (r and σ_0) with a normalization but are presented with physical units in order to be easily compared. The error bars on the data points represent the 1σ statistical fluctuations.

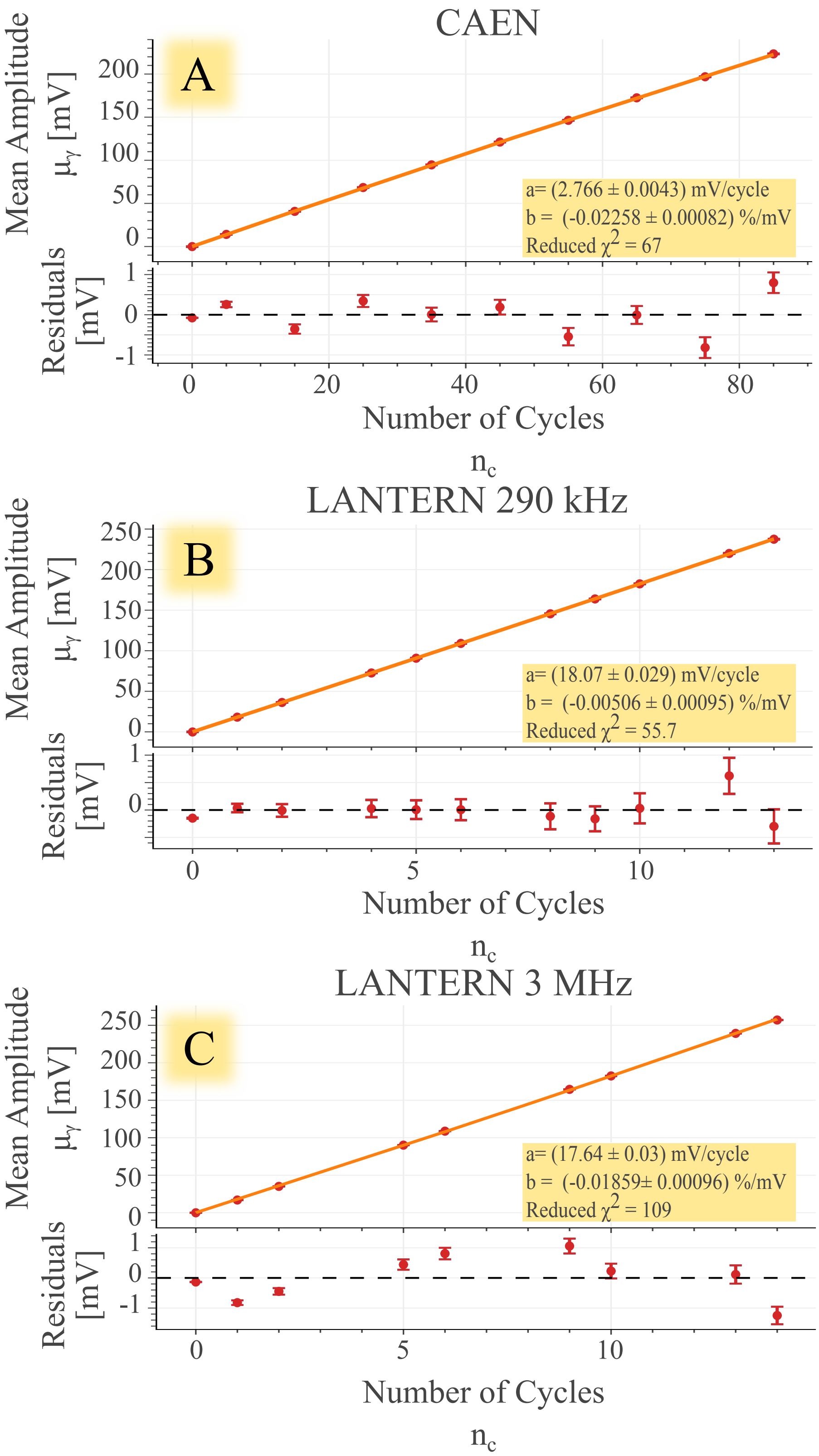

Figure 3.19. Linearization of the response of a $CaWO_4$ based cryogenic detector using LED generated pulses. The linearization was performed using two different triggering frequencies for LANTERN, 290 kHz in panel B and 3 MHz in panel C and the CAEN LED driver in panel A. While the mV per cycle between panels B and C returns compatible, the non-linearity extracted deviates between the fits and whether it is a change of the detector work point, an issue of the sampling or a non-linearity of the setup is still under investigation. For each best fit functions the residuals of the data points from the function are presented in the bottom of the respective panel. The error bars on the data points represent the 1σ statistical fluctuations.

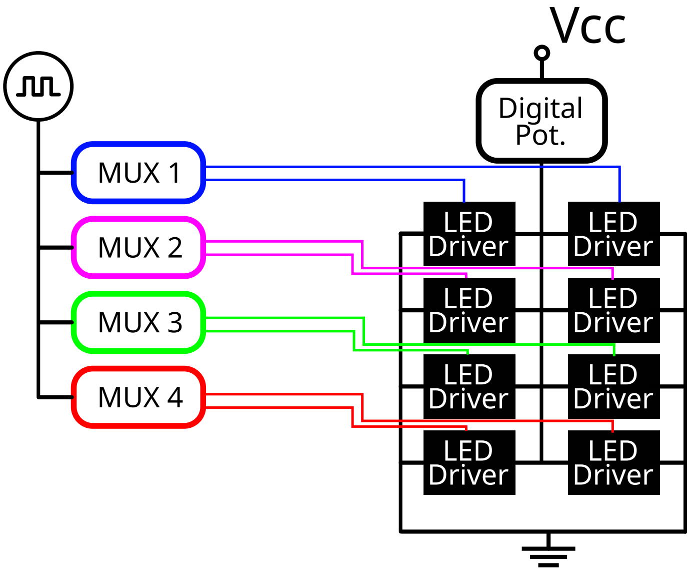

Figure 3.20. Conceptual diagram of the multiplexing solution for LANTERN . The various LED drivers present on the board all share the same bias voltage V_{cc} which is regulated via the digital potentiometer. The choice of which LED to shine is done with the multiplexers, which redirect the trigger signal to the correct LED.

3.3.4 LANTERN: multiplexing and scalability

The prototype of LANTERN's LED driver showed promising results and fulfilled all the required design goals apart from the multiplexing one. As mentioned, this aspect is crucial in order to be able to calibrate with experimental ease highly segmented cryogenic calorimeters. Therefore, a multiplexing strategy has been devised for the final LANTERN electronics, additional features have also been added to complete the system.

The targeted number of optical channels for LANTERN's electronics is 64, but this number can be easily tuned with minimal changes to the electronics. The multichannel LANTERN electronics, of which a conceptual diagram is shown in Figure 3.20, is based on the use of the ADG1406BRUZ [85] multiplexer to forward the trigger signal to the various different LED drivers (one for each LED), this multiplexer was chosen to match the switching frequencies of the triggering signal. This solution was possible due to the considerations made in the last section, where no visible increase of dark count rate was noticed on the PMT when LANTERN is biased but not triggered. The use of multiplexers allows to light up only one LED for each multiplexer used. This is a desired feature since performing the characterization of multiple detectors at the same time might produce some signal cross-talk effect between the LED induced detector pulses, which will produce some systematic effects on the calibrations.

An additional feature worth mentioning in this general description of the multiplexed stage is the luminosity regulation of the LEDs. As visible from Figure 3.20, on the DC bias, which is connected to all the LED drivers, the MCP4011-202 [86] component is mounted. This is a 64 step digital resistor that can be set to the

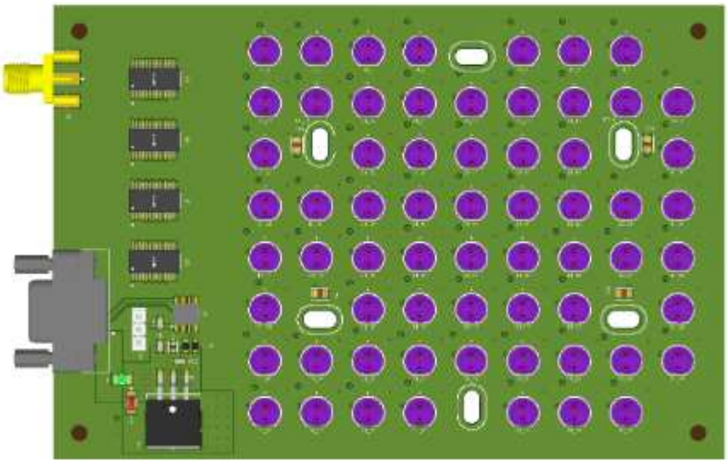

Figure 3.21. Design of the LANTERN board with 64 LEDs and dedicated screw holes for mounting and thermalization inside the cryostat.

desired resistance by using 2 digital pins. This component is required in order to compensate for the different light losses between the optical paths inside the cryostat and the non-uniform luminosity of the LEDs.

As already mentioned, this electronics can be operated inside the outermost cryostat vessel and thermalized at the 300 K stage. In fact, the board design shown in Figure 3.21 has hexagonally placed holes that can be used to fix and thermalize LANTERN to the cryostat. To bring the light from LANTERN's LEDs to the cryogenic calorimeters a bundle of 64 optical fibers will be used, where each fiber will be coupled to the LEDs by the use of *ferrules*, that are fixed to the optical fibers using vacuum compatible epoxy, and LED centering devices that are mechanically coupled to each diode and allow to correctly center the *ferrule* for minimal light loss as shown in the diagram in Figure 3.22.

Since the optical fibers are a direct, albeit weak, thermal connection from 300 K to 10 mK, they can prove to be a non-negligible heating element. To avoid cooling issues in the cryogenic system a custom thermalization for the optical fibers has been designed, it consists of several copper cylinders (one for each temperature stage of the cryostat), each inserted in the middle of the fiber bundle, to minimize the mechanical strain on the fibers, and the fibers are pressed on the cylinder with copper foil. Each copper cylinder is then mechanically and thermally coupled to the cryostat temperature stage using two small copper bars. This thermalization scheme, which is shown in the bottom panel of Figure 3.22, has several advantages: the first one is to have multiple thermalization points with good surface contact between each fiber and the copper, the second is the ease of production using milling techniques on thick copper foils and third is the fact that the copper cylinders can be coupled to the optical fiber bundle before being placed inside the cryostat, which greatly simplifies the mounting procedure. The parts used for the optical setup are listed in Table 3.3.

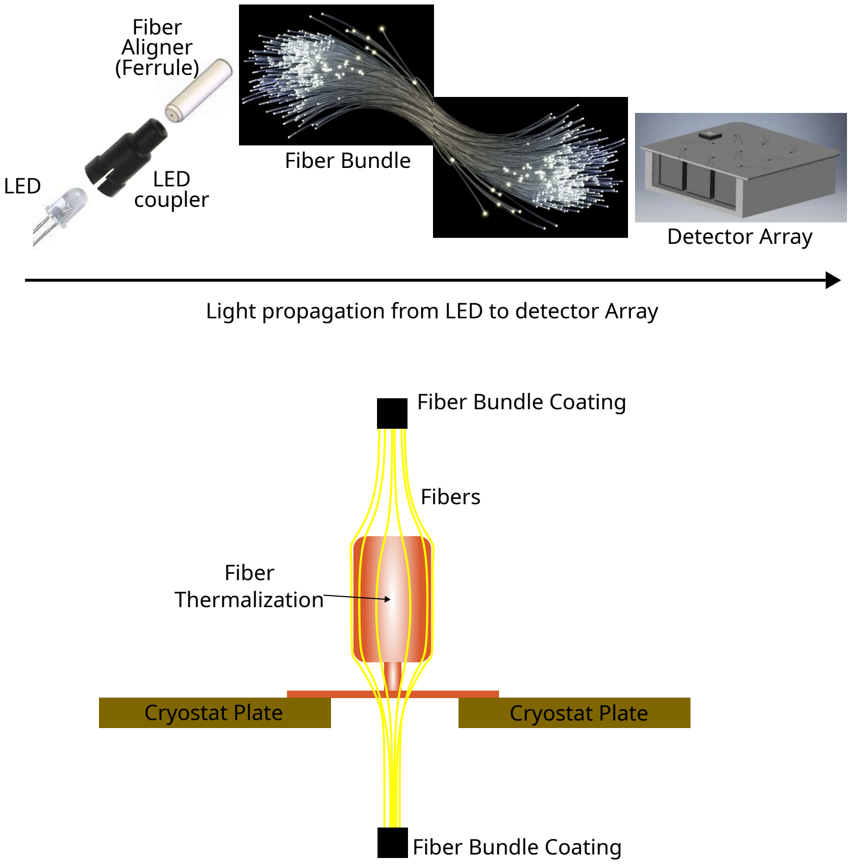

Figure 3.22. Top: LANTERN optical coupling conceptual diagram showing the main elements of the light path from the LED to the detector array. Bottom: diagram of the thermalization piece of the optical fiber bundle.

Table 3.3. LANTERN optical elements

Components	Model	Description
Bundle	SH1064	Super Eska High-Performance 0.265 mm Core Plastic Optical Fiber Bundle 3.25 mm OD Polyethylene Jacket
Ferrule	CF270-10	10.5 mm Long Ceramic Ferrule for MM Fiber, 270 µm Bore Size
LED Coupler	THR_5_22	5 mm LED to fiber plastic coupler

3.3.4.1 Detailed Description of LANTERN's features

The final design of the multichannel LANTERN electronics has several additional features, aside from the multiplexing, with respect to the single LED driver one. As previously mentioned, it makes use of a MCP4011-202 [86] digital potentiometer to regulate the LED luminosity via Transistor Transistor Logic (TTL) communication with the Arduino board. The potentiometer allows a 64 step regulation, which is linear in voltage but not in luminosity due to the intrinsic LED non-linearity.

The choice of using four ADG1406BRUZ [85] 4-bit multiplexers to reach the targeted 64 channels required was made for simplicity during the design phase of the board since they allowed to directly connect all the LEDs to the multiplexers and required only a few logic signals for the desired LED to be chosen. To minimize the number of digital inputs to the board, the 4-bits of the multiplexers are all connected in parallel while the Enable pin of the devices are used to choose between the various multiplexers.

The various elements present on the board require different voltages, for this reason a 12 V DC input is given to the board which is then down-converted to the required voltages using a LM317-N adjustable regulator which guarantees a stable voltage output.

To monitor the working point of the LEDs, two main parameters are essential: the temperature and the biasing voltage. The operation temperature of LANTERN can be easily monitored using the thermometry provided in cryostats, and thus no dedicated device is added to the board. On the other hand, the voltage used to bias the LED drivers is a useful diagnostic tool and is thus measured via the use of a dedicated pin that measures the tension after the digital potentiometer.

The LANTERN board has several components that require digital inputs to set their state but no micro-controller. This is a chosen feature to make it easily coupled to any DAQ system used from the experiments, on the other hand an Arduino board can be placed outside the cryostat (in-vacuum operation is also possible depending on the chosen board) and connected to the board via a commercial electrical vacuum feedthrough (with 15 connections for the 64 LED version). The choice of using an Arduino board was made to keep the possibility to easily implement new characterization features and modes without having to deal with more complex micro-controller programming languages.

Finally, the LANTERN board also has several diodes, fuses and capacitors at the various analogical inputs to protect the more delicate components (mainly the digital resistor) from voltage or current fluctuations.

3.3.5 Multiplexed prototype tests

In order to test the multiplexed electronics, the LANTERN prototype in Figure 3.23 was produced. This prototype was realized using all the components planned for the final board as long as a similar geometry, three of the four LEDs present, are near one another to test for possible cross-talk and for the geometrical dimensions of the optical fiber coupling. The fourth LED present was set in the furthest corner from the other LEDs (~ 15 cm) in order to check the correct transmission of the trigger signal over this distance.

The aim of this prototype was to mainly test the electrical characteristics, since the validation of the LED driver was already performed with the previous prototype. The first test performed consisted of checking whether the trigger signal had deformations between the input to the board and the input of the various drivers. From Figure 3.24, it is clearly visible that aside from a small attenuation (due to the resistors present

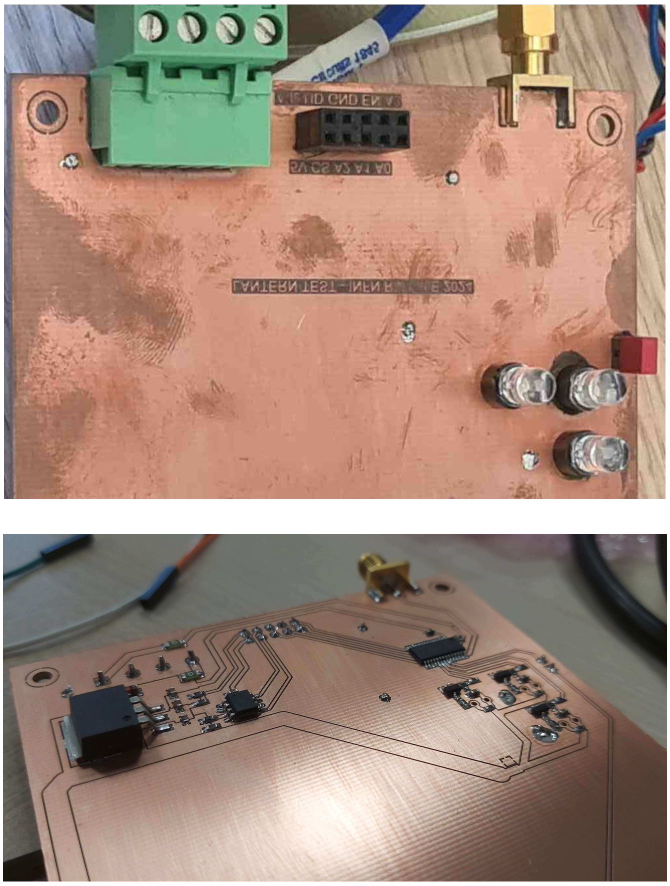

Figure 3.23. Multiplexed prototype of the final LANTERN board. Top: LED side of LANTERN multiplexed prototype realized with the targeted dimensions for 64 LEDs (3 LEDs visible in picture). Bottom: Side of the LANTERN multiplexed prototype showing the electronics.

on the board and a not complete impedance match at the input of the prototype board) the signals have no difference at the level of precision required from this electronics. In particular, if any differences would appear between the pixels they would be between the first three and the fourth which due to the longer path of the signal it could show stronger signal attenuation and deformation.

A second preliminary electrical test performed was to see the effect of the digital potentiometer on the bias voltage. As shown in the left panel of Figure 3.25 the potentiometer was ramped up in resistance producing a smooth drop in the bias voltage of the LEDs.

After that the preliminary electrical tests resulted successfully, a characterization of the optical properties of the multiplexed board was performed. The four LEDs mounted on the board have a 400 nm wavelength (same LEDs as the single driver prototype) in order to match the acceptance of the Hamamatsu R11065-20 PMT used to study the fine structure of the LED light pulses. As for the single driver prototype, the energy delivered by LANTERN to the PMT is measured with the integral of the produced signals in order to approximately have the same response as

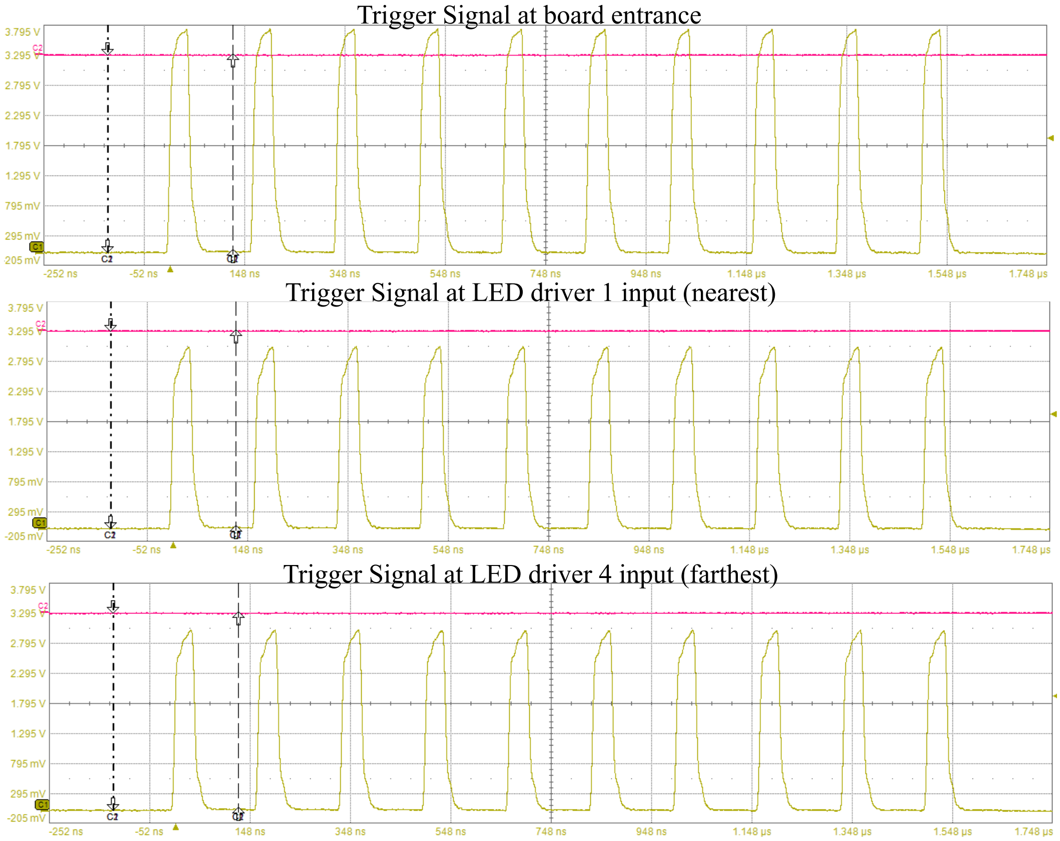
Trigger Signal at board entrance

Trigger Signal at LED driver 1 input (nearest)

Trigger Signal at LED driver 4 input (farthest)

Figure 3.24. Study of the possible deformations of the LANTERN trigger signal on the board (in yellow the trigger signal and in magenta the signal from the PMT). In the plot, the trigger signal is presented at the input of the board (top), at the nearest LED driver (middle) and at the farthest LED driver (bottom). No deformation of the signal is visible.

a cryogenic calorimeter. Following the digital potentiometer electrical test, a optical validation of the resistance change was performed and is shown in the right panel of Figure 3.25. From the plot it is visible that at the lowest settings the potentiometer induces a stable decrease in the luminosity of the LED and around step 30 the biasing is so low that the LED is nearly or completely turned off.

The second optical test performed was to find the correct settings to match the light signal produced by the single driver prototype and the commercial CAEN LED driver. The parameters set for the four pixels are listed in Table 3.4. As visible from Figure 3.26 all the LED drivers present on the prototype board produce very similar light pulses which also match quite well the CAEN ones. From the parameters it is noticeable a slight luminosity decrease with respect to the single driver prototype, since to match the light output the duration of the trigger signal was increased of ~ 40 %. On the other hand, the potentiometer was set at around half, or more, of its range to match the maximum output of the CAEN LED driver, meaning that even if the final LANTERN board has a slight lessening of the luminosity with respect to the single driver prototype it still has a much higher light output with respect to

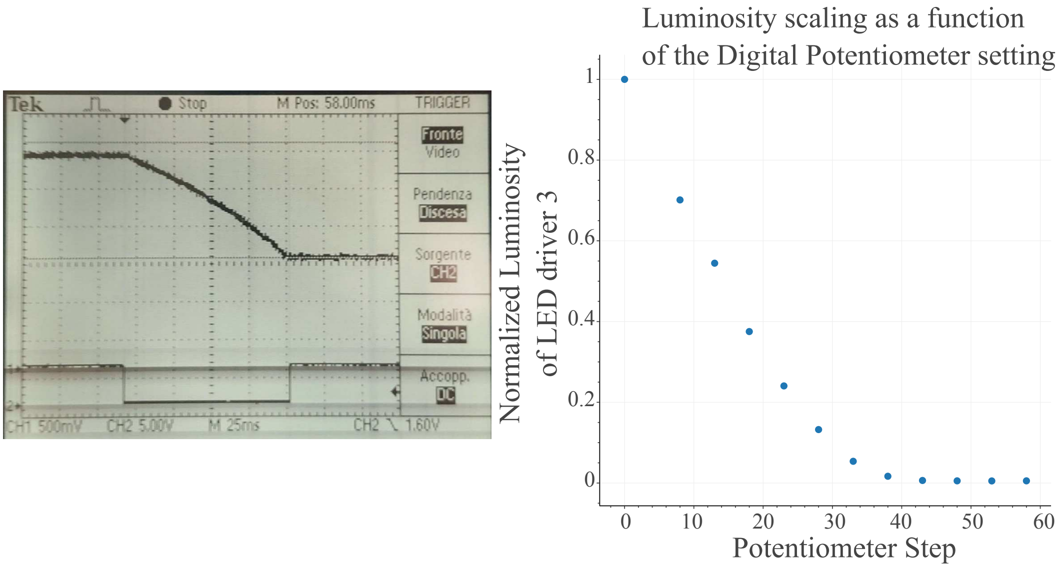

Figure 3.25. Left: quick ramp of the digital potentiometer settings and consequent decrease of the biasing violate. Right: scan of the effect of the potentiometer settings on the luminosity of LED-3 present on the LANTERN multiplexed prototype board.

Table 3.4. Parameters used to match the light pulses produced from the LANTERN multiplexed prototype board with the ones produced from the CAEN LED driver.

LED ID	Trigger Frequency	Duty Cycle	Potentiometer Step
1	5 MHz	20%	39
2	5 MHz	20%	42
3	5 MHz	20%	29
4	5 MHz	20%	34

the commercial system.

A $\sim$ 100 ns delay in the arrival of the PMT signal was noticed when using the trigger signal as an external trigger. This delay was noticed to be the same for all the LEDs present on the prototype board and is not worrisome since the timescale is orders of magnitude smaller than the typical fastest features of the response of cryogenic calorimeters.

To check the maximum trigger frequency that the board supports a small frequency scan was performed which resulted in a stable operation until 6 MHz (the targeted frequency is 5 MHz), above 7 MHz a not full discharge of the LED happened causing a non-uniformity of the light pulses, as shown in Figure 3.27. The maximum triggering frequency accepted by LANTERN can be tuned by changing the resistance in parallel to the LED (resistor R_1 in Figure 3.9), since the discharge time constant is given by $\tau = RC$ the value of R_1 was reduced to allow for a quicker discharge.

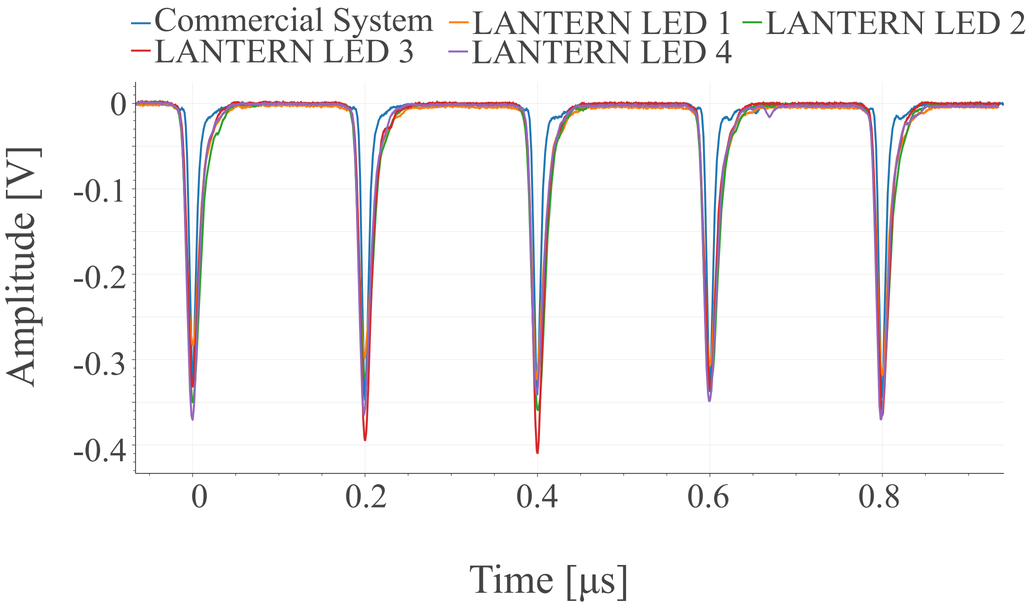

Figure 3.26. Comparison of the light pulses produced by the 4 LED drivers present on the LANTERN prototype board with the CAEN LED driver.

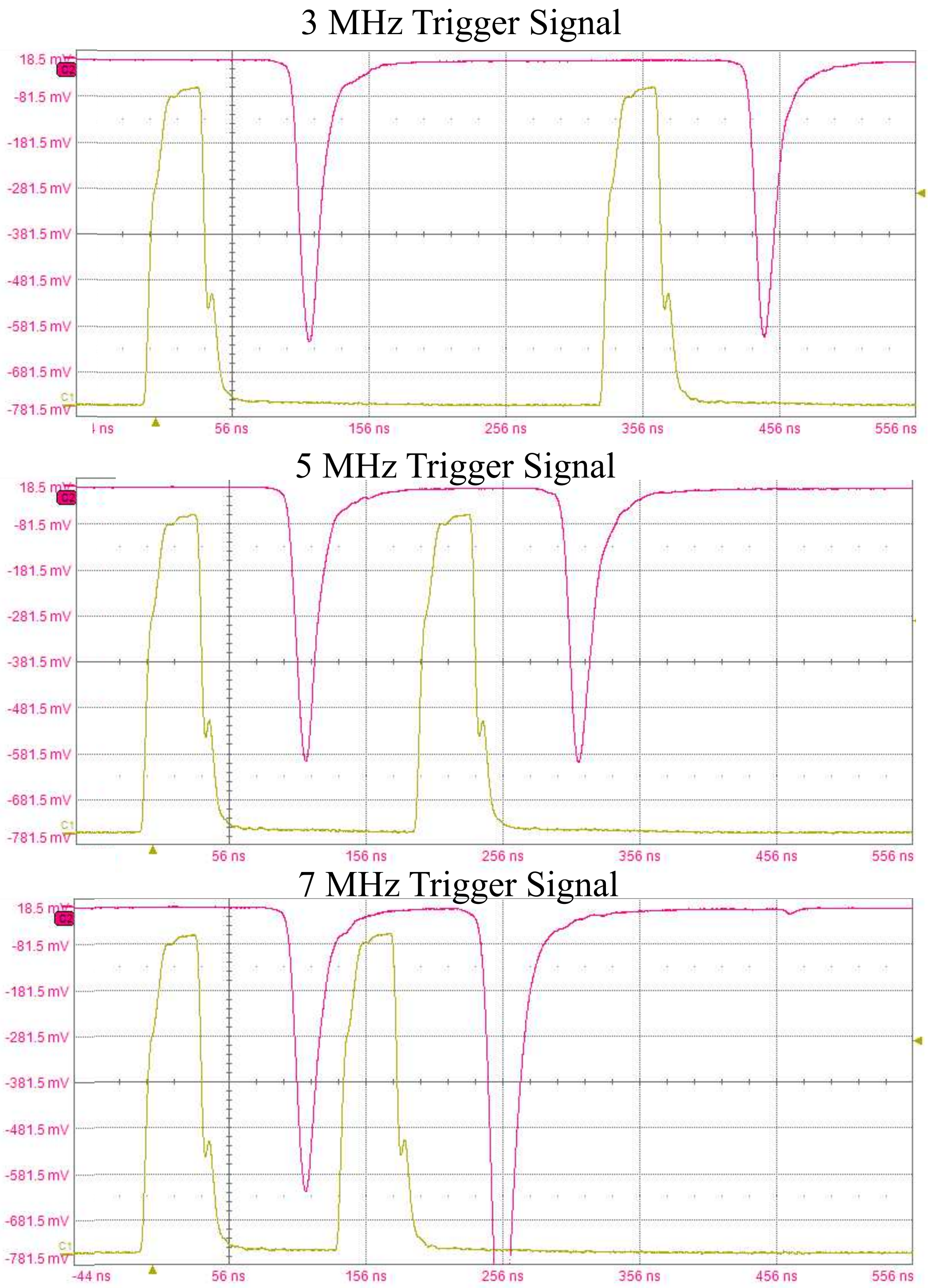

Figure 3.27. Non-uniformity in the light yield given from each trigger cycle due to LED discharge not matching the triggering frequency (in yellow the trigger signal and in magenta the signal from the PMT). In the picture a subset of the triggering frequencies tried is shown, in the top and middle panels (respectively 3 and 5 MHz triggering) there is no visible difference between the two cycles, while in the bottom panel at 7 MHz the light yield of the second cycle is much greater than the one of the first.

Table 3.5. Results of the dark count measurement check with the PMT for the multiplexed LANTERN prototype board.

Configuration	Duration	Counts
1	20 min	734
2	20 min	731
3	20 min	715
4	20 min	702

Finally, a dark count measurement was performed in several configurations in order to double-check that LANTERN produces no additional counting rate. The different dark count tests performed were:

1. a control measurement where all the inputs to LANTERN were turned off;
2. a configuration with a biased LANTERN and a turned on triggering signal but with the Enable of the multiplexers turned off (to check for possible unwanted light pulses during the logical off state of the board);
3. a configuration with LED 1 shining and the measurement taken on LED 4;
4. a configuration with LED 1 shining and the measurement taken on LED 3;

where the last two configurations are taken to check whether any cross-talk between LEDs is occurring. The results for the various configurations are presented in Table 3.5 but they all show a correct behavior where no additional counts with respect to the dark control rate were measured. A drift in the dark count values in the table is visible and this is due to the varying luminosity conditions of the laboratory during the data taking, it was already noticed that the measuring setup is not completely light tight and is partially affected by the environmental luminosity.

Aside from the optical and electrical tests, the in-vacuum operation of the board was tested by operating it for tens of minutes at 10^{-3} mbar with the aid of a small vacuum chamber. To check the correct operation, high currents and number of cycles were used to bias the LEDs to produce enough light for an inspection by eye, to easily check if the components would be able to dissipate enough heat through the limited thermal connections they had or if they would start to heat up and burn. Due to the careful choice of all the electronic components, the vacuum operation test was successful and proved that this setup can be operated inside a cryostat even if provided with a relatively small thermal contact to dissipate the produced heat.

3.3.6 Exploiting Transparency for Stacked Pixel Identification

An initially unforeseen use of LANTERN is to perform pixel identification in the stacked configuration of the BULLKID experiment [79]. Since BULLKID exploits frequency multiplexed cryogenic calorimeters, a geometrical map of the pixels needs to be performed and can be easily done with the multichannel LANTERN electronics. Performing this mapping on a single layer (or wafer) is trivial since all the calorimeters can be exposed directly to an optical fiber. On the other hand, since the BULLKID experiment aims at piling up several wafers, as in the stacked configuration in

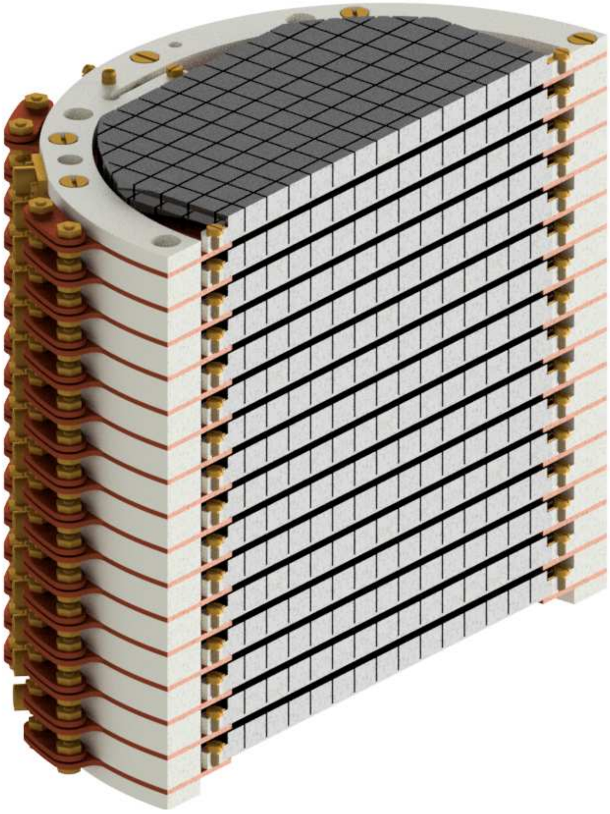

Figure 3.28. Diagram of the stacked setup designed for the BULLKID [79] experiment.

Figure 3.28, it is impossible to expose every calorimeter to an optical fiber for the pixel identification.

Since the BULLKID detectors are made of silicon, they are semitransparent to deep infrared light, so by using LEDs with 1200 nm wavelength it is in principle possible to shine through the wafers to perform the pixel identification on multiple *layers*. A proof of concept using the single driver LANTERN electronics was performed by shining a deep infrared LED through one of the BULLKID wafer and reading out the one on the second layer. The result of this preliminary test is shown in Figure 3.29 where it is clearly visible that only one of the pixels responds to the light signal (because of phononic cross-talk due to the detector geometry nearby sensors give a small response as well) allowing to perform pixel identification.

Calibrating with infrared light proved non-trivial due to two main effects: the first one is that in each layer of the stacked BULLKID configuration there is a preference to absorb the lower wavelength photons, creating a rainbow-like effect. This changes the energy distribution of the photons absorbed in each layer, producing a systematic uncertainty in the energy calibration. The second and more important effect is that, due to the semi-transparency, the photons can be directly deposited in the superconductive sensor without being converted to phonons in the silicon first. This gives a wrong detector response (mainly a much lower calibration constant with respect to the one measured in the phonon-based readout) since absorbing directly

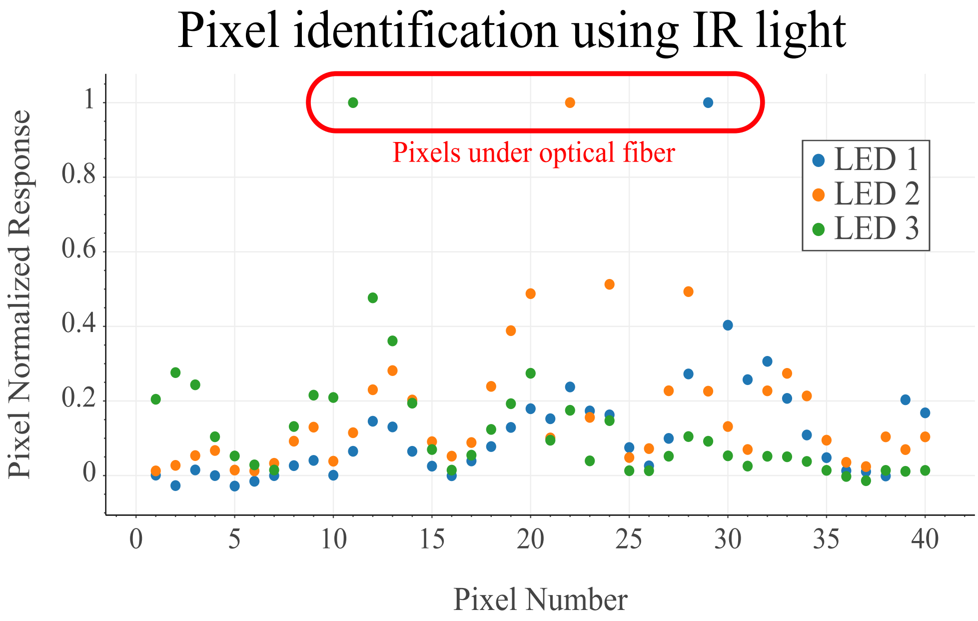

Figure 3.29. Proof of concept for the pixel identification in the BULLKID stacked detector using LANTERN with infrared light.

on the sensor gives a much higher signal. Currently, it was not possbile to disentagle these two problems so the systematic effect on the calibration constant due to the first effect have not been evaluated yet.

3.4 Current status and Considerations

The electronics developed, during the work presented here, for the LANTERN project proved to be well-designed for the intended uses of calibration and general detector characterization. All the conducted prototype tests yielded positive results and the designing phase of the project has been completely finalized. Currently, several units of the final circuit board are being bought to be mounted in the BULLKID and NUCLEUS experiments.

The single LED driver is currently being used by the NUCLEUS and BULLKID experiments, and the full multiplexed version with the optical fiber bundle installation is proceeding in the cryostat used by the latter experiment.

Moreover, all the required control software has already been developed and makes use of the one built in [4] for the CAEN setup.

Some of the described tests and explanations of the project are summarized in [87].

Chapter 4

Nuclear recoil calibration

As already anticipated in chapter 3, calibrating cryogenic calorimeters can be a complex task to undergo for many reasons. When calibrating these detectors with radioactive X-ray sources or with the optical calibration described in chapter 3, the physical interaction happening before the phonon production is the electron recoil. While cryogenic calorimeters are supposed to respond equally to all types of energy depositions (as long as no energy escapes the detector), these photon based calibrations study the response to a different physical process with respect to the nuclear recoils of CEνNS. On the other hand, it is possible, but more experimentally challenging, to probe directly the detector response to nuclear recoils calibrating with thermal neutron absorption.

In this chapter, the first nuclear recoil calibration performed in the NUCLEUS experiment is described. This chapter not only presents one of the main physics measurements that NUCLEUS performed so far, but it also serves as an example to showcase all the data analysis procedures and algorithms developed during this work to study the signals coming from cryogenic calorimeters. This calibration was performed in collaboration with the CRAB experiment, which performed extensive studies to simulate the energy spectrum expected from this measurement.

4.1 Calibrated nuclear Recoils for Accurate Bolometry

The collaboration for Calibrated nuclear Recoils for Accurate Bolometry (CRAB) [88] proposed a way to directly study the response to nuclear recoils at the 100 eV energy scale. The main idea is to produce a several MeV-scale single γ nuclear transition which produces a well-defined nuclear recoil at the targeted energies. As shown in Figure 4.1, when a thermal neutron, i.e. a neutron with kinetic energy of $\sim$ 25 meV, is absorbed by a medium or heavy nucleus it produces a compound excited state that then decays to the ground nuclear state. This decay can happen via the emission of a single γ at the MeV scale, which escapes detection in cm-scale detectors. Simultaneously, a nuclear recoil at the 100 eV energy scale is generated and can be detected.

Single γ nuclear de-excitations are not the only way in which the nuclear decay can

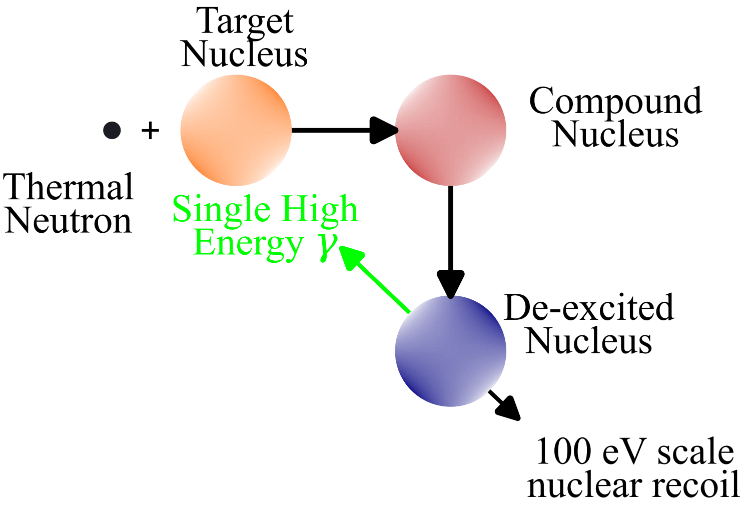

Figure 4.1. Conceptual diagram of the nuclear recoil calibration performed using neutron capture as devised from the CRAB collaboration. Diagram re-adapted from [88].

Table 4.1. Nuclear data for tungsten isotopes. ^{180}W is not considered here because of its low natural abundance of 0.12%. The neutron capture cross-section is for thermal neutrons. Table readapted from [88].

Target nucleus (A)		
Isotope	Natural Abundance (%)	Neutron capture cross-section (barn)
^{182}W	26.50	20.32
^{183}W	14.31	9.87
^{184}W	30.64	1.63
^{186}W	28.43	37.89

happen, in fact, multi-γ cascades can also be produced and pollute the calibration spectrum. While in the measurement described here only the nuclear recoils were measured, in future iterations of this calibration an efficient external γ tagging is planned in order to fully isolate the single γ transitions.

4.1.1 Calibration principle in a CaWO$_4$ cryocube

In order to efficiently perform the nuclear recoil calibration, the target material must have one or more suitable elements in its composition. Tungsten is a particularly good target, in fact it has a high natural abundance of ^{182}W and a high neutron absorption cross-section, as visible from Table 4.1. Moreover, since that the attenuation of a MeV-scale γ in CaWO$_4$ is 3.7×10^{-2} cm/g, the produced photon is likely to escape a cm-scale detector. For this reason, the CaWO$_4$ based cryogenic calorimeter used by NUCLEUS is a suitable target for this calibration.

When the tungsten undergoes a nuclear de-excitation it produces several nuclear recoil peaks in the 100 eV region with energies depending on the initial excited

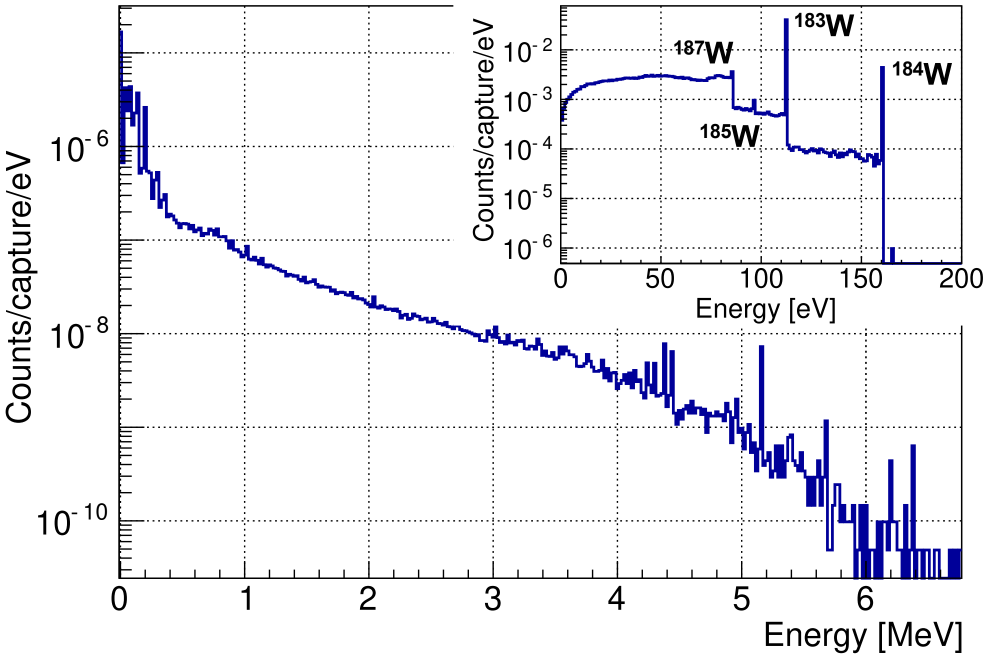

Figure 4.2. Distribution of energy deposits in a 5 mm length cubic crystal of $CaWO_4$ based on a simulation with 10^7 incident thermal neutrons. Inset: zoom to the ROI showing the expected calibration peaks. No resolution effects are included. Figure from [88].

isotope as shown in the inset of Figure 4.2. The most prominent feature is the one given from the decay of ^{182}W which produces a peak at 112.5 eV, other two fairly prominent peaks at 85 eV and 160 eV are also produced but are suppressed by an order of magnitude.

4.1.2 Experimental setup, data taking strategy and expected results

To perform the measurement of the neutron induced nuclear recoils, a specific experimental setup was studied and implemented in order to optimize the quality of the data taken, aiming for the lowest possible source related background while keeping a high interaction rate. The setup for the measurement, shown in Figure 4.3, consisted of a 0.75 g $CaWO_4$ cryocube equipped with a TES with a transition temperature of $\sim$ 20 mK. A shielded sample of ^{252}Cf is used as a neutron source, since ^{252}Cf decays by spontaneous fission with a branching ratio of 3%, emitting on average 3.77 neutrons per fission with an average energy of 2.12 MeV [88].

The cryogenic detector is operated in a dedicated copper holder with a mechanical holding consisting of copper clamps and sapphire balls. Moreover, in order to reduce the detector resolution to match the $\sim$ 7 eV required for the discrimination of the nuclear recoil peak, the detector box was mechanically decoupled from the cryostat vibrations using a prototype *double copper spring.*

The neutron source is surrounded by thick layers of borated polyethylene and graphite

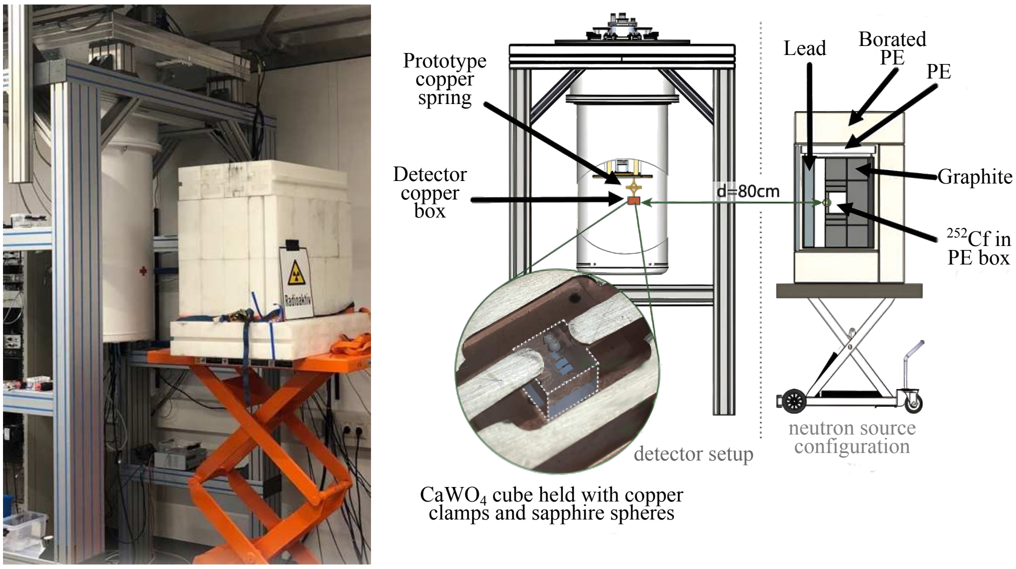

Figure 4.3. Left: Picture of the nuclear recoil calibration setup with the cryostat and the neutron source. Right: Diagram of the setup, re-adapted from [89].

to reduce the radiation dose in the surroundings, while in the direction of the cryostat a 5 cm thick layer of Polyethylene (PE) for neutron thermalization and a 7 cm thick layer of lead to reduce the gamma flux are placed. This configuration was chosen since it was seen, from simulations, to optimize the flux of thermal neutrons emitted in the direction of the cryostat, while reducing the fast neutron and source-induced γ-ray background. The neutron source was placed at a distance of (80 ± 1) cm from the cryogenic detector, which results in a particle rate of 0.52 cps.

With this setup, two datasets were taken, the first one consists of a ~ 20 h acquisition of background data to characterize the ambient background and tune the analysis. The second dataset lasting ~ 40 h was taken with the ^{252}Cf neutron source in place. With the amount of statistics collected in this measurement, the main recoil peak, expected to be measured with an energy of 112.5 eV, should be composed 114 ± 28.5 events. The uncertainty on the predicted number of events is given by the combination of an estimated 15% uncertainty on the source activity and a 20% uncertainty in the description of the geometry and the materials implemented in the simulations.

4.2 Definition of data analysis procedure

As previously mentioned, two different datasets were acquired:

- *background*: lasting 25.3 h where the detector is exposed only to a ^{55}Fe γ calibration source;
- *source*: lasting 40.2 h where the detector is exposed to the ^{55}Fe and ^{252}Cf sources.

The ^{55}Fe X-ray source is used to produce the K$_\alpha$ and K$_\beta$ calibration lines at respectively 5.985 keV (weighted average) and 6.490 keV. Since the optical calibration system was not yet deployed in the NUCLEUS setup, it was impossible to perform the calibration described in chapter 3.

In order to avoid analysis biases, a blinding strategy has been applied to the *source* data. In fact, before applying the analysis to the *source* dataset, all the analysis was developed and tuned on the *background* data. To achieve a better statistical significance on the nuclear recoil peak, the analysis was also tested and fined tuned on events outside the ROI, i.e. events with energies above 150 eV.

The analysis of the data coming from cryogenic calorimeters is typically divided in two stages, in the first one several acquisition windows are analyzed with multiple algorithms in order to extract all the meaningful features of the raw data. This consists in:

- *Offline Triggering*: applying a triggering algorithm to the raw data in order to identify signals;
- *Waveform Preprocessing*: extraction of the main features of a signal;
- *Amplitude Estimation*: estimation of the signal amplitudes using the matched filter to achieve the best resolution;

In the second stage, all the signal features extracted are used to perform data quality cuts in order to select only signals that have the expected pulse shape and have been successfully processed. Finally, the energy spectrum of the selected signals is produced in order to check for the presence of the nuclear recoil peak.

4.2.1 Extraction of the signal features from raw data

In this section, a complete description of the algorithms used to extract the signal features is presented. The quantities estimated here are then used in section 4.3.2 to clean the nuclear recoil calibration datasets.

4.2.1.1 Offline Triggering with the matched filter for lowering the threshold

The data recorded with the NUCLEUS Data Aquisition (DAQ) system consists of a custom binary file format with the continuous data streams from all detectors present (in this case only one) and all the heater channels (also one in this case). In order to analyze the data, an offline trigger software and protocol was developed during this work.

Identifying pulses induced by the heater, like the blue line in Figure 4.4, can be done by checking if on the heater channel there is a sharply rising signal like the one in the orange curve of Figure 4.4. Triggering such a spike is simple, since the heater channel is not affected by noise. On the other hand, identifying self triggers present in the data coming from the cryogenic detectors is more complex due to the requirement of being able to measure low energy depositions, meaning low SNR values to work with.

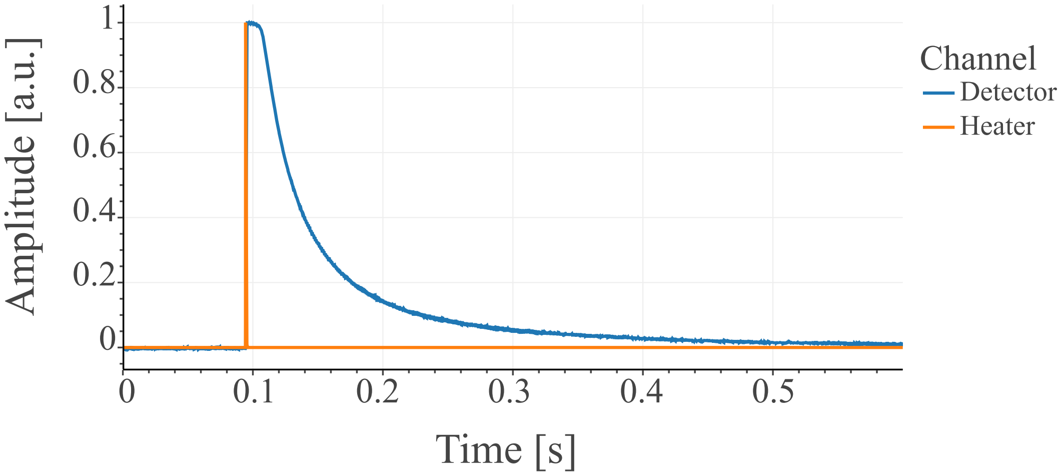

Figure 4.4. Heater pulse (blue) with relative spike in the heater channel (orange). The heater pulse presents saturation.

In fact, the target detectors of the NUCLEUS experiment typically have noise RMS levels of few tens of electronvolt, meaning that performing a simple threshold triggering without any kind of filtering does not allow to efficiently see signals at the 100 eV scale, since typically the threshold level is set at 5 times the noise RMS. For this reason, a filtering based on the matched filter technique was developed using the work done in [90] in order to reach the optimal SNR conditions and allow for triggering thresholds at the level of few tens of electronvolts.

A complete description on how the matched filter works is presented in section 4.2.3 and for the sake of the triggering discussion it is sufficient to say that it is a linear filter that is mathematically proven, under not too stringent hypothesis, to achieve the best possible SNR. To do so, the filter performs a minimization between the raw data and a template signal, describing the expected detector response. The minimization is done keeping in consideration the average features of the noise present in the data (for more details see section 4.2.3.1). To build the filter kernel, two elements are required: a template of the signal and the noise average power spectral density. Fortunately, these can both be extracted directly from the data, as described in section 4.2.3, but the data needs to be triggered once before building the matched filter based trigger. For this reason an initial band-pass filter is applied to the data before performing a threshold triggering in order to then preprocess the data (see section 4.2.2) and, with tight selection cuts, extract the signal template and the noise power spectral densities (as described in section 4.2.3.2) following the diagram in Figure 4.5.

As shown in Figure 4.6, when the matched filter kernel is convoluted, using a Discrete Fourier Transform (DFT), with a calorimeter pulse it results in a filtered pulse that has a drastically different shape with respect to the original but presents a peak (with an amplitude directly proportional to the pulse height) when the signal and the template align and a drastically increased SNR.

In order to perform the matched filtering of a continuous data stream, the latter

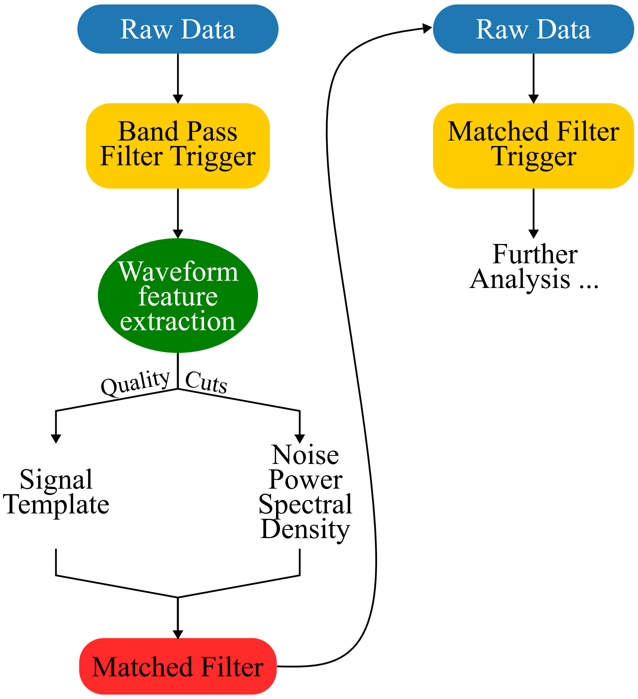

Figure 4.5. Diagram of the double triggering stage. In the first part of the trigger stage (left) a triggering based on a band pass filter is used to perform an initial data selection to build the matched filter which is then used to retrigger the data and perform the complete data analysis (right).

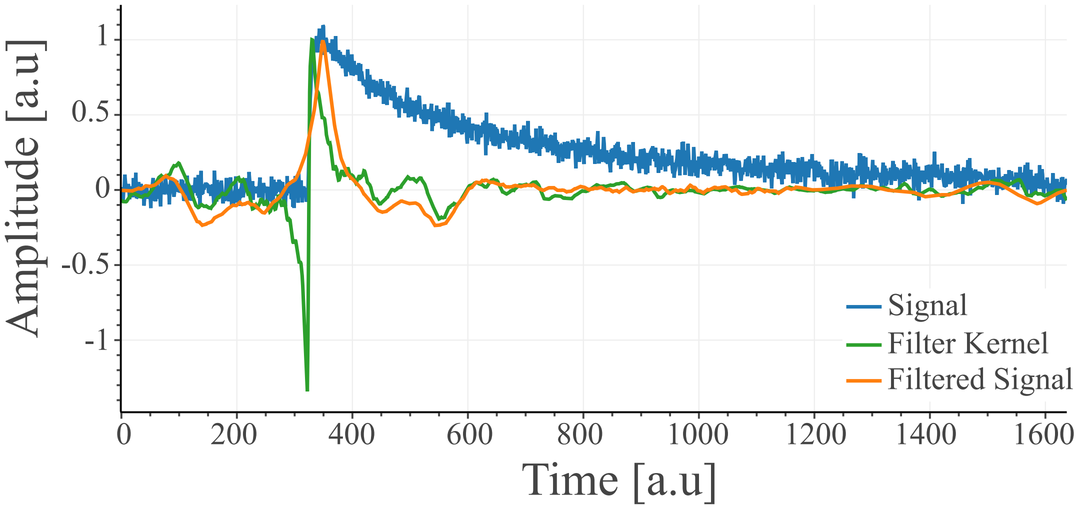

Figure 4.6. Application of the matched filtering to a cryogenic calorimeter pulse: in blue the detector pulse, in green the matched filter kernel and in orange the filtered pulse.

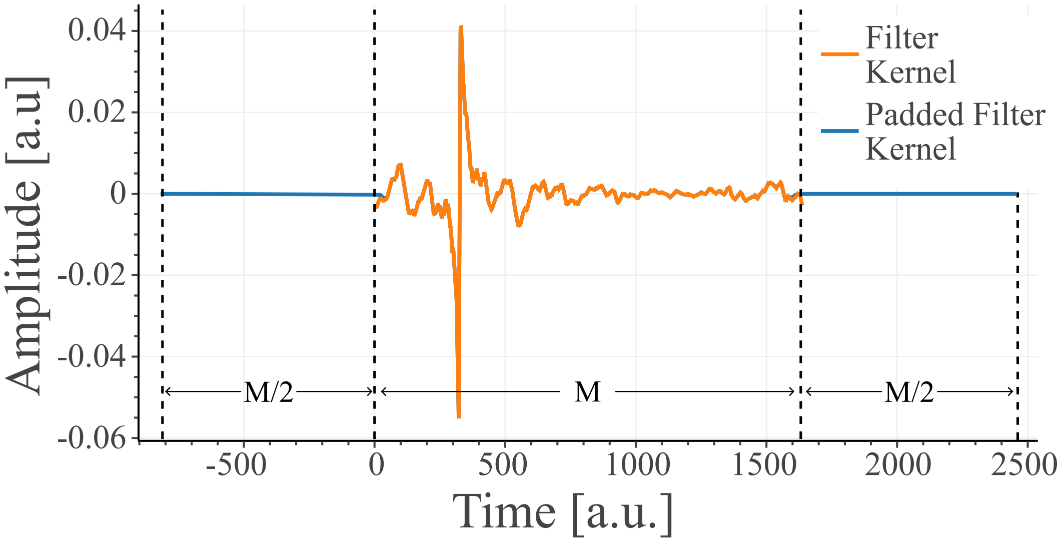

Figure 4.7. Plot showing the padding of the matched filter kernel. In orange the original matched filter kernel is shown, while in blue the padded and smoothed filter kernel used before the triggering is presented. The length of the various sections are highlighted as fractions of M which is the duration data processing window of the signal.

is divided in multiple windows each containing the same number of points M of the filter kernel and each segment is subsequently filtered. DFT algorithms assume that the window to be filtered is periodic, if this is not the case the convolution will pollute the left side of the filtered window with data from the right side and vice versa, this problem is referred to as *DFT convolution wraparound.* This problem is solved by duplicating the filter kernel length, from M to $2M$, by padding each of its borders with $M/2$ zero samples, as shown in Figure 4.7. When padding the filter, since discontinuities that can spoils the DFT might be introduced, the edges of the kernel are also smoothed out in order to reach 0 with a continuous derivative.

The padded filter is then used to filter a portion of the stream that is $2M$ samples long, but only the central M values are kept since they are the only unspoiled part of the convolution. This can be easily checked by performing the several filterings of the padded signal template with the padded filter while performing a time translation of the signal, as shown in the left panel of Figure 4.8. If the trend of the filtered signal amplitude is studied as a function of the time translation, as shown in the right panel of Figure 4.8, it is quickly noticeable that the filtering only returns the exact same and correct value only in the central M values of the filtered stream. Since only M of the $2M$ filtered samples are kept, then the continuous stream is processed in overlapping windows as shown in Figure 4.9 in order to correctly parse all the incoming data.

Once the stream is correctly filtered, a second problem arises, which is the identification of the trigger samples. In fact, while the match filter allows to drastically boost the SNR of the signals studied, it might also introduce *lobes* in the produced filtered stream as visible from the plots shown so far. This is due to the fact that the matched filter produces a filtered stream that has the integral equal to 0, so

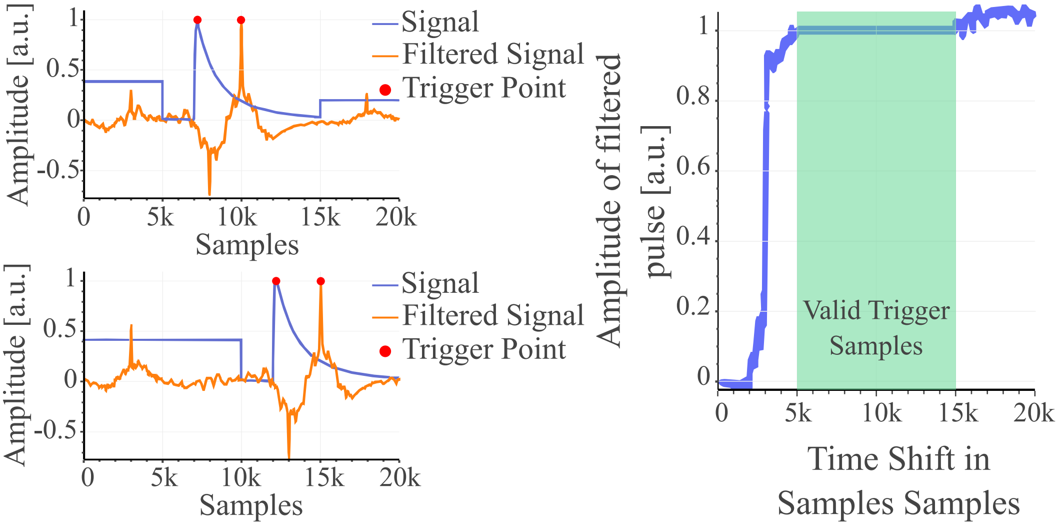

Figure 4.8. Study of interval for which the matched filtered stream is not spoiled by the *DFT convolution wraparound*. Left: filtering of the padded signal template (blue) with various time translations applied (only two are shown as an example). The trigger point is taken at a predetermined sample, which is a function of the known translation applied and the known delay introduced by the filter, and corresponds to the maximum of the filtered signal. Three additional spikes are present in the filtered signal and are due to the discontinuities introduced by the padding present in the blue waveform (the padding added is by choice not set to zero in order to check for pathological behaviors of the filtering). Right: amplitude reconstruction of the filtered signal as a function of the time shift applied.

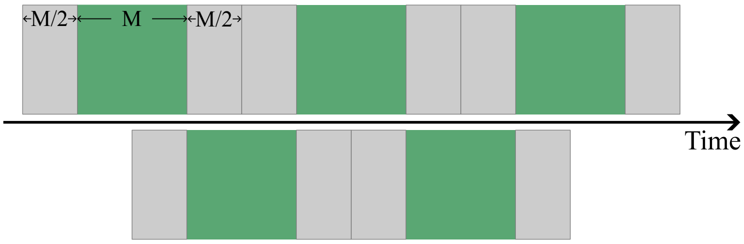

Figure 4.9. Filtering scheme of the continuous data stream. A full triggering window is composed of $2M$ samples, of which the M green ones are the correctly filtered ones and are kept, while the remaining M samples (the two gray rectangles) are divided in two halves at the borders of the correctly filtered ones. The considered triggering windows are overlapping of M samples such that when all the middle samples in green are concatenated, the correct filtering of the whole data stream is recovered. Figure re-adapted from [90].

when a pulse is filtered and a peak is produced in the filtered stream then several upward and downward fluctuations are produced to compensate the increase of the integral. So a simple *peak finding* that uses the concavity of the signal stream might produce false trigger points. In the trigger algorithm then a new procedure was developed to only trigger the correct signal peaks in the filtered stream. The samples in the filtered stream are sorted with decreasing amplitude so that the first one is the correct trigger point of the pulse with the highest response. Then after

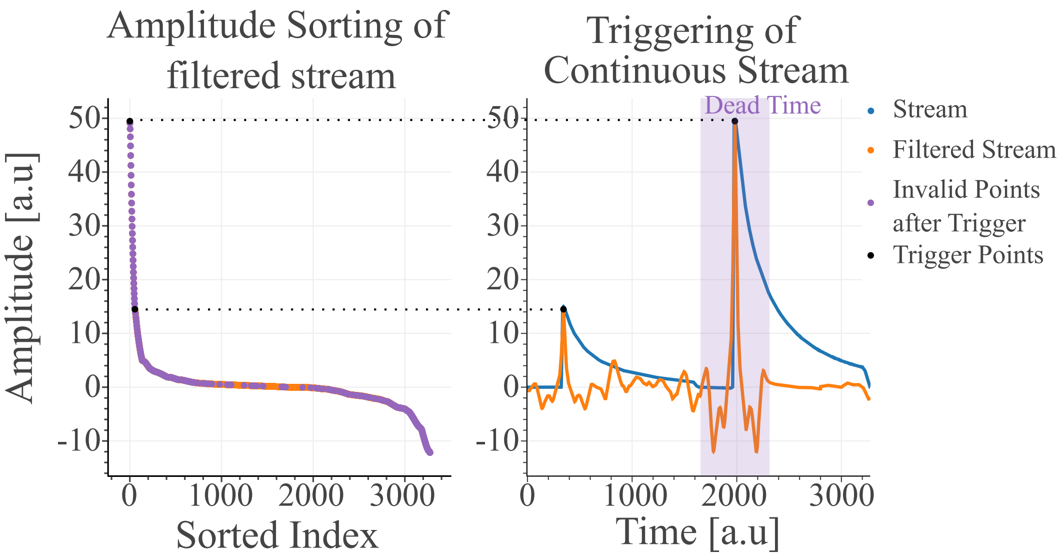

Figure 4.10. Example of the identification of trigger samples. In the right panel a stream (blue) containing two pulses is filtered (orange) and the trigger points (black) are identified and a trigger dead time is set (purple rectangle). In the left panel the choice of the trigger points (black) is shown on the decreasing amplitude sorted stream (orange) and the invalidated points due to the dead time from the first trigger are plotted in purple.

selecting this first sample as a valid trigger point, a dead-time window (usually of $M/5$ long and centered on the trigger position) is applied and all the nearby samples are invalidated. This means that the second greatest and valid sample is the trigger position of the second most energetic registered pulse (as shown in Figure 4.10). The procedure is then repeated until either there are no more valid points present in the stream or the triggering threshold is reached.

After all the aspects concerning the use of the matched filter are taken care, the data can be triggered with a triggering threshold of few tens of electronvolt. In the case of this data analysis, the triggering threshold was set at 5 times the matched filtered noise RMS, meaning a threshold of around 35 eV for both datasets.

Aside from the heater and signal triggers described so far the triggering stage also sets some triggers placed at fixed time intervals in the stream, these are used to sample traces without pulses in order to later perform noise studies.

4.2.2 Waveform Preprocessing

The second step after the data triggering in the analysis protocol is to deploy multiple simple algorithms that calculate the main features of the measured pulses. The quantities calculated in this stage of the analysis are essential in order to perform the data cleaning required to build the matched filter.

The main quantities derived in this analysis stage, some of which are shown in Figure 4.11, are:

- **Baseline**: the mean of the initial points of an acquisition window before the rise of the pulse (pretrigger points). This value has a dual use since it is both the reference from which all the rest of the amplitude values of the pulse are calculated and also carries information on the working point of the detector.
- **Baseline RMS**: the RMS of the pretrigger points. This quantity is a rough estimate of the noise level in the acquisition window. In this analysis, it is used to convert all amplitude measurements from physical units (mV) to multiples of the baseline RMS in order to get a sense on how statistically significant is the estimate of the measured value.
- **Baseline Slope**: derivative of the pretrigger values evaluated performing a linear fit. This quantity is used to study whether the current acquisition window contains part of a previous decaying pulse, meaning that is used to spot pile-ups which might ruin the amplitude reconstruction.
- **Max-Baseline**: rough estimate of the pulse amplitude done by taking the maximum value of the pulse and subtracting the baseline level. The maximum value chosen is not the absolute maximum in the acquisition window, but is the nearest maximum around the trigger position, which is typically placed halfway through the rise. When expressed as a multiple of the baseline, RMS it is roughly the SNR of the unfiltered pulse.
- **Max-Min in Window**: estimate of the full amplitude range of the pulse, including noise fluctuations, by performing the difference between the absolute maximum and the absolute minimum in the acquisition window. This parameter is similar to **Max-Baseline**, but it can detect pile-ups or downward fluctuations of the noise.
- **Min-Baseline**: rough estimate of the pulse amplitude done by taking the absolute minimum value of the acquisition window and subtracting the baseline level. Since the calorimeter pulses are only positive, this quantity is used to spot noise fluctuations or DAQ artifacts.
- **Right-Left Baseline**: difference of the baseline level and the mean value of the last samples in the acquisition window. If a pulse is present, this variable checks whether the pulse is fully contained in the window chosen. Moreover, this quantity is usually able to tag SQUID related artifacts, pile-ups or undesired noise fluctuations.
- **Rise Time 10%-90%**: rough estimate of the duration of the rise of the pulse evaluated between the 10% and the 90% values of the pulse amplitude. This parameter has a wide use to spot pulse deformations in order to perform quality cuts. If position effects are noticeable in the amplitude reconstruction, this parameter should be also affected and can be used to decorrelate the two.
- **Decay Time 90%-30%**: rough estimate of the duration of the decay of the pulse evaluated between the 90% and the 30% values of the pulse amplitude. This value is usually a property solely due to the construction and work-point of the TES and is used to spot pulse shape differences.

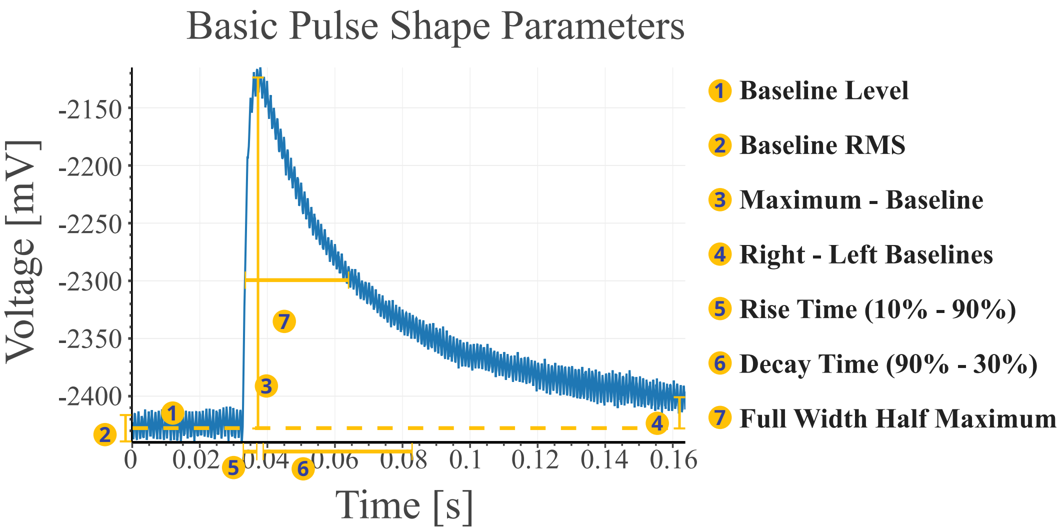

Figure 4.11. Diagram indicating the main pulse shape quantities extracted in the waveform preprocessing stage. Figure re-adapted from [91].

- **Full Width Half Maximum**: rough estimate of the time elapsing from the middle point of the pulse rise to the middle of the decay. For well-behaved pulses this quantity highly correlates with the decay time estimation, but for saturated pulses (which present a plateau at the maximum level) the two can be drastically different. This parameter is used to spot and study the saturation of pulses.

Aside from the parameters just described, a peak finding algorithm is also run on the traces to identify the number of pulses present in order to more easily discriminate pile-ups from good pulses. A full description of the peak finding algorithm is found in [4], but it highly relies on the band-pass filter used for the first triggering stage.

4.2.3 Matched filtering for best amplitude estimation

The matched filter is the central algorithm in the waveform analysis of the TES signals. This algorithm allows to reach the best possible SNR when the filtered signals have an average Noise Power Spectral Density (NPSD) corresponding to the one used to build the filter (this is why the filter is also known as *optimum filter*). To understand in detail the way the filter works in section 4.2.3.1 one of the possible derivations of the filter is presented.

In general terms, the filter performs a χ^2 minimization between the signal $v(t)$ and a signal template $s(t)$. This minimization takes into account the average features of the noise present in the data in order to achieve the best SNR. In this procedure, the signal is supposed to be of the form $v(t) = A \cdot s(t) + n(t)$, where A is a multiplicative constant indicating the amplitude of the signal and $n(t)$ is the noise contribution. The filter transfer function (meaning the expression of the filter in frequency domain) is:

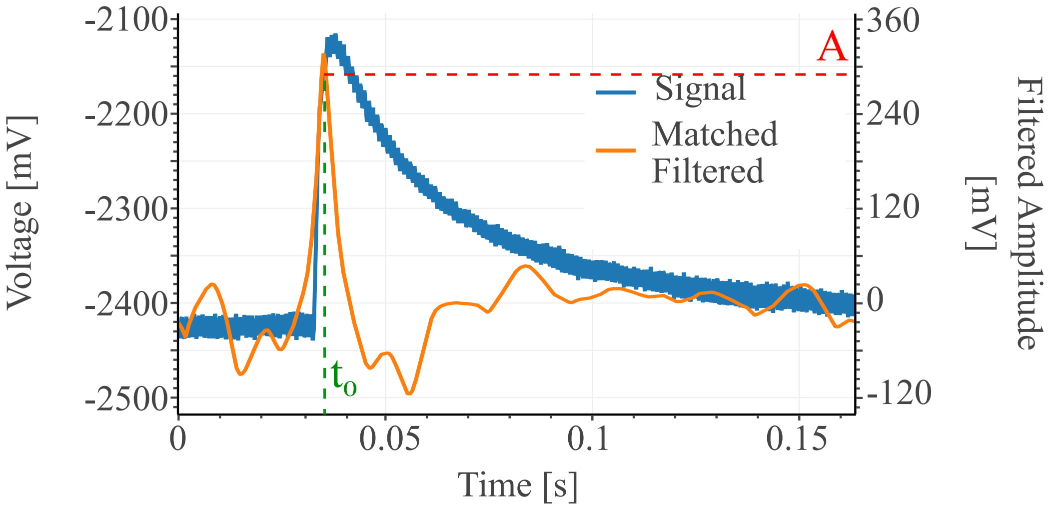

Figure 4.12. Application of the matched filter to a signal (blue) resulting in the filtered signal (orange) from which the amplitude A and the time jitter t_0 can be extracted by searching for the maximum.

$$H(j\omega) = \sigma_n^2 \cdot e^{-j\omega t_0} \cdot \frac{\overline{S(j\omega)}}{N_{PSD}(\omega)} \tag{4.1}$$

where j is the imaginary unit, ω is the angular frequency, t_0 is the time difference between the maximum of the signal and the maximum of the template, $S(j\omega)$ is the Fourier transform of the signal template $s(t)$, $N_{PSD}(\omega)$ is the average power spectral density of the noise and σ_n^2 is the noise variance after the filtering (for the definitions of all these quantities see section 4.2.3.1). For the properties of the Fourier transform, a convolution can be written as:

$$(f * g)(t) := \int f(\tau)g(t-\tau)d\tau = \mathcal{F}^{-1}\left[F(j\omega)G(j\omega)\right] \tag{4.2}$$

with $\mathcal{F}^{-1}$ indicating the inverse Fourier transform operation and $F(j\omega)$, $G(j\omega)$ are respectively the Fourier transforms of $f(t)$ and $g(t)$. By combining this with eq. (4.1) it is clearly seen that the convolution is done weighing the spectral components with the inverse of the NPSD, meaning that only the frequencies with the higher SNR are used.

When a signal is filtered the shaped is not preserved, as visible from Figure 4.12, but its amplitude A is measurable by taking the maximum of the filtered signal, and the time t_0 at which the signal happens by taking the position of the maximum (actually this quantity also keeps track of any delay of the signal with respect to the template, so the template must be correctly placed in the acquisition window). The resolutions on these two parameters are [92]:

$$\sigma_A^2 = \sigma_n^2 = \left[\int_{-\infty}^{\infty} \frac{|S(j\omega)|^2}{N_{PSD}(\omega)} d\omega\right]^{-1} \qquad \sigma_{t_0}^2 = \left[A^2 \int_{-\infty}^{\infty} \frac{|S(j\omega)|^2}{N_{PSD}} \omega^2(\omega) d\omega\right]^{-1} \tag{4.3}$$

When dealing with digitized sampling, the performances of the matched filter can be increased by performing a parabolic interpolation of the three highest points in the filtered stream to detect the position and value of the maximum. The matched filter with interpolation allows to reach precisions, especially on the timing of the signal, that are below the digitization step.

4.2.3.1 Matched Filter Derivation

A derivation of the analytical expression of the filter that shows the property of the SNR maximization is presented here. Suppose to have a signal $v(t) = A \cdot s(t) + n(t)$ which is the combination of a noise trace $n(t)$ and a model or template signal $s(t)$ (normalized to 1) multiplied by an amplitude A, then the application of a filter $h(t)$ to the signal gives a resulting signal $y(t)$:

$$y(t) = \int_{-\infty}^{t} h(t-\tau) v(\tau) d\tau \tag{4.4}$$

where the above integral is the convolution operation. By defining the SNR as:

$$\mathrm{SNR}_y(t) = \frac{|y|^2(t)}{\sigma_n^2} = \frac{\left|\int_{-\infty}^{t} h(t-\tau) x(\tau) d\tau\right|^2}{\sigma_n^2} \tag{4.5}$$

where σ_n^2 is the variance of the noise after the filtering. It is possible to require to have the maximum SNR in order to define $h(t)$. Since the time domain convolution operation is a simple multiplication in the frequency domain, the SNR can be rewritten using the Fourier transform:

$$\mathrm{SNR}_y(t) = \frac{\left|\int_{-\infty}^{\infty} e^{j\omega t} V(j\omega) H(j\omega) d\omega\right|^2}{\int_{-\infty}^{\infty} |H(j\omega)|^2 N_{PSD}(\omega) d\omega} \tag{4.6}$$

where $V(j\omega)$ and $H(j\omega)$ are the Fourier transforms of respectively the signal $v(t)$ and the filter kernel $h(t)$. The power spectral density of the noise $n(t)$ is $N_{PSD}(\omega) := \frac{1}{2\pi}|N(j\omega)|^2$ and is used to encode the variance of the noise (since $N(j\omega)$ is the Fourier transform of the noise) and is weighted with the filter kernel in order to get σ_n^2, the variance of the filtered noise $n_f(t)$. This is derived from Parseval's theorem that gives:

$$\int_{-\infty}^{\infty} |x(t)|^2 dt = \frac{1}{2\pi} \int_{-\infty}^{\infty} |X(j\omega)|^2 d\omega \tag{4.7}$$

where $X(j\omega)$ is the Fourier transform of the function $x(t)$. Meaning that:

$$\sigma_n^2 = \int_{-\infty}^{\infty} |n_f(t)|^2 dt = \int_{-\infty}^{\infty} \left| \int_{-\infty}^{t} h(t-\tau)n(\tau)d\tau \right|^2 d\omega = \tag{4.8}$$

$$= \frac{1}{2\pi} \int_{-\infty}^{\infty} |H(j\omega)N(j\omega)|^2 \, d\omega = \int_{-\infty}^{\infty} |H(j\omega)|^2 \, N_{PSD}(\omega) d\omega$$

where the second equality is given by simultaneously applying Parseval's theorem and the convolution property of the Fourier transform. Since the expectation value of the noise, both filtered and not, is zero then $\int N(j\omega)d\omega = \int H(j\omega)N(j\omega) = 0$, meaning that:

$$\mathrm{SNR}_y(t) = \frac{\left| \int_{-\infty}^{\infty} e^{j\omega t} AS(j\omega)H(j\omega)d\omega + \cancel{\int_{-\infty}^{\infty} e^{j\omega t} N(j\omega)H(j\omega)d\omega} \right|^2}{\int_{-\infty}^{\infty} |H(j\omega)|^2 N_{PSD}(\omega)d\omega} = \tag{4.9}$$

$$= |A|^2 \frac{\left| \int_{-\infty}^{\infty} e^{j\omega t} S(j\omega)H(j\omega)d\omega \right|^2}{\int_{-\infty}^{\infty} |H(j\omega)|^2 N_{PSD}(\omega)d\omega}$$

where $S(j\omega)$ is the Fourier transform of $s(t)$ and the linearity of the transformation in the frequency domain was used. The *Cauchy-Schwarz* inequality states that for two complex functions $U(j\omega)$ and $V(j\omega)$ the following relation is true:

$$\left| \int_{-\infty}^{\infty} U(\omega)V(\omega)d\omega \right|^2 \leq \int_{-\infty}^{\infty} |U(\omega)|^2 \int_{-\infty}^{\infty} |V(\omega)|^2 \, d\omega \tag{4.10}$$

then by applying this to the numerator the SNR expression:

$$\left| \int_{-\infty}^{\infty} e^{j\omega t} S(j\omega)H(j\omega)d\omega \right|^2 \leq \int_{-\infty}^{\infty} \left| e^{j\omega t} S(j\omega) \right|^2 d\omega \int_{-\infty}^{\infty} |H(j\omega)|^2 \, d\omega = \tag{4.11}$$

$$= \int_{-\infty}^{\infty} |S(j\omega)|^2 \, d\omega \int_{-\infty}^{\infty} |H(j\omega)|^2 \, d\omega$$

and if $H(j\omega) = c \cdot e^{-j\omega t} \cdot \overline{S(j\omega)}$, where c is a real normalization constant and the overline indicates the complex conjugate operation, the equality holds, in fact:

$$\int_{-\infty}^{\infty} |S(j\omega)|^2 \, d\omega \int_{-\infty}^{\infty} |H(j\omega)|^2 \, d\omega = c^2 \int_{-\infty}^{\infty} |S(j\omega)|^2 \, d\omega \int_{-\infty}^{\infty} |S(j\omega)|^2 \, d\omega =$$

$$= c^2 \left| \int_{-\infty}^{\infty} |S(j\omega)|^2 \, d\omega \right|^2$$

and

$$\left| \int_{-\infty}^{\infty} e^{j\omega t} S(j\omega)H(j\omega)d\omega \right|^2 = c^2 \left| \int_{-\infty}^{\infty} |S(j\omega)|^2 \, d\omega \right|^2$$

From the inequality in eq. (4.11) the SNR must be less or equal than:

$$\mathrm{SNR}_y(t) \leq |A|^2 \frac{\int_{-\infty}^{\infty} |S(j\omega)|^2 \, d\omega \int_{-\infty}^{\infty} |H(j\omega)|^2 \, d\omega}{\int_{-\infty}^{\infty} |H(j\omega)|^2 N_{PSD}(\omega) d\omega} \tag{4.12}$$

which if the noise present is white, meaning that $N_{PSD}(\omega) = N_{PSD}$ is a constant, then becomes:

$$\mathrm{SNR}_y(t) \leq |A|^2 \frac{\int_{-\infty}^{\infty} |S(j\omega)|^2 \, d\omega \int_{-\infty}^{\infty} |H(j\omega)|^2 \, d\omega}{N_{PSD} \int_{-\infty}^{\infty} |H(j\omega)|^2 d\omega} \tag{4.13}$$

if the expression $H(j\omega) = c \cdot e^{-j\omega t} \cdot \overline{S(j\omega)}$ is substituted for the filter, the maximum value of the SNR is:

$$\begin{aligned} \mathrm{SNR}_y^{max}(t) = |A|^2 \frac{\int_{-\infty}^{\infty} |S(j\omega)|^2 \, d\omega \int_{-\infty}^{\infty} \left|c \cdot e^{-j\omega t} \cdot S(j\omega)\right|^2 d\omega}{N_{PSD} \int_{-\infty}^{\infty} |c \cdot e^{-j\omega t} \cdot S(j\omega)|^2 d\omega} &= \\ = |A|^2 \frac{\int_{-\infty}^{\infty} |S(j\omega)|^2 \, d\omega}{N_{PSD}} \end{aligned} \tag{4.14}$$

and the SNR becomes:

$$\begin{aligned} \mathrm{SNR}_y(t) = |A|^2 \frac{\left|\int_{-\infty}^{\infty} e^{j\omega t} S(j\omega) H(j\omega) d\omega\right|^2}{\int_{-\infty}^{\infty} |H(j\omega)|^2 N_{PSD}(\omega) d\omega} \\ = |A|^2 \frac{\int_{-\infty}^{\infty} |S(j\omega)|^2 \, d\omega}{N_{PSD}} = \mathrm{SNR}_y^{max}(t) \end{aligned} \tag{4.15}$$

Meaning that for white noise if the filter is of the form $H(j\omega) = c \cdot e^{j\omega t} \cdot \overline{S(j\omega)}$ then the filtered signal has the maximum possible SNR. If the noise is not white a whitening filter must be applied, in frequency domain this is simply the division of the signal with the square root of the NPSD as shown in the diagram in Figure 4.13. Due to the application of the whitening filter, the Fourier transform of the signal in input to the matched filter then becomes:

$$V'(j\omega) = \frac{V(j\omega)}{\sqrt{N_{PSD}(\omega)}} = A \frac{S(j\omega)}{\sqrt{N_{PSD}(\omega)}} + \frac{N(j\omega)}{\sqrt{N_{PSD}(\omega)}}$$

meaning that the filter then becomes:

$$H'(j\omega) = \frac{H(j\omega)}{\sqrt{N_{PSD}(\omega)}} = c \cdot e^{-j\omega t} \cdot \frac{\overline{S(j\omega)}}{\sqrt{N_{PSD}(\omega)}}$$

By redefining the filter such that it already includes the whitening stage gives the complete form of the filter for any noise conditions:

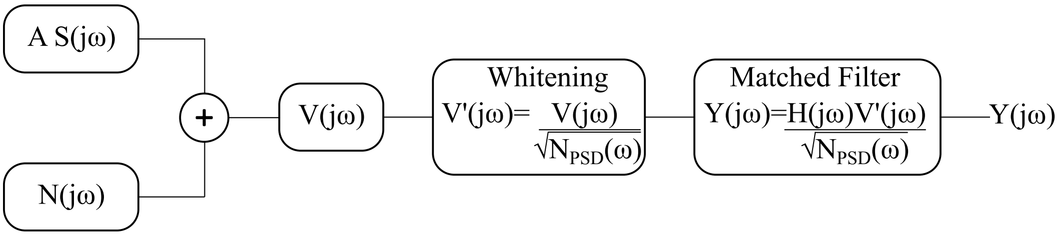

Figure 4.13. Diagram of the decomposition of the matched filter application to signals with a noise condition with power spectral density $N_{PSD}(\omega)$.

$$H''(j\omega)V(j\omega) := H'(j\omega)V'(j\omega) = \frac{H(j\omega)V(j\omega)}{N_{PSD}(\omega)} = c \cdot e^{-j\omega t} \cdot \frac{\overline{S(j\omega)}}{N_{PSD}(\omega)} V(j\omega) \quad (4.16)$$

Moreover, it is possible to define c such that the application of the filter to a signal $v(t) = A \cdot s(t)$, i.e. a signal with no noise, returns a signal with amplitude A. If the filtered signal maximum is, $y(t_{max}) = A$ then it is possible to write:

$$A = \int_{-\infty}^{\infty} e^{j\omega t_{max}} AS(j\omega)c \cdot e^{-j\omega t_{max}} \cdot \frac{\overline{S(j\omega)}}{N_{PSD}(\omega)} d\omega = A \int_{-\infty}^{\infty} c \cdot \frac{|S(j\omega)|^2}{N_{PSD}(\omega)} d\omega \quad (4.17)$$

which gives:

$$c = \left[\int_{-\infty}^{\infty} \frac{|S(j\omega)|^2}{N_{PSD}(\omega)} d\omega \right]^{-1} \quad (4.18)$$

The level of noise after the filtering is:

$$\begin{aligned} \sigma_n^2 = \int_{-\infty}^{\infty} |H(j\omega)|^2 N_{PSD}(\omega) d\omega = \int_{-\infty}^{\infty} \left| c \cdot e^{-j\omega t} \cdot \frac{\overline{S(j\omega)}}{N_{PSD}(\omega)} \right|^2 N_{PSD}(\omega) d\omega = \\ = c^2 \int_{-\infty}^{\infty} \frac{|S(j\omega)|^2}{N_{PSD}(\omega)} d\omega = \left[\int_{-\infty}^{\infty} \frac{|S(j\omega)|^2}{N_{PSD}(\omega)} d\omega \right]^{-1} = c \end{aligned} \quad (4.19)$$

which means that the complete filter used in this analysis is:

$$H(j\omega) = \sigma_n^2 \cdot e^{-j\omega t} \cdot \frac{\overline{S(j\omega)}}{N_{PSD}(\omega)} \quad (4.20)$$

4.2.3.2 Signal Template extraction from data

One of the two crucial steps in building the matched filter is to have a template of the response signal. This template can be built in two main ways, the first one is to parameterize the detector response and build the signal template analytically or numerically as it is done in the field of gravitational waves, the second way is to extract it directly from the data. The second way has the advantage that it does not require a model of the detector response, but it introduces noise, that is usually negligible, in the signal template.

To build the signal template directly from the data, it is necessary to average together several (at least $\mathcal{O}(100)$) *good* pulses in order to average away the noise fluctuations. The *goodness* of a pulse is defined starting from the parameters defined in the preprocessing stage (section 4.2.2), tight quality cuts are set on these values in order to only consider a single type of pulse. An even better situation to produce the signal template is to have a control population, this is the case when the LED system described in chapter 3 is used to produce pulses in the ROI of the measurement.

In the analysis here presented, the cuts used to produce the template pulse are shown in cascade in Figure 4.14. The first cut on **Baseline Slope**, shown in panel A, is performed in relative units and serves to remove any pile-up pulse, the presence of the decaying slopes in the signal windows can be seen by the left shoulder present in the distribution in the plot. A following cut on **Max-Baseline** (panel B) in relative units is used to select a high enough SNR range on the pulses without incurring in non-linearities due to detector saturation. In panel C a cut on **Max-Min in Window** is used both to select the right SNR but also to work in combination with the previous cut to further remove pile-ups. A cut on the **Decay Time** (panel D) is used to select the correct pulse shape to use for the template and a cut on **Right-Left Baseline** is used to select pulses that are fully contained in the acquisition window. The last cut in panel F is performed on the absolute value of **Max-Baseline** in order to select the pulses below the calibration lines produced by ^{55}Fe, this choice was made in order to produce a signal template minimally affected by detector non-linearity. A total of 292 pulses (out of 41136 total events) are used to produce the signal template, or average pulse, shown in Figure 4.15.

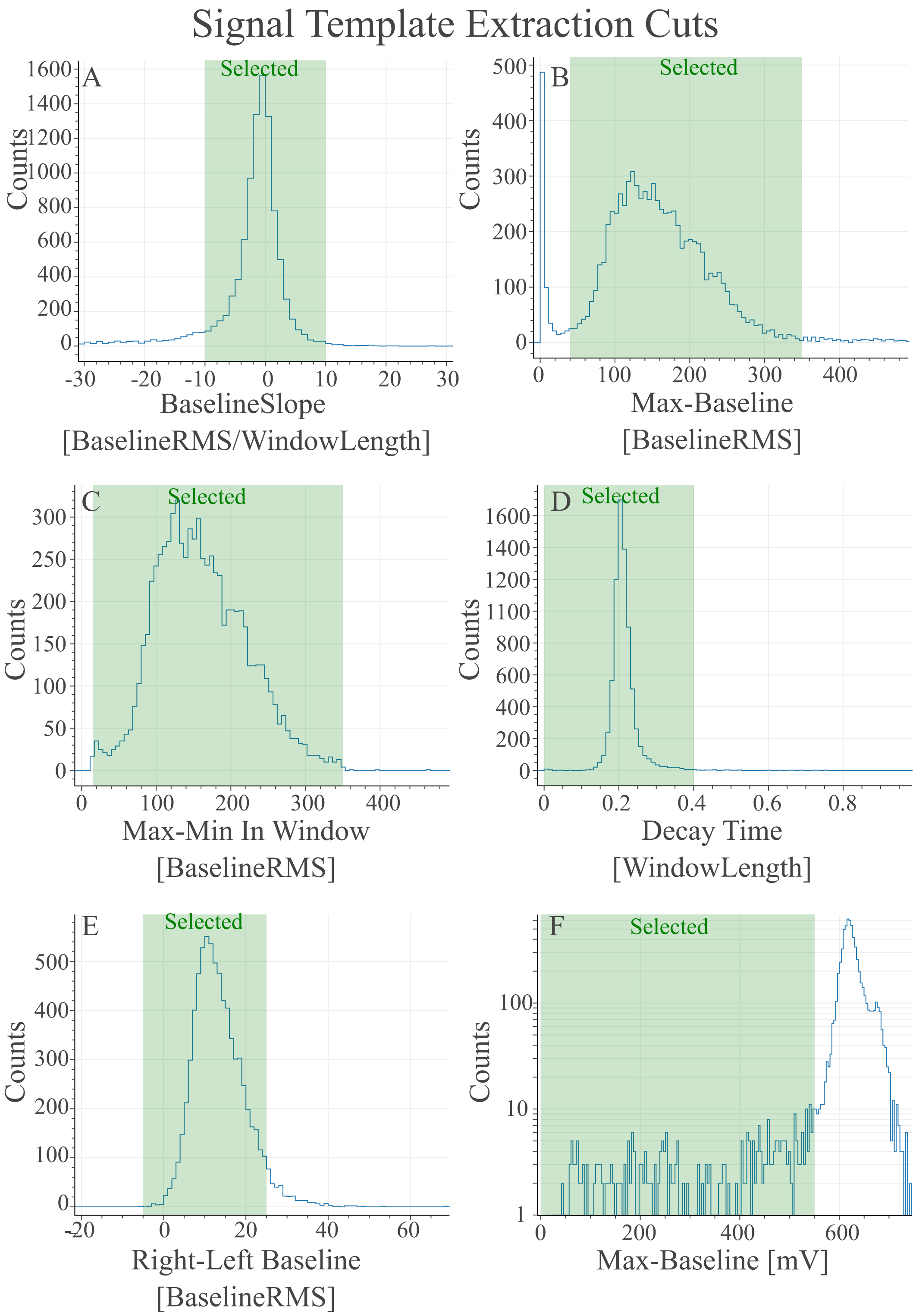

Figure 4.14. Data quality cuts applied to select the pulses to build the signal template. The cuts are applied in succession in the plots from A to F. In the F panel, the cut on the Max-Baseline is applied to select pulses below the ^{55}Fe calibration lines (which are visible on the right side of the histogram).

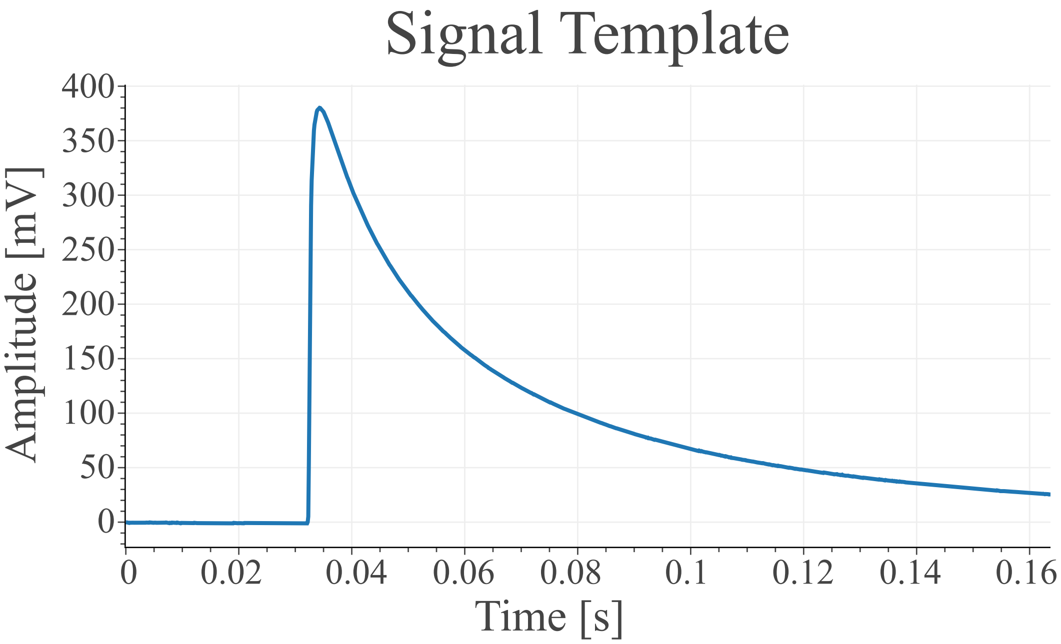

Figure 4.15. Resulting signal template achieved by averaging the 292 pulses selected with the cuts shown in Figure 4.14.

4.2.3.3 Building the Noise Power Spectral Density from data

A second crucial step in building the matched filter is the estimation of the Noise Power Spectral Density (NPSD). Starting from randomly selected traces, a subset of *empty baselines*, meaning acquisition windows without pulses, is selected and used to build the NPSD.

In order to build the NPSD the absolute value of the Fourier transforms of the noise traces are averaged together to extract the common spectral features of the noise, meaning that the average power spectrum is calculated. When the power spectrum is then normalized with the width of the frequency binning, the NPSD is obtained.

To build the NPSD in this analysis, the quality cuts to select the empty baselines are shown in Figure 4.16. The first cut applied, panel A, is to select 0 pulses detected from the pulse finding algorithm described in section 4.2.2, the parameters for the search are set to efficiently find pulses by also regarding noise fluctuations above 3 RMS as signals. Once only empty baselines are present, a second cut that further removes pulses and selects the maximum fluctuations of the noise is implemented by selecting low values for the **Max-Min In Window** (panel B). The final cut on **Baseline Slope**, panel C, is the same as the one used for building the signal template. This last cut is particularly important to select noise traces that do not have the decaying slope of a previous signal, in fact not only this would give an incorrect increase in the noise level but also increases the frequency bins of the NPSD that are also present in the signal template thus reducing the efficacy of the matched filter. Once all these cuts are applied 63447 noise traces are selected (out of 90896) and used to build the NPSD in Figure 4.17. From the figure it can be noticed that the majority of the signal is present in low frequency bins, which are

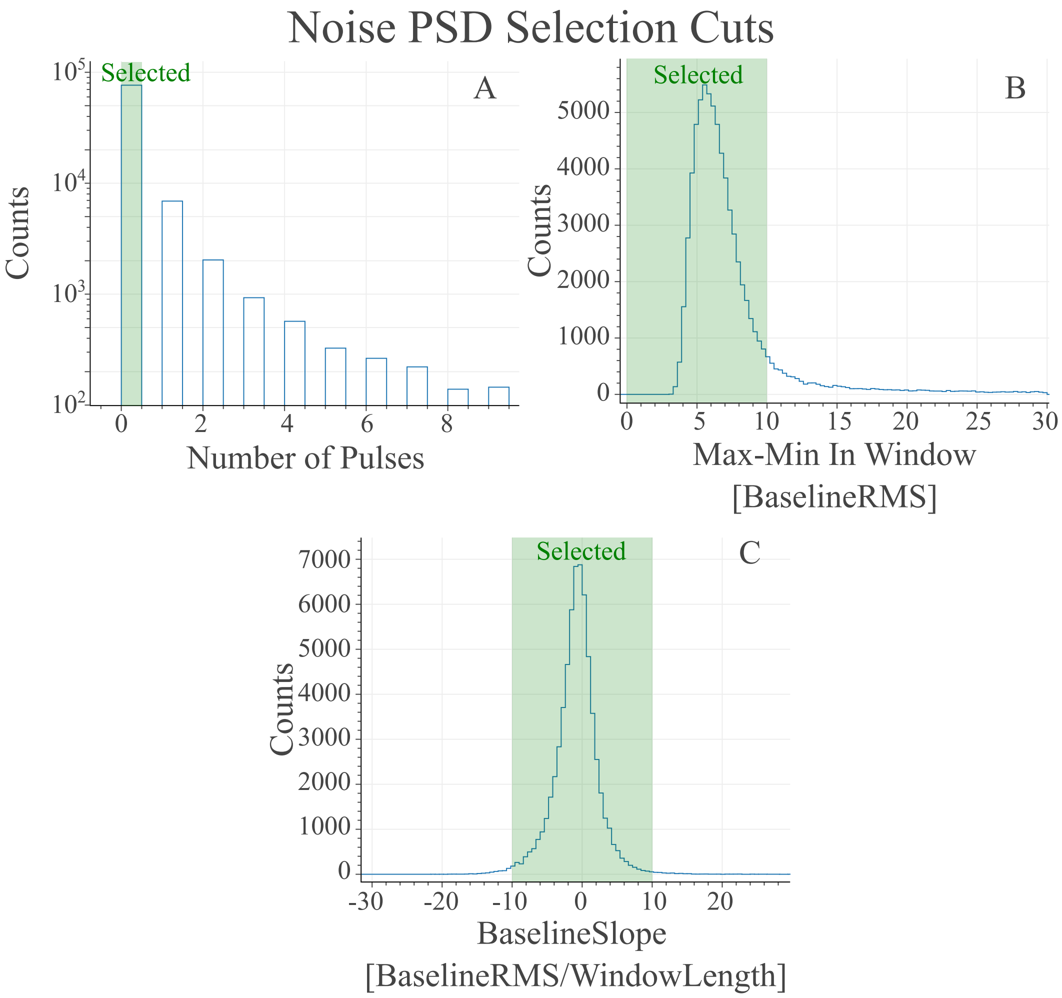

Figure 4.16. Quality cuts to select noise traces to build the NPSD.

the main ones being used by the matched filter.

Integrating the resulting NPSD the detector resolution before the application of the matched filter can be evaluated and is ∼5 mV. By using eq. (4.3) the resolution after the application of the matched filter is expected to be ∼0.67 mV. Since the filtering preserves the pulse amplitude (the gain of the filter is set to 1 by choosing the appropriate normalization), the application of the matched filter lowered the noise level of a factor $\frac{5 \text{ mV}}{0.67 \text{ mV}} \approx 7.5$, which directly impacts the SNR and the resolution on the amplitude reconstruction.

4.2.3.4 Noise Equivalent Power for Cryogenic Calorimeters

The Noise Equivalent Power (NEP) is a useful figure of merit used to quantify the performances of bolometers and which definition can be extended to calorimetric signals. In general terms, the NEP is the noise to signal ratio (inverse of SNR) of each frequency component in the detector signal. If a calibration constant is provided, then the use of the NEP makes comparing detector performances easy

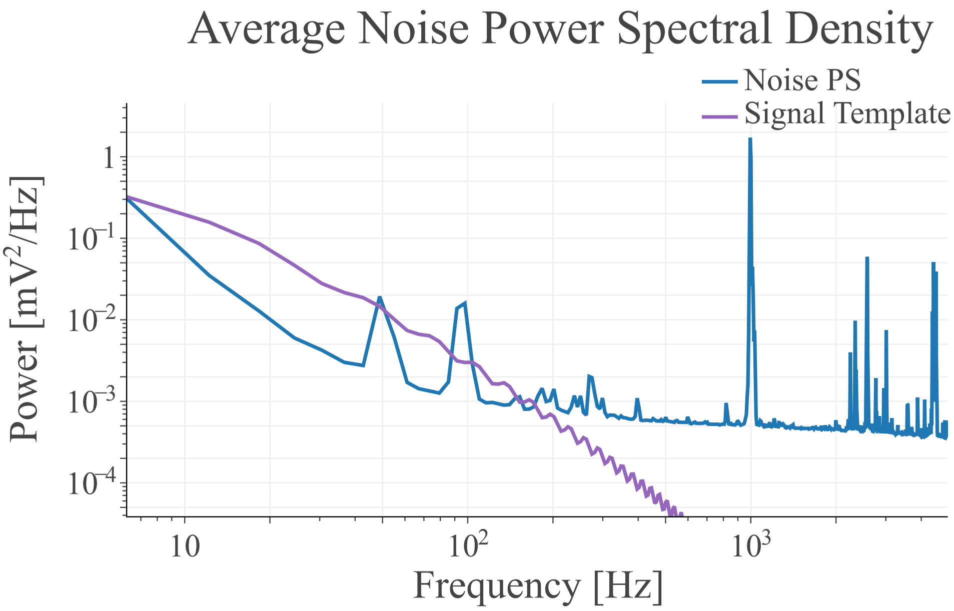

Figure 4.17. NPSD extracted by averaging the power spectra of the 63447 noise traces selected with the cuts in Figure 4.16. In blue the NPSD is shown and in purple the power spectral density of the template pulse (normalized to match the range of the NPSD) is plotted for comparison.

since in volts they might differ due to working conditions.

To build the NEP the first thing is to convert the NPSD, which is in $\frac{\mathrm{mV}^2}{\mathrm{Hz}}$, to $\frac{J^2}{Hz}$ by multiplying it with the square of the calibration constant (converted to $\frac{\mathrm{J}}{\mathrm{mV}}$). The second step is to get the signal template normalized to have unitary amplitude and compute its power spectral density, which is in Hz^{-1}. The NEP is thus defined as:

$$\mathrm{NEP}(f) = \frac{\sqrt{N_{PSD}^{\mathrm{joule}}(f)}}{|S(f)|} \qquad \left[\frac{\mathrm{W}}{\sqrt{\mathrm{Hz}}}\right] \tag{4.21}$$

where $N_{PSD}^{\mathrm{joule}}(f)$ is the double-sided NPSD converted to $\frac{J^2}{Hz}$ and $S(f)$ is the power spectral density of the normalized template signal. From the NEP the resolution of the detector after the application of the matched filter can be extracted, in fact:

$$\sigma_n^2 = \left[\int_{-\infty}^{\infty} \frac{|S(f)|^2}{N_{PSD}(f)} df\right]^{-1} = \left[\int_{-\infty}^{\infty} \frac{1}{\mathrm{NEP}(f)^2} df\right]^{-1} \tag{4.22}$$

Anticipating the result of the detector calibration described in section 4.3.1, the calibration constant can be used to evaluate the NEP for the detector used for the nuclear recoil calibration (see Figure 4.18). As mentioned before and visible from Figure 4.18 the lowest frequencies have the best SNR and the NEP is almost constant meaning that a small contamination due to the signal decay is present (which is unavoidable since the decay is exponential). Moreover, it can be seen that the 50 Hz frequency, typical of the electrical power lines, and its harmonics can be

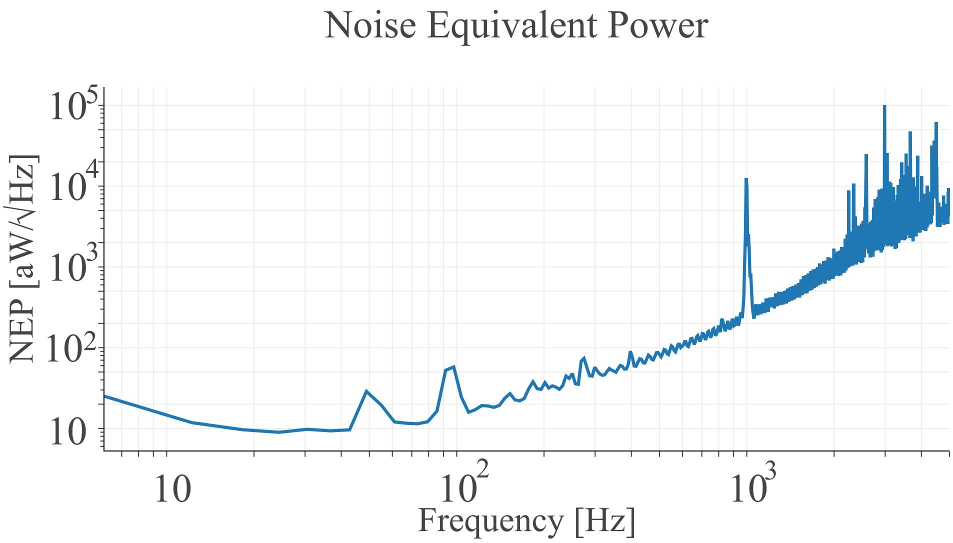

Figure 4.18. NEP of the cryogenic detector used for the detection of neutron induced nuclear recoils, built with the signal template in Figure 4.15 and the NPSD from Figure 4.17.

seen in the detector and affect the resolution of the detector since they are in the same frequency band as the signal. From this NEP the detector resolution after the application of the matched filter is expected to be:

$$\sigma_n \approx 6.3 \text{ eV} \tag{4.23}$$

A brief discussion on how the template signal and the noise affect the NEP in the case of cryogenic detectors can be found in appendix B.

4.2.4 Matched filter χ^2, χ_L and χ_R as low SNR data quality parameters

It is possible to measure how much a signal $v(t)$ differs from the signal template by calculating the integral of the squared difference of their content. This difference cannot be calculated in the time domain since the noise may have a non-zero auto-correlation and must be performed in the frequency domain, where the auto-correlation can be easily accounted for since its Fourier transform is equal to the NPSD. Then one can build the following parameter:

$$\chi^2_{MF}(A, t_0) = \int_{-\infty}^{\infty} \frac{\left|V(j\omega) - A \cdot e^{-j\omega t_0} S(j\omega)\right|^2}{N_{PSD}(\omega)} d\omega \tag{4.24}$$

where $V(j\omega)$ is the Fourier transform of the signal, A is the amplitude of $v(t)$ and t_0 is the time jitter between the signal and the template which has a Fourier transform equal to $S(j\omega)$. It can be shown that the best estimate, i.e. the values for which χ^2_{MF} is minimum, of the amplitude A and t_0 are given by the ones obtained by applying the matched filter.

The $\chi^2_{MF}(A, t_0)$ parameter is distributed, for signals of the form $v(t) = A \cdot s(t) + n(t)$, as a χ^2 distribution with as many degrees of freedom as the number of samples present in the acquisition window and can then be normalized in order to be distributed around 1. Once A and t_0 are estimated with the matched filter, the value of the normalized $\chi^2_{MF}(A, t_0)$ is a powerful data cleaning variable since it allows to spot overall pulse deformation with respect to the considered template. Cutting on this parameter has the main advantage of being defined for any amplitude A without diverging when A reaches 0. This means that $\chi^2_{MF}(A, t_0)$ can be evaluated and used efficiently also at extremely low SNRs, actually it is well-defined and can be used also on noise traces to study the noise distribution (by taking t_0 as a fixed number, i.e. without the maximum search).

Relying only on a data quality selection made with $\chi^2_{MF}(A, t_0)$ is not enough, since a very small pulse shape deformation is averaged away from the integral. For this reason, another type of low SNR variable can be built in the time domain:

$$\chi(t, t_0) = \frac{v^f(t) - \alpha(t) \cdot v^f_{max}}{\sqrt{\sigma_n^2 \cdot (1 + \alpha(t)^2) - 2\alpha(t) \cdot R(t - t_0)}} \quad \text{with:} \quad \alpha(t) = \frac{s^f(t)}{s^f_{max}} \tag{4.25}$$

where $v^f(t)$ is the signal $v(f)$ after the application of the matched filter and $v^f_{max} = v^f(t_0)$ is its maximum value, $s^f(t)$ is the filtered signal template with maximum s^f_{max}, σ_n^2 is the filtered noise variance and $R(t - t_0)$ is the auto-correlation of the noise between the time t and t_0. This difference (normalized with the corresponding standard deviation) describes how much a signal $v(t)$ differs from a template $s(t)$ at a given value of t after the application of the matched filter, meaning that if $v(t) = A \cdot s(t) + n(t)$ then $\chi(t, t_0)$ is normally distributed around 0 with variance 1 and $\chi^2(t, t_0)$ is a χ^2 distribution with 1 degree of freedom. Since this parameter does not have any integration, it is much more sensitive than $\chi^2_{MF}(A, t_0)$ to small deviations of the pulse shape. The data quality selection using this parameter is performed by requiring a maximum on its squared value, an example of the distribution built from a Monte Carlo simulation is presented in Figure 4.19.

In practice, if $\chi(t, t_0)$ is evaluated at times t very far from t_0 it basically only compares the filtered noise and if t is too near t_0 then the deviation from the filtered template is too low to be measured efficiently. For this reason, two values of t are chosen at the extremes of the FWHM of the filtered template as shown in Figure 4.20. The two values of t are referred to as t_L and t_R, since they are *left* and *right* of the signal maximum t_0, and give rise to two pulse shape parameters referred to as $\chi_{L,R} := \chi(t_{L,R}, t_0)$ for the same reason.

All these matched filter based parameters described so far are distributed as expected only for signals of the type $v(t) = A \cdot s(t) + n(t)$, meaning that the detector is completely linear and the pulse shape does not have any dependence on the amplitude A. This means that these quantities have a converging and finite limit for $A \to 0$, i.e. they can be used to perform valid pulse shape cuts even on noise traces.

A cryodetector signal cannot always be represented as $v(t) = A \cdot s(t) + n(t)$, and this introduces non-linearities which change the distributions of the described variables.

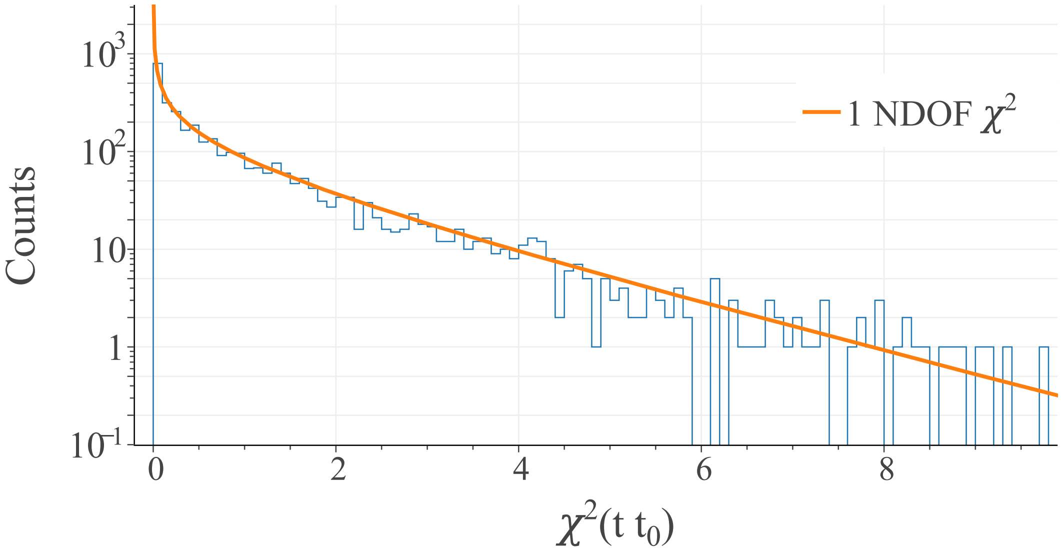

Figure 4.19. Distribution of $\chi(t, t_0)$ built from a Monte Carlo simulation of the detector pulses. As comparison, the 1 degree of freedom (NDOF) χ^2 distribution is superimposed.

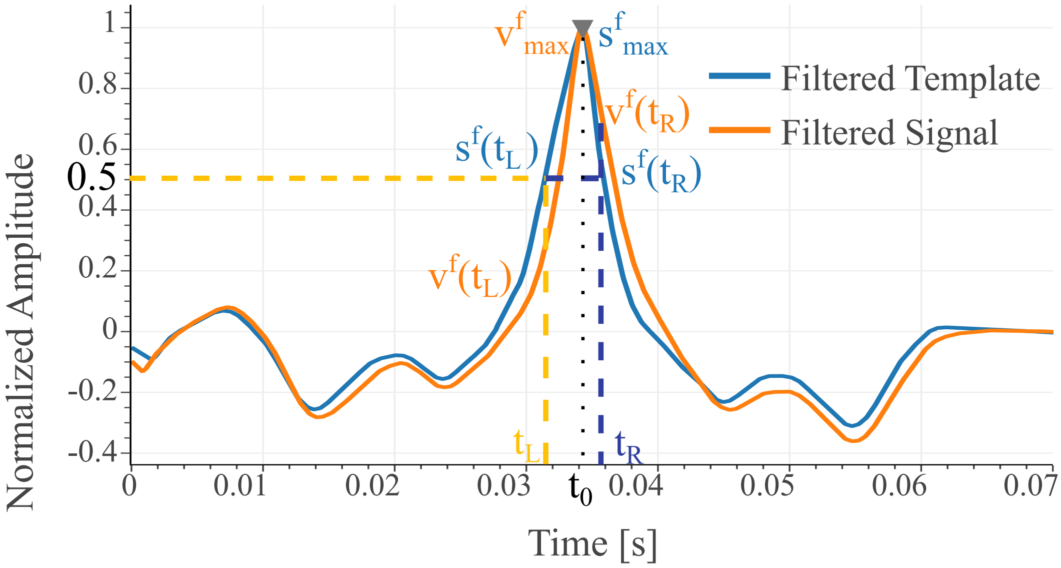

Figure 4.20. Diagram with highlighted the considered points in the evaluation of χ_L and χ_R. In blue, all the quantities relative to the filtered template are shown, while in orange the ones of the filtered signal are presented.

This can be dealt with in two different ways, the simplest one can be applied if the dependence on the amplitude of the pulse shape is not drastic and consists in simply enlarging the quality cuts set on these parameters and results usually sufficient for χ^2_{MF}. On the other hand, if the dependence is more pronounced, it is possible to perform a *linearization* of these parameters. A way of linearizing χ_L and χ_R is presented in appendix C.

Table 4.2. Parameters extracted from the fitting of the ^{55}Fe calibration lines.

Parameter	Background	Source
$\langle A_{\mathrm{K}_\alpha} \rangle$ [mV]	613.83 ± 0.18	634.46 ± 0.16
$\langle A_{\mathrm{K}_\beta} \rangle$ [mV]	669.02 ± 0.63	691.23 ± 0.73
$\sigma_{\mathrm{K}_\alpha}$ [mV]	9.88 ± 0.14	10.14 ± 0.13
$\sigma_{\mathrm{K}_\beta}$ [mV]	10.96 ± 0.52	11.53 ± 0.64
I_{K_α}	9482 ± 2.50	13078 ± 304
I_{K_β}	1166 ± 94	1176 ± 104
χ^2/DOF	1.07	1.12

4.3 Data Analysis Application

After having defined all the crucial parameters being evaluated during the waveform analysis, the focus will now be shifted to the higher level analysis. In the following sections the data cleaning, detector calibration and energy spectrum extraction are described. As already mentioned, both a *background* and a *source* dataset are present and each step was repeated independently on both in order to check consistency.

All the analysis presented in this section was performed using the `DIANA` analysis framework [91], already used in the CUORE, CUPID and BULLKID experiments. During this work a python based extension of the framework was built and is briefly described in appendix D.

4.3.1 Detector Calibration and non-linearities

The first step in the analysis is to calibrate the amplitudes of the signals obtained with the matched filter. In both datasets, the detector is exposed to a ^{55}Fe source, meaning that two calibration lines are available at respectively $\mathrm{K}_\alpha = 5.985$ keV (weighted average) and $\mathrm{K}_\beta = 6.490$ keV. The position of the calibration lines is extracted by performing a fit of the histograms in Figure 4.21 with a function composed of the sum of two Gaussians (one for each peak) and a first degree polynomial, in order to keep into account the presence of background counts. The results of the fit (performed with a Poisson log-likelihood minimization) are shown in Table 4.2. In Table 4.3 the ratios between intensities and mean amplitudes of the calibration lines are shown, and it can be seen that in the background they are fairly similar to the expected values (even though the amplitude one shows a small non-linearity discussed later) while in the source there is a bit of deviation in the ratio of the intensities. It needs to be kept in consideration that these ratios, especially the intensity one, are quite sensitive to the selection cuts applied to the data and are only indicative. The spectra in Figure 4.21 were, in fact, obtained by applying loose cuts on $\chi^2_{L,R}$ and χ^2_{MF} in order to consider only correctly reconstructed pulses, the cuts were then completely redefined for the following steps of the analysis.

To extract the calibration constant it is then possible to fit the values of the mean amplitudes in Table 4.2 as a function of their expected energy with a first degree polynomial with zero anchoring (forced to pass at y=0 for x=0). This fit, shown in Figure 4.22, allows to easily calculate the uncertainty on the calibration constant

Table 4.3. Position and intensity ratios of the two calibration lines produces by the ^{55}Fe X-ray source. The reported errors are the 1σ statistical fluctuations propagated from the best fit errors presented in Table 4.2.

	Expected	Background	Source
$\frac{\langle A_{\mathrm{K}_\beta}\rangle}{\langle A_{\mathrm{K}_\alpha}\rangle}$	1.101	1.09 ± 0.03	1.09 ± 0.02
$\frac{I_{\mathrm{K}_\alpha}}{I_{\mathrm{K}_\beta}}$	8.333	8.1 ± 0.7	11.1 ± 1.0

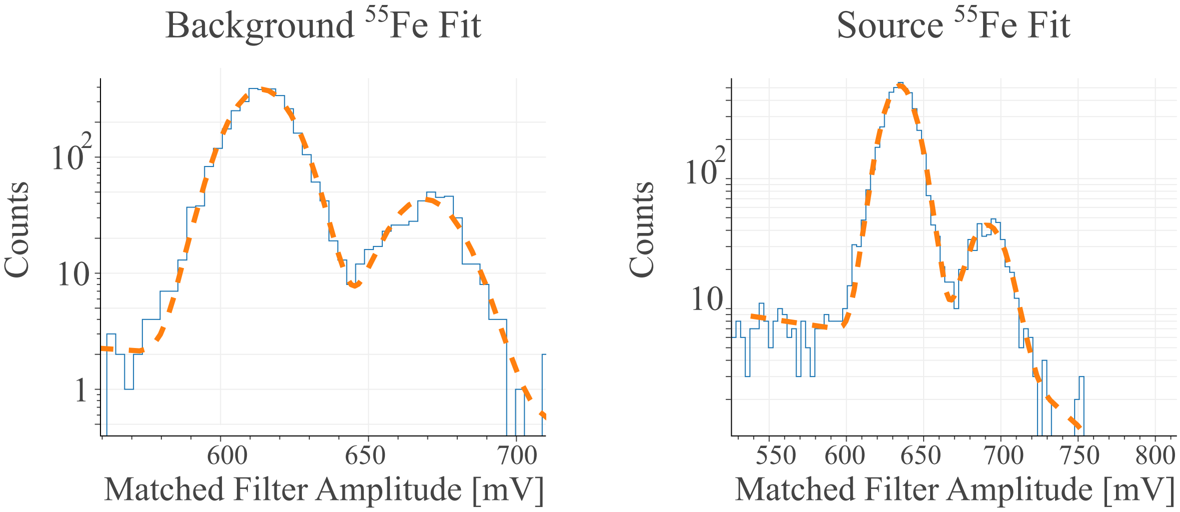

Figure 4.21. Extraction of the ^{55}Fe calibration lines parameters with a double Gaussian plus first degree polynomial. On the left the fit of the *background* dataset is shown and on the right the one for the *source* data is presented.

Table 4.4. Calibration constant for the source and background datasets extracted from the fits in Figure 4.22. The errors presented are only statistical.

	Background	Source
Calibration Constant $\left[\frac{\mathrm{eV}}{\mathrm{mV}}\right]$	9.613 ± 0.003	9.297 ± 0.002

and get a hint on the detector non-linearity, in fact it can be seen that K_β has a slightly lower amplitude than it should have if the detector was fully linear. The calibration constants for the two datasets are shown in Table 4.4 and while they are similar, meaning that the detector was operated roughly in the same working point in the two datasets, the difference is statistically significant so for each dataset the respective calibration constant was used.

4.3.1.1 Non-Linearity Estimation

From the residuals in Figure 4.22 it is already noticeable how a linear model with zero anchoring $E(A) = k \cdot A$ does not well represent the energy scaling in the detector, since the amplitude value of K_β is slightly suppressed with respect to the expected one. Two different ways have been identified in order to estimate the non-linearity: a

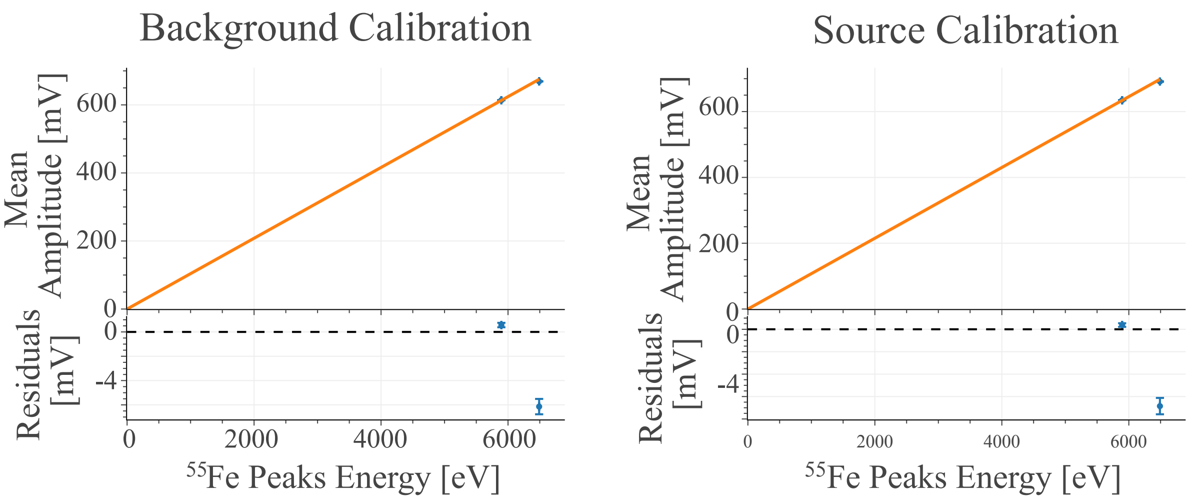

Figure 4.22. Extraction of the calibration constant with a fit on the average amplitudes of the ^{55}Fe lines with a first degree polynomial with zero anchoring. On the left and on the right, the fits are shown for respectively the *background* and *source* datasets. The error bars represent the 1σ statistical fluctuations as extracted from the best fit parameters in Table 4.2.

parabolic fit of the iron lines and an estimation of the read-out intrinsic non-linearity, described in section 2.3.1.

The first method consists of assuming a parabolic scaling, with zero anchoring, of the amplitude with respect to the energy like $A = aE \cdot (1 + bE)$. Since in the data only two calibration lines are available and this model has two parameters, the estimation of a and b is analytical. Once the model parameters were extracted from the calibration peaks, the shift in the reconstruction of the energy with respect to the linear model at the expected nuclear recoil peak energy of 112.5 eV was estimated to be $\sim 10\%$ for both background and source data, as shown in the green curve in Figure 4.24.

The second method is to build a model starting from the readout circuit diagram described in section 2.3.1 and estimate the missing parameters from the data. In fact, it was already derived, in eq. (2.4), that the measured TES response is given by:

$$\Delta V_S = gI_B \left[\frac{c \cdot E + R_0}{c \cdot E + R_0 + R_S} - \frac{R_0}{R_0 + R_S} \right]$$

where the SQUID gain $g = 1.705\ \frac{\text{V}}{\mu\text{A}}$, the bias current $I_B = 2.5\ \mu$A and the shunt resistor $R_S = 40$ mΩ are known quantities from the setup and input readout parameters. The values of c and R_0 need instead to be predicted from the data. From the left panel in Figure 4.23 one can see that the highest detected heater amplitude (which produce saturated pulses) is $V_{sat} \approx 1.5$ V. The right panel in Figure 4.23 shows the heater amplitude as a function of its injected DC power (which

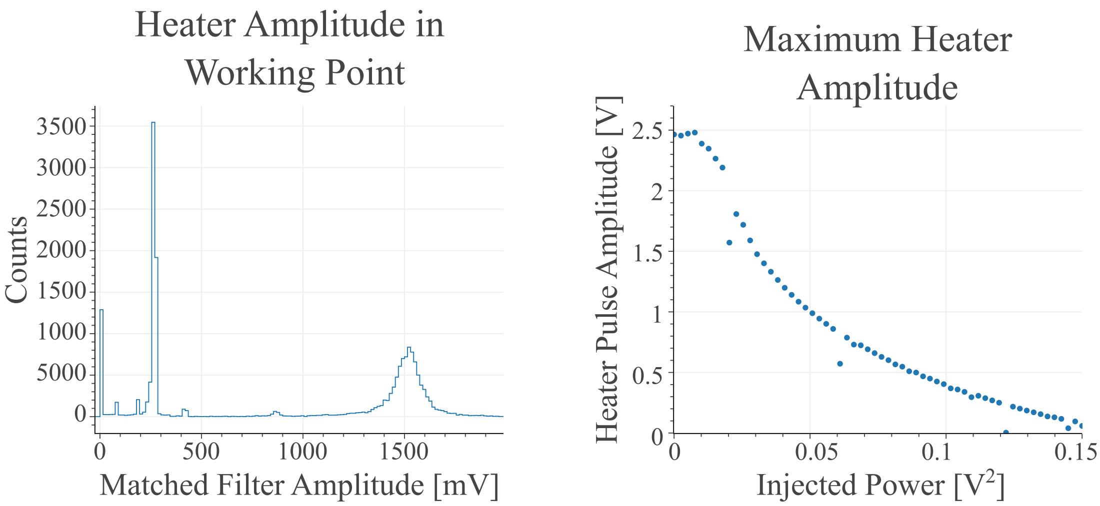

Figure 4.23. Left panel: Reconstructed amplitude of the heater generated pulses during detector operation. Right: Sweep of heater amplitude with respect to the injected DC heater power to study the transition shape.

determines the working point of the TES), this is a way of measuring the shape of the superconductive transition, and from the plot it is visible that the maximum possible heater amplitude is $V_{sat}^{max} \approx 2.5$ V. Combing these two pieces of information it is possible to extract R_0, which is the resistance at the operation point, in fact from eq. (2.4):

$$V_{sat}^{max} = gI_B\left[\frac{1}{1+\frac{R_{max}}{R_S}} - \frac{1}{1+\frac{0}{R_S}}\right] \rightarrow R_{max} = \frac{R_S}{\frac{gI_B}{V_{sat}^{max}} - 1} = 56.7\ \text{m}\Omega$$

$$V_{sat} = gI_B\left[\frac{1}{1+\frac{R_{max}}{R_S}} - \frac{1}{\frac{R_0}{R_S}+1}\right] \rightarrow R_0 = \frac{R_S}{\left[\frac{1}{1+\frac{R_S}{R_{max}}} - \frac{V_{sat}}{gI_B}\right]^{-1} - 1} = 12.3\ \text{m}\Omega$$

The calibration factor c can be determined from the known ^{55}Fe energy ($\text{K}_\alpha = 5.985$ keV) and observed pulse height (the average between the source and the background dataset is $\langle A_{\text{K}_\alpha}\rangle = (0.62 \pm 0.01)$ V). The measured amplitude at the iron can be written as:

$$V_{\text{Fe}} = \langle A_{\text{K}_\alpha}\rangle = gI_B\left[\frac{1}{1+\frac{R_{\text{Fe}}}{R_S}} - \frac{1}{1+\frac{R_0}{R_S}}\right] \rightarrow R_{\text{Fe}} = \frac{R_S}{\left[\frac{1}{1+\frac{R_S}{R_0}} - \frac{V_{\text{Fe}}}{gI_B}\right]^{-1} - 1} = 24.5\ \text{m}\Omega$$

meaning that:

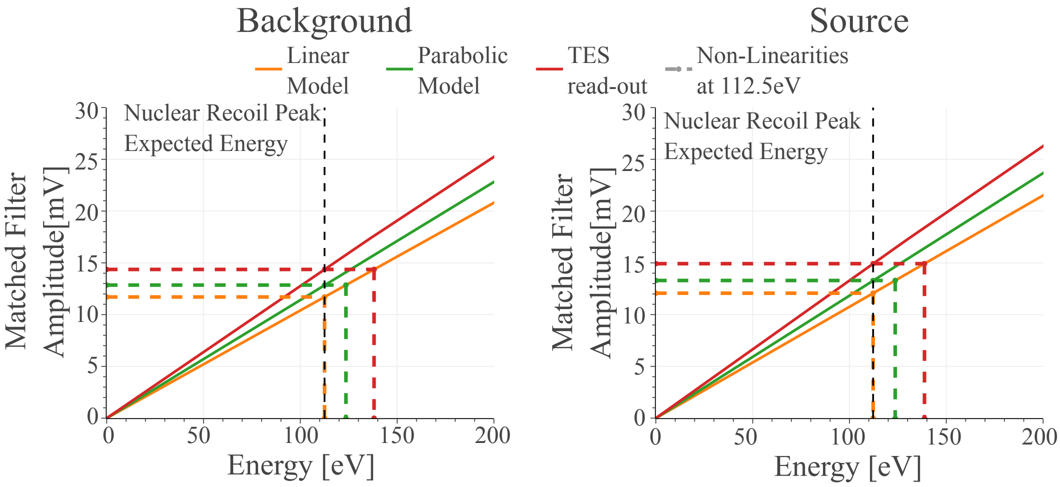

Figure 4.24. Estimation of the non-linearity in the energy reconstruction for both the background (left) and source (right) datasets. In orange the linear model is presented, in green the parabolic model is shown and in red the non-linearity estimated due to the readout is plotted. The effect on the nuclear recoil peak expected energy of 112.5 eV is highlighted with dashed lines of the corresponding colors.

$$c = \frac{R_{\mathrm{Fe}} - R_0}{\mathrm{K}_\alpha} = 2.08\ \frac{\mathrm{m}\Omega}{\mathrm{keV}}$$

At this point the behavior of the read-out amplitude V_S can be plotted as a function of the deposited energy E as shown with the red line in Figure 4.24. The estimated deviation of the energy at the 100 eV scale is $\sim +23\%$ for both the background and source data.

Due to the lack of calibration lines in the spectrum to further check the non-linearity models and the different energy corrections estimated, it was chosen not to correct the energy reconstruction but to consider a $\pm 20\%$ systematic uncertainty on the energy reconstruction in the 100 eV energy region.

4.3.2 Data Cleaning

Once an energy calibration is established for both datasets, the next step in the analysis is to perform data cleaning. As mentioned before, a blinding scheme is applied: all the data quality variables and procedures are defined on the background dataset and the cuts are adjusted on the high energy region of the source dataset.

Pulses deriving from ~100 eV energy depositions have amplitudes of ~10 mV that are immersed in a noise RMS level of ~5 mV (which on the amplitude estimation is reduced to ~0.7 mV after the application of the matched filter). Performing an effective pulse shape discrimination on a pulse with SNR≈ 2 is not trivial, and this is why the new matched filter based variables have been defined in section 4.2.4.

The first cut applied is on the normalized χ^2_{MF} which is required to be less than 20. As showed in Figure 4.25, this cut is quite loose and is aimed to remove most of the

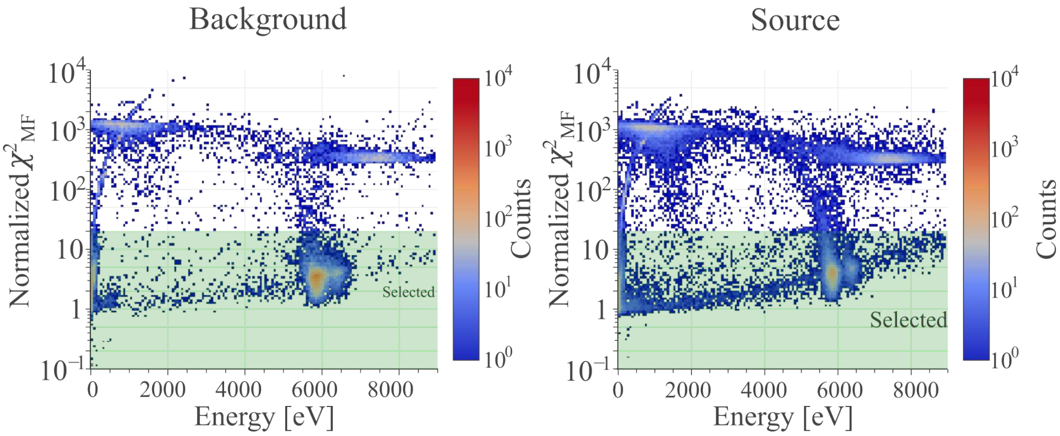

Figure 4.25. Pulse shape cut performed using the normalized χ^2_{MF} variable, the green shading represents the selected region. The cut is shown for both the background (left) and the source (right) datasets.

wrongly reconstructed pulses up to the iron energy. The value was chosen to be as low as possible without majorly impacting the pulses produced by the ^{55}Fe source. The rise of χ^2_{MF} (visible in the band of events characterized by χ^2_{MF}<20) with the energy present in both background and source data implies the presence of a pulse shape change with the energy.

In order to have tighter cuts with the $\chi^2_{L,R}$ variables, the non-linearity of the pulse shape needs to be addressed. The full linearity correction procedure described in appendix C cannot be performed in this measurement due to the lack of reference populations throughout the spectrum, for this reason another strategy was devised. By definition the $\chi^2_{L,R}$ parameters are correctly distributed on the noise traces, but on the iron induced pulses they are not due to the pulse shape non-linearity. Assuming that an iron induced pulse after the matched filter application can be modelled as $v_f(t) = [s_f(t)+\beta(t)]\cdot A+n_f(t)$, i.e. the filtered and normalized template $s_f(t)$ plus a deviation $\beta(t)$ all scaled by an amplitude A and with an added noise $n_f(t)$, then the measured $\chi^2_{L,R}$ can be written from eq. (4.25) as:

$$\chi^2_{L,R} = \frac{\left[v_f(t_{L,R}) - s_f(t_{L,R})\cdot v^f_{max}\right]^2}{\sigma^2_{eff}(t_{L,R})} = \frac{[\beta(t_{L,R})\cdot A + n_f(t_{L,R})]^2}{\sigma^2_{eff}(t_{L,R})} \tag{4.26}$$

where $\sigma^2_{eff}(t_{L,R})$ is the square of the full denominator of eq. (4.25) evaluated in the $t_{L,R}$ points. The expected mean value (where the mean operation is done over several pulses) of $\chi^2_{L,R}$ is, remembering that $\langle n_f(t_{L,R})\rangle = 0$ and $\langle n^2_f(t_{L,R})\rangle = \sigma^2_{eff}(t_{L,R})$:

$$\langle\chi^2_{L,R}\rangle = \frac{\beta^2(t_{L,R})\cdot\langle A^2\rangle + \sigma^2_{eff}(t_{L,R})}{\sigma^2_{eff}(t_{L,R})} = \frac{\beta^2(t_{L,R})}{\sigma^2_{eff}(t_{L,R})}\langle A^2\rangle + 1 \tag{4.27}$$

then one can estimate $\frac{\beta^2(t_{L,R})}{\sigma^2_{eff}(t_{L,R})}$ inverting the previous relation and doing the average over the iron induced pulses obtaining:

Table 4.5. Linearization effect on the $\chi^2_{L,R}$ pulse shape parameters.

	Expected	Background	Source
$\langle\chi^2_L\rangle_{^{55}\mathrm{Fe}}$	-	47.48	52.64
$\langle\chi^2_{L\|lin}\rangle_{^{55}\mathrm{Fe}}$	1	0.99	0.99
$\langle\chi^2_R\rangle_{^{55}\mathrm{Fe}}$	-	640.21	1061.16
$\langle\chi^2_{R\|lin}\rangle_{^{55}\mathrm{Fe}}$	1	1.00	0.99
$\sigma^{^{55}\mathrm{Fe}}_{\chi^2_L}$	-	48.28	50.53
$\sigma^{^{55}\mathrm{Fe}}_{\chi^2_{L\|lin}}$	$\sqrt{2} \approx 1.4142$	1.00	0.95
$\sigma^{^{55}\mathrm{Fe}}_{\chi^2_R}$	-	738.35	858.45
$\sigma^{^{55}\mathrm{Fe}}_{\chi^2_{R\|lin}}$	$\sqrt{2} \approx 1.4142$	1.16	0.80

$$\xi_{L,R} := \frac{\beta^2(t_{L,R})}{\sigma^2_{eff}(t_{L,R})} = \frac{\langle\chi^2_{L,R}\rangle_{^{55}\mathrm{Fe}} - 1}{\langle A^2\rangle_{^{55}\mathrm{Fe}}} \tag{4.28}$$

then the estimated *linearized* parameters are:

$$\chi^2_{L,R|lin} = \frac{\chi^2_{L,R}}{1 + \xi_{L,R} \cdot A^2} \tag{4.29}$$

where A is the matched filter reconstructed pulse amplitude. This parameter, like the χ^2_{MF}, is defined for pulses of 0 amplitude, meaning that it can be applied on the noise traces which become a viable control population. Since the two iron lines are near in energy, they are considered as one line with mean energy and amplitude as the weighted average of the respective quantities for the single lines.

The effect of this linearization can be seen from Figure 4.26 and from the mean and standard deviation of the distributions before and after the linearization presented in Table 4.5. As it can be seen from the table, the linearization is not perfect since it does not fully renormalize the standard deviations of the distributions, but the linearized distributions are close enough to the nominal ones and thus a pulse shape quality cut can be applied.

As visible from Figure 4.26 a tight cut on these linearized variables, with $\chi^2_{L|lin} < 3$ and $\chi^2_{R|lin} < 3$, was set in order to get rid of most of the remaining background. The integral of a 1 degree of freedom χ^2 distribution up to 3 is $\sim 92\%$, which is the expected percentage of events kept from these cuts. On the background and source data, the percentage of kept iron pulses is around 95%. which for the level of precision of this linearization procedure is satisfactory.

After the application of the three data quality cuts described so far, the low energy *background* spectrum can be inspected to check whether more cuts can be applied to further reduce the unwanted events. The effect of the described cuts can be seen in Figure 4.27 which, as desired, shows little effect on the energy distribution of the iron pulses while reducing the background counting rate between 100 eV and 1 keV

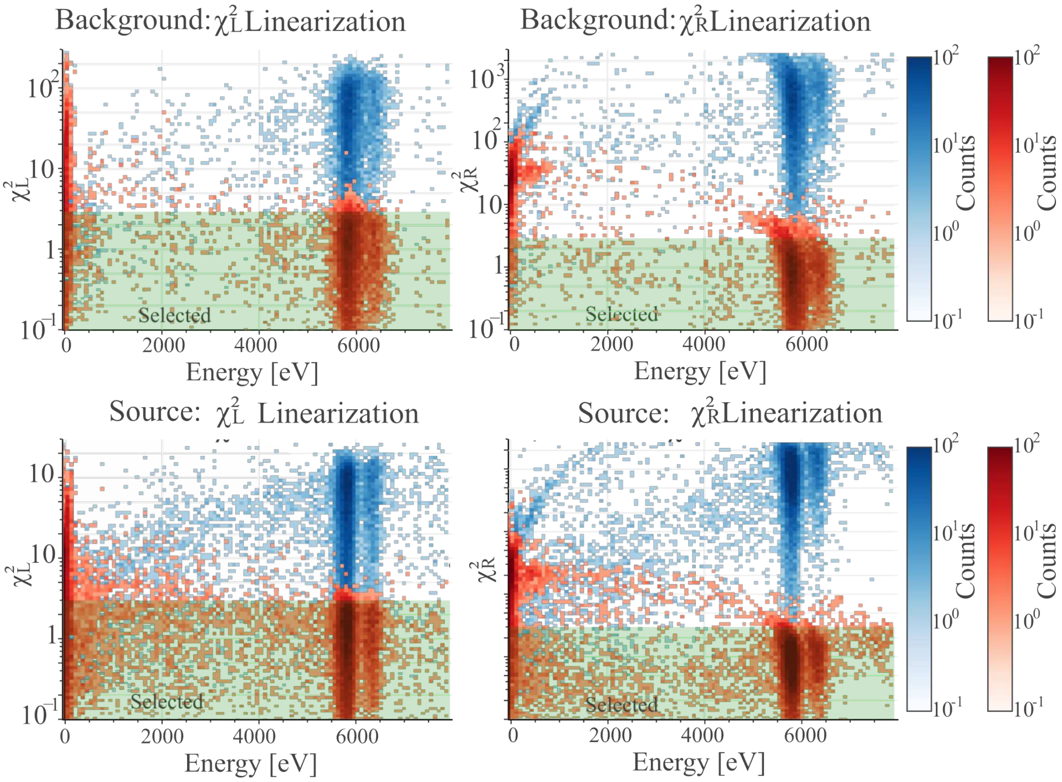

Figure 4.26. Linearization effect on the $\chi^2_{L,R}$ pulse shape parameters. In blue the distributions of $\chi^2_{L,R}$ are shown and in red the linearized $\chi^2_{L,R}$ are plotted, while the green band shows the selected regions for the latter parameters. In the top (bottom) row, the effect on the two parameters for the background (source) dataset is shown.

of more than an order of magnitude. An example of the rejected or kept waveforms are shown in Figure 4.28.

Two features of the spectrum are worrisome for the detection of the nuclear recoil peak: the first is the rise in the event rate at low energies ($\leq$ 100 eV) due to the LEE (see section 2.4.3) and the other is the small peak in the background counting rate present at $\sim$ 180 eV. The latter is particularly dangerous since, due to the high uncertainty in the energy calibration, it could mimic the nuclear recoil peak.

A manual inspection of the pulses composing the $\sim$ 180 eV peak showed that they are all of the type shown in Figure 4.29 and show a more step-like behavior with respect to the expected pulse shape shown in Figure 4.15. Due to the low SNR the parameters considered so far are not able to discriminate these pulses but in the variable definitions in section 4.2.2 it is clear that the **Right-Left Baseline** parameter is suited for this task.

The **Right-Left Baseline** pulse shape parameter cannot be used directly to perform quality cuts since, if the acquisition window is not long enough, it has a linear dependence with the amplitude of the pulse, meaning that a *linearization* must be performed also in this case. Supposing that **Right-Left Baseline** scales as:

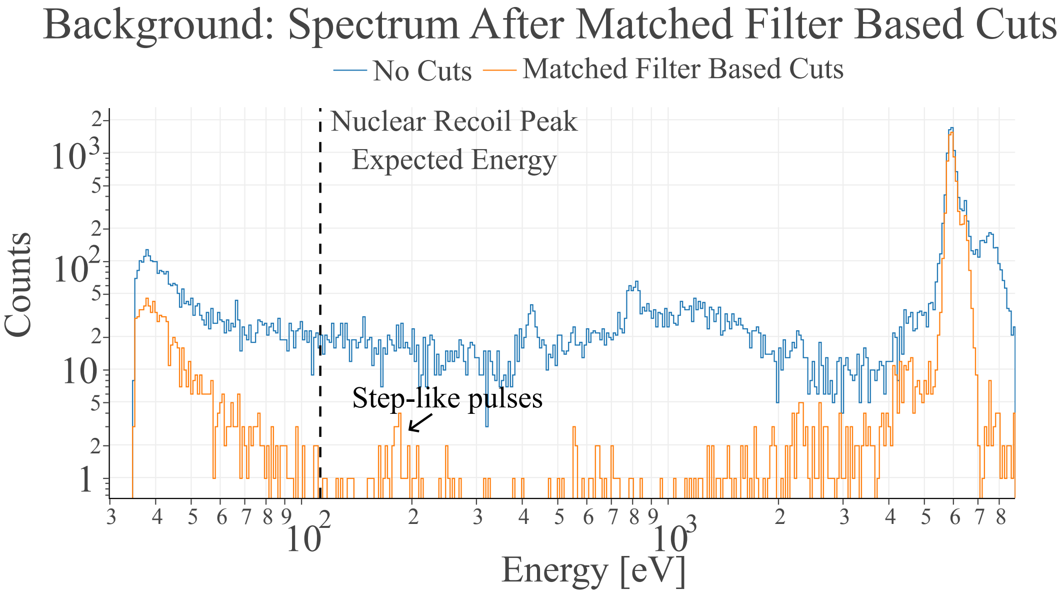

Figure 4.27. Effect of the matched filter based cuts on the energy spectrum of the *background* dataset. In blue the spectrum with no cuts is shown and in orange the spectrum after the matched filter based cuts is plotted. In the orange spectrum a small peak at ∼ 180 eV is visible, this feature is composed by step-like pulses like the one in Figure 4.29.

$$\langle \mathrm{RLB} \rangle = k_\mu \cdot \langle A \rangle + q_\mu$$

$$\sigma_{\mathrm{RLB}} = k_\sigma \cdot \langle A \rangle + q_\sigma$$

The parameters k_μ, q_μ, k_σ, q_σ can be evaluated directly from the data using the iron and noise amplitude and **Right-Left Baseline** distributions:

$$k_\mu = \frac{\langle \mathrm{RLB} \rangle_{^{55}\mathrm{Fe}} - \langle \mathrm{RLB} \rangle_{\mathrm{noise}}}{\langle A \rangle_{^{55}\mathrm{Fe}}} \qquad q_\mu = \langle \mathrm{RLB} \rangle_{^{55}\mathrm{Fe}} - \langle A \rangle_{^{55}\mathrm{Fe}} \cdot k_\mu$$

$$k_\sigma = \frac{\sigma_{\mathrm{RLB}}^{^{55}\mathrm{Fe}} - \sigma_{\mathrm{RLB}}^{\mathrm{noise}}}{\langle A \rangle_{^{55}\mathrm{Fe}}} \qquad q_\sigma = \sigma_{\mathrm{RLB}}^{^{55}\mathrm{Fe}} - \langle A \rangle_{^{55}\mathrm{Fe}} \cdot k_\sigma$$

where $\langle A \rangle_{^{55}\mathrm{Fe}}$ is the average amplitude of the ^{55}Fe induced pulses, $\langle \mathrm{RLB} \rangle_{^{55}\mathrm{Fe}}$ and $\langle \mathrm{RLB} \rangle_{\mathrm{noise}}$ are the mean values of the **Right-Left Baseline** distribution for respectively the ^{55}Fe pulses and the noise traces and $\sigma_{\mathrm{RLB}}^{^{55}\mathrm{Fe}}$ and $\sigma_{\mathrm{RLB}}^{\mathrm{noise}}$ are the standard deviations of the **Right-Left Baseline** distribution for the ^{55}Fe pulses and the noise traces.

The **linearized Right-Left Baseline** can now be defined as follows:

$$\mathrm{RLB}_{lin} := \frac{\mathrm{RLB} - (k_\mu \cdot A + q_\mu)}{k_\sigma \cdot A + q_\sigma}$$

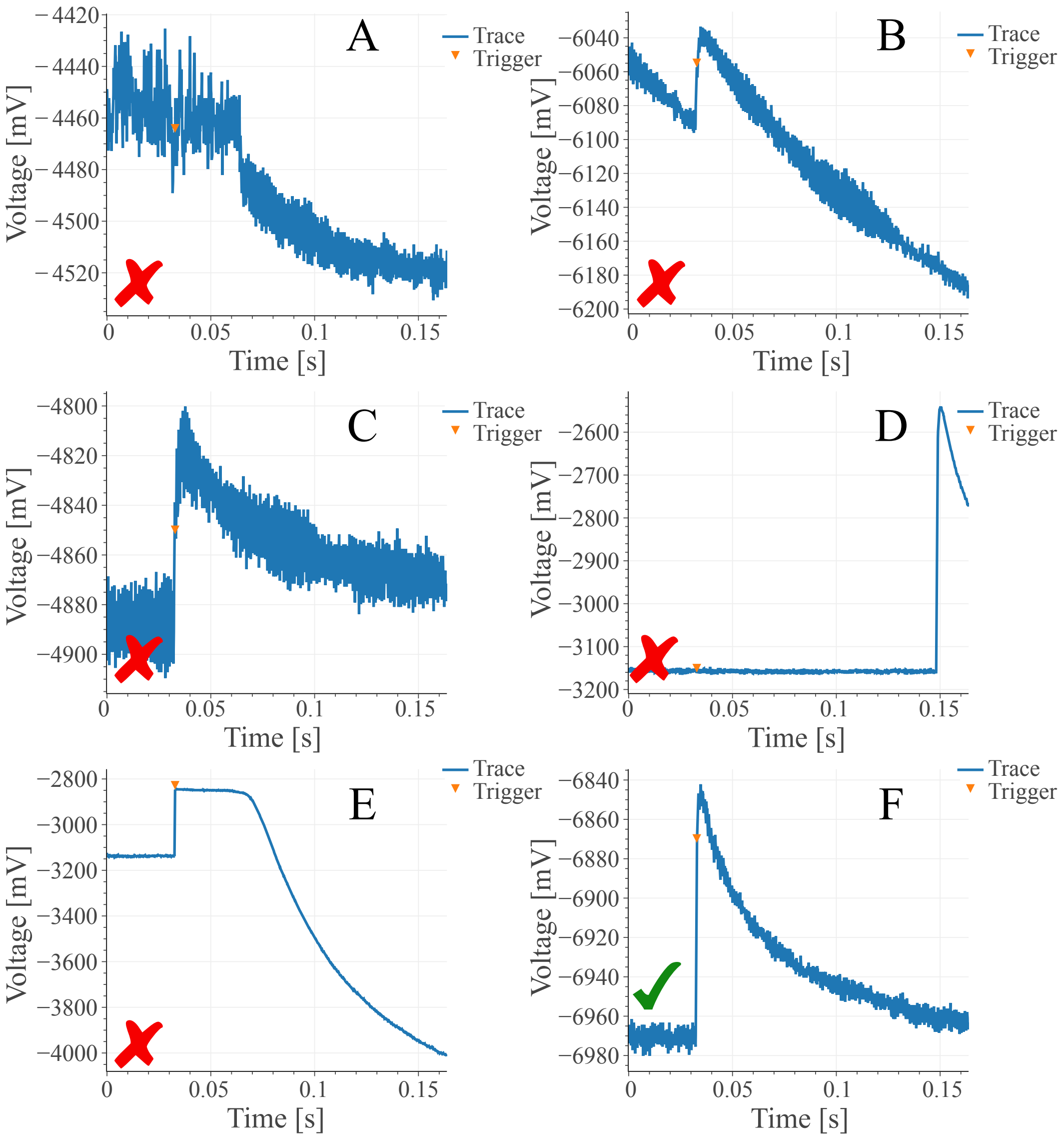

Figure 4.28. Examples of waveforms that are removed by the pulse shape cuts applied are shown in panels A to E. An example of a kept pulse is shown in panel F.

where RLB is the **Right-Left Baseline** parameter. This definition generates a distribution of the **linearized Right-Left Baseline** RLB_{lin} such that the mean value is 0 and the standard deviation is 1, making this parameter a pure number. The linearization guarantees that RLB_{lin} has a distribution independent of the amplitude of the recorded pulses, meaning that it can be equally applied on noise traces and ^{55}Fe induced pulses without showing any type of divergence. The effect of the linearization can be seen in Figure 4.30 and it can be seen that it is now equally distributed over the considered energy range.

By looking at Figure 4.31 it can be seen that at ~ 180 eV there are events are out of the main distribution band, then by placing a selection cut such that $|\text{RLB}_{lin}| \leq 2$ gets rid of most of these events. The spectrum of the remaining events is shown in

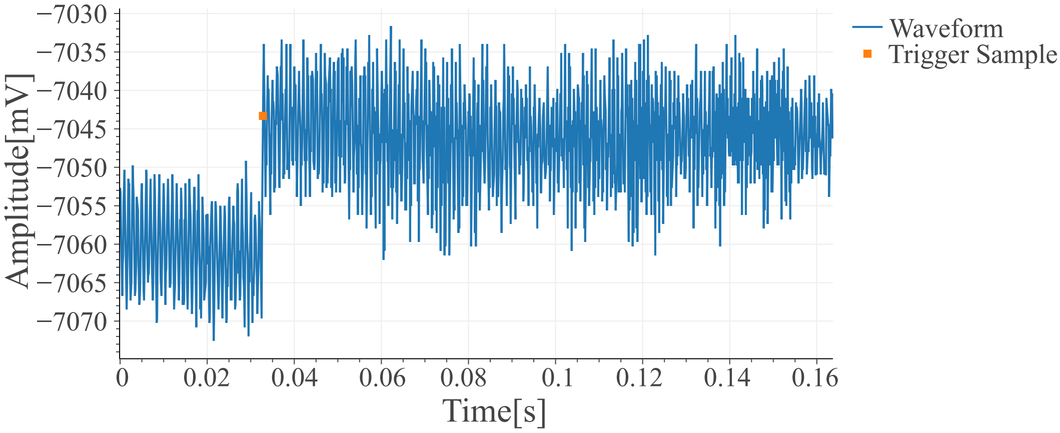

Figure 4.29. Example pulse taken from the ∼ 180 eV counting rate peak. The pulse is not similar to the expected pulse shape in Figure 4.15 but has a more step-like behaviour.

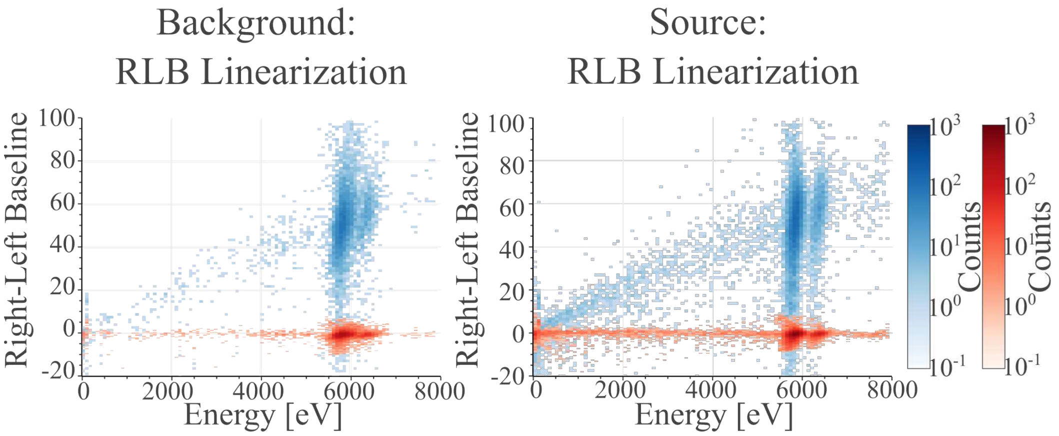

Figure 4.30. Linearization effect on the **Right-Left Baseline** pulse shape parameter In blue the distributions of **Right-Left Baseline** are shown and in red the **linearized Right-Left Baseline** are plotted. In the left (right) panel the effect on the parameter for the background (source) dataset is shown.

Figure 4.32, and, as designed, the effect on the population of the iron induced pulses is minimal while in the 100 eV to 1 keV region the background counts are greatly reduced and the 180 eV peak was mostly removed. In Figure 4.33 the distributions of the noise traces are shown with the associated Gaussian fits from which it can be seen that the energy resolutions for both datasets is around 6.5 eV. This is also the expected resolution on the nuclear recoil peak, since due to its low energy it is expected that the fluctuations on the amplitude reconstruction are dominated by the intrinsic noise of the detector.

4.3.2.1 Efficiency Evaluation

An important step to be performed when looking at spectra after triggering, amplitude reconstruction and quality cuts is to normalize the counts by the efficiencies of all these steps. The efficiency is defined as:

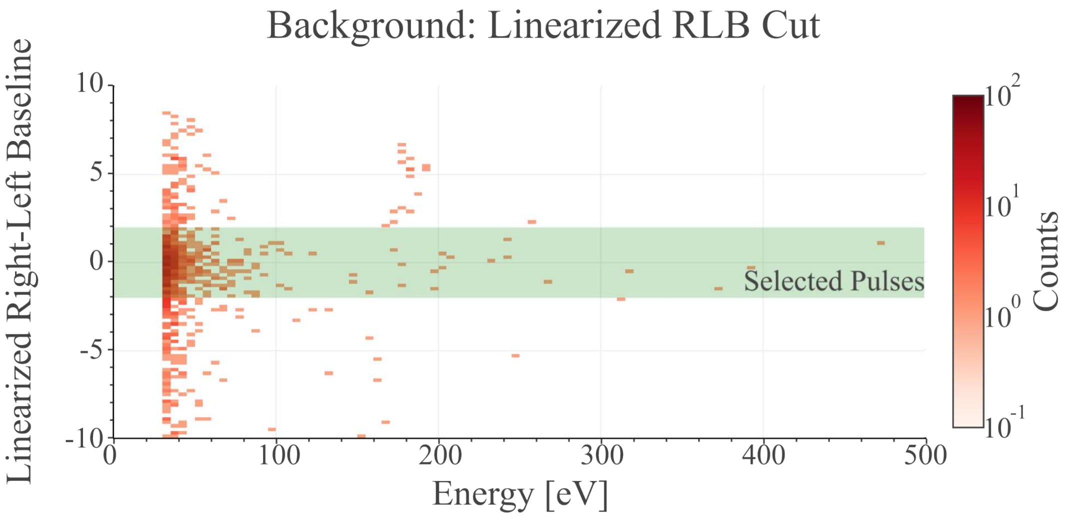

Figure 4.31. Zoom in the 100 eV region in the distribution of the **linearized Right-Left Baseline** parameter for the background dataset. At ∼ 180 eV the pulses making the peak appear separated from the main distribution band.

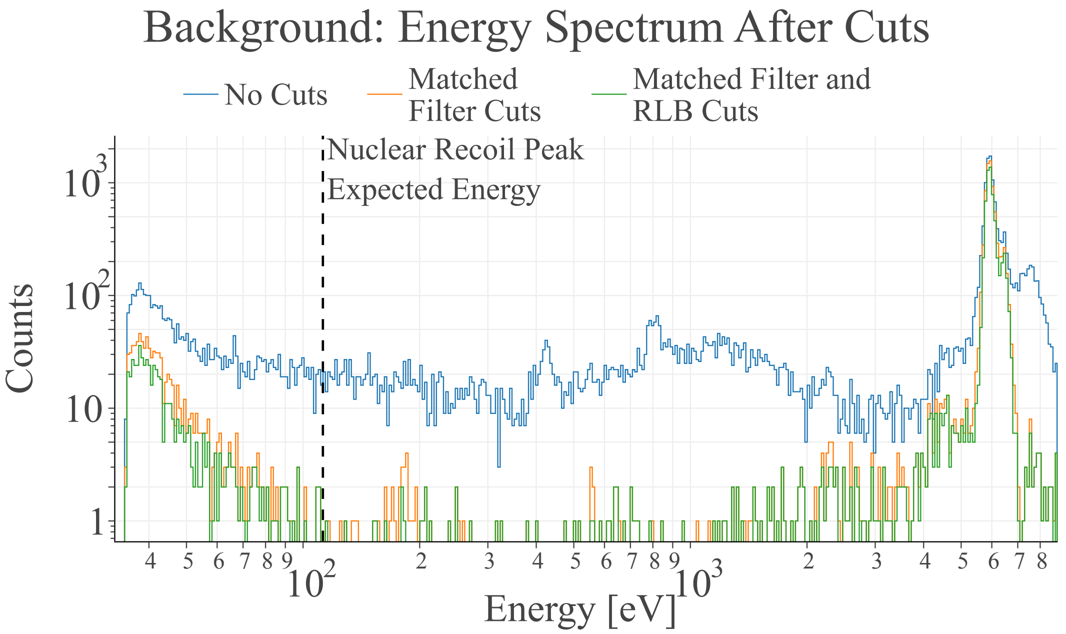

Figure 4.32. Background energy spectrum: in blue the spectrum with no cuts is plotted, in orange the spectrum with only the matched filter based cuts is shown and in green the spectrum after all cuts is shown.

$$\epsilon = \frac{N_p}{N_t} \qquad \sigma_\epsilon = \sqrt{\frac{\epsilon \cdot (1-\epsilon)}{N_t}} \tag{4.30}$$

where N_t is the total number of events in the considered population, N_p is the number of events in the population after the application of the analysis step and the error σ_ϵ is the binomial error associated with being or not in the N_p population.

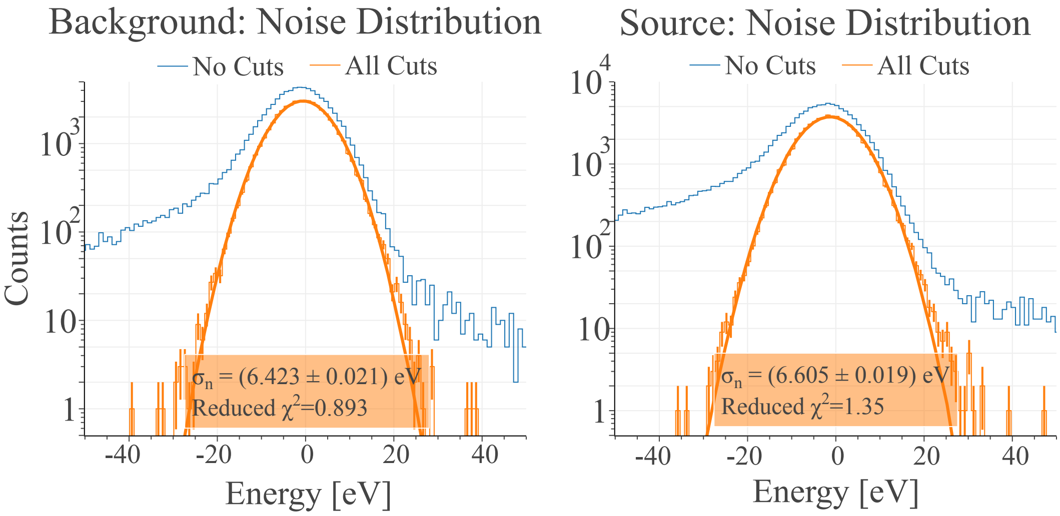

Figure 4.33. Noise distribution for the background (left) and source (right) datasets. In blue the amplitude distributions built from all triggered noise traces before cuts are shown, while in orange the distributions after all cuts are plotted with the associated Gaussian fit. The error bars on the fitted histograms (orange) represent the 1σ statistical fluctuations of the bin heights following the Poisson statistics.

Table 4.6. Cut efficiency for the background and source datasets for both the noise traces and the iron induced pulses. The reported errors are the 1σ statistical fluctuations.

	Background	Source
Noise Efficiency ϵ_n^c	0.673 ± 0.002	0.648 ± 0.002
^{55}Fe Efficiency $\epsilon_{^{55}\mathrm{Fe}}^c$	0.754 ± 0.006	0.775 ± 0.005

From this definition, it is clear that to calculate the efficiencies, control populations must be present in the data. The signal pulses and the heater pulses present in the data have different pulse shapes and the cuts defined for the analysis eliminate most of the heater pulses from the spectrum, thus this population cannot be used to estimate the cut efficiency. This means that the only two available distributions are the ^{55}Fe induced events and the noise traces. This is the reason why the effort of linearizing all the data quality variables has been made, in fact, with only two control populations at the very edges of the energy spectrum, having data quality parameters and cuts that by construction do not show any dependence with the deposited energy is imperative to have an energy independent efficiency.

As mentioned, to evaluate the cut efficiency, the noise and iron traces are used. This means that for the noise population a $\pm 2\sigma_n$ interval around zero is considered to be the reference population in order to not include too many outliers that are present due to the randomness of this type of trigger. For the ^{55}Fe pulses, only the K_α ones are used (as shown in Figure 4.34) to select a population with minimal outliers, meaning that the chosen interval is $\langle A_{\mathrm{K}_\alpha} \rangle \pm 2\sigma_{\mathrm{K}_\alpha}$. The cut efficiencies for the source and background datasets are shown in Table 4.6.

To evaluate the trigger and amplitude reconstruction, it is not possible to use the

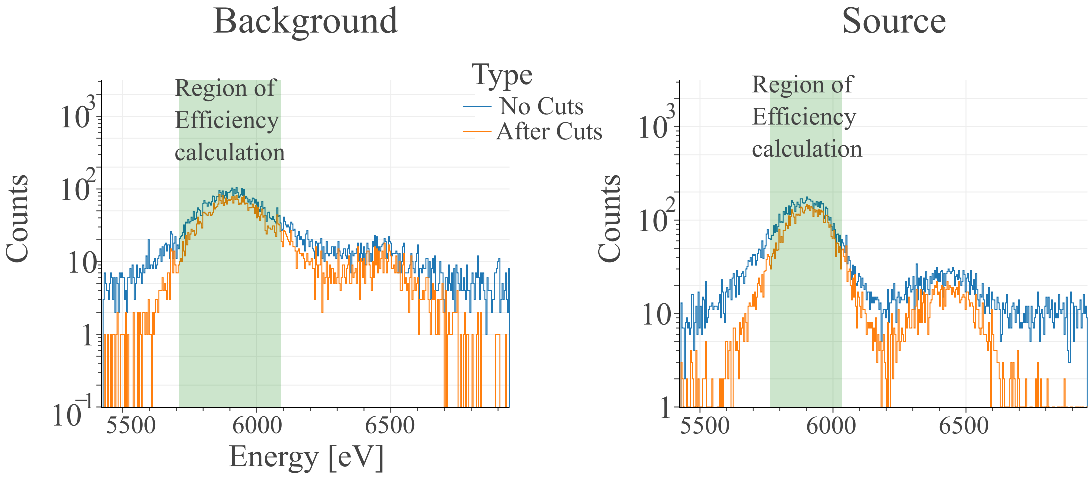

Figure 4.34. Energy distribution of the pulses induced by the ^{55}Fe calibration source before (blue) and after (orange) the pulse shape cuts are applied. In green, the region used for the efficiency estimation is highlighted. The spectra for the *background* and *source* dataset are shown respectively in the left and right panels.

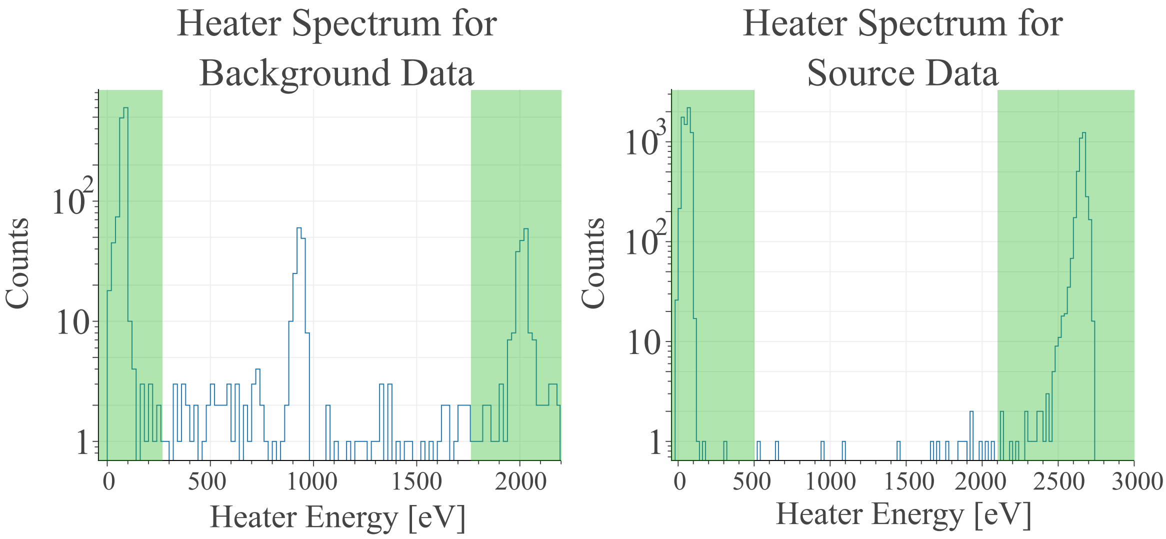

Figure 4.35. Spectra of the pulses induced by the heater for both the background (left) and source (right) datasets. On the spectra, the low and high energy heater populations used to evaluate the trigger and amplitude reconstruction efficiencies are highlighted.

populations discussed above since a way of tagging the desired populations without relying on the trigger threshold or the amplitude reconstruction is needed. For this reason, it was necessary to use the pulses produced by the heater. As shown from Figure 4.35 a low and a high energy heater pulses populations were chosen to match the procedure developed for the cut efficiency. The two populations are distinguished using an available parameter from the DAQ, the Heater Pulse Amplitude (HPA), that is proportional to the injected power in the heater.

Since both the triggering and the amplitude evaluation are based on the matched

Table 4.7. Efficiency of the matched filter based trigger algorithm on heater induced pulses for both the source and background datasets. The efficiency is presented for both the low and high energy heater populations. The reported errors are the 1σ statistical fluctuations.

	Background	Source
Low Energy ϵ_l^t	0.841 ± 0.012	0.800 ± 0.029
High Energy ϵ_h^t	0.865 ± 0.012	0.864 ± 0.025

Table 4.8. Efficiency of the matched filter based amplitude reconstruction on heater induced pulses for both the source and background datasets. The efficiency is presented for both the low and high energy heater populations. The reported errors are the 1σ statistical fluctuations.

	Background	Source
Low Energy ϵ_l^A	0.849 ± 0.012	0.782 ± 0.011
High Energy ϵ_h^A	0.923 ± 0.009	0.828 ± 0.009

filter and the heater and particle pulses have different pulse shapes, it is not possible to use the same matched filter used so far to evaluate this efficiency. For this reason a dedicated matched filter was built with the same NPSD but with a template pulse obtained from the heater pulses. The assumption here made is that by being in the same *optimality* condition, it is possible to replicate on the heater pulses the same performances obtained on the particle events.

To obtain the trigger efficiency, the triggering algorithm was rerun with the heater based matched filter, which runs in parallel to the logical trigger already described section 4.2.1.1. This means that for each logically triggered heater pulse there is a possibility that a self trigger is also present. For every heater event, which add up to N_t, it is then sufficient to check whether a self trigger is present to obtain the N_p population of equation eq. (4.30). The trigger efficiency results are shown in Table 4.7.

The amplitude reconstruction efficiency parametrizes the probability with which a pulse of known energy is estimated to have said energy. For example, if a heater pulse of known energy occurs during a work point fluctuation, the reconstructed amplitude will not match the expected one, meaning that the event ends up in a different region of the energy spectrum and this is an inefficiency that needs to be accounted for. The work point fluctuation is just an example, but there might be other reasons why an amplitude misreconstruction could occur. To calculate the amplitude reconstruction efficiency, the heater based matched filter was used for the amplitude estimation for the same reasons described above. For the two heater populations selected a range centered on the mean reconstructed amplitude and 3 standard deviations of the distributions wide was chosen, all the heater amplitudes ending up in this range compose N_p. The amplitude reconstruction efficiency results are presented in Table 4.8.

Once all the efficiencies are evaluated, they can be combined to obtain the low and high energies total efficiencies, indicated respectively with ϵ_l and ϵ_h:

Table 4.9. Total data analysis efficiency for both the source and background datasets. The high and low energy efficiencies are reported along with their average value over the full energy spectrum. The reported errors are the 1σ statistical fluctuations.

	Background	Source
Low Energy ϵ_l	0.497 ± 0.010	0.406 ± 0.016
High Energy ϵ_h	0.602 ± 0.011	0.554 ± 0.017
Average $\langle\epsilon\rangle$	0.55 ± 0.07	0.48 ± 0.11

$$\epsilon_l := \epsilon_n^c \cdot \epsilon_l^t \cdot \epsilon_l^A \qquad \epsilon_h := \epsilon_{^{55}\mathrm{Fe}}^c \cdot \epsilon_h^t \cdot \epsilon_h^A \tag{4.31}$$

which values can be found in Table 4.9. In the table it can be seen that in the source dataset reduced efficiency values are found, this is probably due to the presence of higher counting rate due to the presence of the neutron source. Since the analysis was developed to nominally have the same efficiency over all the energy range considered, the efficiency considered to normalize the histogram counts is the mean between the low and high energy ones and their discrepancy was used to evaluate the systematic error on the value considered (which amounts to a few percent). This is not an ideal situation, but due to the lack of calibration lines in the spectrum it was considered to be the best option available. Moreover, it can be noticed that in all the different efficiencies the source dataset has always a slightly lower value that the background one, this is due to the source induced background which causes a higher interaction rate generating pile-ups which lower the data analysis efficiencies since each analysis step discards them.

At this point, it is possible to normalize the background and source energy spectra with the cut efficiency. To be able to compare the two spectra it is necessary to also normalize for the measuring time and the used bin width in the plot, by also considering the detector mass then the spectra in dru (counts/keV/kg/day) are obtained as shown in Figure 4.36, which is the usual unit used in this field. In this unit it is possible to compare the intensity of the iron lines, which should match between the two datasets, to check the consistency of the evaluated efficiency. The efficiency-corrected ^{55}Fe count rate matches within 3% between the *background* and *source* spectra.

4.4 First Detection of nuclear recoils in NUCLEUS

After the definition of all the data analysis procedure, it is possible to unblind the source data and look at the 100 eV region in search for a nuclear recoil peak. From the source spectrum in Figure 4.37 a feature in the counting rate can be seen just above 100 eV. Moreover, an increase in the overall counting rate level with respect to the background dataset is visible and is due to the presence of the neutron source.

To check the significance of the peak candidate, a statistical test was performed. Due to the presence of the unmodelled LEE (see section 2.4.3) a background model could not be made from first principles but an effective double exponential, with

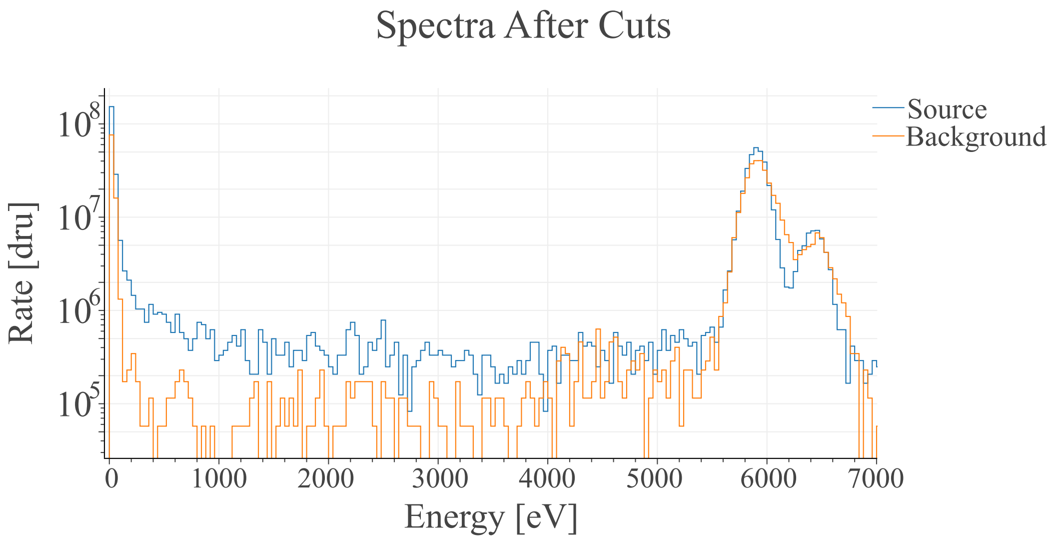

Figure 4.36. Comparison of the energy spectra of the background (orange) and source (blue) datasets after cuts and efficiency normalization. A broadening of the main ^{55}Fe peak is visible in the background data, this is due fluctuations in the working point of the detector. This broadening is estimated to be at the few percent level, therefore it was decided neglect it since it is smaller than the rest of the uncertainties and is present only in the background spectrum.

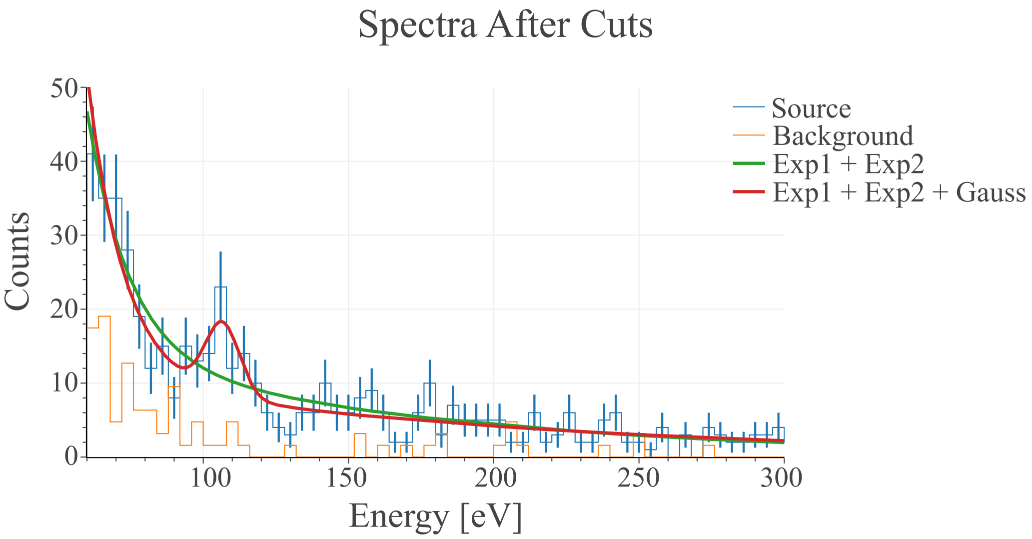

Figure 4.37. Comparison of the energy spectra in the 100 eV region of the background (orange) and source (blue) datasets after cuts. In green the best fit for the background only option is shown, while in red the best fit for peak detection is plotted.

4 free parameters, presented in eq. (4.32) is used. This background model choice is validated by the quality of the agreement between the fit and the data outside the peak region. To model the peak the Gaussian function with 3 free parameters is used, meaning that the total fitting function for the peak detection is a double

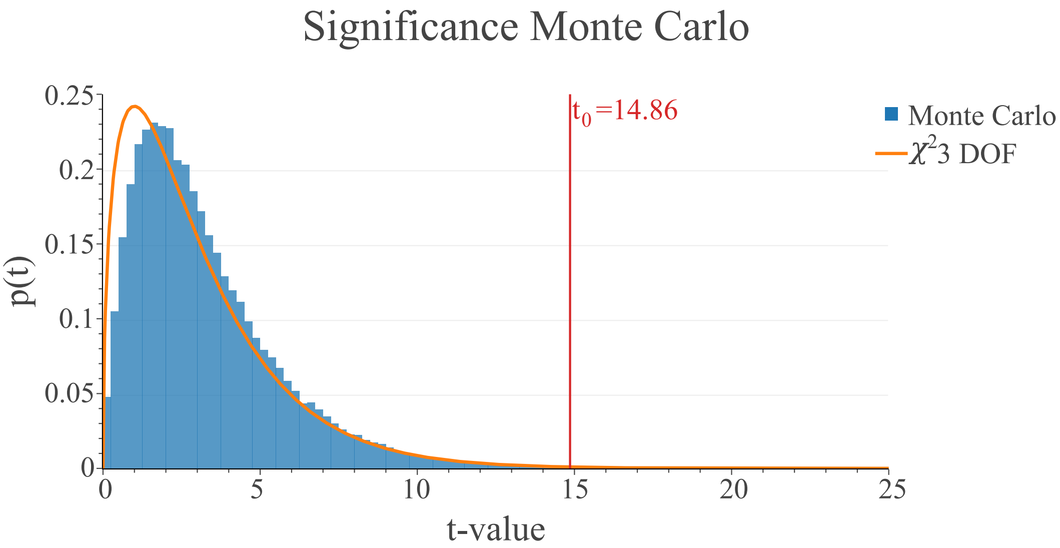

Figure 4.38. Probability density function of the statistical test t performed for the peak search (blue histogram). For comparison, the χ^2 law for 3 degrees of freedom is shown in orange. The t_0 extracted from the likelihood test is shown in red.

exponential plus a Gaussian as in eq. (4.33):

$$f_{bck}(E) = A \cdot e^{s_1 \cdot E} + B \cdot e^{s_2 \cdot E} \tag{4.32}$$

$$f_{bck+sig}(E) = \frac{I}{\sigma\sqrt{2\pi}} e^{-\frac{1}{2}\left(\frac{E-\mu}{\sigma}\right)^2} + f_{bck}(E) \tag{4.33}$$

To perform the test two binned likelihood fits are performed in the energy range from 60 eV to 300 eV, with (Bck+Sig) and without (Bck) the contribution of the Gaussian and all parameters are left free. By evaluating the ratios between the likelihoods $\mathcal{L}$ in the two cases, it is possible to build the following statistical test parameter:

$$t = -2 \ln \left(\frac{\mathcal{L}_{\text{Bck}}}{\mathcal{L}_{\text{Bck+Sig}}} \right) \tag{4.34}$$

which is expected to be distributed as a 3 degrees of freedom χ^2 distribution. To check this hypothesis, a Monte Carlo distribution of the t-values is obtained by generating a large sample of pseudo-experiments, which are randomly drawn statistical realizations of the background model. For each realization, the two likelihood fits are performed, giving the distribution shown in Figure 4.38. As it can be seen by the distribution, it slightly deviates from the expected 3 degrees of freedom χ^2 distribution. Due to the small deviation from expectation, the numerically computed distribution is chosen to evaluate the significance instead of the expected χ^2 law for 3 degrees of freedom.

The fits performed and shown in Figure 4.37 yield the parameters presented in Table 4.10 and a t-value of $t_0 = 14.86$, meaning that the probability to obtain a

Table 4.10. Results of the two likelihood fits for the identification of the peak significance.

	Background (Bck)	Background + Peak (Bck+Sig)
$A\ \left[\frac{10^2}{4\ \text{eV}}\right]$	9.3 ± 1.1	34 ± 4
s_1 [eV^{-1}]	-0.056 ± 0.002	-0.074 ± 0.002
$B\ \left[\frac{1}{4\ \text{eV}}\right]$	18.1 ± 1.1	13.3 ± 0.9
s_2 [eV^{-1}]	-0.0072 ± 0.0004	-0.0058 ± 0.0004
I [counts]	-	36.8 ± 9.7
μ [eV]	-	106.7 ± 2.0
σ [eV]	-	6.0 ± 1.5

t-value larger than t_0 from purely statistical fluctuations is only 0.0018, giving a significance of the presence of the calibration peak in the data at the 3.1σ level (2-sided). The fit was performed on an energy spectrum presented in counts in order to avoid the efficiency correction due to the fragility of their evaluation procedure. Anyhow, correcting for the detector efficiency, the ratio of the measured to predicted number of events in the peak is 0.70 ± 0.29.

The same principle of the statistical test can also be applied to the full recoil spectrum induced by neutron captures to measure the significance on top of the expected backgrounds. To do such a test, a *background* model is needed and was built by summing the ambient background component taken from the *background* dataset and the simulated source related background which is induced by the scattering of the fast neutrons from the source. The simulated background was obtained with a Geant4 simulation, and the ambient background was obtained by fitting an exponential plus a constant offset to the background dataset. To generate a model of the presence of the nuclear recoil peak induced by neutron capture, the simulated detector response to this process is added to the previous background model.

When fitting the models to the data, the ambient background contribution is always kept fixed while two independent normalization factors K_{Bck} and K_{Sig} are applied to the simulated background and signal-only spectra respectively. Aside from the normalization factors both models have a parameter α that accounts for a linear rescaling of the energy calibration, which for a correct calibration is expected to be 1, and a σ_0 parameter encoding the effect of the finite detector resolution, and is thus expected to be similar to the measured resolution and to the width obtained for the peak from the previous fit. Due to the nature of this fit, the t-value is not obtained from the likelihoods but from the difference of the two χ^2 values of the fit.

The Monte Carlo distribution of the t-values for this test is obtained by generating pseudo experiments from the background only model, as it was done previously, and is shown in Figure 4.39. Since the signal contribution is modelled only with the single extra parameter K_{Sig} the distribution is then expected to follow a 1 degree of freedom χ^2 law. As for the previous test, a small deviation from expectation is measured, where by comparison it can be seen that the degrees of freedom of the Monte Carlo distribution are between 1 and 2.

The results coming from the fitting of the two models are shown in Table 4.11 and

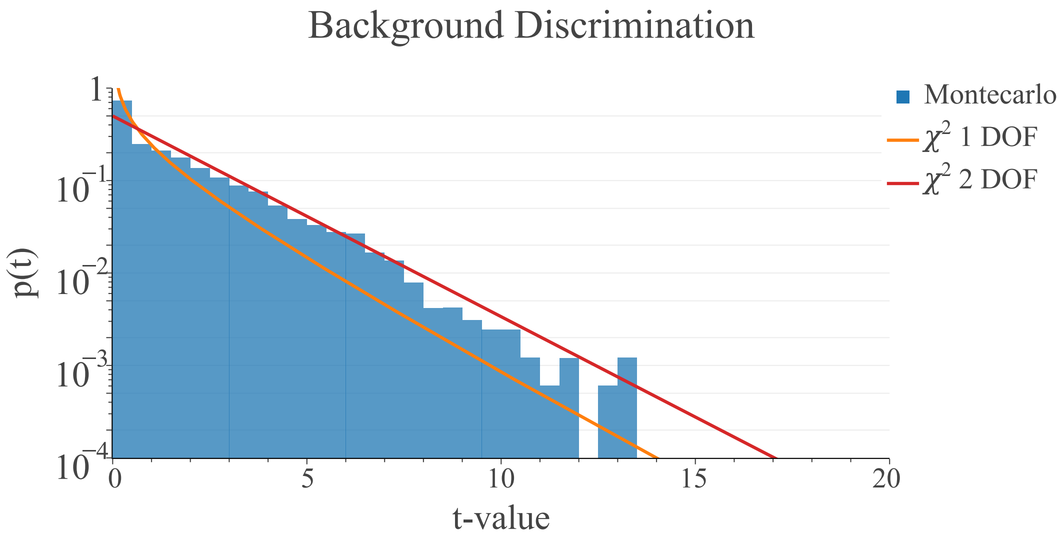

Figure 4.39. Probability density function of the statistical test t performed for the background to signal comparison. For comparison, the χ^2 law for 1 and 2 degrees of freedom are shown in respectively orange and red.

Table 4.11. Results of the two fits performed to test the existence of the recoils induced by neutron captures.

Parameters	Background (Bck)	Background + Peak (Bck+Sig)
α	1.017 ±0.031	0.946 ±0.014
σ_0 [eV]	5.970 ±0.501	6.004 ±0.465
K_{Bkg}	1.039 ±0.062	0.702 ±0.082
K_{Sig}	-	0.739 ±0.144
χ^2	100.39	58.08
degrees of freedom	60	59

yield a t-value of $t_1 = 42.3$. Due to the extremely high t-value, it is quite costly, computation wise, to generate a statistically significant Monte Carlo distribution up to such values. For this reason, to perform the statistical test, the conservative hypothesis of a 2 degrees of freedom χ^2 distribution was taken. This choice yields a more than 6σ significance to the measured contribution of the recoils induced by neutron capture.

Summarizing, the nuclear recoil peak induced by nuclear de-exitation following neutron capture was observed at the expected energy (within uncertainties) with a 3σ significance with a deviation from the background only hypothesis of more than 6σ. This detection is an important milestone for the experiment, since it proves the signal equivalence between nuclear and electron recoils, and was a collaboration-wide effort and the data analysis described here was the main contribution given in the context of this work. Moreover, it is a direct proof of the capability of this technology and experiment to probe the nuclear recoils produced by reactor neutrinos. Following the publication [89] also the CRESST experiment [93], a dark matter experiment with similar calorimetric technology, has reported the same finding with an increased statistics reaching the 6σ significance.

Chapter 5

NUCLEUS Commissioning at TUM

The NUCLEUS collaboration tested the interplay of the various experimental systems developed by commissioning them at the Technische Universität München (TUM). The aim of this pre-reactor phase is to demonstrate the ability of having good and stable operation conditions of the *cryocubes* while simultaneously running the muon veto and the COV. Since satisfying detector performances had been reached, a long (few weeks) data taking were conducted to assess the background level affecting the experiment. The goal of this data taking is to evaluate the current background level and, more importantly, to assess the ability of reproducing the background with simulations. For this reason, particular attention was given to implement the complete commissioning setup and location in a Geant4 simulation in order to accurately predict the expected counting rate measured in the various detectors.

In this chapter, the commissioning of the experiment is briefly described and the data coming from this long acquisition is analyzed, providing evaluations of the background.

5.1 Experimental Setup

With respect to setup used for the nuclear recoil calibration (see section 4.1.2) the experimental layout described in this section is much more similar to the final one planned for the first phase of NUCLEUS. Inside the cryostat vessels the installation of all the SQUIDs, the mounting of the final vibrational decoupling system along with the whole set of cryogenic shields and muon veto (as visible from left panel of Figure 5.1) and the installation of optical fibers was conducted. Simultaneously, the shields and muon veto surrounding the cryostat were also mounted and tested. At the coldest stage of the cryostat and suspended via the vibrational decoupling system, a single COV crystal was installed along with two *cryocubes* respectively $CaWO_4$ and Al_2O_3. A peculiarity of the installed Al_2O_3 cryocube is that it is instrumented with two TESs, meaning that it is possible to have a double readout of the energy deposition in the crystal. This type of detector was already mentioned

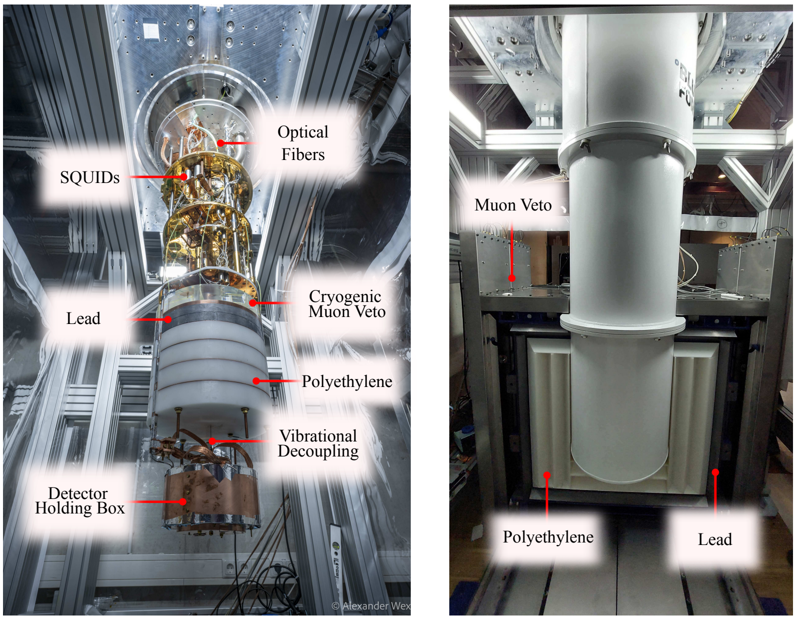

Figure 5.1. Commissioning setup: on the left the inside of the cryostat is shown highlighting the SQUIDs, the cryogenic muon veto, the lead and the polyethylene, the end of the vibrational decoupling system, the optical fibers and the detector box (which holds the *cryocubes* and the COV crystal). On the right, the room temperature part of the shields and the muon veto are shown. In the right panel only half of the shield is show in its opened configuration to highlight the various layers present.

in section 2.4.3 and is referred to as *double TES* module.

With this setup, it was possible to use the LANTERN electronics to conduct the optical calibration of the detectors. Moreover, it was possible to test and develop the coincidence analysis of the cryodetectors with their vetoes.

When comparing the setup just described (see Figure 5.1) with the one planned NUCLEUS phase 1 (see Figure 5.2) it is clear that the two setups are quite similar but with the following key elements missing: the B_4C Becker, the inner veto and the mirror wafer. Moreover, only one of the six COV crystals are installed, meaning that it is impossible to efficiently veto the γ background component. Due to the absence of the inner veto, which is the mounting structure of the cryocubes, only two of the 18 target detectors are installed, so the full detector mass of the experiment is not reached. The cryocubes are instead mounted in copper shields placed inside the detector holding box visible in Figure 5.1.

To compensate for the lack of the full COV, the setup was commissioned in the Underground Laboratory(UGL) which provides 15 m.w.e. of shielding. Moreover, all the components inside the cryostat that are placed near the *cryocubes* have been thoroughly cleaned in order to eliminate as many radioactive impurities as possible and ensure optimal thermalization.

The typical cooldown time of the cryostat with only the *cryocubes* is of 2 days but from the beginning of the cooldown cycle of the setup, the system took 12 days to

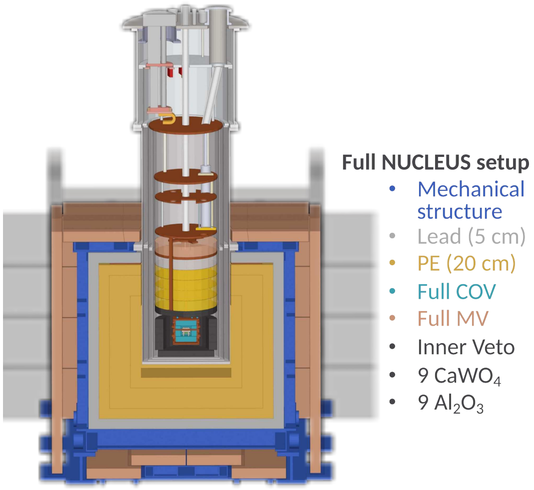

Figure 5.2. Diagram of the full NUCLEUS setup planned for the first phase of the experiment. The diagram is discussed in chapter 2 and shown here as comparison.

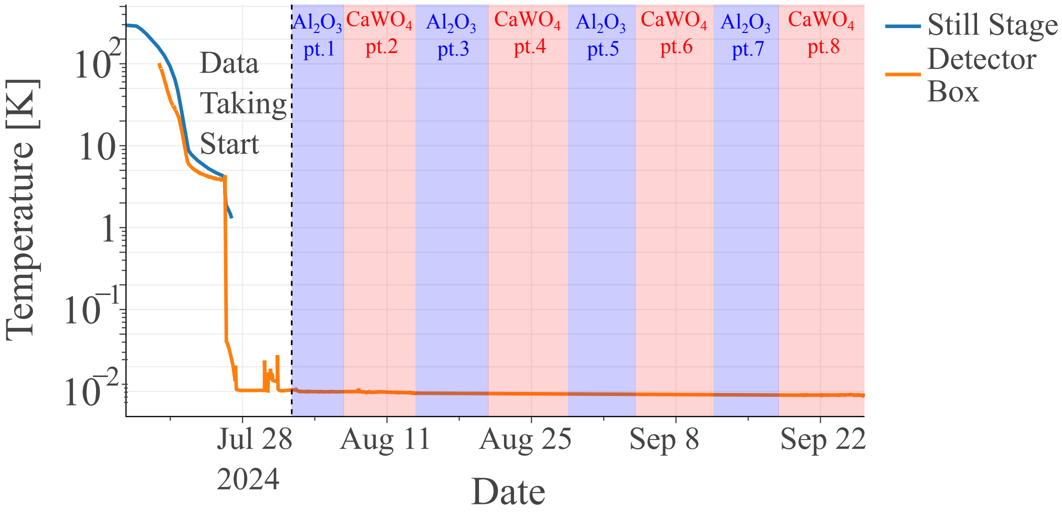

Figure 5.3. Plot of the temperature of the cryostat as a function of time. In blue, the temperature of the still stage of the cryostat is presented. It stops when the thermometer is under calibration range. In orange the temperature of the detector box is shown, the line starts with a temporal offset with respect to the blue since at high temperatures the thermometer is above the calibrated range. The vertical black dotted line indicates the beginning of the data taking, while in the colored bands the periods of data taken with the two *cryocubes* are highlighted in blue and red for respectively the Al$_2$O$_3$ and CaWO$_4$ detectors.

reach the base temperature, as shown in Figure 5.3. This increase in the cooldown time is due to the much higher mass, mostly given from the cryogenic shields and muon veto, that has to reach temperatures below 4 K.

5.2 Expected Background From Simulations

Before the start of the data taking, some preliminary Geant4 simulations were performed to predict the expected counting rate measured in the various detectors. The results from these simulations are here described and are later compared to the analysis results. More detailed simulations will follow in other studies presented by the collaboration.

The expected counting rates of *cryocubes* when deployed in the commissioning setup, with and without the anticoincidence cut with the vetoes, are shown in Figure 5.4. From the last two panels of Figure 5.4 it is possible to notice that due to the incomplete geometry of the COV an anticoincidence cut with this detector has only a $\sim 5\%$ efficacy in reducing the counting rate on the *cryocubes*. For this reason, using the COV is mainly a test of the hardware setup and does not produce any significant result when used as a veto.

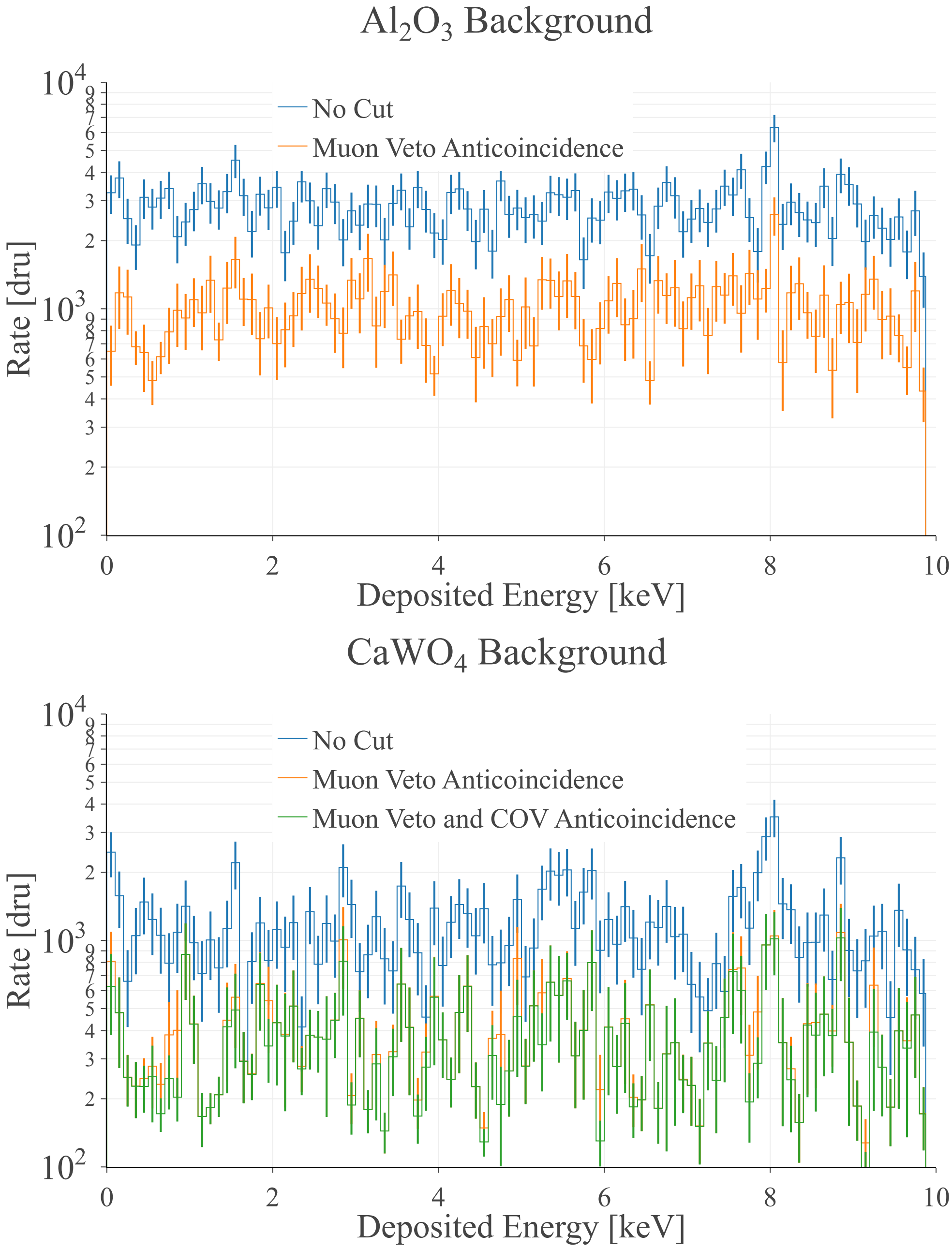

Figure 5.4. Simulated counting rate of the Al_2O_3 (top) and $CaWO_4$ (bottom) detectors. The colors indicate the type of vetoing cut applied: in blue the direct counting rate of the detectors are plotted, in orange the rate after the application of the muon veto cut and in green the application of the muon veto cut in combination with the COV anticoincidence (only for the $CaWO_4$ detector). The most noticeable feature for both detectors is a peak at around 8 keV which is due to the K_α X-ray copper line (material that surrounds both detectors).

5.3 Data Taking Strategy

In the commissioning setup, two different DAQ systems are employed: the cryodetector DAQ, used for the *cryocubes* and the COV crystal, and the muon veto DAQ, which is synchronized with the first one. The current version of the cryodetector DAQ is limited to a maximum of two acquisition channels. This limitation gives rise to the need of creating the two following data taking detector groupings:

1. Al_2O_3 *cryocube* (*double TES*) and muon veto;
2. $CaWO_4$ *cryocube*, muon veto and the COV crystal.

The Al_2O_3 detector cannot be readout at the same time as the COV since it requires both DAQ channels due to the double readout, but the absence of the COV is not a problem from a background estimation point of view due to the limited coverage(see section 5.2). In the future, the current DAQ system will be upgraded to its next version containing all the necessary acquisition channels to readout all the detectors simultaneously.

The two groupings are alternated with a weekly period during the data taking. At the beginning and ending of each acquisition period (also referred to as configuration) an optical calibration is performed to check the detector performances, as visible from the diagram in Figure 5.5. The total number of hours of analyzable data acquired is 1135 h (572 h on Al_2O_3 and 563 h on $CaWO_4$), meaning about a 10% dead time in the data collection. The dead time is mainly due to three reasons: human errors during the setting of the two DAQs, problems with the synchronization of the acquisition electronics and detector calibrations.

The signals coming from the muon veto panels are acquired with a 125 MHz sampling frequency and are automatically preprocessed from the DAQ to extract the amplitude of the signals. Moreover, the signals incoming from the various panels are automatically combined, meaning that when a muon deposits energy in the veto the DAQ produces a single event with the time of the trigger and the amplitude registered on all panels. The *cryocubes* and the COV are acquired with the same format as described in chapter 4 using sampling frequencies of: 100 kHz for the COV, 50 kHz for both TESs of the Al_2O_3, cryodetector and 10 kHz for the $CaWO_4$ cryocube.

The LANTERN system was used to perform all of the optical calibrations on both cryocubes. Aside from the calibration data, this optical calibration hardware was used to generate pulses from the triggering threshold to detector saturation, allowing for a full characterization of analysis and its efficiencies.

5.4 TES waveform analysis

In this section, the analysis of the data acquired with the Al_2O_3 *double TES* detector is described. In section 5.5 the combination of the TES data with the muon veto and the consequent anticoincidence study is performed.

The Al_2O_3 *double TES* module was chosen as the main focus for this analysis since

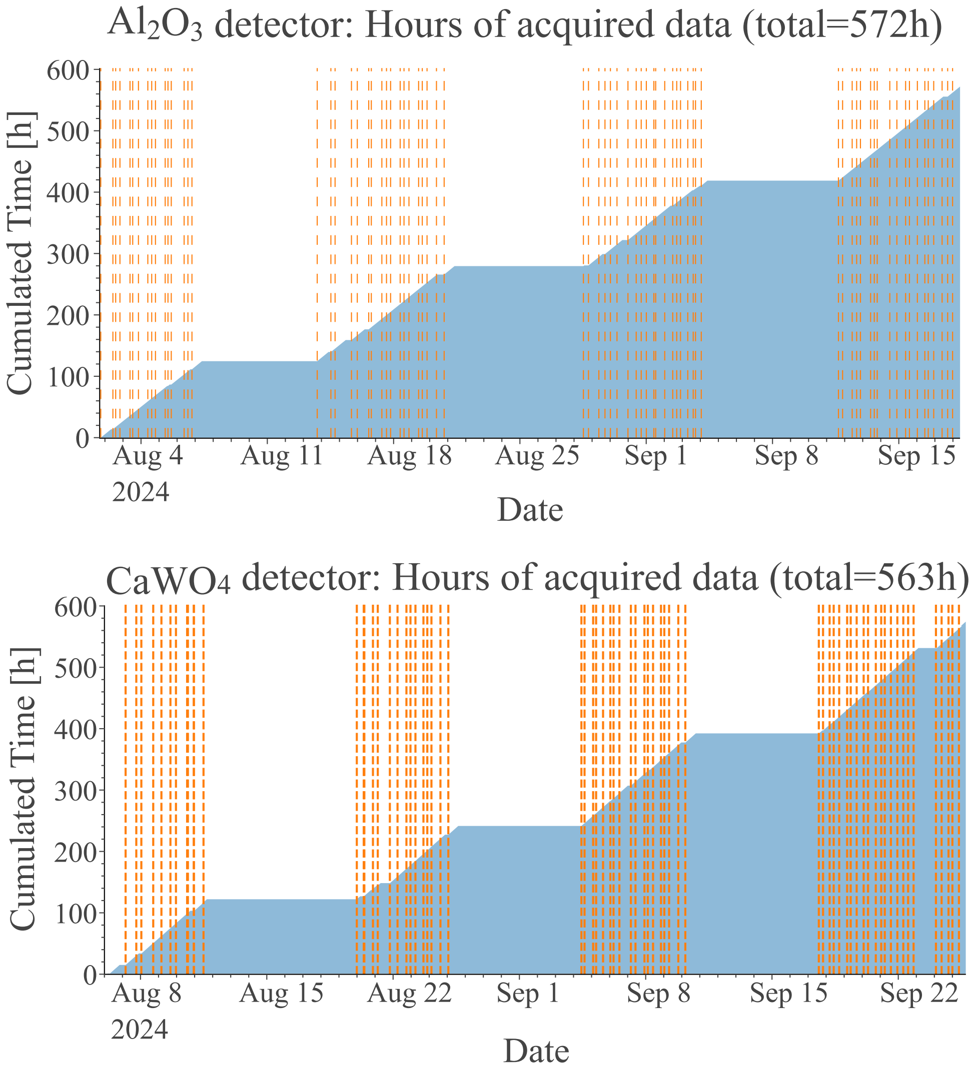

Figure 5.5. Diagram of the data taking for both the Al_2O_3 (top) and $CaWO_4$ (bottom) detectors. The plot shows the amount of hours of data acquired during the commissioning run (blue), with the orange dashed lines the beginning of each file acquired during the run is highlighted.

it allows to develop and test a multi-sensor analysis (which can later be fine-tuned to the needs of the final NUCLEUS setup). The double readout, which the $CaWO_4$ *cryocube* does not have, makes the *double TES* particularly suitable for studies of both the background at the few keV scale and in the region of the Low Energy Excess (LEE).

The analysis here performed on the TES signals highly relies on the procedures described in chapter 4, but two additional steps are added. The first one is to use the double readout of the signal as described in section 5.4.5 to classify background events. The second step is to add an additional triggering algorithm to the ones already presented in chapter 4 used to study the rate of false positive triggers due to noise fluctuations. This trigger algorithm uses the exact same procedure as the signal (or self-triggering) one, but the data stream being processed is mirrored (i.e. the pulses are now facing downward) by changing the sign of the recorded voltage. The reason of this is that the noise is expected to have zero average amplitude, so statistically there are as many upward noise fluctuations as the downward ones, and by mirroring the data stream it is possible to study the behavior of the analysis on downward noise fluctuations (i.e. without being affected by the presence of small pulses). Thus, by assuming that the analysis protocol produces the same results on the upward and downward noise fluctuations, it is possible to characterize the presence of false positives in the final results of the analysis.

For the rest of this chapter, the two TESs present on the Al_2O_3 detector will be referred to as "TES 1" and "TES 2" and the mirrored false positive waveforms are dubbed as *reversed*.

5.4.1 Optical Calibration and Matched Filter

As mentioned, at the beginning of each data taking week (or configuration) an optical calibration was performed. This data was used to study the characteristics of the detector while simultaneously building the signal template and average NPSD as described in sections 4.2.3.2 and 4.2.3.3 which are then used to build the matched filter (see section 4.2.3). Building the matched filter from the optical calibration data is a requirement for this analysis, since the setup is deployed in a low background environment and there are very few high SNR particle pulses that can be used to build the signal template.

The filter built from the initial calibration of the week is then used to trigger and analyze the data taken during the configuration. At the end of the data taking week, a second optical calibration is performed and analyzed with the same matched filter. This is done to check whether the detector characteristics have changed throughout the week.

The first calibration of the first configuration is here described in detail as an example and in section 5.4.1.1 a summary of the results from all the performed calibrations is presented.

A typical pulse coming from the Al_2O_3 detector has a duration of 20 ms (which corresponds to the length of the used acquisition window), with a rise time of $\sim 50\ \mu$s, as visible from the left panel of Figure 5.6. To perform the optical calibration successfully, it is required that the duration of the LED pulses is at most an order of magnitude less than the rise time of the detector. For this reason, an LED triggering frequency of 3 MHz was chosen since it allows to have enough granularity when probing the energy spectrum. To be able to save clean noise samples between the LED pulses a minimum LED rate of 1 Hz was set, meaning that two LED triggers are 50 acquisition windows distant. Being able to trigger unpolluted noise traces is a requirement to correctly build the NPSD used for the matched filtering.

The generation of the pulses for the optical calibration is done using the single

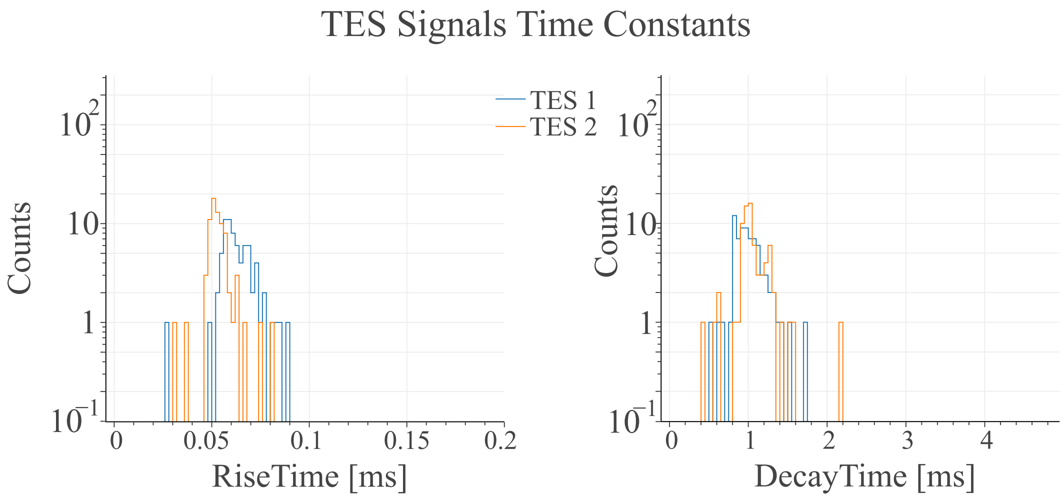

Figure 5.6. Histograms of the rise (left) and decay (right) time constants of the signals coming from the two TESs of the Al_2O_3 cryodetector (TES 1 and TES 2 are respectively shown in blue and orange). The histogram is made considering particle pulses with SNR between 50 and 300 acquired during the first week of data taking.

Table 5.1. Effect of the matched filtering on the noise RMS. The noise reduction factor is defined as the ratio of the noise RMS before and after filtering.

Sensor	Noise RMS[mV]	Filtered Noise RMS[mV]	Noise Reduction Factor
TES 1	8.4	3.3	2.5
TES 2	5.3	2.2	2.4

LANTERN driver, described in section 3.3.2, coupled with an LED emitting photons at 255 nm (corresponding to 4.86 eV). During the analysis of the LED induced pulses, it is imperative to be able to efficiently discriminate them from the rest of the signals present (much like the heater pulses in chapter 4). For this reason, the LED trigger signal is sent simultaneously to LANTERN and to the cryodetector DAQ systems to be saved in the acquisition file as an independent TTL channel. The identification of the LED induced pulses in the TESs data streams is performed in the exact same way as for the heater signals described in section 4.2.1.1, meaning that a threshold triggering is applied to the noiseless TTL LED trigger data stream saved in the file.

By averaging together several LED pulses it is possible to build the signal template required for the matched filter. The templates for both TESs are shown in the top panel of Figure 5.7, while in the bottom panel the average noise power spectra of the two sensors are plotted before and after filtering. As visible from the expected noise RMS values in Table 5.1, taken from the integral of the NPSD, a factor ~ 2.5 improvement in the SNR of the amplitude reconstruction is achieved by filtering.

To perform the detector calibration, 12 different LED pulses distributions were acquired spanning the whole linear range of the detector, which goes from ~ 30 eV to ~ 4 keV as will be discussed in the next sections. Once the amplitudes of the LED pulses are estimated using the same matched filtering plus peak search combination

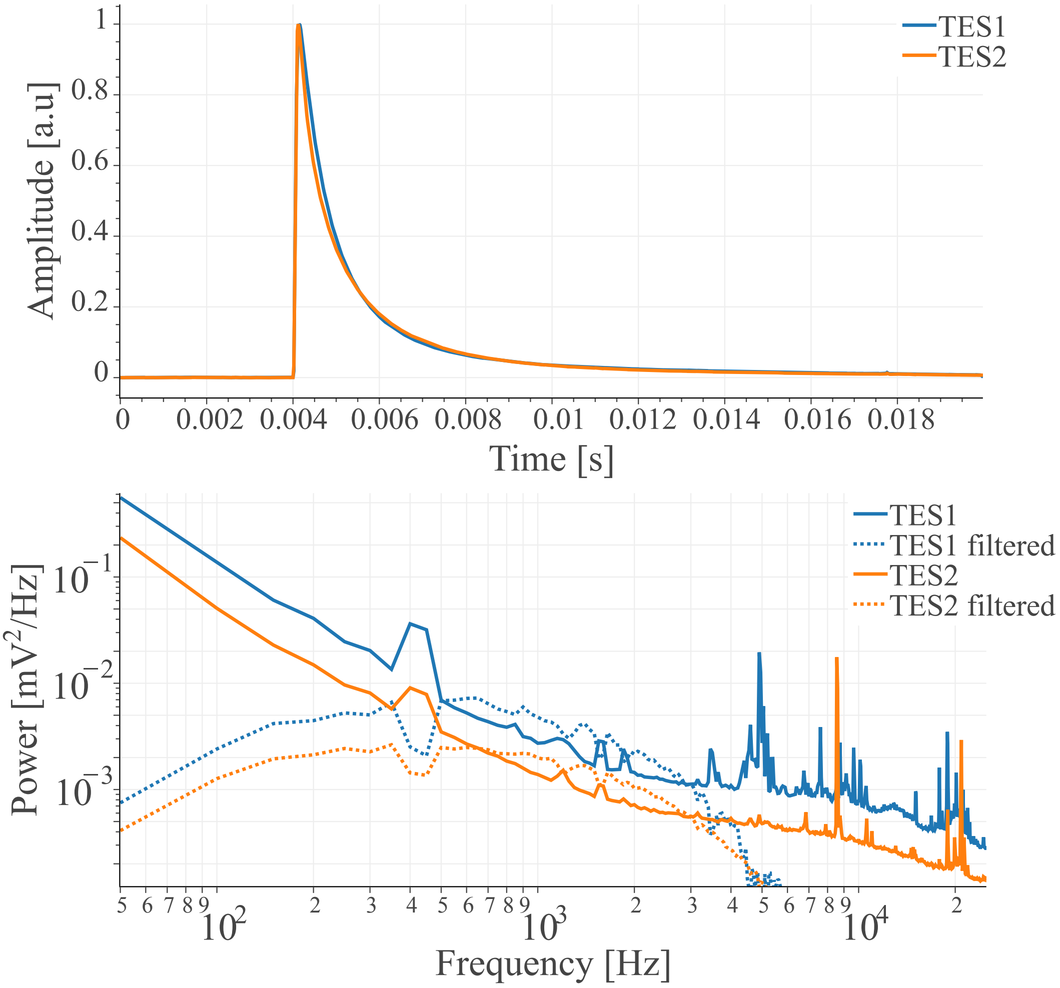

Figure 5.7. In the top panel the signal templates extracted by averaging the LED pulses of the first optical calibration is shown for both TESs. In the bottom panel the average NPSD is shown for the two TESs before (solid lines) and after (dashed lines) filtering.

as described in section 4.2.3, their distributions can be plotted and fitted with a Gaussian model as presented in section 3.1. This is done to extract their mean and standard deviation, which are required to perform the calibration. The amplitude distributions and their fits are shown in Figure 5.8 for both TESs, while the optical calibration is shown in Figure 5.9. From both plots, good agreement between the data and the fitting models can be seen, the main deviation is due to the lowest energy deposition in which the asymmetry of the Poisson distribution is starting to be noticeable.

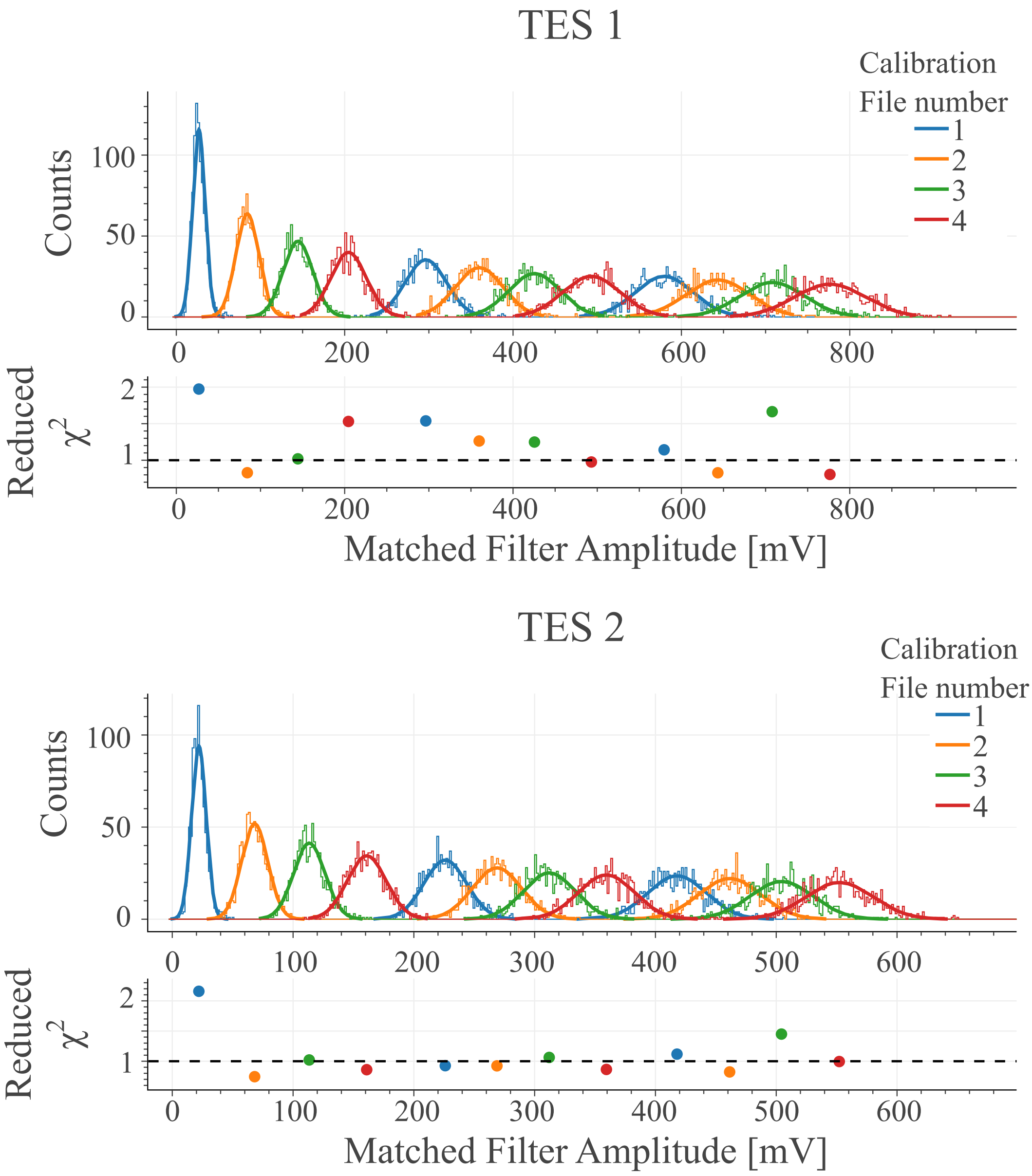

Figure 5.8. Gaussian fit of the distribution of the LED amplitudes for both TES 1 (top) and TES 2 (bottom). The colors indicate the various calibration files acquired, each file has 3 equally spaced distributions.

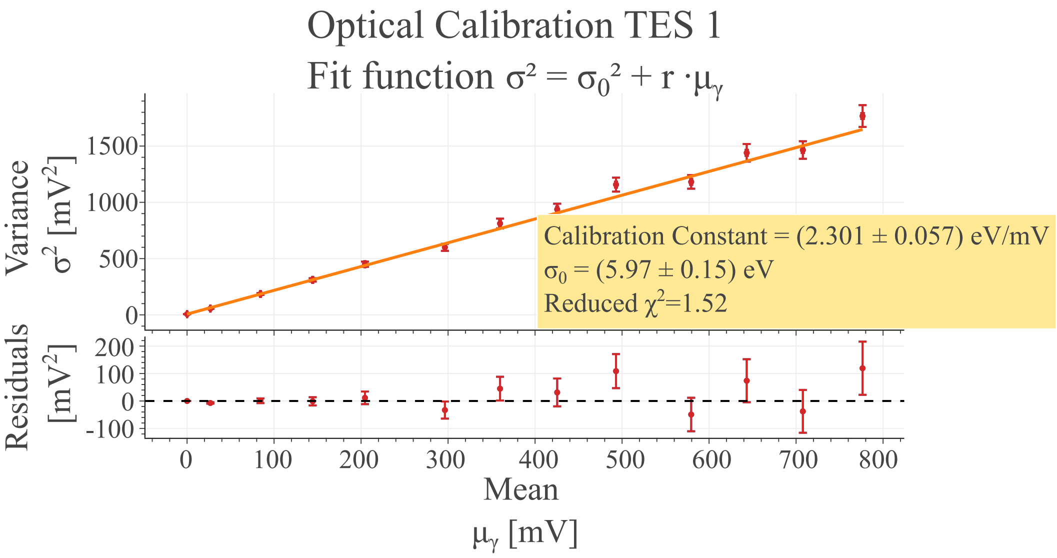

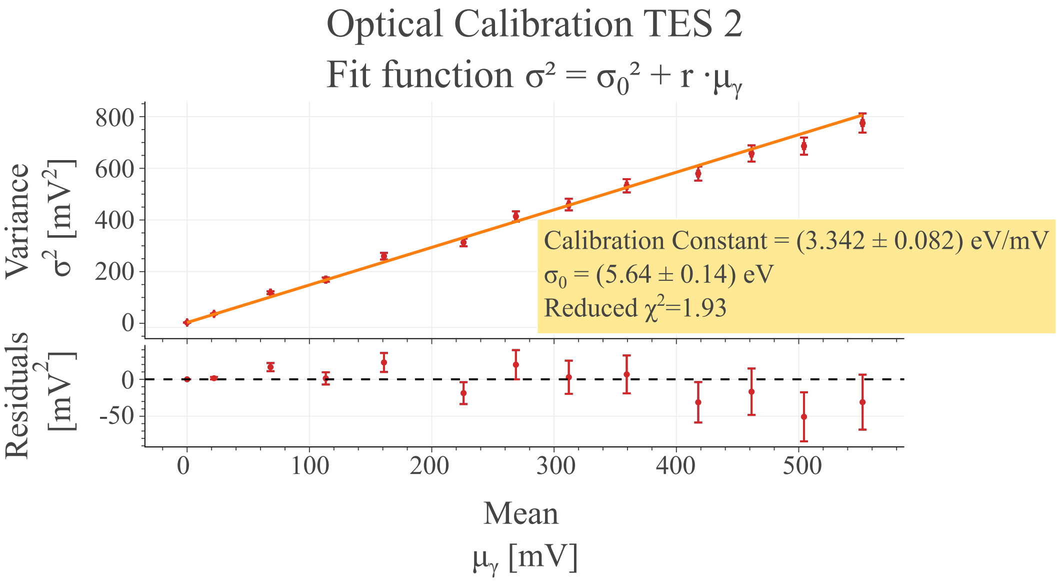

Figure 5.9. Plot of the variance versus the mean of the amplitude distributions of the LED pulses for both sensors (TES 1 in the top panel and TES 2 in the bottom panel). For both detectors, the optical calibration fit is shown in orange. In the inset of the plots, the calibration constant (extracted by diving the single photon energy by the fitted value of the "r" parameter) is shown along with the noise resolution σ_0 converted to electronvolts. The error bars presented are the 1σ statistical fluctuations extracted from the Gaussian best fit errors.

As visible from Figure 5.9 a point with an average amplitude around 0 mV is present in for both sensors, this point describes the distribution given by the noise present in the detector. In fact, the matched filter allows for the estimation of the amplitude of noise traces (which fluctuates around zero with a standard deviation equal to the filtered noise RMS) as described in chapter 4. By generating the histogram of the noise amplitudes, it is possible to perform the same Gaussian fit as for the LEDs in

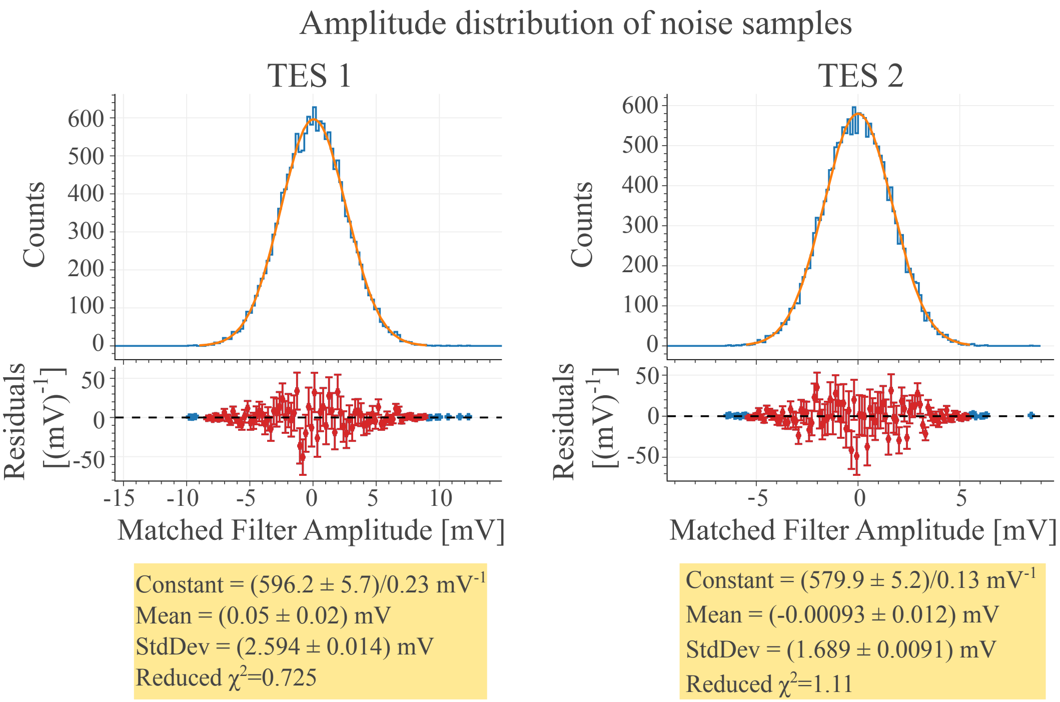

Figure 5.10. Gaussian fit of the noise distributions for TES 1 (left) and TES 2 (right). The best fit values are reported in the orange panels below the plots.

order to estimate directly the mean and variance of the noise distribution, allowing for a direct estimation of the detector's noise resolution. This point is important for the optical calibration fit since it gives a strong constraint on the σ_0^2 parameter present in the calibration function. The Gaussian fits of the noise distributions of the two sensors are shown in Figure 5.10.

As described in section 3.1.1, the non-linearity affecting the signals coming from the two TESs can be estimated by studying the scaling of the average mean amplitude of the LED distributions with the number of cycles n_c (which is linearly proportional to the deposited energy). In Figure 5.11 the best fits for the non-linearity estimation on both TESs are shown, from the estimated parameters a maximum non-linearity of around 20% affects the data (this is obtained by multiplying the "b" parameter from the fits shown in Figure 5.11 with the maximum amplitude reconstructed for the corresponding sensor visible from Figure 5.12). Moreover, during the data taking the LANTERN electronics was damaged making it highly non-linear (anticipating section 5.4.1.1) and an estimation of the detector non-linearity was impossible during half of the data taking (the damage probably occurred when supplying a wrong bias voltage to the board, this issue is already addressed in the multiplexed board presented in chapter 3). Due to this reason and the fact that no peak is expected to be measured in the data, it was decided, for simplicity, to not proceed with the linearization procedure.

Finally, an estimation of possible detector effects on the calibration was estimated following the procedure in section 3.1.2. From the best fits shown in Figure 5.13

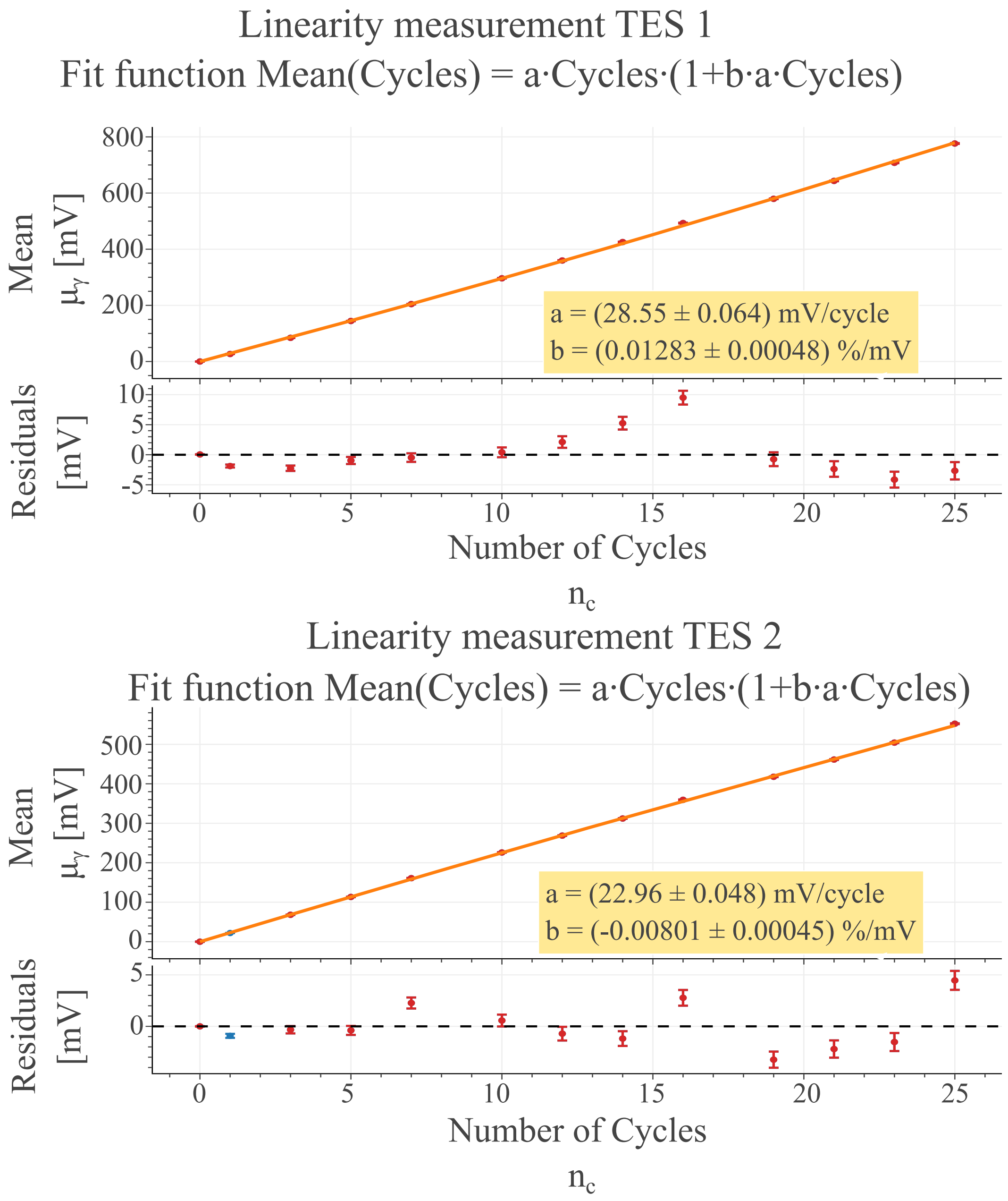

Figure 5.11. Fits of the amplitude non-linearity performed for both TES 1 (top) and TES 2 (bottom). The best fit values are shown in the inset of the plots. The error bars presented are the 1σ statistical fluctuations extracted from the Gaussian best fit errors.

it is visible that these effects (modeled with the presence of the w parameter) are negligible and compatible with zero in less than 3σ. For this reason, these effects have been disregarded in the following analysis. This is also a further proof that the TESs are probably more linear than what estimated in Figure 5.11, since a high non-linearity would produce non-negligible values of w.

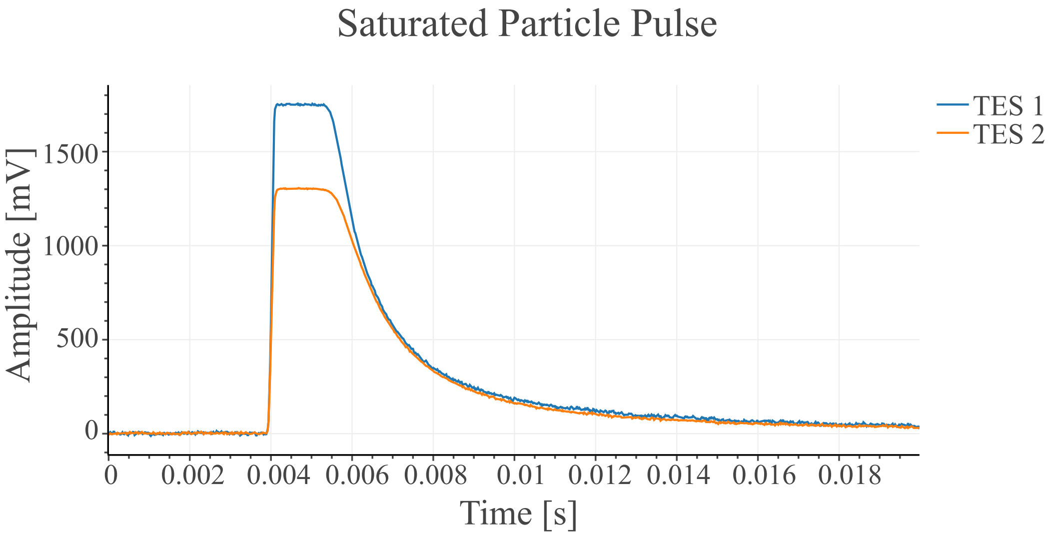

Figure 5.12. Example of an energy deposition for a muon hitting the Al_2O_3 substrate and generating two saturated pulses on TES 1 (blue) and TES 2 (orange) respectively.

Now that the detector is characterized, it is possible to study what is the dynamic range of the two TESs by converting their saturation voltage in the equivalent energy. From the saturated pulses shown in Figure 5.12 it is visible that TES 1 and TES 2 saturate respectively at $\sim$ 1750 mV and $\sim$ 1300 mV. Multiplying these values by the relative calibration constants (which are presented in Figure 5.9) gives a maximum detectable energy of around 4 keV for both TESs, making the Al_2O_3 detector mostly suitable for low energy studies.

As a useful exercise in Figure 5.14 is plotted the NEP for the two TESs. From the plot it is visible that the spectral components between 100 Hz and 3 kHz have the lowest noise-to-signal ratio (i.e. lowest NEP) and thus are the ones that influence more the matched filtering. From the rise of the NEP at low frequency one can conclude that very little signal tails are present in the acquired noise traces (a constant NEP means that the NPSD has the same spectral shape as the signals, while a varying NEP means that the signal contributions to the NPSD are negligible with respect to other noise sources). This could be due to the low background environment (i.e. lower interaction rate) and to the fact that the signals of the *double TES* module are an order of magnitude faster with respect to the cryodetector used in the analysis presented in chapter 4.

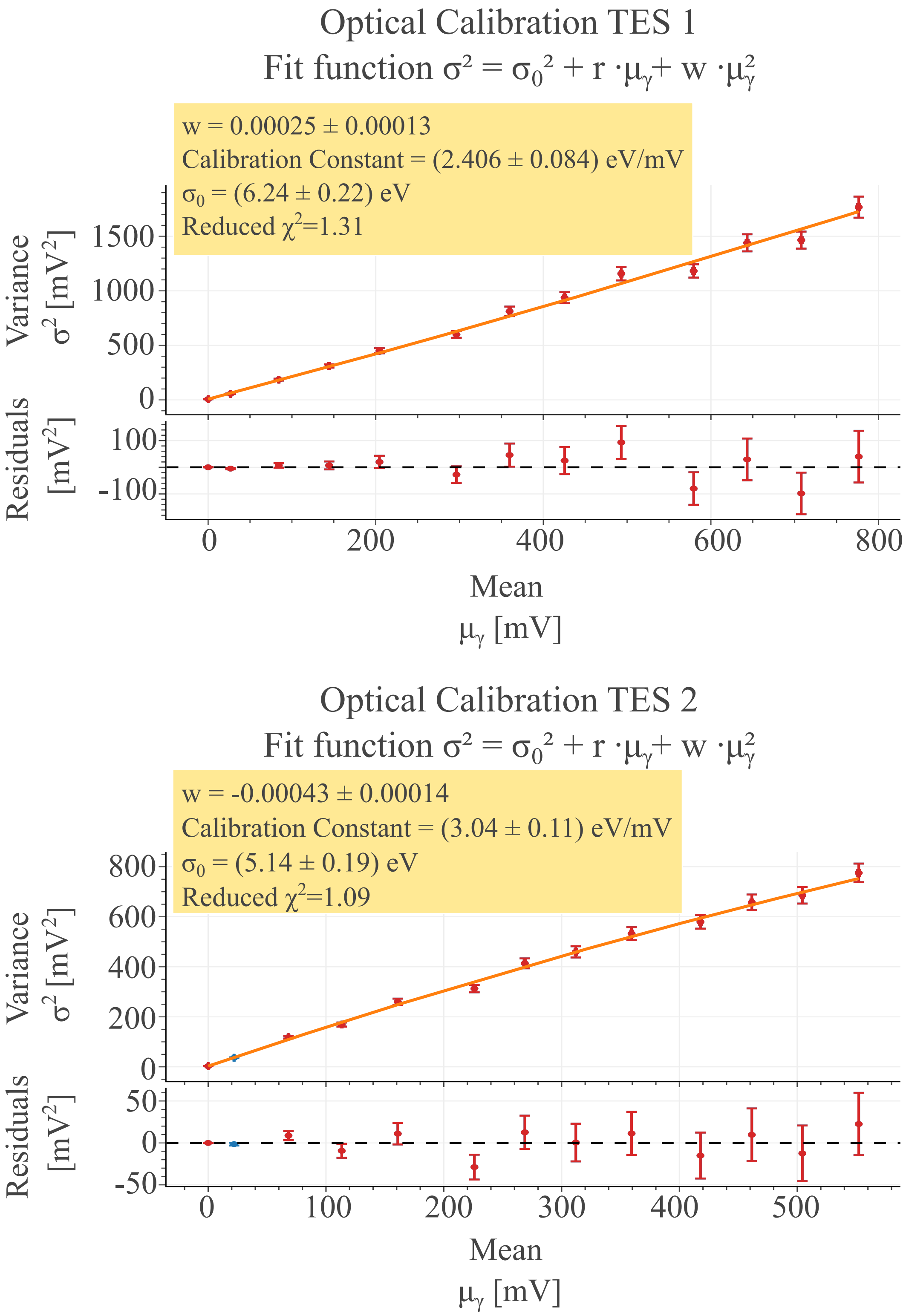

Figure 5.13. Optical calibration fit, including the w parameter which encodes possible detector effects (see section 3.1.2). The calibration constant and the baseline resolution σ_0 are extracted from the best fit parameters in the same was as was done in Figure 5.9. The error bars represent the 1σ statistical fluctuations on the mean and variance as extracted from the Gaussian fitting procedure.

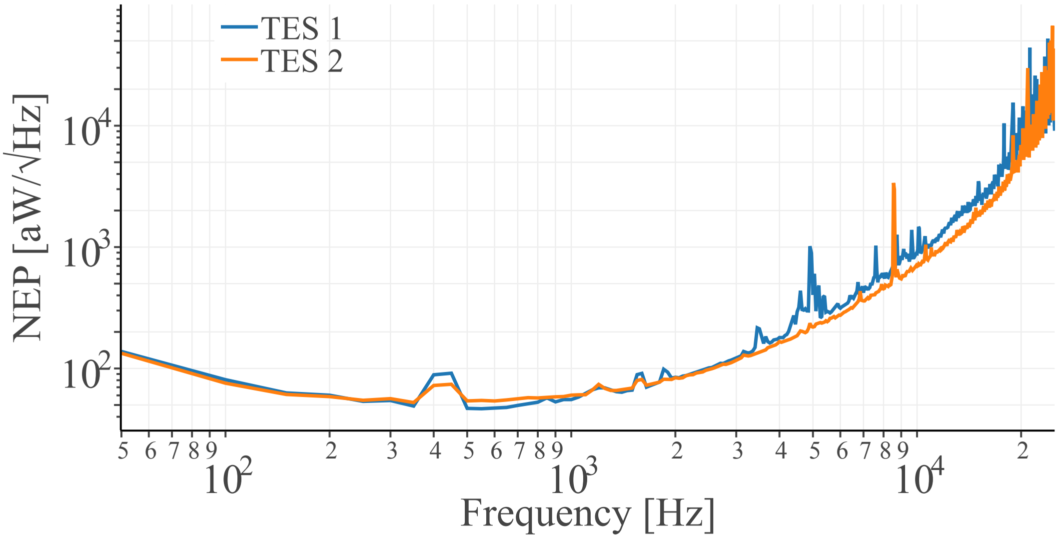

Figure 5.14. NEP evaluated for the two TESs present on the Al_2O_3 detector.

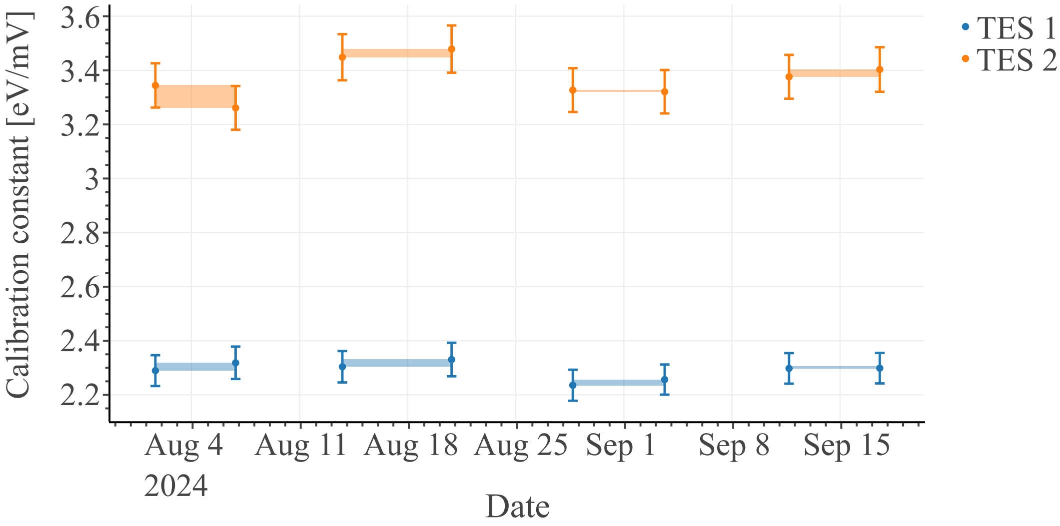

Figure 5.15. Summary of the evolution of the calibration constant of the two TESs present on the Al_2O_3 *cryocube*. The corresponding initial and final optical calibrations of each week are associated by a colored area in between the points. The height of the colored area indicates the difference between the calibration constants, while the error bars are the 1σ statistical fluctuations. From the scatter plot, it is clearly visible that all the calibrations performed produced compatible results.

5.4.1.1 Optical Calibration overview

The above calibration was described as an example to show the procedure employed in this data analysis. Since several calibrations, two for each data taking week, have been performed, a summary of their results are here presented. In Figure 5.15 a scatter plot with all the estimated calibration constants of the two TESs are shown, and it is visible that during the data taking the detector had a stable working condition.

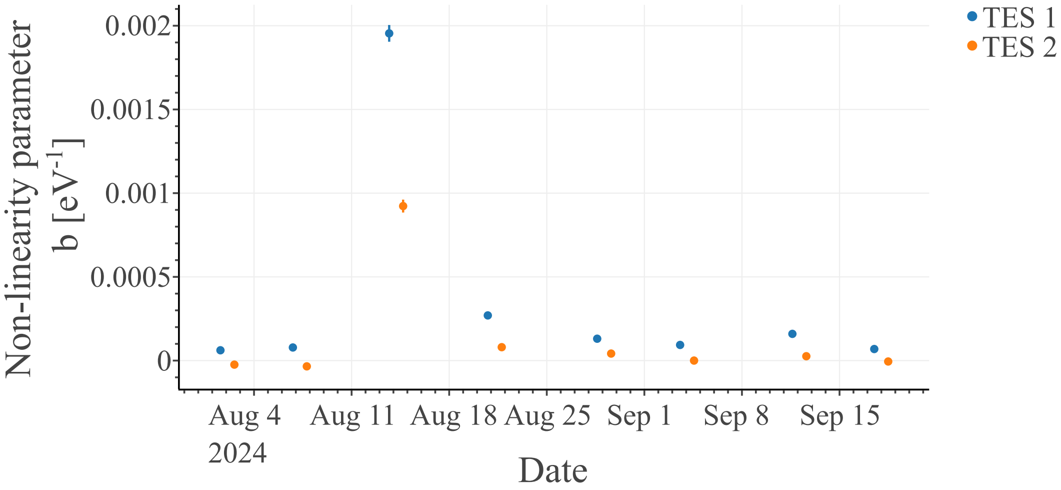

Figure 5.16. Time evolution of the non-linearity parameter for both sensors of the Al_2O_3 double TES module. The module showed stable non-linearity throughout the overall data taking, but after August 11 the LED hardware suffered a damage which made it non-linear. After August 25 the damage was repair and nominal conditions were restored. The error bars indicate the 1σ statistical fluctuations.

During the data taking, an increase in the estimated non-linearity was observed, as visible from Figure 5.16. This increase was quickly tracked down to be caused by a damage occurred in the LED driver during the handling, which was promptly repaired. Once the LED driver was working again, it is visible that the initial value estimated for the non-linearity was recovered. It is worth noticing that while the non-linearity estimation was affected by the damaged LED driver, the evaluation of the calibration constant remained unaffected since it is a relative comparison between the mean and the width of the distribution of the deposited photons.

5.4.1.2 Comparison of the optical calibration with X-ray lines

During this run no other calibration sources are present but due to the long detector operation it is possible to see the copper X-ray lines, which is the most present material near the detectors, activated by the passing of muons (the most probable X-ray line produced by copper has an energy of 8.05 keV [94]). Due to the low saturation of the Al_2O_3 module it is not possible to observe these energies, but the other $CaWO_4$ detector has a much higher saturation level ($\sim$ 12 keV) and can instead be used for this purpose. From the histogram plotted in Figure 5.17 the copper, lines are clearly visible and have a reconstructed energy of $\sim$ 9.4 keV. The $CaWO_4$ detector was calibrated using the same optical calibration setup and procedure as the Al_2O_3 *cryocube*, this means that a mismatch in the energy reconstruction of the copper lines with the optical calibration is at the 15% level. This mismatch is comparable with the calibration uncertainties and is not worrisome for this analysis. A systematic study of this discrepancy will be the objective of a dedicated study that will be undertaken by the collaboration in the upcoming runs.

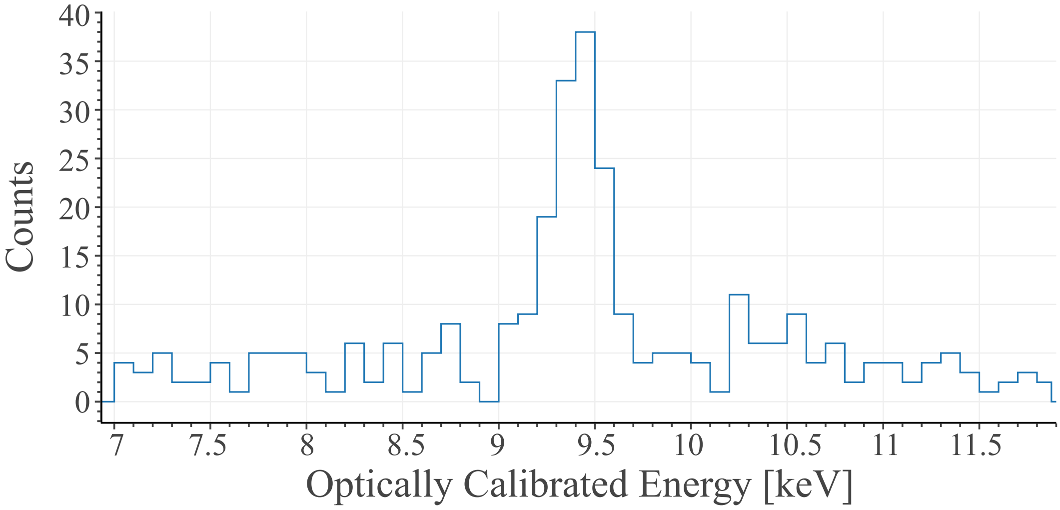

Figure 5.17. Energy spectrum measured with the $CaWO_4$ detector between 7 keV and 12 keV. The energy scale is calibrated using the optical calibration. A peak at ~ 9.4 keV is visible and corresponds to the K_α X-ray copper line (which is expected at ~ 8.0 keV).

5.4.2 TES Pulse shape analysis

The analysis of the pulse shape of the TES signals closely follows the one described in chapter 4 but since no spectral features need to be extracted the quality cuts applied to the data will not be pushed to their limit for the sake of analysis simplicity and efficiency. A key difference, from the analysis point of view, between the detector described in chapter 4 and the one considered here is the presence of the double readout. This is not a common feature of the NUCLEUS detectors, so it was decided to implement a single TES analysis by focusing on the signals coming from TES 1 and then use TES 2 at a later stage mainly for LEE studies. For this reason, the pulse shape analysis defined here only regards the signals recorded by TES 1.

Several weeks of data have been acquired and processed, the data cleaning is then performed in a modular fashion. In fact, each configuration, which starts and ends with an optical characterization and lasts about one week, is processed separately and the LED pulses generated in the first of the weekly calibrations are used to check and tune the data quality cuts. This modularity allows, in principle, to define different quality cuts, which is needed in case of a change in the working conditions of the detector. In practice, the detector was extremely stable during the whole acquisition and the same cuts and procedures have been applied to the whole dataset (see section 5.4.3).

In this section, the definition of the quality cuts is presented and the effect on the first data taking configuration is shown as an example. The cuts are applied and shown in cascade, meaning that the plots have the previously defined cuts already applied.

The first pulse shape cut used is a fairly loose selection made with χ^2_{MF} (see section 4.2.4). This cut is used to remove all of the waveforms that present easily noticeable deformations. The cut consists in requiring $\chi^2_{MF} < 20$, and the effect of

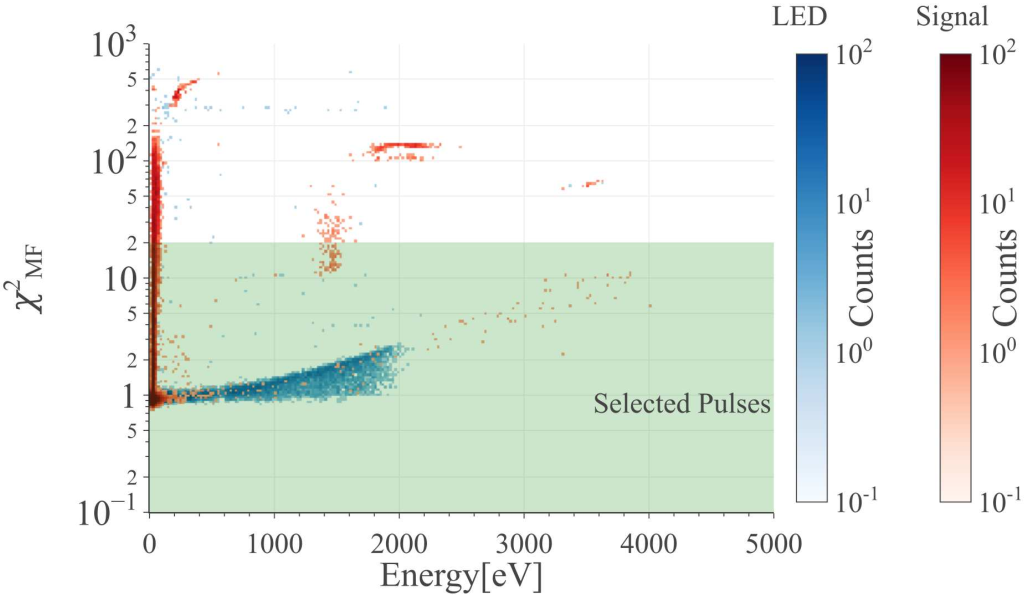

Figure 5.18. Heatmap of χ^2_{MF} versus the reconstructed energy showing the distributions of LED and Signal (self-triggered) pulses respectively in blue and red color scales. The green shaded area show the data quality cut applied.

the cut on the particle events and on the LED pulses can be seen in Figure 5.18.

The second pulse shape cut is on the **Right-Left Baseline** parameter expressed in multiples of the **BaselineRMS** of the waveform (see section 4.2.2). When studying the behavior of this parameter with the pulse energy (done using the LED deposition) a clear linear correlation with the mean value of **Right-Left Baseline** distributions can be noticed, as visible from the left panel of Figure 5.19. On the other hand, from the right panel of Figure 5.19 it is visible that there is not a strong dependence of the standard deviation of this parameter with the pulse amplitude. Analogously to what was done in section 4.3.2, a linearized version of **Right-Left Baseline** can be defined as:

$$\mathrm{RLB}_{lin} := \frac{\mathrm{RLB} - (k_\mu \cdot A + q_\mu)}{q_\sigma} \tag{5.1}$$

where k_μ and q_μ are the parameters describing the average linear scaling of **Right-Left Baseline** with the pulse energy while q_σ is the average standard deviation of the pulse shape variable, the parameters are extracted with the fits shown in Figure 5.19. The above definition of RLB_{lin} corresponds to the one given in chapter 4 with $k_\sigma = 0$. Once RLB_{lin} is defined, a pulse shape cut corresponding to $-3 < \mathrm{RLB}_{lin} < 3$ is placed. The effect of this cut is shown in Figure 5.20.

To remove potential pile-ups a data quality cut on **Baseline Slope**, presented in relative units (see section 4.2.2), is placed by requiring this parameter to have values

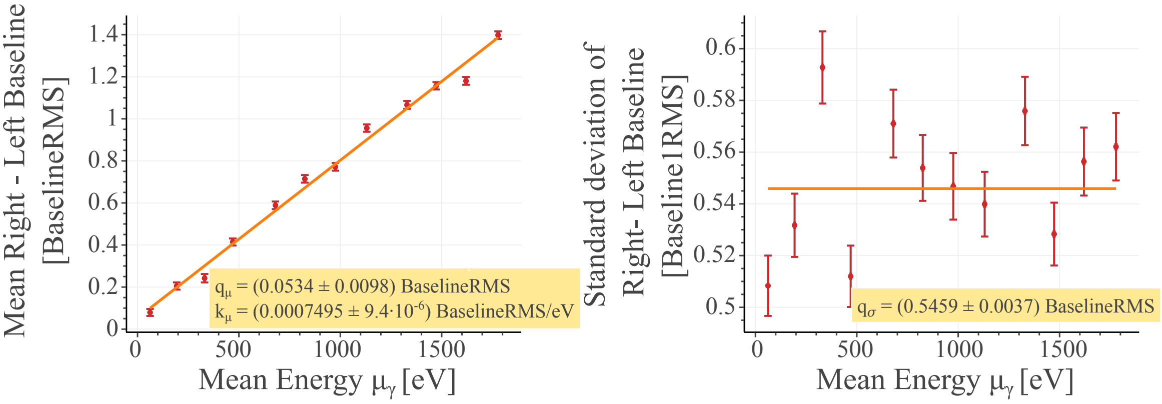

Figure 5.19. Study of the behavior of the **Right-Left Baseline** parameter, expressed in multiples of the noise RMS, with respect to the pulse energy. Left: Linear fit of the average **Right-Left Baseline** with respect to the pulse energy. Right: Constant fit of the standard deviation of **Right-Left Baseline** with respect to the pulse energy. The best fit values are shown in the insets of the plots. The error bars represent the 1σ statistical fluctuations.

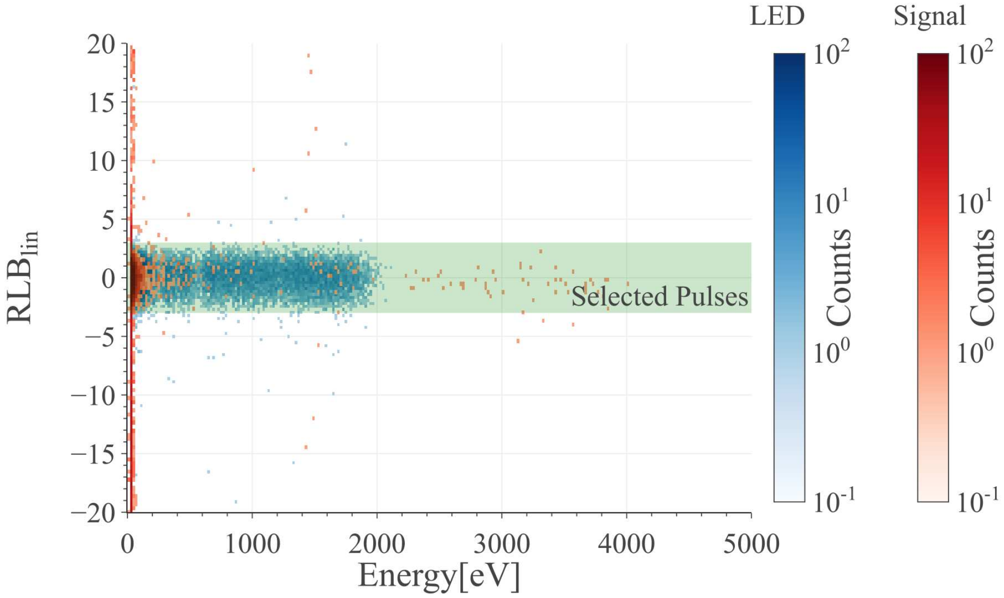

Figure 5.20. Heatmap of RLB$_{lin}$ versus the reconstructed energy showing the distributions of LED and Signal (self-triggered) pulses respectively in blue and red color scales. The green shaded area show the data quality cut applied.

contained in the interval $[-20, 20]$. The selection made with this cut is shown in Figure 5.21.

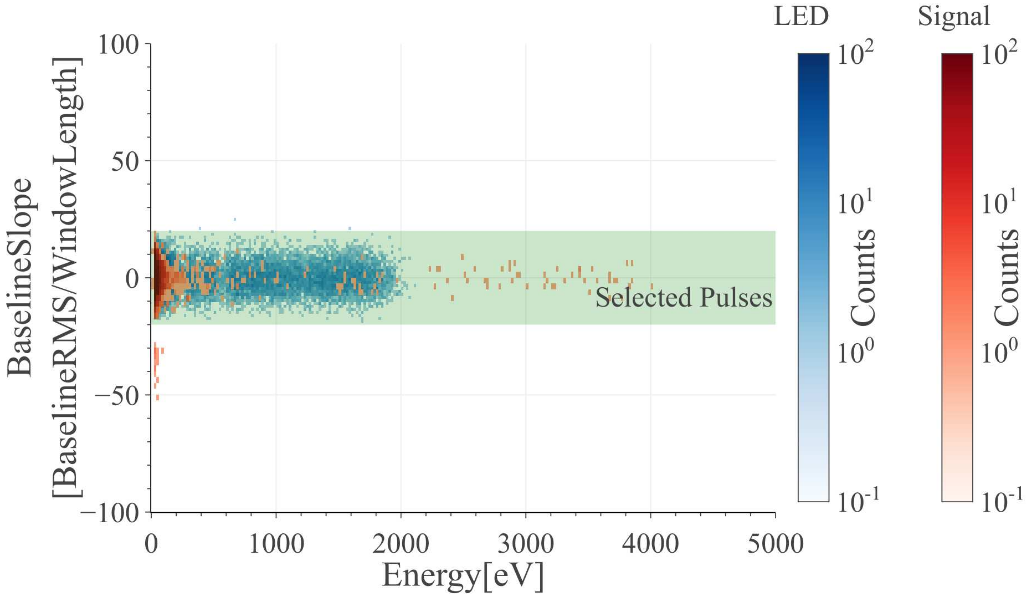

Figure 5.21. Heatmap of **Baseline Slope** (expressed in relative units) versus the reconstructed energy showing the distributions of LED and Signal (self-triggered) pulses respectively in blue and red color scales. The green shaded area show the data quality cut applied.

Another cut introduced to remove further bad pulses consists in requiring that χ_L has values between -10 and 3. As already described in section 4.2.4, this value is expected to be normally distributed for all energies, unless detector non-linearities are present. From Figure 5.22 it is visible that this parameter shows a dependence with the pulse energy. In principle, the linearization described in appendix C could be applied, but it was decided not to push the cuts to their limits, as instead was done for the nuclear recoil calibration in chapter 4, in order to achieve the highest possible analysis efficiency. In fact, in chapter 4 a spectral feature needed to be extracted in a low signal-to-background environment, meaning that background discrimination was a key element for the observation, on the other hand the aim of this analysis is a general characterization of the background level and no spectral feature needs to be extracted.

In case extremely noisy periods of data are present, a cut on the **BaselineRMS** parameter (see section 4.2.2) was set, requiring it be contained in the interval $[3.5\ \mathrm{mV}, 7.0\ \mathrm{mV}]$ as shown in Figure 5.23.

Finally, the last pulse shape cut applied is on the maximum under-fluctuation allowed in a waveform. This is imposed by requiring that the **Min-Baseline** parameter (see section 4.2.2) must be more than $-30\mathrm{mV}$. As visible from Figure 5.24, this cut has almost no effect on LED or particle pulses, but it is highly effective in cleaning the *reversed* triggered waveforms which might have downward pointing pulses in the window (as visible from Figure 5.25). These pulses are not wanted in the analysis since they do not represent noise fluctuations but are triggering artifacts due to the

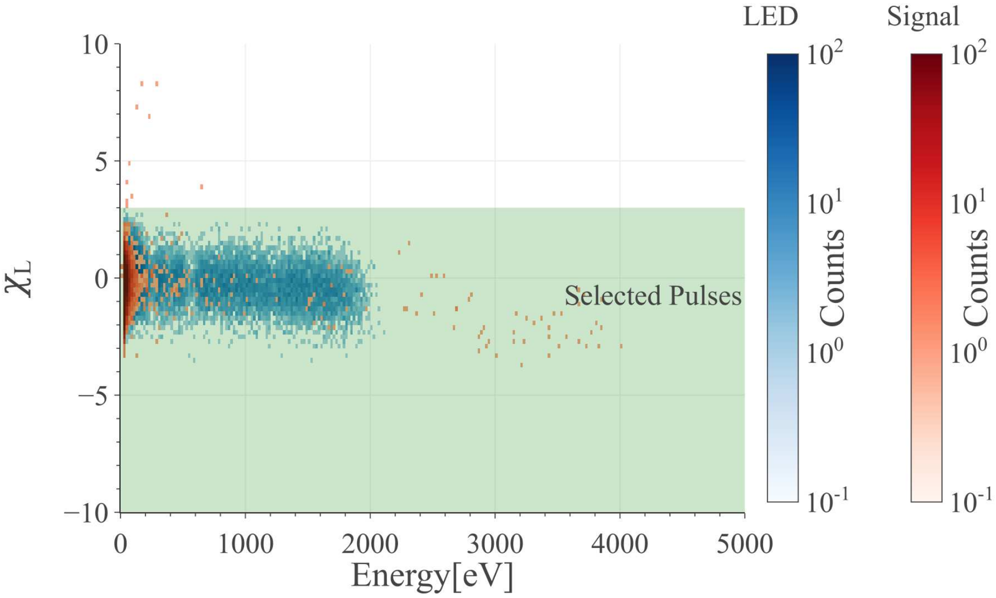

Figure 5.22. Heatmap of χ_L versus the reconstructed energy showing the distributions of LED and Signal (self-triggered) pulses respectively in blue and red color scales. The green shaded area show the data quality cut applied.

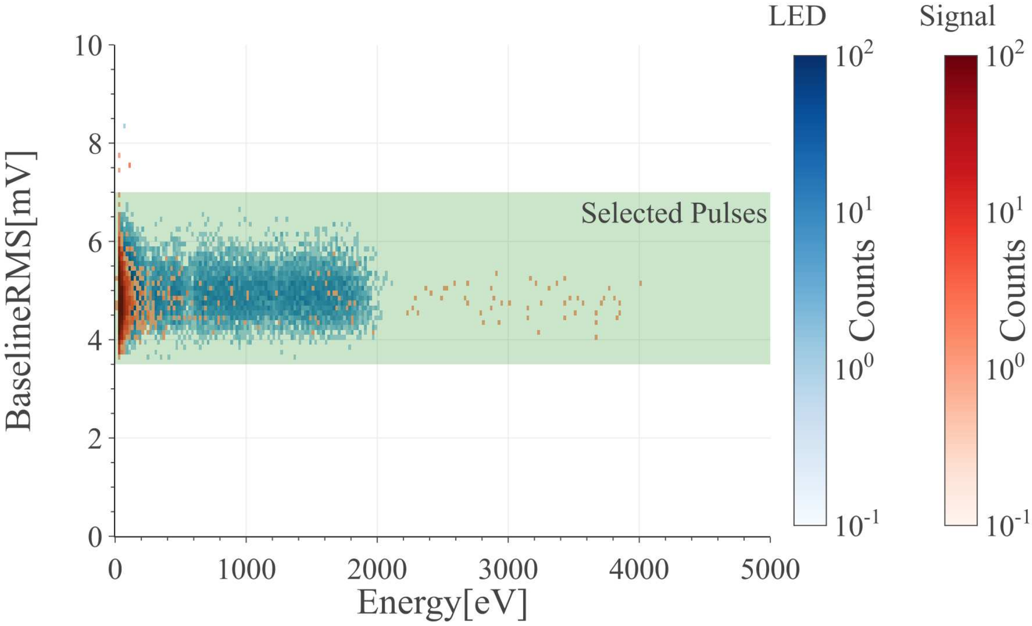

Figure 5.23. Heatmap of **BaselineRMS** versus the reconstructed energy showing the distributions of LED and Signal (self-triggered) pulses respectively in blue and red color scales. The green shaded area show the data quality cut applied.

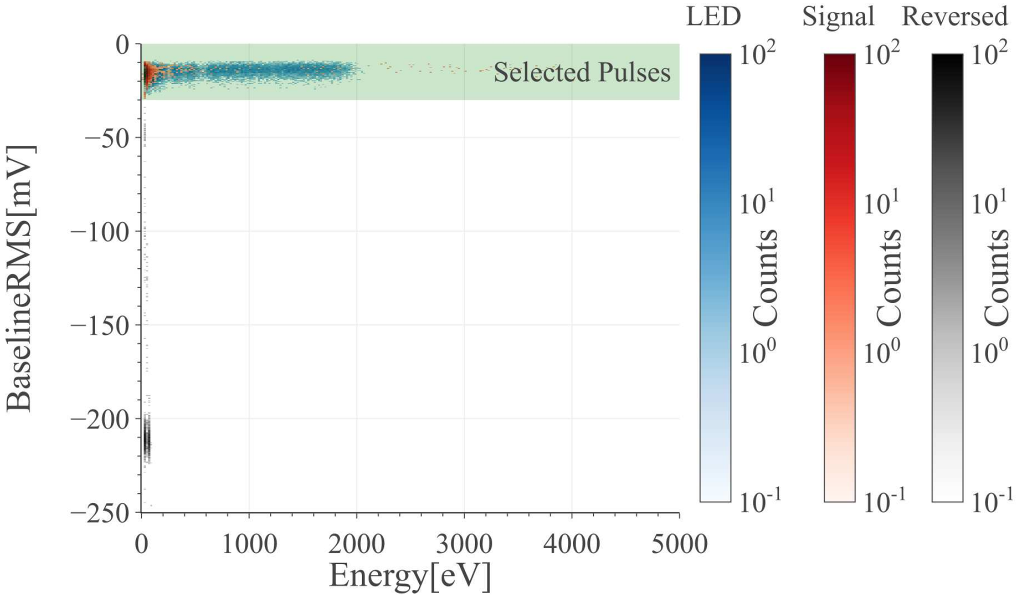

Figure 5.24. Heatmap of **Min-Baseline** versus the reconstructed energy showing the distributions of LED, Signal (self-triggered) and Reversed (false positive) pulses respectively in blue, red and gray color scales. The green shaded area show the data quality cut applied.

high SNR of the downward pulse. When such triggers happen in the self triggered waveforms they are already removed by other data quality cuts, that on the other hand are optimized for upward signals and do not efficiently remove such downward fluctuations. The effect of this selection is shown in Figure 5.24.

The application of all the cuts described has the effect of removing and keeping pulses like the ones shown in Figure 5.26.

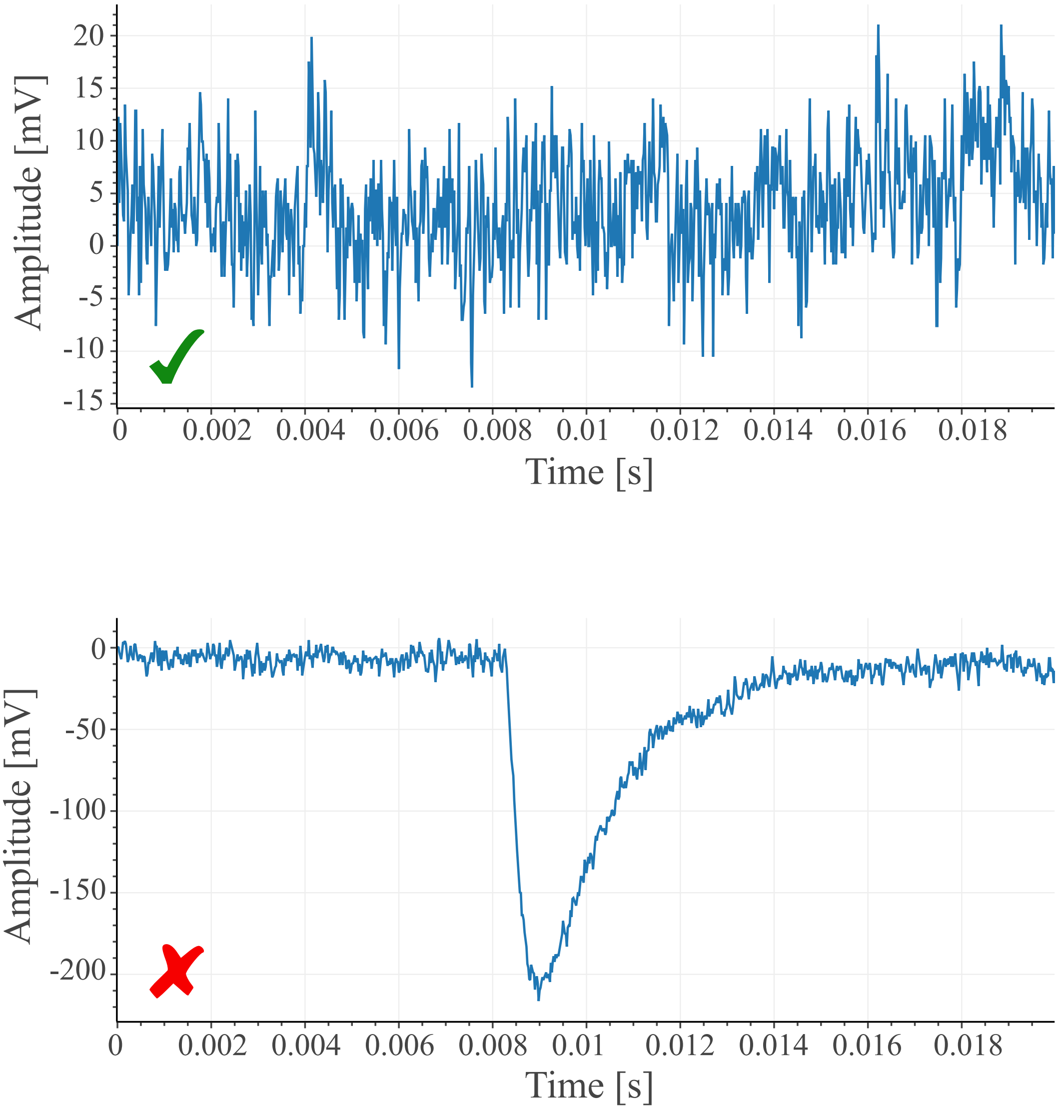

Figure 5.25. Example of *reversed* triggered pulses. In the top panel a waveform passing the quality cuts is shown (including the **Min-Baseline** cut), while in the bottom panel a waveform removed by the **Min-Baseline** selection is plotted.

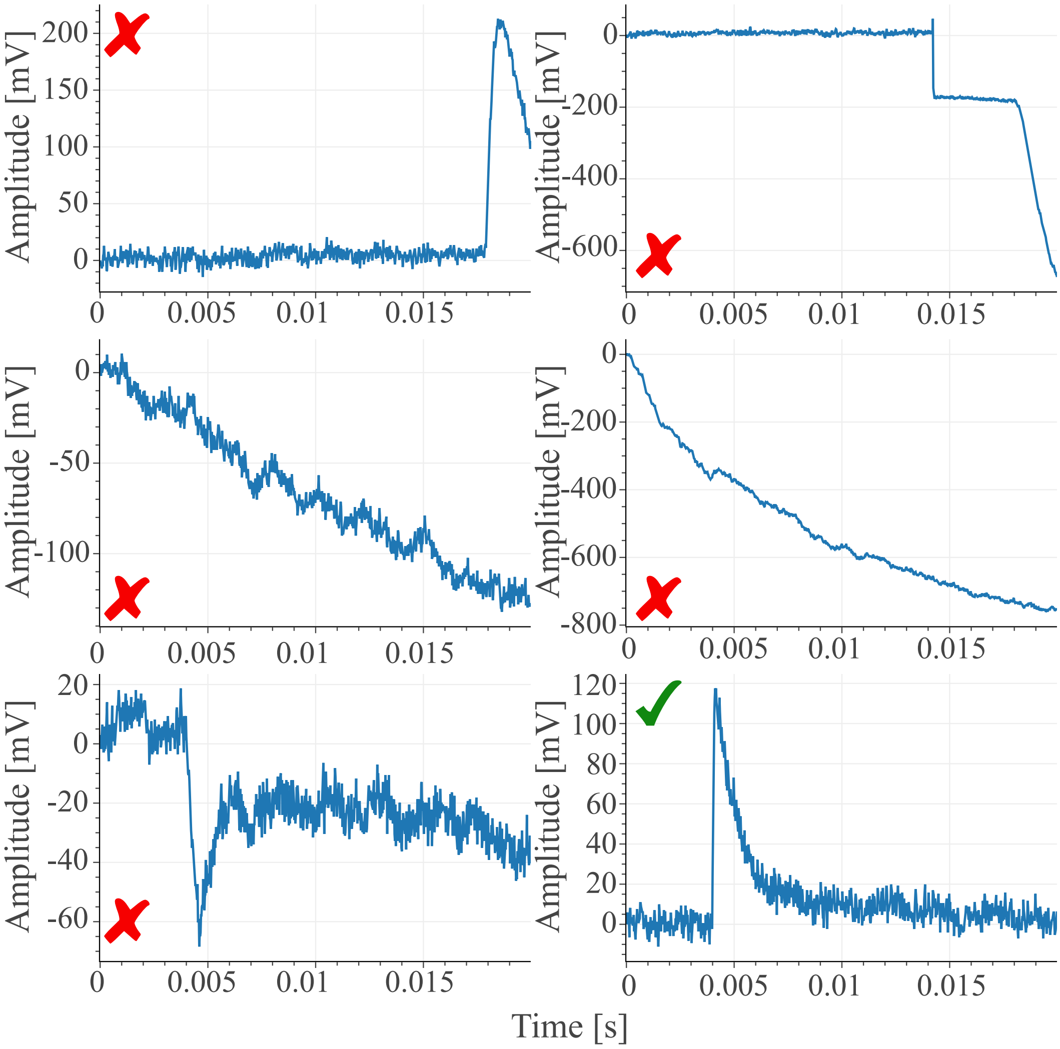

Figure 5.26. Example of pulses removed by the data cleaning procedure so far described (marked with red crosses). A pulse surviving the data cleaning is shown in the last panel marked by a green check.

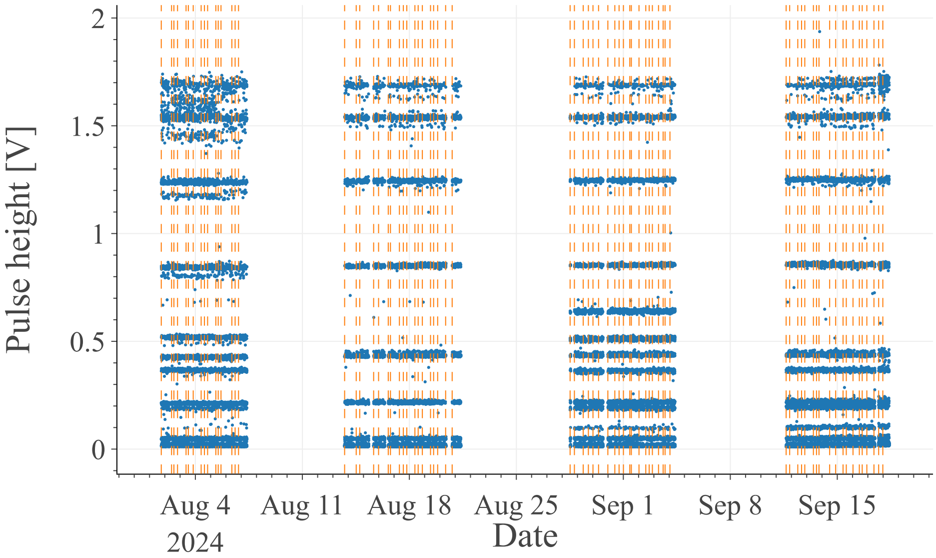

Figure 5.27. Amplitude of the heater induced pulses recorded on TES 1 as a function of time. The vertical orange lines indicate the start of the different data files acquired.

5.4.3 Detector Stability

An important control that must be performed during this type of analysis is to evaluate the stability of the detector and, if required, remove some data taking periods. As already anticipated during the description of the calibration, the observations here reported show no worrisome change of the detector working conditions and thus no data was removed from the analysis.

In section 5.4.1.1 it is presented that the two sensors always had a stable calibration constant, indicating that the work point of the TESs has not varied between the data taking configurations.

Ten different amplitudes of heater induced pulses have been continuously injected on the sensors throughout the whole data taking period. The heater pulses provide a useful monitoring tool to check TES stability. In Figure 5.27 the amplitude of the heater pulses is plotted as a function of time, it is visible that the Al_2O_3 module shows constant heater amplitudes, meaning that TES 1 had a stable operation over the whole data taking period.

Once the working point stability of the TES is assured, an evaluation of noise of the detector is performed. Figure 5.28 shows a good stability of the noise except for the very last period where a small noise increase can be spotted on TES 1. Since the increase is under 10% it has been decided to not remove this data from the analysis. The noise increase is expected to translate in a higher false positive counting rate, but this contamination can be measured thanks to the presence of the *reversed* triggers.

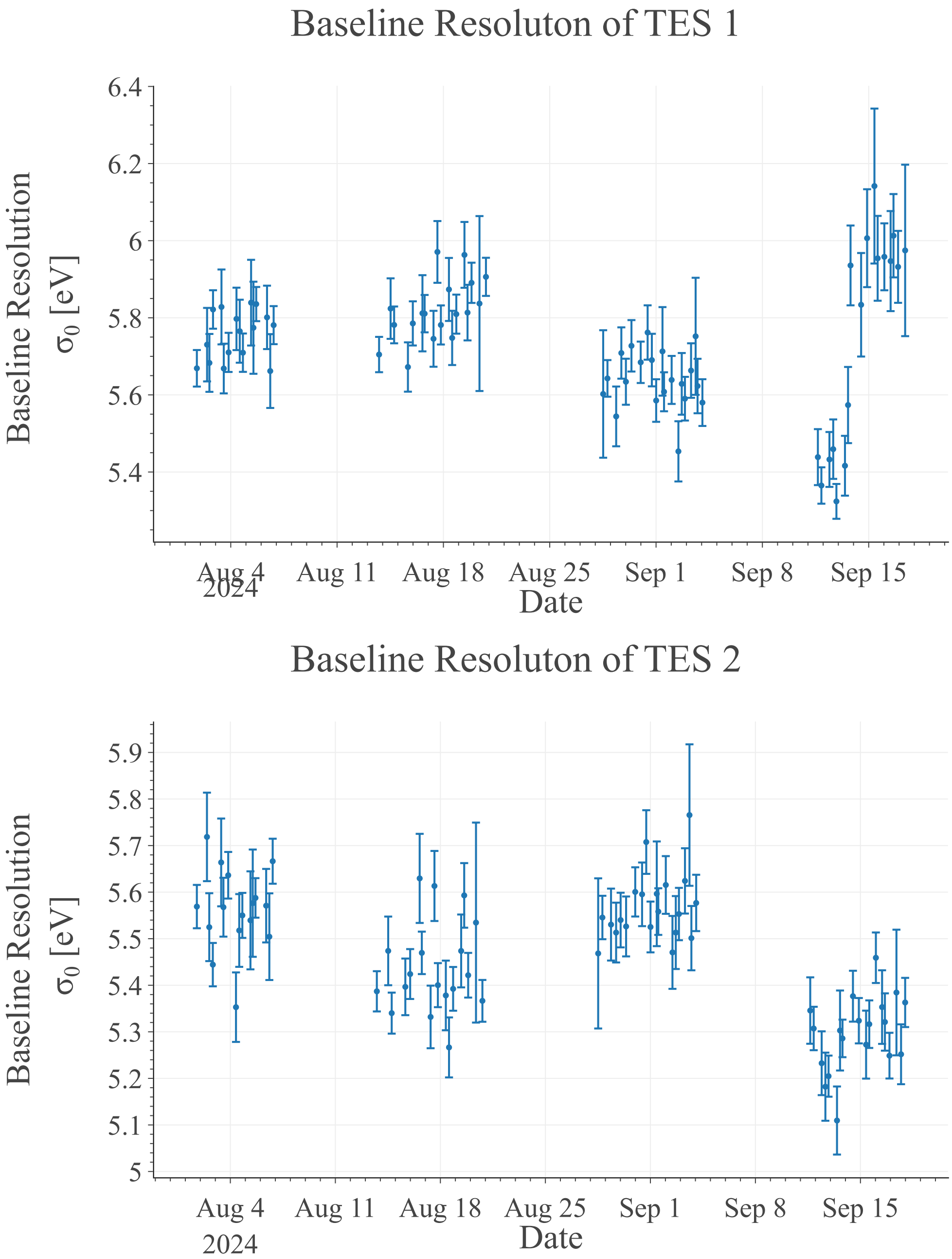

Figure 5.28. Evolution of the baseline resolution for both TES 1 (top) and TES 2 (bottom). At the beginning of the fourth week of data acquisition it is visible that the resolution of both TESs got lower, while this remained true for TES 2, a 10% noise level increase happened for TES 1 around the 15th of September.

5.4.4 Analysis Efficiency

Once the analysis is defined, it is necessary to evaluate what is the overall efficiency of the procedure. As described in chapter 4, this analysis is affected by 3 different sources of inefficiencies: triggering, reconstruction and data cleaning.

In this section, the analysis efficiency will be evaluated using LED pulses. For each data taking week, the corresponding LED calibration distributions will be used to perform efficiency studies. Since the calibrations do not cover exactly the whole dynamic range of detectors, during the run a dedicated dataset of LED distributions has been acquired spanning the whole response range of the detector. This last dataset is included in the efficiency evaluation and no strong deviations from the calibration data has been observed.

5.4.4.1 Trigger and Reconstruction Efficiency

To estimate the trigger efficiency as a function of pulse energy it is necessary to evaluate how many of the LED pulses, that are part of the same energy distribution, get triggered. The selection of these pulses can be easily done by comparing to the external LED trigger. To assign a LED induced event to a certain energy distribution can be non-trivial. In fact, while in the data taken with the purpose of the efficiency evaluation a single LED distribution is present in each raw file, during the calibration data 3 energy distributions per file are generated simultaneously. At the moment, the only way to separate the different LED distributions is with the definition of energy ranges. This separation, on the other hand, is affected by the efficiency of the amplitude reconstruction, meaning that for this data the triggering and reconstruction efficiency have to be evaluated simultaneously.

Operatively this is done in the following way:

1. count the number of LED triggers present in the data file;
2. assign an equal fraction of the number of LED triggers to each energy distribution;
3. by knowing the number of *cycles* n_c used to generate each LED deposition (see section 3.1) assign an expected mean energy to each LED distribution;
4. define energy ranges spanning a $\pm 5\sigma$ region from the average energy of the distribution. If two distributions have overlapping ranges, then the overlap is redistributed according to the ratio of their standard deviations.
5. count how many LED pulses included in a certain energy range have a corresponding self trigger.
6. for each energy range, make the ratio between the number of LED fulfilling the requirements and the total number of expected LEDs defined in item 2.

The ratio evaluated at the last point corresponds exactly to the efficiency, for a specific energy range, given by the triggering and amplitude reconstruction steps of the analysis. The evaluation of the total number of pulses for each distribution described in item 2 can be done with a ± 1 event uncertainty (out of ~ 1000 total LED events present in each distribution). This uncertainty in the total number of LEDs is more than one order of magnitude smaller than the one affecting the efficiency, meaning that it is extremely subdominant and can be disregarded. The energy ranges definition and the dependence of the efficiency on the pulse amplitude for the first week of data are shown in Figure 5.29.

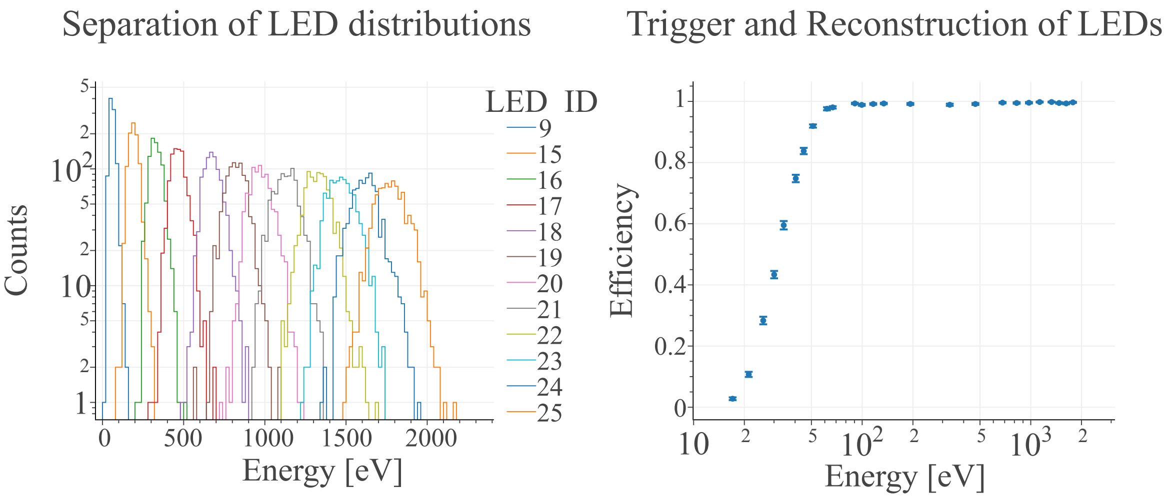

Figure 5.29. Left: histogram of the different LED depositions (for readability only the data from the calibration files are plotted, which are also the only files for which the LED separation applies). Right: scaling of the triggering and reconstruction efficiency as a function of the average deposited energy, plot made with both the LED calibration and the efficiency evaluation datasets.

With the LED files containing a single distribution, it is possible to estimate the trigger threshold, which is expected to be 28 eV (four times the resolution of the detector). In fact, if the pulses used to estimate the trigger efficiency are normally distributed, the expected trigger probability of a pulse of reconstructed energy E, distributed normally around μ with variance σ^2, is given by:

$$P(E|\mu) = \frac{1}{\sqrt{2\pi\sigma^2}} e^{-\frac{(E-\mu)^2}{2\sigma^2}} \tag{5.2}$$

which gives the trigger efficiency of:

$$\epsilon(\mu) = \int_{E_{th}}^{\infty} P(E|\mu) dE \tag{5.3}$$

where E_{th} is the triggering threshold, in Figure 5.30 a graphical representation of this step is shown.

It is possible to perform the Gaussian integral above, obtaining the following model:

$$\epsilon(\mu) = \frac{1}{2} + erf\left(\frac{\mu - E_{th}}{\sqrt{2}\sigma}\right) \tag{5.4}$$

where σ is the standard deviation of the measured energy distribution and erf is the error function. With the LEDs, it is possible to vary μ in order to map the full $\epsilon(\mu)$ function. On the other hand, when this study is performed with LED pulses one needs to take into account that σ^2 has a contribution given by the Poisson statistics. This means that the expected resolution in electronvolts is given by:

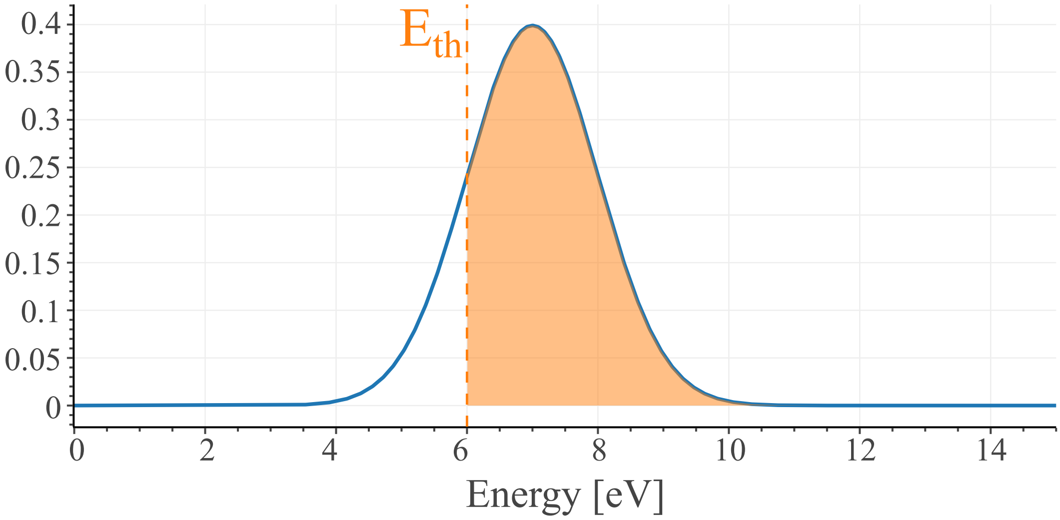

Figure 5.30. Representation of the effect of a lower threshold (dashed orange vertical line) on the probability of triggering pulses (orange area) when they are normally distributed (blue).

$$\sigma^2 = \sigma_0^2 + \epsilon_\gamma \cdot N\gamma = \sigma_0^2 + \epsilon_\gamma^2 \cdot N\gamma = \sigma_0^2 + \epsilon_\gamma \mu \tag{5.5}$$

which make the trigger efficiency function:

$$\epsilon(\mu) = \frac{1}{2} + erf\left(\frac{\mu - E_{th}}{\sqrt{2(\sigma_0^2 + \epsilon_\gamma \mu)}}\right) \tag{5.6}$$

As previously mentioned, during the data taking a dedicated dataset of LED pulses was acquired in order to study the trigger threshold. The data is calibrated using the calibration constant given by the corresponding optical calibration of the week. Estimating the mean energy of these distributions directly from the recorded energies can be subject to biases, since to estimate the pulse amplitude a maximum search is performed and could be heavily contaminated by noise fluctuations due to the low energy of the generated events. For this reason, it is necessary to estimate the deposited energy for each LED cycle n_c (see chapter 3) by taking the average amplitude of the most energetic light deposition. Knowing the energy per cycle while also knowing the cycles used to generate each distribution, it is possible to estimate the expected mean energy.

By measuring the number of self-triggered pulses in the LED distribution it is possible to evaluate the trigger efficiency which can be plotted as a function of the average deposited energy. This plot is shown in Figure 5.31 and the data can be fitted with eq. (5.7):

$$\epsilon(\mu) = \frac{A}{2} + A \cdot erf\left(\frac{\mu - t \cdot \sigma_0}{\sqrt{2(\sigma_0^2 + \epsilon_\gamma \mu)}}\right) \tag{5.7}$$

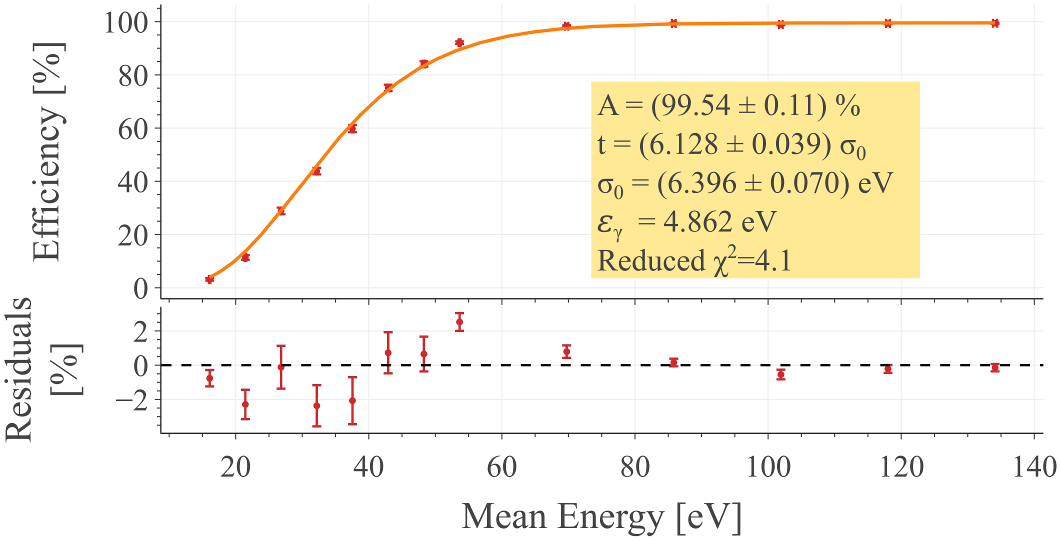

Figure 5.31. Fit of eq. (5.7) to the trigger efficiency evaluated using LED pulses. The best fit values are shown in the inset of the plot. The error bars represent the 1σ statistical fluctuations.

where the function is directly taken from eq. (5.6) but the normalization parameter A is used to model a fixed efficiency loss and the threshold energy is expressed as a multiple of the noise RMS $E_{th} = t \cdot \sigma$. From the best fit parameters, shown in the inset of Figure 5.31, it is possible to see that the trigger threshold is at $\sim 6\sigma_0$ which is more than the expected $4\sigma_0$ level. This is due to a bias present in the matched filter based trigger algorithm during the maximum search, in fact the procedure tends to trigger more high SNR pulses with respect to lower amplitude ones (see section 4.2.1.1).

Moreover, eq. (5.7) is performed under the approximation that the Poisson distribution can be modeled with a normal distribution. This approximation is only true when a high enough number of photons (≥ 5) is integrated in the same response pulse. By comparing the energies at play with the single photon energy $\epsilon_\gamma = 4.862$ eV, it is clear that this is not the case (an average of 2.4 ± 0.1 photons per cycle are delivered to the detector and the minimum energy studies is given by ~ 3 photons). In this case one would need to study the cumulative of a Poisson distribution with a Gaussian smearing, due to the mathematical difficulty of modeling this distribution it was decided not to perform this further refinement.

To study whether the deviation from expectations of the trigger level is due to the trigger algorithm or to a wrong model, it was decided to generate a Monte Carlo data file. This data is built by randomly adding the signal templates, scaled by a user defined amplitude, to portions of the real data stream and adding an external trigger to identify them. These Monte Carlo files effectively behave the same as the LED single distribution files, but the distribution broadening due to the Poisson statistics is absent. This means that the trigger threshold model defined in eq. (5.8) is valid for these pulses: overestimated.

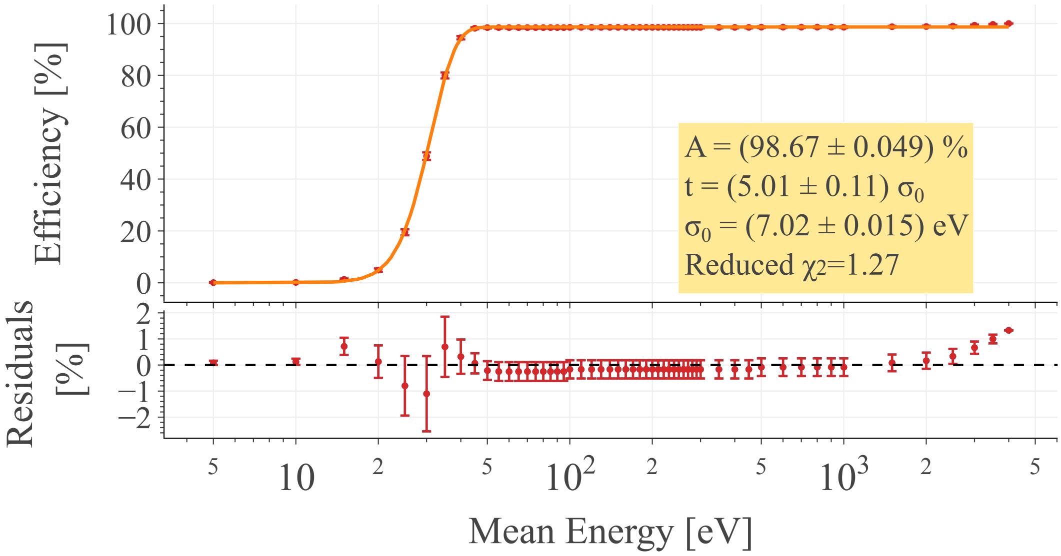

Figure 5.32. Fit of eq. (5.8) to the trigger efficiency evaluated using Monte Carlo pulses. In the inset of the plot, the best fit values are shown. The error bars represent the 1σ statistical fluctuations.

$$\epsilon(\mu) = \frac{A}{2} + A \cdot erf\left(\frac{\mu - t \cdot \sigma_0}{\sqrt{2\sigma_0^2}}\right) \tag{5.8}$$

where the parameters are the same as in eq. (5.7) with σ^2 set equal to σ_0^2. The drawback of using such a Monte Carlo is that most detector effects (like non-linearities or position effects) are not reproduced and the efficiency is expected to be slightly overestimated. Moreover, in the generation of these Monte Carlo files, always the same portion of data stream was used for all the points in Figure 5.32 and the simulated signals are added with a fixed time interval, meaning that there are no statistical fluctuations considered in the data. By performing, on the Monte Carlo files, exactly the same type of threshold fit as for the LED case but removing the Poisson term, the triggering threshold was measured to be 35 eV (see Figure 5.32). This means that the bias towards higher energies present in the matched filtered based triggering algorithm is confirmed and slightly increases the threshold. Anyhow, a 5σ threshold was reached and was deemed sufficient for this analysis.

5.4.4.2 Data cleaning efficiency

The remaining analysis efficiency to be evaluated is the one due to the data cleaning. This is fairly straight forward to evaluate since once the LEDs have been divided in energy ranges (as described in the previous section) it is sufficient to count how many of the self triggered LED pulses of a certain range pass the selection cuts.

The scaling of the data quality efficiency with respect to the pulse energy is shown in Figure 5.33 where an almost constant behavior can be noticed. Overall, the data cleaning has an average efficiency above the 99% level, meaning that the triggering and the reconstruction are the dominant efficiency loss steps.

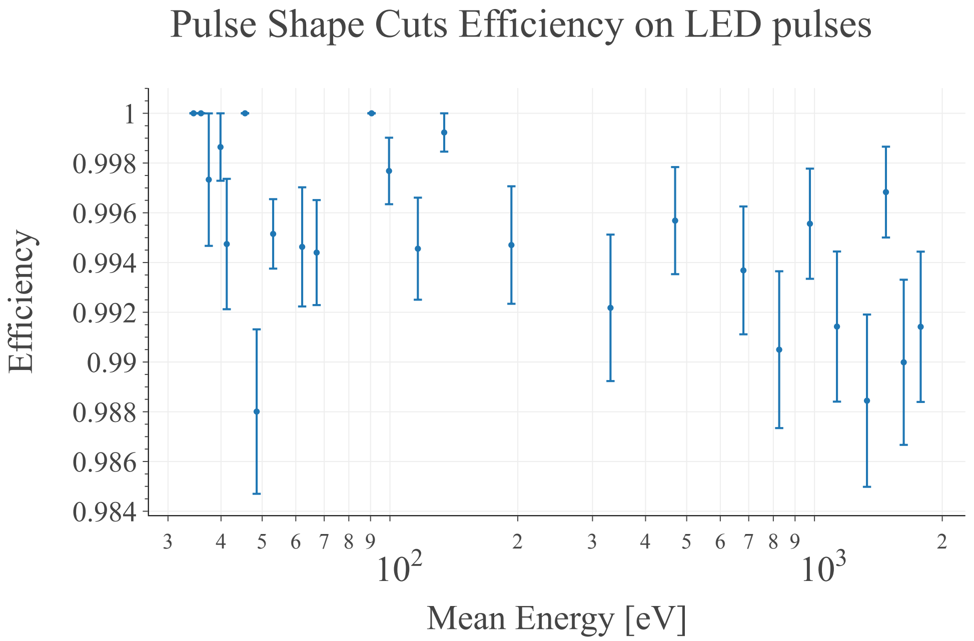

Figure 5.33. Scaling of the data quality cuts efficiency as a function of the average energy. The efficiency plotted here is evaluated on the calibration files of the first data taking week and dataset acquired for efficiency evaluation. An averagely constant efficiency of above 99% is measured. The error bars on the plots are the 1σ statistical fluctuations given from the binomial distribution characteristic of the efficiency evaluation.

5.4.4.3 Total Pulse Shape Analysis Efficiency Summary

To apply the analysis efficiency to the data, it is necessary to combine the efficiency evaluated previously. This can be done by simply multiplying the efficiencies with one another and propagate the associated binomial errors as plotted in Figure 5.34 which shows the efficiency combination for the first data taking configuration.

In Figure 5.35 the total efficiency for all the data taking weeks is shown. To estimate the efficiency in between the data points, it was decided that connecting the points with a spline curve was a sufficiently precise procedure without having to completely model the efficiency scaling. The spline model is applied to both the efficiency and its error.

5.4.5 Double Readout analysis

As mentioned before, the second TES present on the Al_2O_3 *cryocube* is used to identify the nature of the recorded pulses. The two sensors are expected to measure the same energy deposition when a particle interaction happens in the crystal, so any signal that does not fulfill this requirement has a different origin can be classified as background. An extreme example of this type of background can be seen in Figure 5.36, which shows the two simultaneous traces of coming from the two TESs. From the plot it is clearly visible how a pulse is present on TES 1 but is completely absent on TES 2, this is a very different behavior from what is expected from particle

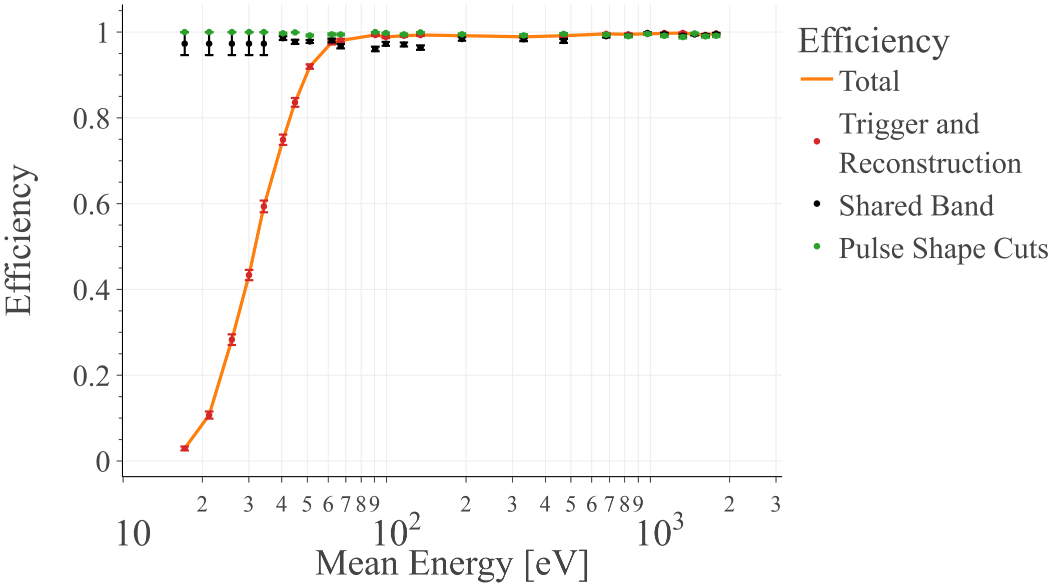

Figure 5.34. Combination of the triggering, reconstruction and pulse shape cuts efficiencies in a total (orange) efficiency characterizing the dataset. This plot is made with the data coming from the first week of Al_2O_3 data, and the error bars are the 1σ statistical fluctuations given by the efficiency binomial distribution.

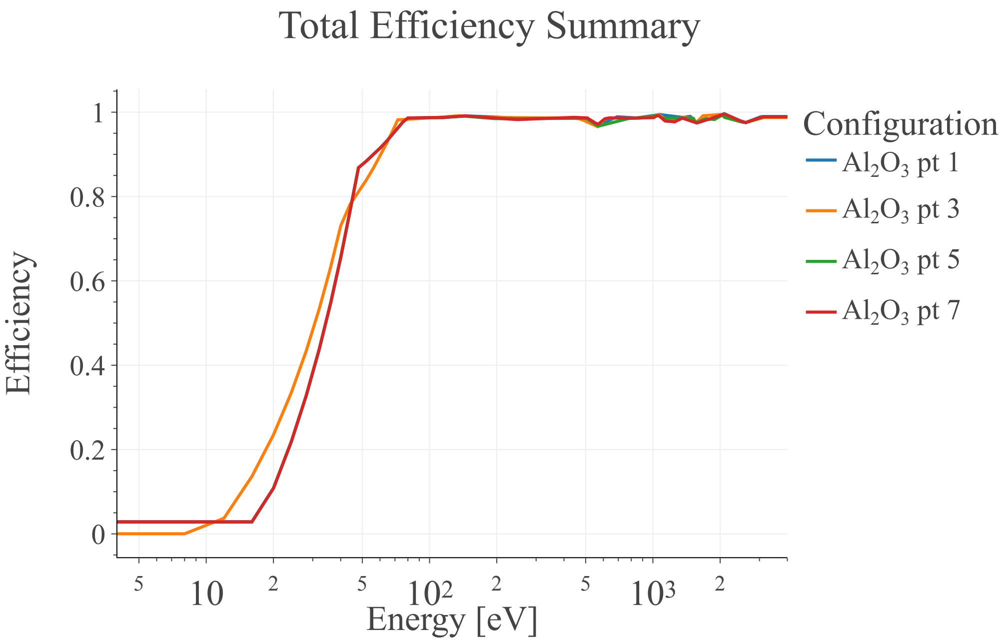

Figure 5.35. Summary plot showing the total efficiency (cuts, triggering and reconstruction) characterizing each data taking configuration. The configurations are defined in Figure 5.3

interactions. Since the waveform on TES 1 passes all the data quality cuts described so far, this type of event can only be classified as background by studying the energy sharing between the two sensors.

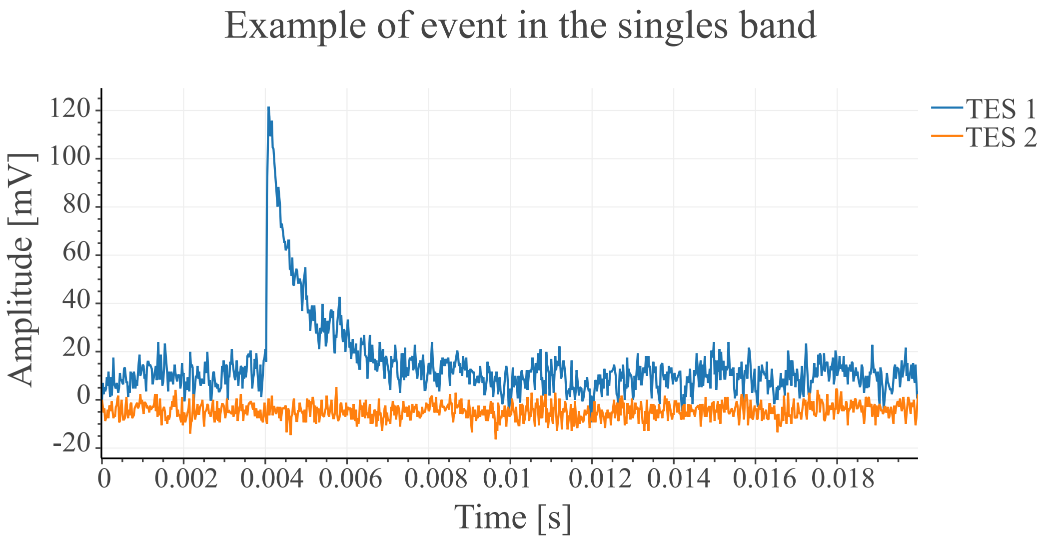

Figure 5.36. Example of an event that generates a signal in TES 1, but no pulse is visible in TES 2.

To define a variable encoding the energy sharing between the sensors that is able to discriminate this background also near the detection threshold, a few aspects need to be taken into consideration. In fact, simply doing the energy ratio between the two sensors does not work since for an energy that tends to zero this parameter diverges. On the other hand, it is possible to follow a procedure similar to the linearization of the **Right - Left Baseline** pulse shape parameter. The first step is to measure what is the average behavior of the energy ratio between the detectors:

$$R(E_1) := \left\langle \frac{E_1}{E_2} \right\rangle_{E_1}$$

where E_1 and E_2 are respectively the energies measured on TES 1 and TES 2 for the same interaction, the averaging is done on multiple events recorded having the same (or similar) E_1. The energy ratio is expected to be distributed around one, but from Figure 5.37 it is evident that this is not the case. If this deviation from expectation was due to a calibration error, the energy ratio would still be constant but distributed around a different value with respect to one. On the other hand, the presence of a slope (which is clearly visible from the plot) indicates some type of feature in the transition curves of the sensors, which translates to a low energy non-linearity. For this reason, a linear fit of the form:

$$R(E_1) = k_R E_1 + q_R \tag{5.9}$$

was used to effectively describe the average behavior of the energy ratio with respect to the energy recorded in TES 1. Once $R(E_1)$ is estimated, it is possible to build the energy sharing variable:

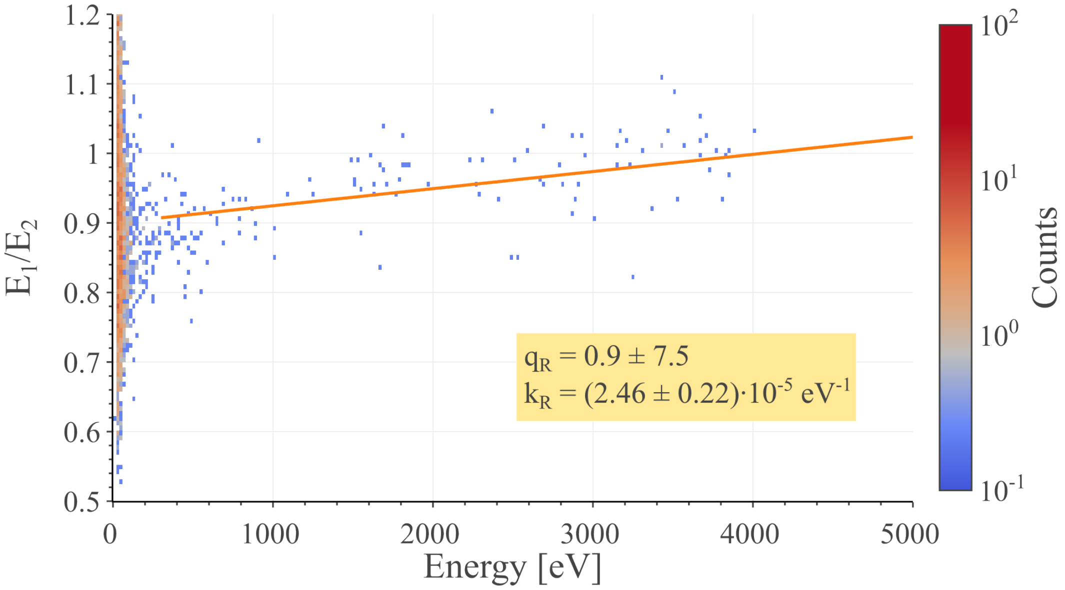

Figure 5.37. Linear fit of the average behavior of the $\frac{E_1}{E_2}$ energy ratio as a function of the TES 1 energy E_1. The best fit values are presented in the orange inset.

$$\psi = \frac{E_1 - E_2 \cdot R(E_1)}{\sqrt{\sigma_1^2 + \sigma_2^2 \cdot R^2(E_1)}} \tag{5.10}$$

where σ_1 and σ_2 are the noise resolution of respectively TES 1 and TES 2 (see section 5.4.3). This parameter is expected to be normally distributed around 0 with a unitary standard deviation when pulses have the expected energy sharing and are near the detector threshold.

By studying the standard deviation of the ψ distribution of LED pulses (see Figure 5.38) it is clear that it correlates with the signal amplitude. For this reason, a linearized version of ψ is defined in order to have a parameter that maintains the same standard deviation through the energy spectrum and allows to set a constant efficiency data quality cut. This is done first by performing a linear fit of the scaling of the variance of ψ with respect to the average energy of an LED deposition, as shown in Figure 5.38. Once a description of the scaling of the variance is extracted, one can define:

$$\psi_{lin} = \frac{\psi}{\sqrt{\sigma_\psi^2(E_1)}} = \frac{\psi}{\sqrt{k_\psi E_1 + q_\psi}} \tag{5.11}$$

where k_ψ and q_ψ are the parameters of the linear fit of the variance of the ψ variable marked as $\sigma_\psi^2(E_1)$.

Now ψ_{lin} can be used to set a constant efficiency data quality cut. In particular, for this analysis the data quality cut is set such that $|\psi_{lin}| \leq 3$, which means that a deviation of more than 3 standard deviations between the energies reconstructed

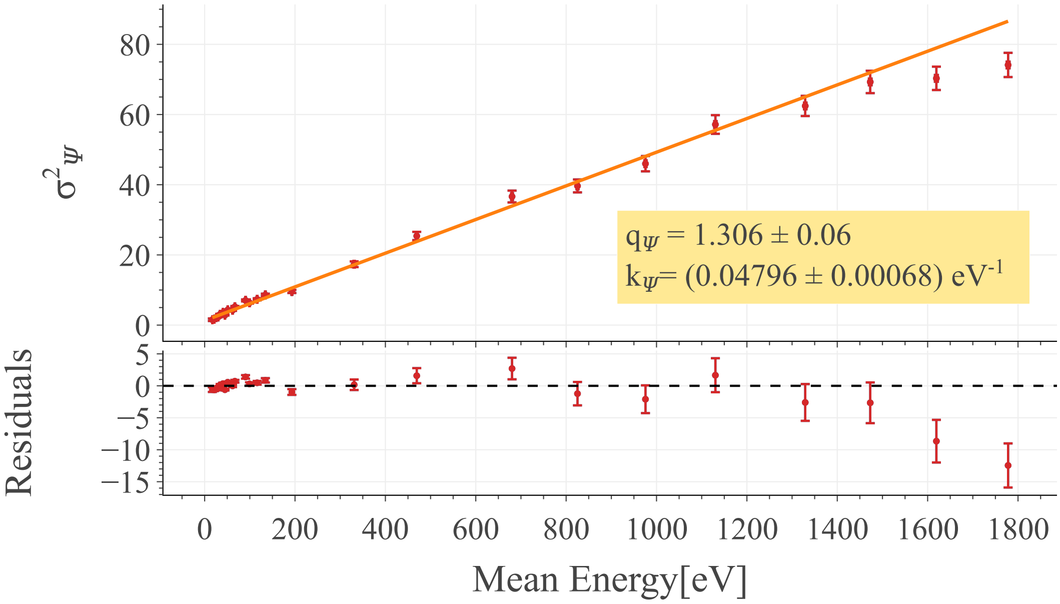

Figure 5.38. Plot of the variance of the ψ parameter as a function of the mean energy for the LED distributions. The variance is fitted with a linear model to extract the parameters required for eq. (5.11) (in the inset the best fit values are shown). The best fit parameters are shown in the orange inset, while the error bars represent the 1σ statistical fluctuations.

in the two sensors is flagged as a wrong energy sharing and thus is a background. The pulses fulfilling this requirement are said to be part of the *shared band*, while the ones that do not are in the *singles band*. The effect of this cut can be seen in Figure 5.39 where it is shown that most of the signal and LED pulses lie in the *shared band*. The cut range was previously defined and is the same as the one used in [81].

Since this procedure relies on the energy reconstructed in TES 2, choosing the sensor with the best resolution to perform this cut is beneficial. In fact, if TES 2 had a resolution worse than TES 1 it would not have been possible to have a discriminating data quality cut down to the threshold of TES 1.

5.4.5.1 Double Readout Efficiency

As for the pulse shape cuts defined before, also the *shared band* cut has an efficiency. This efficiency can be evaluated with the LED generated distributions, like the data quality cuts one. In the left panel of Figure 5.40 it is possible to see the efficiency associated with this cut for the first week of data taking, while in the right panel the total efficiency applied to the *shared* band spectra is shown for all data taking configurations. The total efficiency consists simply of the multiplication of the efficiency plotted in Figure 5.35 with the efficiency associated with this cut.

When spectra of the *singles band* are shown, the same efficiency as the *shared band* is applied, since these are background events and their analysis efficiency is not well defined.

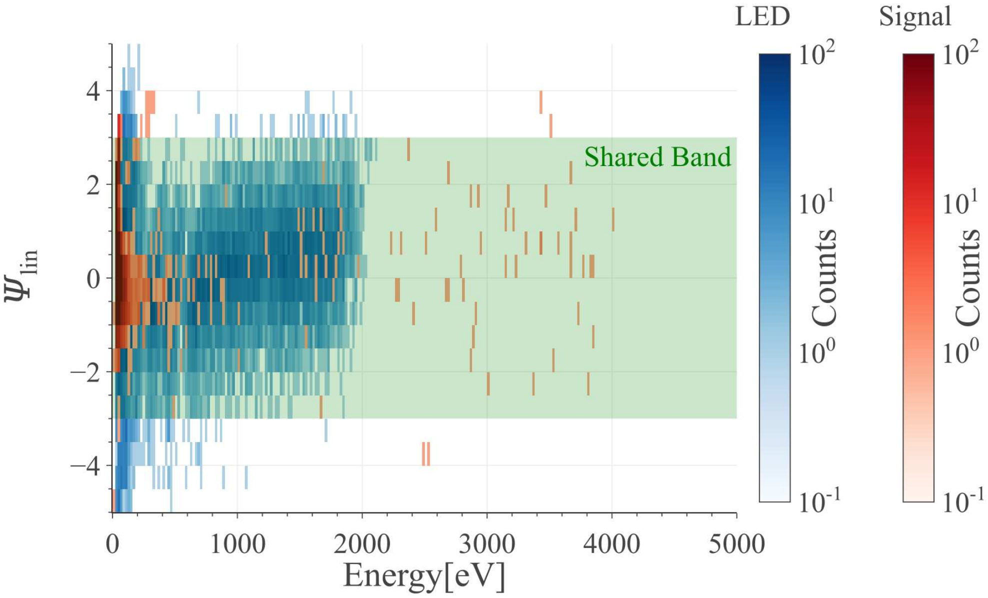

Figure 5.39. Heatmap of ψ_{lin} versus the reconstructed energy showing the distributions of LEDs and Signal (self-triggered) pulses respectively in blue and red color scales. The green shaded area show the definition of the *shared band*.

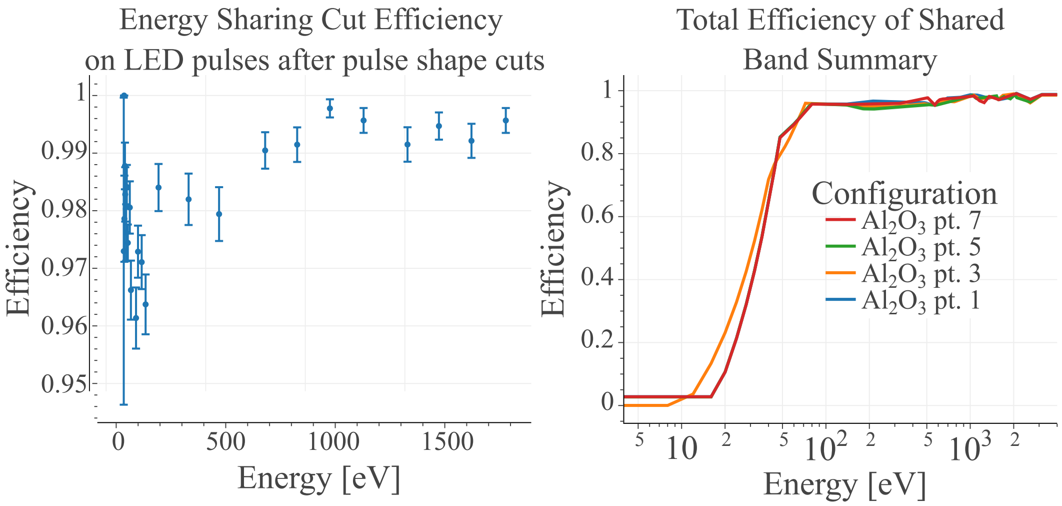

Figure 5.40. Characterization of the efficiency introduced from the shared band definition. Left: efficiency solely due to the shared band plotted for the first week of data taking (configuration Al_2O_3 pt. 1). Right: summary of the total efficiency affecting the shared band in each of the 4 data taking configurations.

5.5 TES and Muon Veto combined analysis

Now that all the analysis of the TESs waveforms has been defined, the focus is shifted to the introduction of the muon veto, used to further lower the level of the present background. This section will start with a quick description on how the

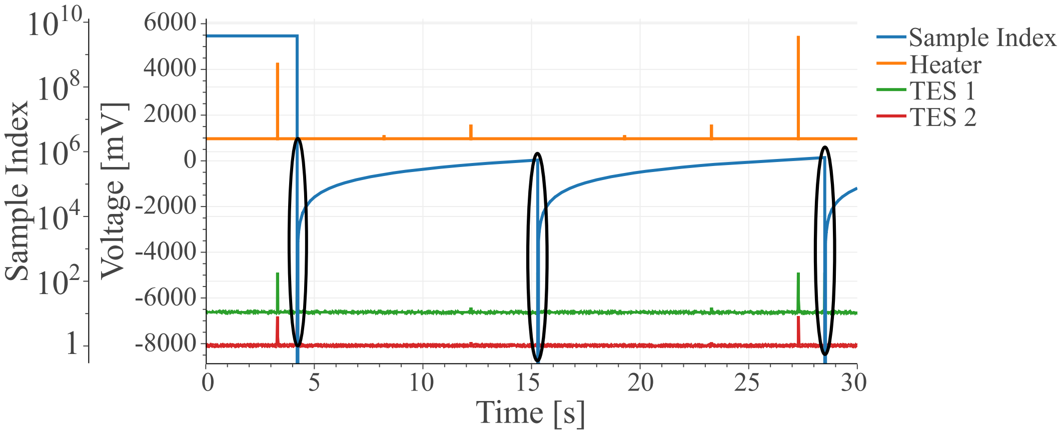

Figure 5.41. Plot of a portion of a raw data file coming from the cryodetector DAQ system. Three time resets (highlighted with black circles) are present in the *sample index* data stream. The last time reset is the one used for the file synchronization.

synchronizations of the two DAQ systems is done and then the coincidences between TES 1 and the muon veto are defined and characterized.

5.5.1 Veto Synchronization and data file combination

As anticipated before, the muon veto DAQ produces a triggered data file, for each entry of the file (i.e. for each trigger) a tuple with all the amplitudes recorded on all the muon veto slabs is saved along with the time of the event. The muon veto DAQ shares the same clock as the cryodetector DAQ system, meaning that the time differences inside the respective files match with a precision lower than the sampling frequencies of either detector.

Since the acquisition of the data files on the two DAQ systems is started manually, a way of setting a common zero needs to be introduced. This is done by resetting the clock on the cryodetector DAQ which in turn also resets the clock on the muon veto one. In the files produced by the latter, the time reset updates the timestamp of the triggered events to match the time stamp of the cryodetector DAQ. In the cryodetector files, instead, a dedicated data stream is added which shows a counter of how many samples have elapsed from the last time reset, and, as visible from the blue trace in Figure 5.41, when a time reset is sent this counter is set to 0. By detecting this downward spike of the sample counter and rescaling the time accordingly, during the raw data analysis, it is possible to synchronize the two acquired files.

Once the two files have been synchronized, they are then combined in a time ordered fashion in the same analysis file. This step is done after all the waveform analysis on the TESs has been performed. This combination of the two data files while being conceptually trivial needs to be performed with care due to the $\sim$ 200 Hz triggering rate of the muon veto, meaning that the computational cost needs to be reduced to a minimum otherwise it can become the bottleneck of the analysis procedure. A detailed description of the operations made to combine the events of the two DAQs is beyond the scope of this thesis, making this analysis step effectively a time sorting of the events coming from the two acquisition systems dedicated to the different types of detectors.

5.5.2 Coincidence Window Definition

After the combination of the events coming from the two DAQs the definition of the coincidence criterion between muon veto and TES 1 needs to be defined. The coincidence between the two detectors is done by requiring that for a given time of a TES trigger there is a narrow time window in which a muon veto event must lie.

The first step in this procedure is to accurately evaluate the time at which a TES trigger happens. Taking directly the timing of the trigger position might not be the most accurate option, since this could be subject to small fluctuations and is anyhow limited by the sampling frequency of the detector. On the other hand, the matched filter can be used to estimate the time at which a detector signal happens, as described in section 4.2.3, and by performing a parabolic interpolation of the three points near the maximum of the filtered signal it is possible to evaluate this timing with a precision lower than the resolution given by the sampling frequency. In section 4.2.3 the precision on the timing reconstruction is said to scale like $\sigma_{t_0} \propto A^{-1}$, this can be studied with the LED pulses as shown in Figure 5.42 where the points are fitted with the function:

$$\sigma_{t_0}(E_1) = k_{t_0} \cdot E_1^{p_{t_0}} + q_{t_0} \tag{5.12}$$

where E_1 is the energy recorded on TES 1, k_{t_0} is a normalization constant, q_{t_0} is a constant offset and p_{t_0} is the power law scaling of the time resolution and is expected to be -1. As visible from the inset in Figure 5.42, the best fit value of p_{t_0} is -1.09 ± 0.03, which is compatible with expectations within 3σ.

Once the time of the TES event has been accurately evaluated, the width and the offset of the coincidence window must be determined. To perform an unbiased evaluation of these two quantities, the time differences between a TES event and all the muon veto triggers in a ± 1 ms time window centered around the first is performed and are then used to fill the histogram in Figure 5.43. As visible from the plot, a peak is visible at around 0.025 ms (the structure is actually bimodal and the difference between the two peaks corresponds to the difference between two data samples in the TES waveform), which corresponds to the coincident events. This peak sits on top of a offset of events, visible from the sidebands of the histogram, which corresponds to the rate of random coincidences. By fitting the histogram with the following function:

$$Ae^{-\frac{1}{2}\left(\frac{\Delta t - \mu_{\Delta t}}{\sigma_{\Delta t}}\right)^2} + c \tag{5.13}$$

which consists of a Gaussian distribution, with parameters A, $\mu_{\Delta t}$ and $\sigma_{\Delta t}$, used to model the peak and a constant offset c to model the accidental coincidences, it is possible to extract the mean and the width of this distribution (the best fit values

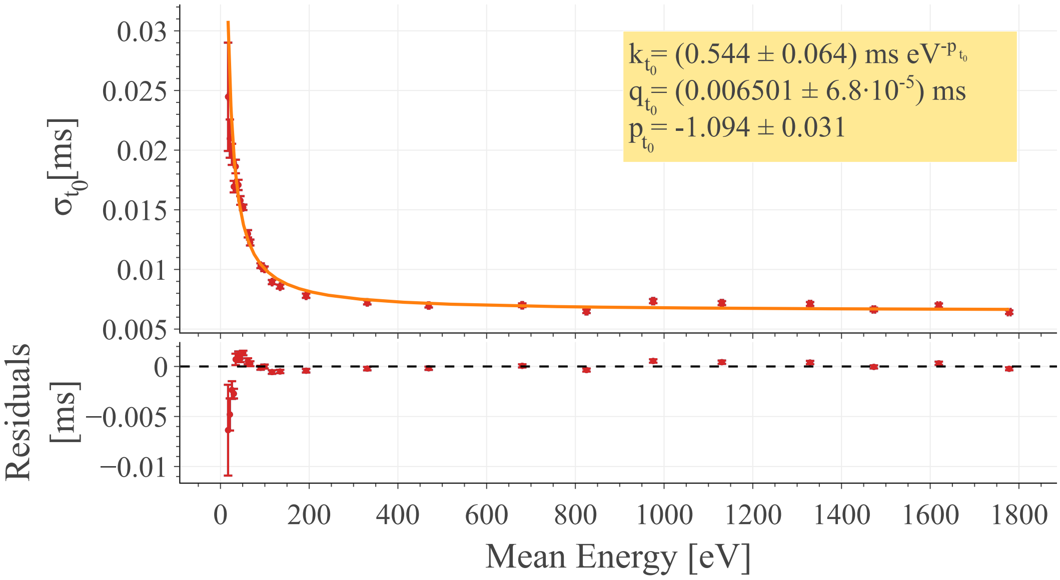

Figure 5.42. Scaling of the time reconstruction resolution done with the matched filter as a function of the reconstructed TES 1 energy E_1. The plots are expected to be distributed like E_1^{-1}. The best fit of eq. (5.12) to the data is plotted in orange, with the extracted values shown in the inset of the plot. The error bars represent the 1σ statistical fluctuations.

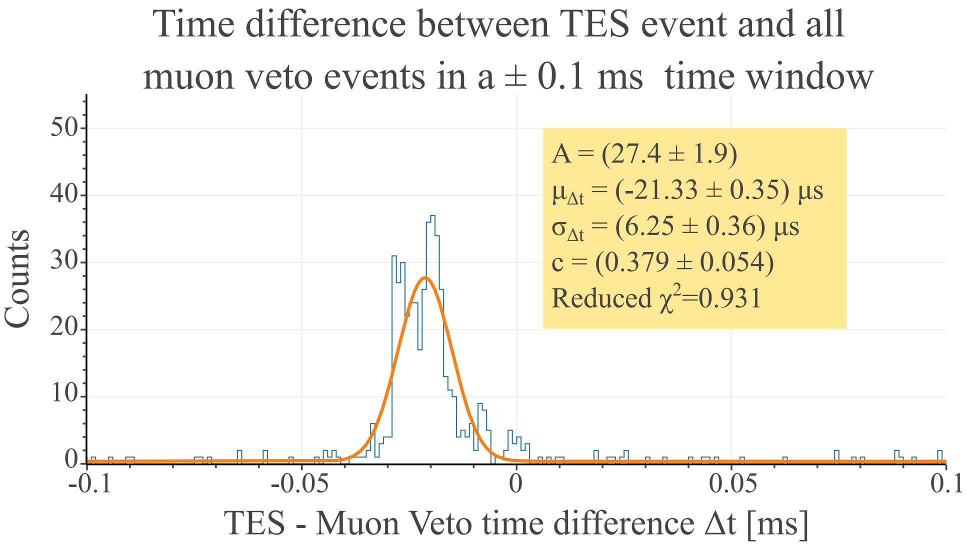

Figure 5.43. Histogram of the time differences between a TES event and all the muon veto triggers in a ±1 ms time window. The histogram is shown in the ±0.1 ms window for readability. In orange, the best fit of eq. (5.13) is shown with the best fit values written in the inset of the plot.

are shown in the inset of Figure 5.43). The $\mu_{\Delta t}$ parameter is particularly important at this stage since it defines the offset of the coincidence window.

Once $\mu_{\Delta t}$ is evaluated, to each TES 1 event time t_0 the muon veto event nearest to

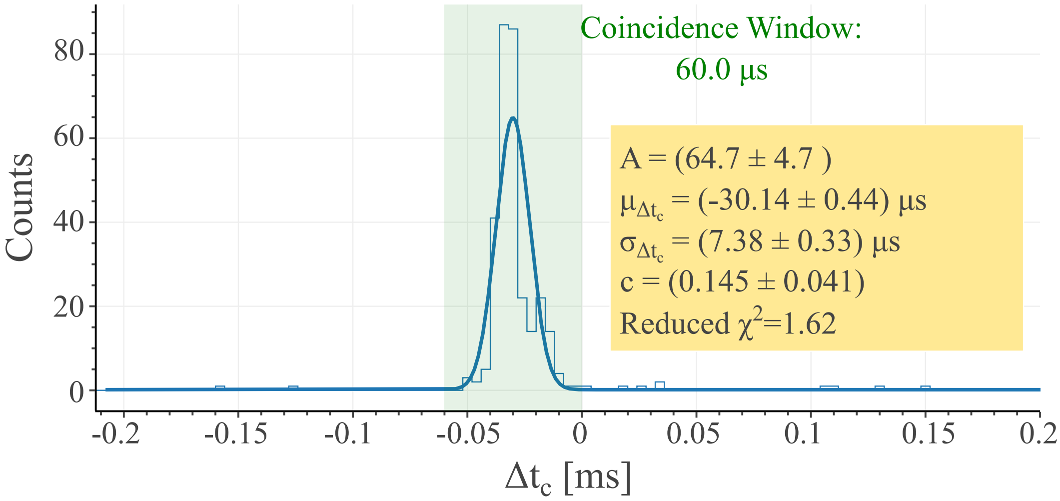

Figure 5.44. Histogram of the time difference between a TES 1 event and the nearest muon veto event. The best fit of the histogram with eq. (5.15) is shown in blue, with the fit parameters presented in the inset. The coincidence window is shown with the green shaded area. As noticeable the distribution is not centered at 0 as one would expect, this is due to the fact that the events used for the fit shown in Figure 5.43 are not as tightly selected as the ones considered here giving a fit result not completely representative of the considered population, for this reason a new fit is here performed in order to correct for this effect.

$t_0 + \mu_{\Delta t}$ is associated. Once each TES has an associated muon veto event, the time difference between the two is defined as:

$$\Delta t_c = t_0 + \mu_{\Delta t} - t_{MV} \tag{5.14}$$

where t_0 is the timing of the TES pulse, $\mu_{\Delta t}$ is the constant offset between the detectors and t_{MV} is the time of the muon veto trigger. Plotting the histogram of Δt_c allows to determine the coincidence window definition. In fact, as visible from Figure 5.44 it is possible to fit the function eq. (5.15) as before to extract what is the position and the width of the coincidence window.

$$Ae^{-\frac{1}{2}\left(\frac{\Delta t_c - \mu_{\Delta t_c}}{\sigma_{\Delta t_c}}\right)^2} + c \tag{5.15}$$

The coincidence window is then set to be $\Delta t_c \in [-60\ \mu\text{s}, 0\ \mu\text{s}]$, which corresponds to 3 acquisition points of the cryodetector data stream. An offset is still present in the distribution and is due to the different population of events that contribute to Figure 5.43 and Figure 5.44, in fact, the first is produced with no data quality selection while the second histogram is generated after the application of the waveform pulse shape cuts.

5.5.2.1 Study of accidental coincidences

Once the coincidence window between the muon veto ad TES 1 is set, it is important to check what is the rate of accidental coincidences induced in the analysis. Since the muon veto has a rate of around 200 Hz and is completely dominant with respect to the TES (which has a rate of particle interactions of around $10^{-}4$ Hz), the accidental probability can be approximated as the product between the muon veto rate and the width of the coincidence window:

$$p_{\text{acc}} \approx 200 \text{ Hz} \cdot 60 \ \mu\text{s} = 0.012$$

meaning that around 1.2% of the total TES 1 events could be mistakenly marked as being in coincidence with the muon veto.

This is a rough first estimation of accidental probability. A more refined one derives from the results of the fit shown in Figure 5.44. In fact, computing the integral of the constant offset inside the coincidence window and dividing it by the total number of events in the coincidence window (i.e. by summing the integral of the offset and of the Gaussian distribution) gives an estimate of p_{acc}. In practical terms, this translates to:

$$p_{\text{acc}} = \frac{c \cdot 60 \ \mu\text{s}}{A\sqrt{2\pi}\sigma_{\Delta t_c} + c \cdot 60 \ \mu\text{s}} = 0.0073 \pm 0.0022$$

where the parameters c, A and $\sigma_{\Delta t_c}$ are the ones in eq. (5.15) and 60 μs is the width of the coincidence window. With respect to the previous evaluation, this value appears underestimated but is still compatible with expectation within three times the statistical error.

Finally, a direct measurement of the accidental coincidence rate can be made by checking how many heater pulses are accidentally vetoed by the muon veto. As visible from Figure 5.45, throughout the energy spectrum there is a stable coincidence rate of $p_{acc} = 0.0114 \pm 0.0003$ which is closer to the first estimation done.

The first and the last estimations of the accidental coincidence rate point to a value of $p_{acc} \approx 1.2\%$. These two estimations are direct and do not rely on the fit quality as instead does the second evaluation of p_{acc} and are thus more trustworthy. Anyhow, the second evaluation of p_{acc} is compatible with the previous two under 3σ.

5.6 Energy Spectrum at the keV scale

Now that the whole analysis procedure is defined, it is possible to have a look at the energy spectra produced. Each data taking configuration is analyzed independently, meaning that all the histograms presented in this section have been separately generated for each acquisition week and have subsequently been stacked in order to analyze the full statistics. While stacking up histograms in counts is trivial, since it is just the sum of the bin contents, it is also necessary to study the plots normalized to Dark Matter Rate units (counts/keV kg day)(dru) in order to account for analysis

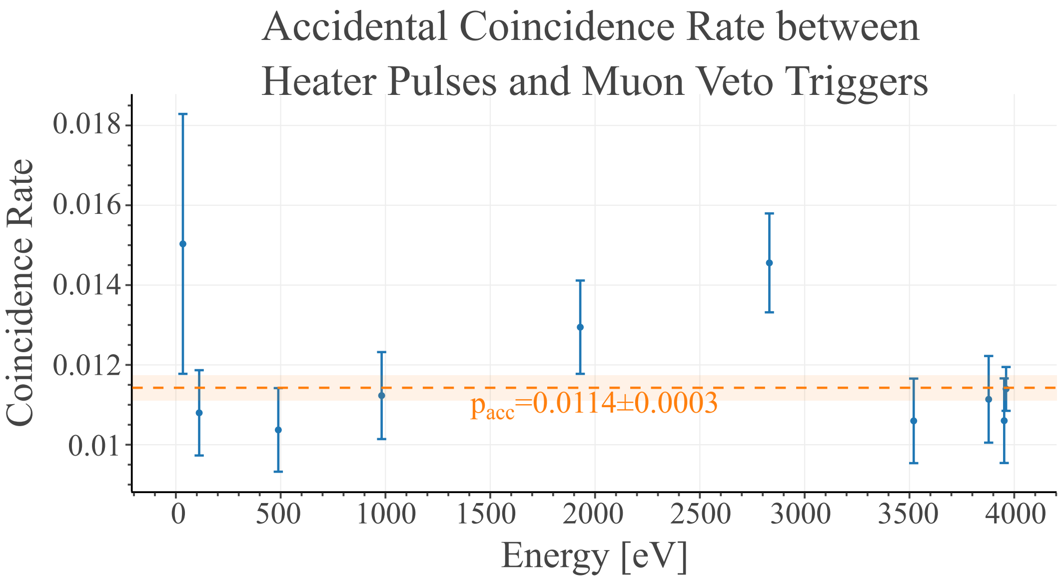

Figure 5.45. Evaluation of the accidental coincidence rate between the muon veto and heater induced pulses. The average value of p_{acc} is reported with the orange dashed line, and the orange area denotes the $\pm 1\sigma$ fluctuations of the parameter.

efficiencies. To produce the following normalized distributions, the strategy here described has been used.

The first step is to sum the counts present in the respective bins of the histograms generated by each configuration:

$$H_i = \sum_j h_i^j \tag{5.16}$$

where j is an index identifying the configuration while i is the index of the histogram bin, meaning that h_i^j is the bin i of the histogram generated in week j. The total histogram, in counts, is represented by H_i. The efficiency corresponding to this histogram is:

$$\varepsilon_i = \frac{\sum_j t^j \epsilon_i^j}{\sum_j t^j} \tag{5.17}$$

where, following the same notation as before, ϵ_i^j is the efficiency affecting the bin i of histogram j, t_j is the total measuring time contributing to histogram j and ε_i is the efficiency affecting the bin H_i. With this said the total normalized histogram is:

$$K_i = \frac{H_i}{(\sum_j t^j) \cdot m \cdot b_w \cdot \varepsilon_i} = \frac{H_i}{m \cdot b_w \cdot (\sum_j t^j \epsilon_i^j)} \tag{5.18}$$

where $m = 0.76 \times 10^{-3}$ kg is the mass of the Al_2O_3 cryocube, b_w is the bin width used for the histogram in keV and t_j is the total duration of the jth configuration expressed in days. Since $\sum_j t^j \epsilon_i^j$ corresponds to the total live-time of the measurement of bin i, the above definition corresponds exactly to the same histogram that one would obtain analyzing the data all together.

In Figure 5.46 the energy spectra for measured on TES 1 is plotted in dru and shows a rise in the event rate below 500 eV which will be discussed in section 5.7. On the other hand, in this section a discussion of the spectra above 1 keV is presented. The upper energy limit of this analysis is set at 3 keV in order to be certain that minimal detector non-linearities are introduced, on the other hand, as visible from the histogram the inclusion of also the region between 3 keV and 4 keV does not substantially alter the results. Moreover, choosing the range going from 1 keV to 3 keV completely removes the possibility of contamination due to false positives.

From Figure 5.4 it is visible that the expected energy spectra measured on the Al_2O_3 *cryocube* before and after the application of the muon veto anticoincidence cut are essentially flat in the range from 1 keV to 3 keV. For this reason, a fit of a single constant was used to get the average rate in this range was performed on the data. Since the histogram is in dru it was not possible to simply perform a Poisson log-likelihood minimization fit, but a *weighted log-likelihood fit* using the bin standard deviation was used in order to get the correct error on the parameters. This procedure is definitely overly complicated for the fit of a single constant, but, on the other hand, it allows to fit more complex functions to the data in future studies and was therefore implemented and tested.

As visible from Figure 5.46, the average counting rate on the Al_2O_3 double TES module before the use of the muon veto is of $(6.34 \pm 0.42) \cdot 10^3$ dru. After the application of the muon veto anticoincidence, the average counting rate is of $(2.30 \pm 0.26) \cdot 10^3$ dru as visible from Figure 5.47. The first consideration that can be made is that a $\sim 10\%$ statistical uncertainty has been reached on the evaluation of the background level of the experiment in this commissioning setup. Moreover, one can see the effect of the muon veto, which reduced the background level of a factor 2.75 ± 0.36. Finally, no noticeable features are present in the energy spectra above 1 keV for either before or after the application of the muon veto cuts.

5.6.1 Comparison with $CaWO_4$ detector and simulations

It is useful, to check the consistency of the analysis, to compare the results so far obtained with the ones from the $CaWO_4$ detector. It is worth mentioning that the analysis on the $CaWO_4$ *cryocube* is conceptually similar to the one presented so far, but it was conducted independently of this work. For this reason, just the few results useful to the understanding of the Al_2O_3 data are here presented.

Simultaneously to the comparison between the analysis results obtained with two *cryodetectors*, the results expected from the Geant4 simulations are also compared to check the level of disagreement. The simulations predict an almost flat background for the two detectors since the LEE currently cannot be simulated, this means that the comparisons here presented are conducted above the LEE region. In Table 5.2 a comparison of the expected and measured counting rates on the two detectors is shown.

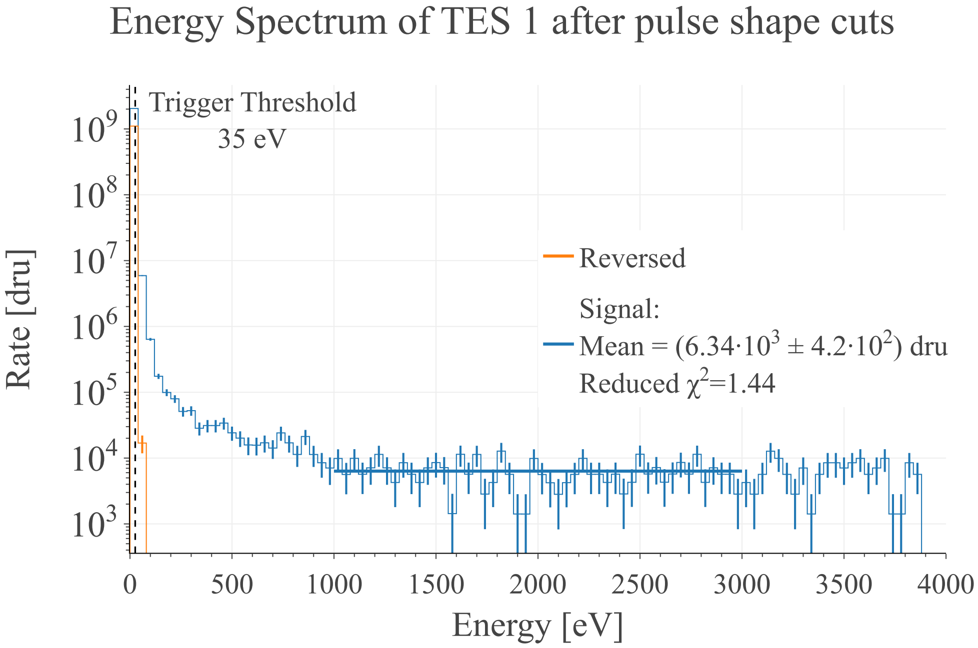

Figure 5.46. Energy spectrum recorded with the Al_2O_3 double TES module after the pulse shape cuts. In blue the histogram of the Signal (self triggers) events is plotted, while in orange the spectra of the Reversed (false positive) pulses is shown. A weighted likelihood fit (solid blue line) of a constant is performed between 1 keV and 3 keV to extract the average background value (the best fit values are shown in the legend). The error bars represent the 1σ statistical fluctuations on the height of the histogram, possible calibrations systematics were not included since they are still under investigation.

The first thing to notice is that the ratio between the rate measured on the Al_2O_3 detector and the $CaWO_4$ *cryocube* matches quite well the expected value from simulations, both before and after the use of the muon veto anticoincidence cut (see the last row of Table 5.2). In fact, by looking at the rightmost columns of the table, it is visible that the measured muon veto background attenuation factor matches the expected one at less than the 1σ level for both detectors. The fact that the two independent analyses of the cryodetectors are compatible with one another and give the same relative predictions as the simulations do is a strong confirmation of the validity of the conclusions made on the measured data.

Unfortunately, not all comparisons with simulations are in agreement. In fact, the absolute background level has been measured to be ~ 2.5 times higher than the one predicted from simulations. This increase in the overall rate is present in both cryodetectors and at all analysis steps. By making only this consideration, it is tempting to state that the muon flux is underestimated of a factor ~ 2.5 in the simulations. On the other hand, if one compares the measured muon spectrum with the simulated one (see Figure 5.48) one obtains almost perfect agreement (the agreement is at the level of a few percent), meaning that the muon flux is correctly estimated. This discrepancy is currently unexplained and its cause is being tracked down by the collaboration. The main suspects for the discrepancy are either a

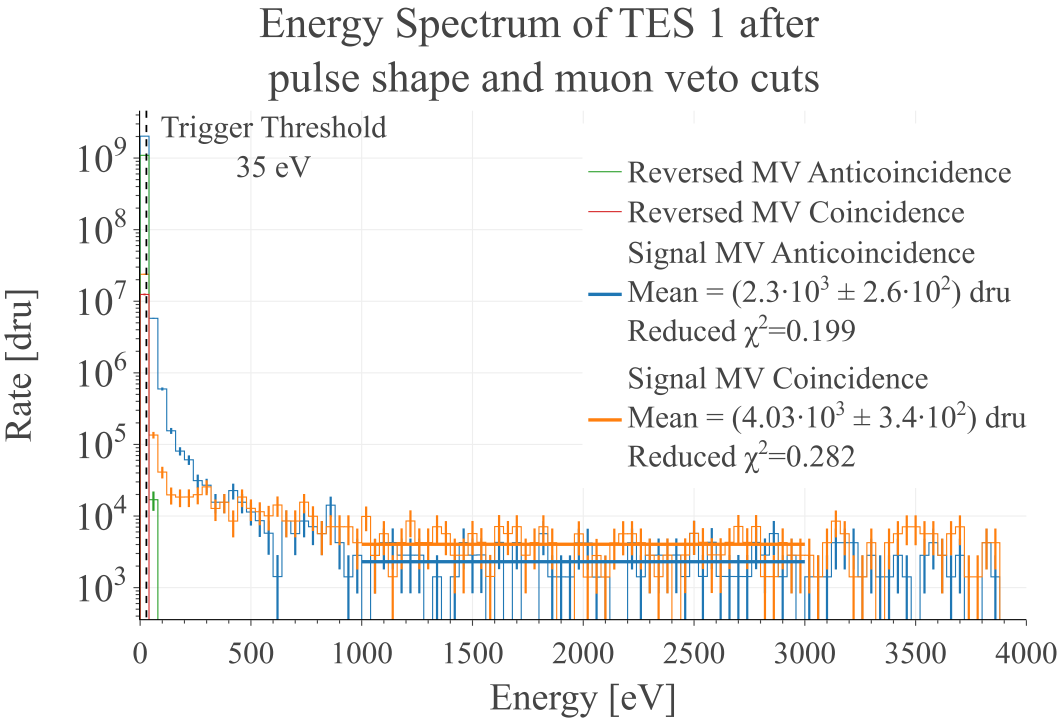

Figure 5.47. Energy spectrum recorded with the Al_2O_3 double TES module after the pulse shape cuts and the muon coincidence and anticoincidence cuts. The plot shows: in blue the histogram of the Signal events in anticoincidence with the muon veto, in orange the spectra of the Signal events in coincidence with the muon veto and in red and green the spectra of the Reversed triggers respectively in coincidence and anticoincidence with the muon veto. A weighted likelihood fit (solid blue and orange lines) of a constant is performed between 1 keV and 3 keV to extract the average background value for the two signal distributions (the best fit values are shown in the legend). The error bars represent the 1σ statistical fluctuations on the height of the histogram, possible calibrations sistematics were not included since they are still under investigation.

difference in the commissioned setup with respect to the simulated one or a wrong implementation of the physics processes that happen when a muon delivers energy inside the setup volume. The discrepancy with simulations much greater (more than a factor 2) than any non-linearity or detector effect that was not considered in this work, effectively making them negligible for this comparison (also they are comparable with the statistical uncertainty achieved). Moreover, due to the excellent agreement between the results from the independent analyses conducted on the Al_2O_3 and $CaWO_4$ detectors, it is unlikely that this mismatch is due to an analysis mistake.

5.7 Low Energy EXCESS

The previous section dealt with the comparison of the known background levels as reported from the analysis and the expectations from simulations. In this section, on the other hand, a discussion of the LEE is presented focusing on the energy range under 1 keV.

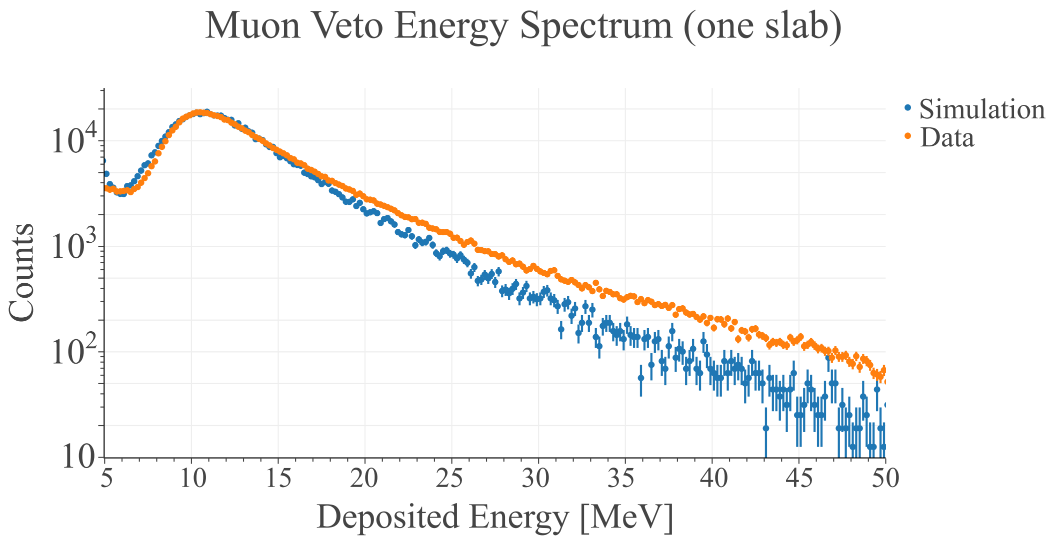

Figure 5.48. Comparison between simulations(blue) and data(orange) of the muon rate measured with one of the muon veto slabs. The peak visible at around 10 MeV is due to the ambient γ background, signals below this peak were classified as non-physical since the region is heavily populated by cross-talk signals coming from other muon veto slabs.

Table 5.2. Comparison table between the rate measured with the Al_2O_3 and $CaWO_4$ detectors and the corresponding simulations. The energy ranges considered are [1 keV, 3 keV] for the Al_2O_3 detector and [2 keV, 5 keV] for the $CaWO_4$ cryocube (the different ranges were necessary due to the differences in resolution and dynamical range). The rates before and after the application of the muon veto anticoincidence cut are reported, and the agreement with simulations is computed as the distance in terms of standard deviations. In the last three columns, the same operation is performed for the muon veto attenuation factor (defined as the ratio between the rates before and after the anticoincidence cut. In the last row of the table, the ratio between the rates in the two detectors is computed. All the reported errors are the 1σ statistical fluctuations.

	Before Muon Veto Cut			After Muon Veto Cut			Muon Veto Attenuation		
	Meas [dru]	Sim. [dru]	Dist. [σ]	Obs. [dru]	Sim. [dru]	Dist. [σ]	Obs.	Sim.	Dist. [σ]
Al_2O_3	6335 ±424	2490 ±76	8.9	2302 ±256	866 ±38	5.5	2.75 ±0.36	2.88 ±0.15	0.32
$CaWO_4$	2486 ±146	950 ±46	10	832 ±85	349 ±23	5.5	2.99 ±0.35	2.72 ±0.22	0.64
Ratio	2.55 ±0.23	2.62 ±0.15	0.27	2.77 ±0.42	2.48 ±0.20	0.62			

From the triggering study shown in Figure 5.32, the threshold was estimated to be $5\sigma_0 \approx 35$ eV and from Figure 5.49 it is possible to see that the distribution of the *reversed* triggers extends to 60 eV, meaning that above this energy it is highly unlikely to have the presence of false positives. For this reason, the analysis threshold is set at 60 eV.

As visible in Figure 5.49 there is a rise in the event rate under 500 eV which is not compatible with either the simulation expectations nor the false positives rate. As mentioned before in section 2.4.3, this rise is dubbed as Low Energy Excess (LEE). Since the Al_2O_3 double TES module allows to check for the origin of a signal by studying the energy sharing between the two sensors it is possible to define a region where the sharing follows expectations (*shared band*) and a region where it does not (*singles band*), for the formal definitions see section 5.4.5. In Figure 5.50 it is possible to see the spectra of these two populations. The first detail to notice is that the *reversed* distribution is mostly attributed to the *singles* population, this is expected since it is unlikely that there is a simultaneous noise fluctuation on both sensors with the correct energy ratio. Another detail that can be noticed is that the *singles* are extremely subdominant with respect to the *shared* band events, but both present a rise at low energies not compatible with noise false positives.

In the energy range from 60 eV to 1 keV there are 72 events classified as *singles* and 1636 events in the *shared* band. There are 58 *singles* like the one shown in Figure 5.36 and the rest are of the type shown in Figure 5.51 which present pulses on both sensors but with an unequal energy sharing. With this evaluation it is important to consider that at 60 eV stating whether a pulse is present in a waveform is not trivial due to the low SNR, by increasing the lower bound of the region 80 eV there are 14 *singles* events of the first type and 16 of the second. For the first type of event one could argue that the energy deposition happens in only one of the TESs giving rise to a single signal. On the other hand, for the second type of *singles* it is unclear what could be the origin of the unequal energy sharing but a dependence on the position of the interaction could still be a cause. From the double TES analysis the main difference seen with respect to previous runs is the relative rate of *singles* and *shared*, usually the first was always measured to have a similar or even a dominant contribution to the LEE with respect to the latter but instead in this run they result in only a 4% contribution, meaning that there is very little difference between the total and the shared low energy excess. For this reason, in the following considerations only the total LEE rate will be considered for simplicity.

During the EXCESS workshop of 2024 [95] the NUCLEUS experiment presented the LEE spectra shown in Figure 5.52. As visible from the histograms, in March 2024 the experiment measured an unexpectedly low level of LEE with respect to previous measurements and by further investigation it was concluded that it was not due to the fact that the measurement was done in the low background environment of UGL (same setup placing as this analysis), since by repeating the observation after a remounting of the Al_2O_3 cube the EXCESS rate raised again to surface-like levels. In fact in the first measurement the detector had been mounted in its holding structure for over a year and went through several thermal cycles while in the second UGL measurement the *cryocube* was recently remounted, it was suggested that the main source of the measured LEE could be due to mechanical stress which is relaxing over the time-span of months. This new data tends to disfavor this hypothesis since the time elapsed from the last remounting is of a most a few months, but the lowest level of EXCESS ever measured by NUCLEUS was observed. In sight of this new data, a better interpretation is that the possible component due to mechanical stress can be removed by performing a long precooling stage of the setup. As Figure 5.3

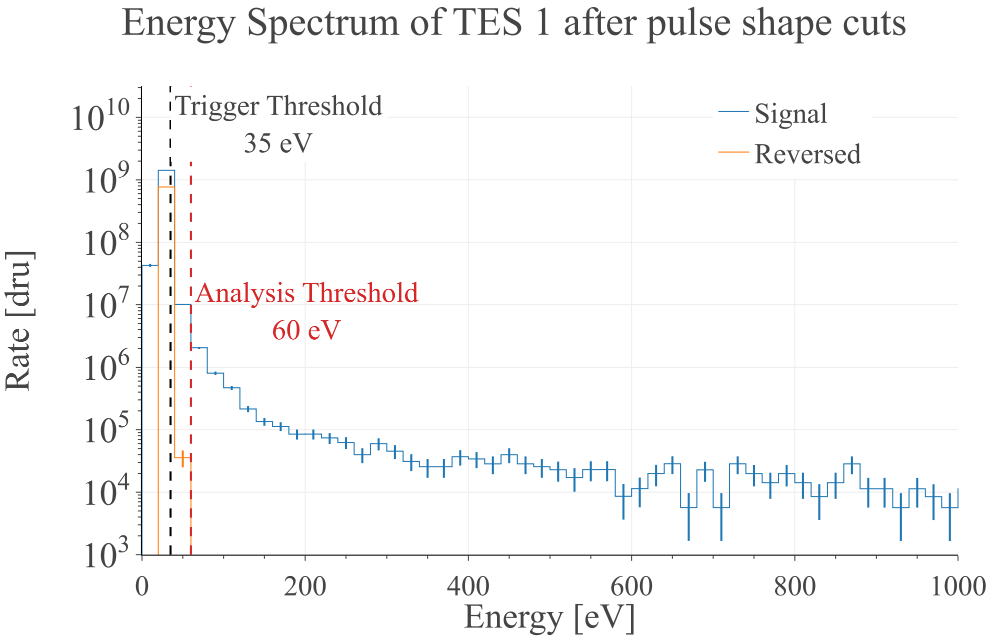

Figure 5.49. Spectrum of the LEE region for the reversed and the signal distributions. The black and red vertical dashed lines show the triggering and analysis thresholds. The error bars represent the 1σ statistical fluctuations on the height of the histogram.

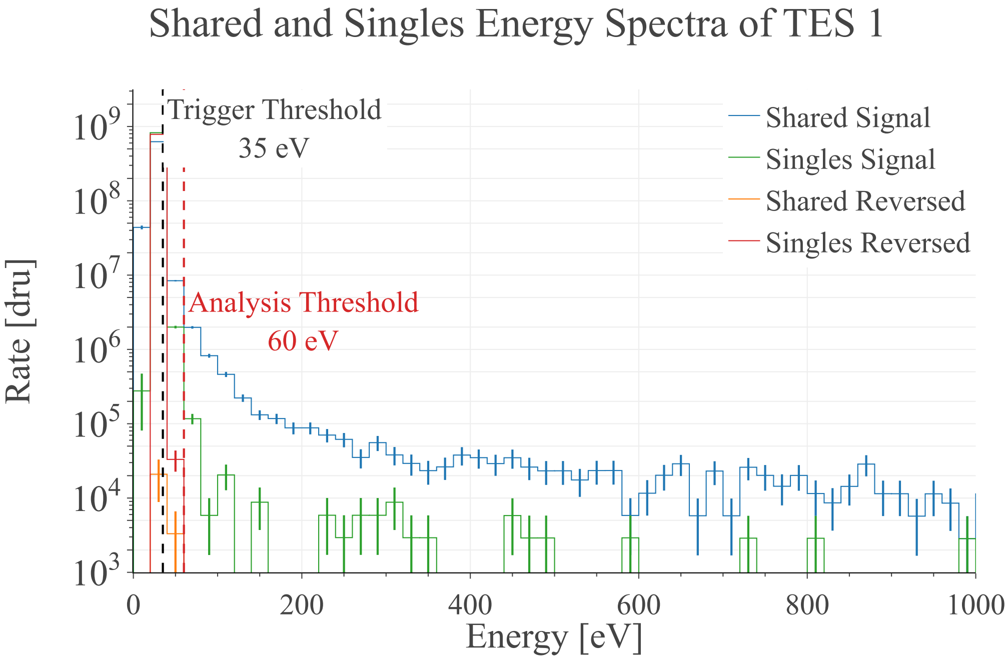

Figure 5.50. Spectrum of the LEE region for the *singles* and *shared* band distributions for both the reversed and the signal triggers. The black and red vertical dashed lines show the triggering and analysis thresholds. The error bars represent the 1σ statistical fluctuations on the height of the histogram.

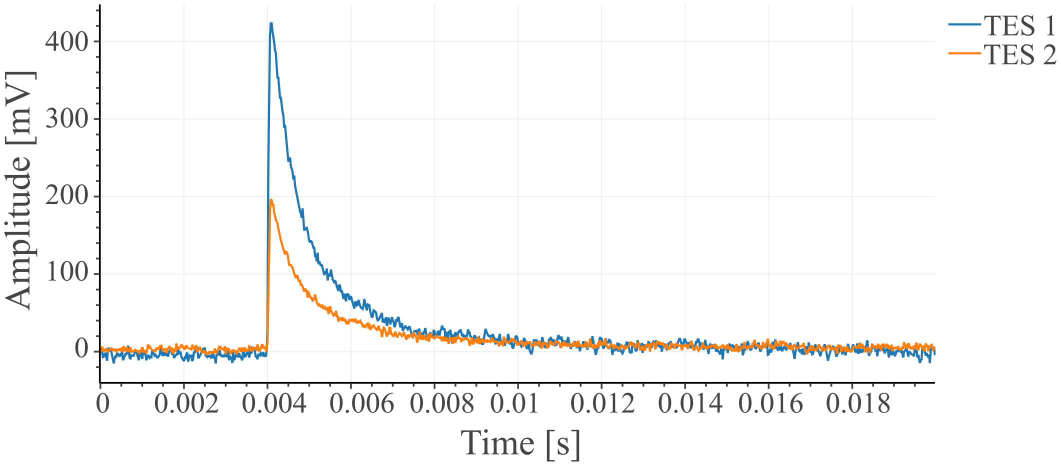

Figure 5.51. Event classified as being part of the *singles* band showing pulses on both TES but with an unequal energy sharing.

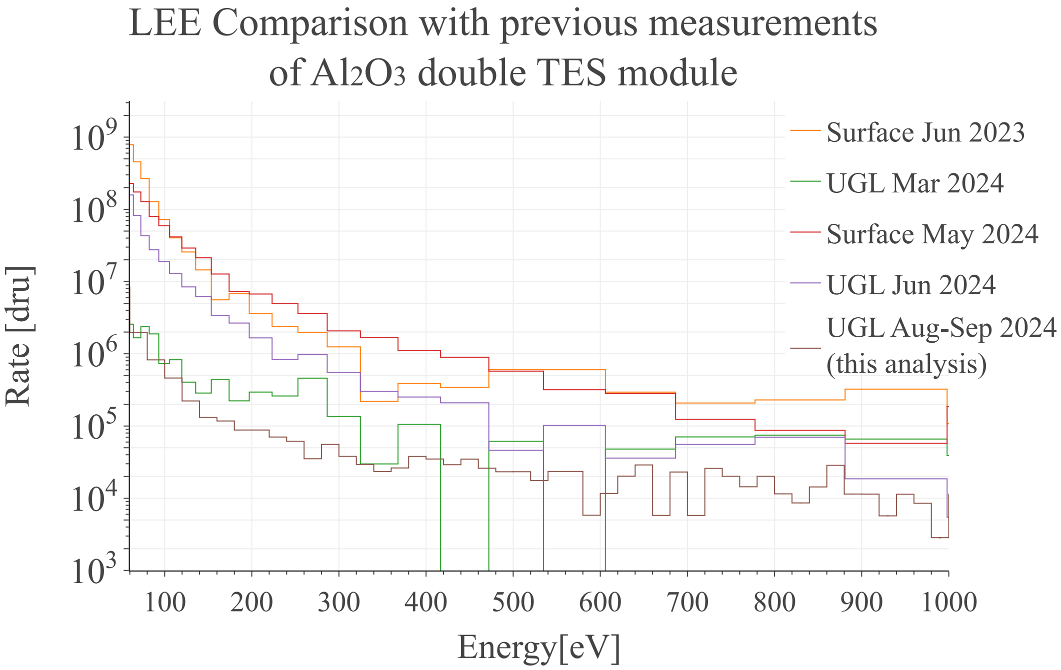

Figure 5.52. Comparison of the LEE region for multiple measurements done with the Al_2O_3 *cryocube* (presented in [81]). The spectra are labeled by the location (surface or UGL) and the date of the measurement. Between the Mar 2025 and May 2024 spectra the Al_2O_3 double TES module was remounted.

shows, the cooldown of this run took several days, while the usual cooldown time is around 48 h.

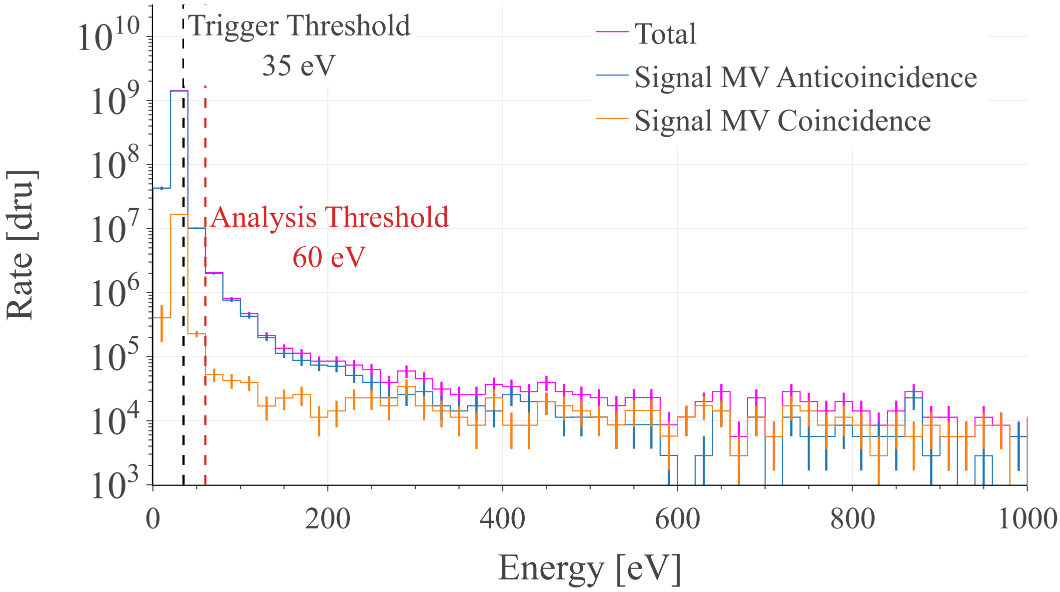

Figure 5.53. Energy spectrum of the LEE region shown for both the total energy spectrum and for the events in coincidence and anticoincidence with the muon veto. The black and red vertical dashed lines show the triggering and analysis thresholds. The error bars represent the 1σ statistical fluctuations on the height of the histogram.

To further investigate the origin of the LEE with the current setup, it is possible to check what happens when the muon veto is used. In Figure 5.53 the plot of the energy spectrum below 1 keV is shown with the muon veto coincidence and anticoincidence cuts applied. In Figure 5.54 the measured coincidence rate for each non-zero energy bin is shown, and it can be noticed that in the range from 60 eV to 200 eV there is a coincidence rate not compatible with the accidental rate but not yet in agreement with the expected true coincidence rate. This is an understandable behavior, in fact by comparing the spectra shown in Figure 5.53 it is visible that the events in coincidence with the muon veto produce an almost flat background on top of which sits the distribution of the LEE events.

In section 2.4.3 it was shown that there is a time decay of the LEE which is here investigated for this run. Two energy ranges have been decided to report the time decay results: the first one ranges from 60 eV to 120 eV which is the same as the one used in [80], the second one goes from 100 eV to 300 eV which was used by the collaboration to present the results at the EXCESS workshop. In Figure 5.55 the time evolution of the LEE rate is shown for the total spectrum, the spectra of events in coincidence and anticoincidence with the muon veto. To measure the decay constant the following decaying exponential was fitted to the data points:

$$Ae^{-\frac{t}{\tau}} + c \tag{5.19}$$

where A is a normalization constant, t is the time elapsed from the beginning of the cooldown, τ is the time decay constant and c is an offset. The decay of the total LEE spectrum shows a time constant of around 10 days for both energy ranges

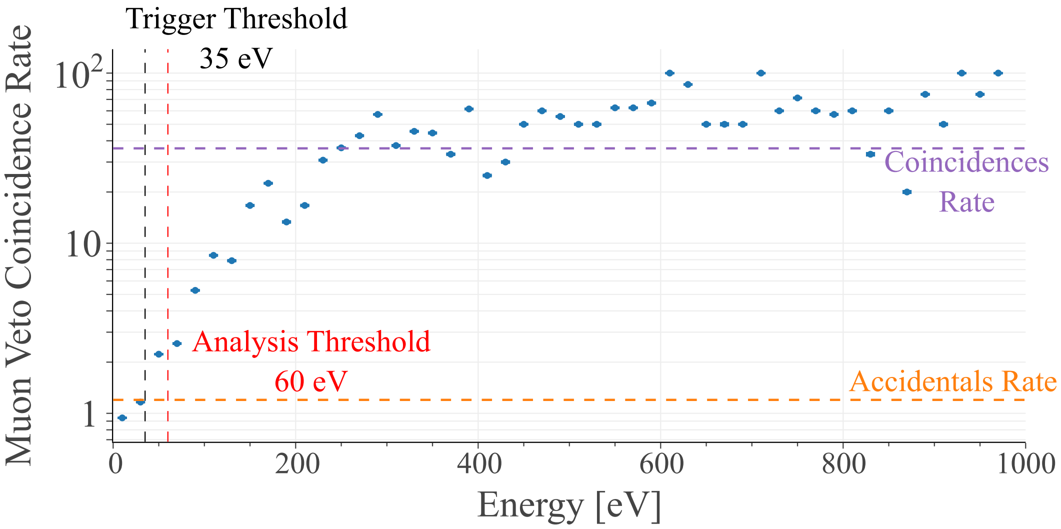

Figure 5.54. Muon Veto coincidence rate computed using only the non-zero bins of the spectra shown in Figure 5.53. The black and red vertical dashed lines show the triggering and analysis thresholds. The horizontal orange dashed line shows the accidental coincidence rate, while the horizontal purple dashed line is the measured rate of the true coincidences (the inverse of the attenuation factor in Table 5.2). The data points are above the purple line, since only the non-zero bins are considered in the evaluation of the scatter data. The error bars represent the 1σ statistical fluctuations of the data points.

considered, moreover the same conclusion is true for the spectrum with the muon veto anticoincidence cut. In the time dependence of the LEE in coincidence with the muon veto, no decay can be seen by eye or is spotted by the fit for the 100 eV to 300 eV energy range. On the other hand, a very fast decay of $\tau = (1.5 \pm 1.3)$ d is spotted in the 60 eV to 120 eV range but due to the wide error bars of the points it is not a statistically significant observation (by fitting a single constant a reduced $\chi^2 = 0.368$ is achieved showing essentially the same level of fit quality as the exponential function). The fact that the LEE in coincidence with the muon veto does not appear to decay is also expected, since the muon flux remained fairly constant throughout the data taking.

Comparing with [80], the total LEE decays at a smaller (but same order of magnitude) time constant as the faster decay rate mentioned in the article, which is $\tau = (18 \pm 7)$ d. The CRESST collaboration also reported the observation of a slower decay constant of ~ 150 days, which cannot be measured with this analysis due to the timescale of the measurement. The LEE decay measured in previous findings reported by NUCLEUS showed a time constant in the range of few days, meaning that in this measurement there was a slower decay. This is speculated to always be caused by the long cooldown time, if, in fact. there are multiple sources of LEE each with its own decay constant, then it is easy to imagine that during the cooldown the components of the spectrum with a time constant of at most a few days have completely decayed.

Summarizing, from this data three main observation on the LEE were made. The first is that the measured rate is the lowest ever observed by the NUCLEUS collaboration, with an unexpected low contribution of *singles* events to the spectra. The second is that the anticoincidence cut with muon veto does not remove the bulk of the LEE but only a $\sim 10\%$ contribution which is compatible with the spectrum of muon veto coincident events at higher energies. And lastly the decay constant of the LEE (only for the component in anticoincidence with the muon veto) was measured to be around ~ 10 days which is larger than previous observations made by NUCLEUS with the same detector.

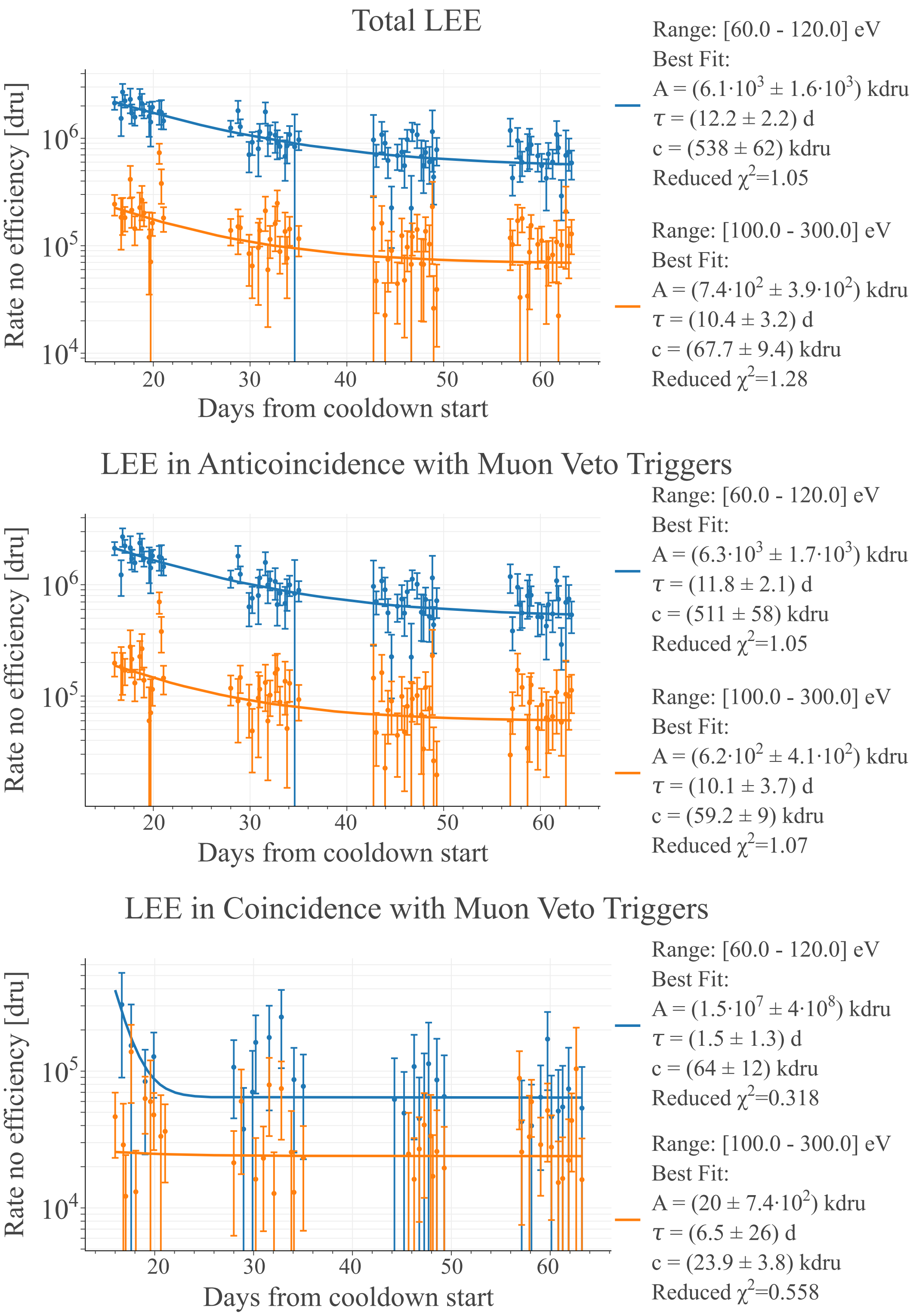

Figure 5.55. Decay of the LEE measured in two energy ranges: the first goes from 60 eV to 120 eV to match [80], the second goes from 100 eV to 300 eV to match [81]. The study is performed for the total spectrum (top) and for the events in coincidence and anticoincidence events in respectively the bottom and middle panels. The fit of function eq. (5.19) and the best fit is shown with the solid line of the respective color. The best fit values are shown in the legends of the plots and the error bars on the points are given by the 1σ statistical fluctuations.

5.8 Final Remarks

In this chapter the commissioning of the NUCLEUS setup was described, and it was shown that satisfactory and stable detector performances have been reached. The first data analysis on the Al_2O_3 *cryodetector* deployed in this setup is described in detail and the results on the background characterization have been shown. While a factor ~ 2.5 increase with respect to the expectation from simulations was measured in both the Al_2O_3 and $CaWO_4$ cryodetectors, the counting rate of the muon veto follows expectations. Moreover, it was seen that all the relative comparisons between the rates in the Al_2O_3 and $CaWO_4$ detectors match between analysis and simulations. This hints to a wrong implementation in the simulation of the particles produced by muons inside the detector shielding. Anyhow, the source of this discrepancy is currently being studied and is one of the main efforts of the collaboration.

Moreover, thanks to the peculiar properties and low noise RMS of the Al_2O_3 *double TES* module, a study of the LEE was conducted. From this analysis, it was possible to observe the lowest LEE measured by the NUCLEUS collaboration. The measured LEE also shows a time decay of $\sim$ 10 days, which is in contrast with previous observations done with the same detector, which showed a decay constant of at most a few days. This decay change, along with the overall lower LEE level, is speculated to be due to the long cooldown time of the commissioning run, which allowed for all the mechanical tensions to relax. Finally, the first characterization of the LEE with a muon veto was performed showing that $\sim 10\%$ of the LEE events between 60 eV and 200 eV are in coincidence with muon veto events which is not compatible with the 1.2% accidental coincidence rate. On the other hand, by studying the energy spectrum of the coincident events it is visible how their distribution is flat in all the measured energy range, meaning that the LEE is sits on top of this muon induced background and is not reduced with the vetoing. The last observation made regarding the Low Energy Excess is that with respect to previous measurements, the presence of events in the *singles* population is drastically reduced, contributing to only 4% of the LEE. With this data it is not possible to further understand the origins of the LEE and further observations need to be made to either find out its origins or a procedure that removes it.

In the context of this work the contributions given to reach the results presented in this chapter were the development and testing of the LANTERN LED driver, and most importantly the analysis of the data recorded with the Al_2O_3 detector in its full energy range. In particular, the analysis presented in this chapter was conducted by combining the results and methodologies presented in chapter 3, for the optical calibration procedure, and chapter 4 for the definition of data analysis protocols. The combined study of the data recorded with two TESs with the addition of the muon veto coincidence is a specific analysis step being performed for the first time, in the NUCLEUS experiment, with this analysis.

Chapter 6

Conclusions

In this thesis, multiple topics regarding the cryogenic calorimeters developed by the NUCLEUS collaboration are addressed. Particular attention is given to develop procedures to achieve a full detector characterization in view of the Coherent Elastic Neutrino-Nucleus Scattering measurement.

The two main difficulties in studying the behavior of these detectors are due to the low energies that they are built to detect (at the scale of few hundred electronvolts) and the fact that for a Coherent Elastic Neutrino-Nucleus Scattering measurement they need to be deployed in a low background setup. These requirements made the use of a radioactive calibration source of difficult implementation. For this reason, a new calibration procedure based on optical photons was devised and is here presented. To perform this calibration LANTERN, a custom hardware setup for the NUCLEUS experiment, was both completely developed and thoroughly characterized during the activities presented in this dissertation. LANTERN proved to be a versatile and cost-effective solution to perform the optical calibration of cryogenic calorimeters and was deployed in the commissioning of the NUCLEUS setup. In this work, it has been shown that the optical calibration gives results in line with the more classic X-ray calibration but drastically improves the characterization of the detector response, by giving the possibility of testing the calibration model.

To confirm that the NUCLEUS calorimeters respond equally to electron and nuclear recoils, a measurement using thermal neutrons as a calibration source was performed and is presented in this work. The absorption of such neutrons by the tungsten nuclei present in the detectors induces a nuclear recoil peak at ~100 eV. The data analysis, fully developed in the scope of this thesis, is aimed at detecting said peak, meaning that it had to be suitable to work in both a low Signal-to-Background environment and a low Signal-to-Noise regime. As a result from this analysis, the nuclear recoil peak was observed with a 3σ significance at the average energy of $106.7 \pm 2.0(\text{stat.}) \pm 10(\text{syst.})$ electronvolts in compatibility with expectations. This result was a milestone for the NUCLEUS experiment, since it proved that the target detectors are able to measure nuclear recoils at the 100 eV scale and that their response is independent of the original energy deposition. Moreover, since the data taking conditions of the CEνNS measurement are expected to be similar, the analysis here presented laid the groundwork for the one that will be used to extract the neutrino signal once the experiment is deployed at the Chooz-B nuclear power plant.

In the last chapter of this work, the knowledge acquired by the previous studies is combined to contribute to the commissioning of the NUCLEUS experimental setup in the Underground Laboratory present at the Technische Universität München. In the commissioned setup, the full NUCLEUS passive shield was deployed (except for the B_4C Becker) along with the muon veto and a single germanium crystal of the Cryogenic Outer Veto. One of the contributions given to the commissioning was the deployment of the LANTERN optical calibration system, which was used for the first time by the experiment to characterize two cryogenic calorimeters respectively built with Al_2O_3 and $CaWO_4$ substrates. In this work the analysis of the Al_2O_3 based cryogenic detector is presented and consisted of the full characterization of its response using the optical calibration as well as the use of the low Signal-to-Noise Ratio protocols previously developed to produce an estimation of the measured background level. Moreover, the first simultaneous operation of the NUCLEUS cryogenic calorimeters with the full muon veto was performed during the commissioning and the combined analysis of these two types of detectors was built and is here presented. This analysis resulted in a thorough characterization of the measured background level, which is then compared with expectations. This comparison showed an increase in the overall event rate above 1 keV of a factor 2.5 and is confirmed by the independent analysis performed on the $CaWO_4$ detector. On the other hand, the same event rate discrepancy is not visible in the muon veto, where the agreement with expectations is at the few percent level. This hints to a possible wrong simulation of the secondaries produced by the background interacting in the experimental volume or a wrong description of the setup geometry. An analysis mistake is unlikely since the two independent analyses performed of the Al_2O_3 and $CaWO_4$ data essentially give the same conclusions.

Finally, exploiting both the low noise level and the double signal readout characteristic of the Al_2O_3 based *double TES* detector, an evaluation of the background below 1 keV was performed. This region is characterized by an unexplained event rate increase seen by most of the low noise cryogenic calorimeter community, dubbed Low Energy Excess (LEE for short). The lowest level of the LEE ever recorded by the NUCLEUS collaboration was observed during the commissioning run, with an unusual contribution of the different populations identifiable via the use of the double readout. Moreover, a slower time decay constant of the Low Energy Excess with respect to previous measurements was observed. It has been speculated that all of the above features could be explained by the long time the system took to reach base temperature (> 10 days), but this statement requires further investigation. A last characterization of the LEE was done by employing the muon veto, which showed a 10% contribution due to muon induced events to this region of the energy spectrum. This contribution is compatible with the muon rate measured at higher energies, meaning that the Low Energy Excess does not appear to be removed by the use of the muon veto. This last evaluation is by itself a valuable piece of information since it is the first combined study of the LEE with a 4π muon veto coverage.

Summarizing, this thesis presents a way to characterize cryogenic calorimeters with detection thresholds at the scale of few tens of electronvolts that are deployed in low background environments. Moreover, a low Signal-to-Noise Ratio analysis has been developed to be used in combination with such detectors to achieve a fruitful detection of the nuclear recoils produced by the Coherent Elastic Neutrino-Nucleus Scattering. Finally, the analysis of the first data coming from the commissioning of the NUCLEUS setup is presented, allowing for a discussion and estimation of the background affecting the experiment.

Appendices

Appendix A

Basic Working Principle of a SQUID

In section 2.3.1.1 the SQUID was introduced simply as a device that converts a current I_s to a readout voltage V_s following the law:

$$V_s = g \cdot I_s \tag{A.1}$$

where g is the gain of the device. It can be useful to provide an intuitive explanation of its working principle to understand why it is an essential device to read out small I_s currents. The following discussion is extracted from the Mr. SQUID user manual [96] which provides an intuitive and effective discussion on the basic working principles and practices of a SQUID.

A SQUID is essentially a superconductive ring with two small interruptions (the Josephson junctions [97]). Let's start by analyzing the properties of a fully connected superconductive loop in order to easily introduce the junctions at a later stage.

A.1 Superconductive loops

In a normal conductive material the distribution of the electrons is described by multiple unrelated wavefuctions (one for each particle), on the other hand, when the material is in a superconductive state a single wavefunction describes all the pairs of electrons present (Cooper pairs [98]). This wavefunction may differ in phase from one point to another within the superconductor, but knowing the function in one place determines it in another (in jargon this is referred to as a many-body wavefunction). From quantum mechanics it is possible to derive that in a superconductive ring the product of the magnetic field passing through it and the area enclosed by the loop has to be an integer multiple of the *flux quantum* $\Phi_0 = h/2e$ (h is the Planck's constant and $2e$ is the charge of a Cooper pair). This phenomenon is the *magnetic flux quantization*, which can be explained by the following qualitative reasoning.

As mentioned above, knowing the phase of the wavefunction in one point of a superconductor determines it in all the material, when this is applied to a ring

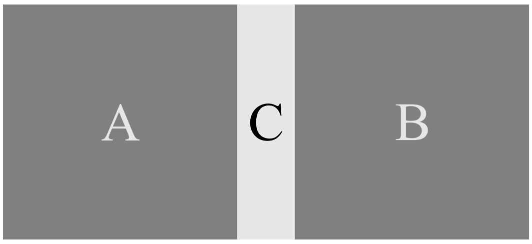

Figure A.1. Diagram of a Josephson junction where the two superconductors A and B are separated by a weak link C.

geometrical constraints come into play. In fact, by traveling around the ring one full circuit one ends up in the same initial position, meaning that the phase change for this path must be 2π for the wavefunction to have a single value at a given point in space. By combining this with the fact that applying a given amount of magnetic fields creates a specific phase change in the wavefunction, it is understandable that the magnetic flux inside a superconductive ring must be quantized. In fact, to maintain the single valuedness of the wavefunction, the phase change induced can only be a multiple of 2π, meaning that only discrete values of the magnetic flux are acceptable.

Magnetic flux quantization is the reason why current flows indefinitely in superconductive circuits. In fact, if a superconductive ring in cooled down in a one Φ_0 magnetic field which is then turned off, by Faraday's law of induction a current is generated in the ring that tries to oppose the change of the magnetic field. If the ring was normal conducting this current would quickly decay due to internal resistance, but since in a superconductor only magnetic fields that are an integer multiple of Φ_0 are allowed, there can be no decay but only a sudden stop of the current. This sudden stop would require that all electrons transition into another state simultaneously, which is an extraordinarily unlikely event, meaning that the current has to flow indefinitely (this phenomenon has been measured multiple times since the discovery of superconductivity).

A.2 Josephson Junction

In 1973 the Nobel Prize was awarded to Brian Josephson for the discovery of a peculiar interaction occurring when two superconductors are placed near each other. When two superconductors A and B are in proximity and are separated by a small enough weak link C, as in Figure A.1, the two electronic wavefunctions will be related, meaning that such a junction acts as a superconductor itself and currents can flow from A to B with zero resistance. The term *weak link* comes from the fact that Josephson junctions generally have a much lower critical current I_c, which is the maximum current that can be carried before resistance starts to appear, than the two superconductive materials.

This type of electrical component has no classic equivalent and is a completely new device which has proven essential in the development of superconductive electronics.

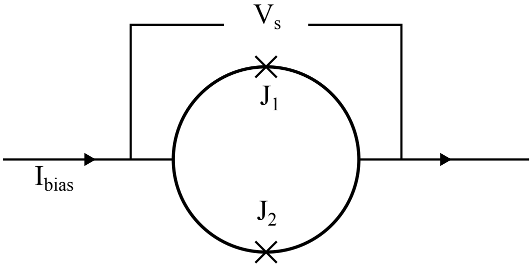

Figure A.2. Schematic representation of the DC SQUID. The bias current is indicated as I_{bias}, the readout voltage is V_s and $J_{1,2}$ are the two Josephson junctions.

A.3 DC SQUID

A DC SQUID consists of two Josephson junctions connected in parallel on a closed superconductive loop, as show in Figure A.2. If a bias current I_{bias} is sent through the SQUID and the device is symmetrical with two identical junctions, then the current will split equally in half on each side. The current I_{bias} flowing through the device will encounter no resistance as long as it does not surpass the critical current of the two junctions. On the other hand, when the critical current is surpassed the device starts to show resistance the readout voltage V_s is different from zero.

When the two junctions in the SQUID are identical, the loop is symmetrical and the applied magnetic field is zero, both junctions will show resistance for the same current flow, meaning that the critical current of a SQUID is twice the critical current of its junctions (which as typical values of 10 μA).

If on the same device one applies a magnetic field different from zero then a screening current I_s flows in the superconductive loop opposing the applied magnetic field (see Figure A.3). The current flowing in the two junctions becomes asymmetric: one of the junctions (J_1 in Figure A.3) experiences a lower current, meaning that higher I_{bias} are allowed, while the other junction (J_2 in Figure A.3) experiences a higher current, which makes it easier to reach its critical current. The presence of a magnetic field then creates an unbalanced situation which effectively lowers the critical current of the SQUID, meaning that lower values of I_{bias} are allowed before the device starts showing resistance. In fact, when J_2 goes normal conducting all the current passes through J_1, which makes it go normal conducting as well and the SQUID shows resistance.

The screening current I_s increases with the applied magnetic flux, but when the flux reaches a multiple of half a flux quantum Φ_0 the two junctions go momentarily normal conducting and the continuity of the superconductive loop is destroyed long enough for one quantum of magnetic flux to pop inside the loop, the superconductivity is then restored. This phenomenon can be understood by considering what happens to the screening current. In fact, it is less energetically convenient to generate a current I_s strong enough to counteract a magnetic field change of $0.51\Phi_0$ while it is more convenient to let one Φ_0 inside the loop (remember that the magnetic field inside a superconductive loop must be always an integer of Φ_0) and then generate a current to compensate the $0.49\Phi_0$ introduced (meaning that I_s changes direction),

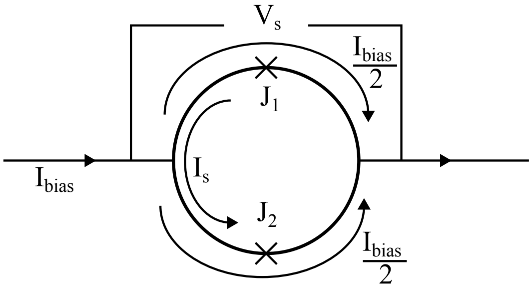

Figure A.3. DC SQUID behavior in the presence of an externally applied magnetic field, generating the screening current I_s.

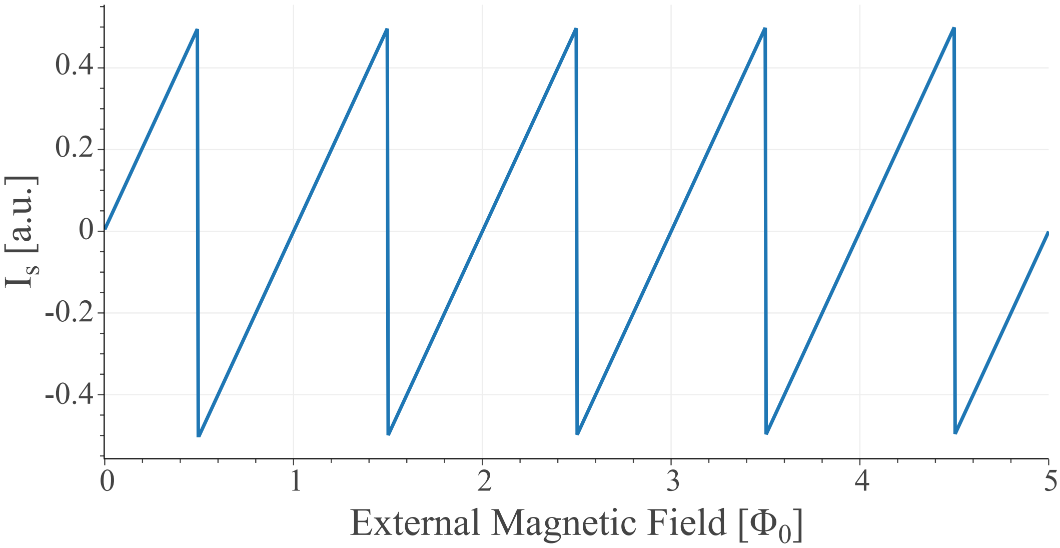

Figure A.4. Relationship between screening current and applied magnetic flux.

this behavior is shown in Figure A.4.

From the above discussion, it is clear that I_s is periodic with respect to the applied magnetic flux (with period Φ_0) and that the critical current of a SQUID depends on the applied magnetic field. This means that the critical current of a SQUID has a periodic dependence on the applied magnetic flux, as shown in Figure A.5. Supposing that the SQUID is biased with a current I_{bias}, slightly greater than its critical current, when no magnetic field is applied, then when an external magnetic flux of $\Phi_a = n\Phi_0$ is present (where n is an integer) the screening current I_s is zero and voltage V_s shows a minimum. Instead, when $\Phi_a = \left(n + \frac{1}{2}\right)\Phi_0$ the screening current I_s is maximum and V_s shows a maximum.

This relation between the applied magnetic field and the output voltage of a SQUID makes it a magnetometer, and since Φ_0 is extremely small ($\Phi_0 = 2.067 \times 10^{-15}$ Wb) the SQUID is extremely sensitive to small changes of the magnetic field. By converting a current I in a magnetic field using an inductor, it is then possible to measure extremely small currents with the SQUID making it a suitable device to measure the current passing through the readout circuit in section 2.3.1.1.

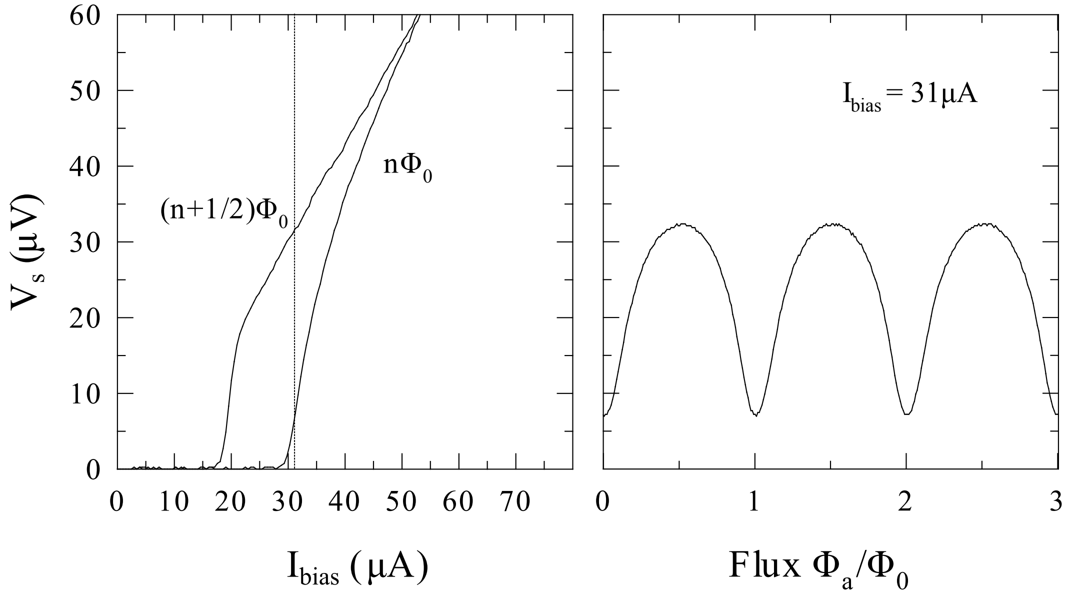

Figure A.5. Voltage-Current (left) and Voltage-Flux (right) characteristics of a DC SQUID showing the periodic dependence of the device readout voltage as a function of the applied flux for a fixed bias current I_{bias}. Figure from [96].

This qualitative discussion on the working principle of a SQUID is useful to understand the basic concepts, but it is not complete since it does not show the quantum interference happening between the wavefunctions of the two junctions which creates an interference pattern on how the critical current varies with the applied magnetic flux. For a more complete discussion, refer to [76].

Appendix B

Noise Equivalent Power

In section 4.2.3.4 the NEP was introduced to study, in absolute units, the response of cryogenic calorimeters after the application of the matched filter. The definition of the NEP is:

$$\mathrm{NEP}(f) = \frac{\sqrt{N_{PSD}(f)}}{|S(f)|} \tag{B.1}$$

where $S(f)$ is the Fourier transform of the signal template in Hz^{-1} and $N_{PSD}(f)$ is the NPSD expressed in $\frac{\mathrm{eV}^2}{\mathrm{Hz}}$. Taking a toy model signal of the form:

$$s(t; t_0, \tau_D, \tau_R) = \left(e^{-\frac{t-t_0}{\tau_D}} - e^{-\frac{t-t_0}{\tau_R}}\right)\theta(t-t_0) \tag{B.2}$$

where t_0 is the starting time of the signal, τ_D and τ_R are respectively the rise and decay time constants of the pulse and $\theta(t)$ is the Heaviside step function. The Fourier transform of this toy model signal shape is:

$$S(f) = e^{-2j\pi f t_0}\left(\frac{\tau_D - \tau_R}{(2j\pi f\tau_D + 1)(2j\pi f\tau_R + 1)}\right) \tag{B.3}$$

where j is the imaginary unit. Both the time domain and frequency domain representations of the signal toy model are presented in Figure B.1.

With this expression of the pulse shape, the NEP becomes:

$$\mathrm{NEP}(f) = \sqrt{N_{PSD}(f)}\left[\frac{(1+4\pi^2 f^2\tau_D^2)(1+4\pi^2 f^2\tau_R^2)}{(\tau_D - \tau_R)^2}\right]^{\frac{1}{2}} \tag{B.4}$$

By making the assumption that $\tau_R \ll \tau_D$, which is in general true since they are usually distant more than an order of magnitude, the NEP is simplified to:

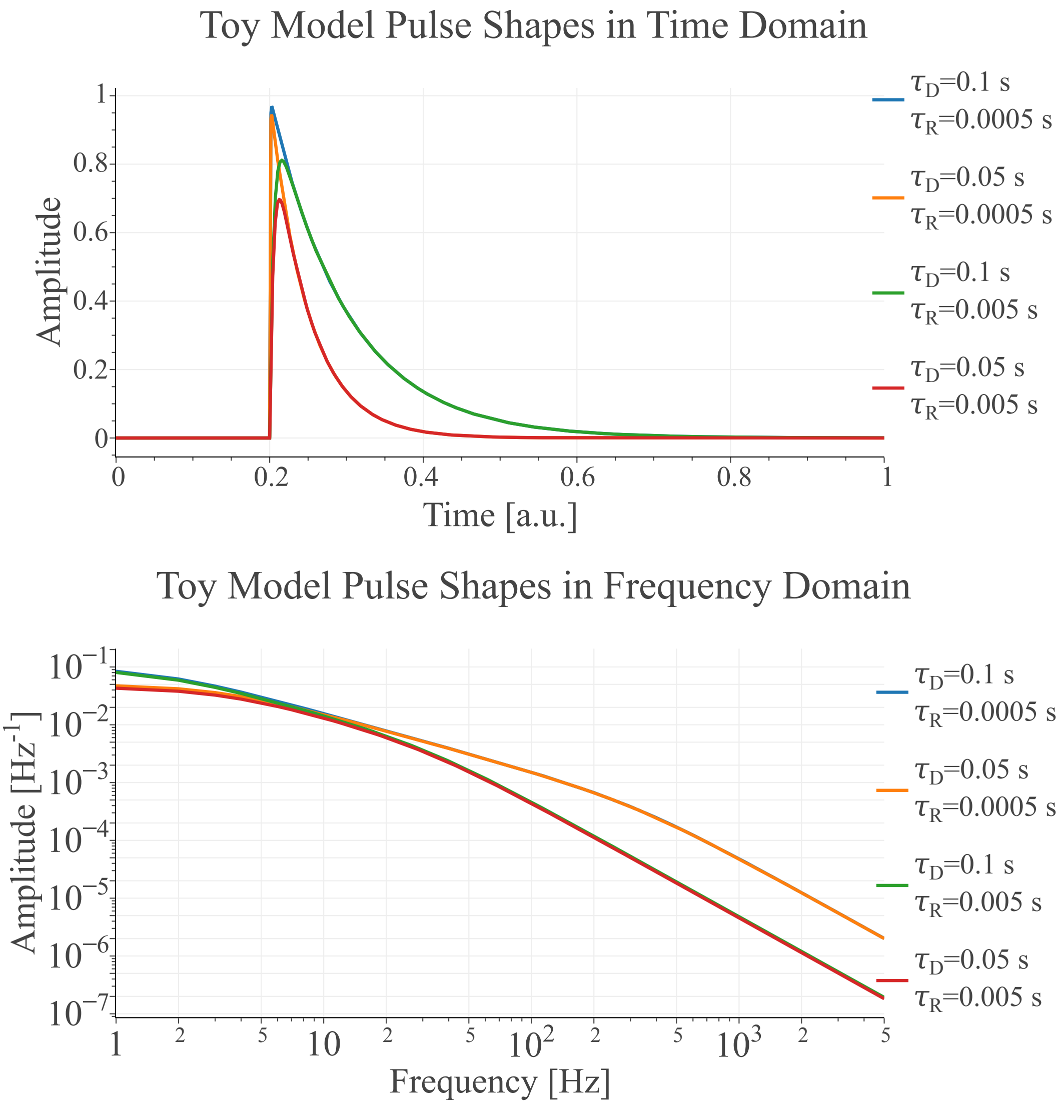

Figure B.1. Time domain (top) and frequency domain (bottom) representations of the signal toy model plotted for various combinations of τ_D and τ_R.

$$\mathrm{NEP}(f) \approx \sqrt{N_{PSD}(f)}\left[\frac{1}{\tau_D^2} + 4\pi^2 f^2 + 16\pi^4 f^4 \tau_R^2\right]^{\frac{1}{2}} \tag{B.5}$$

For low frequencies then the NEP is essentially dominated by the decay constant of the detector, in fact:

$$\mathrm{NEP}(0) = \frac{\sqrt{N_{PSD}(0)}}{\tau_D} \tag{B.6}$$

and since a lower NEP means a lower resolution, then having a very long decaying pulse is in general beneficial (this obviously depends on the shape of the NPSD). On the other hand, at high frequencies the f^4 term dominates giving:

$$\mathrm{NEP}(f \gg 0) \approx \sqrt{N_{PSD}(f)}\left(4\pi^2 f^2 \tau_R\right) \tag{B.7}$$

which shows that having fast rising pulses (i.e. with small τ_R) lowers the resolution. This is an intuitive fact, by increasing τ_D and lowering τ_R the frequency band of the signal is expanded, meaning that the SNR is high over more frequency components.

B.1 Optimizing Detector Parameters for best resolution

The resolution of the detector in electronvolts can then be expressed, starting from the NEP, as:

$$\sigma_n^2 = \left[\int_{-\infty}^{\infty} \frac{1}{\mathrm{NEP}(f)^2} df\right]^{-1} \tag{B.8}$$

and by making some assumptions on the shape of the NPSD it is possible to extract its behavior with respect to the τ_D and τ_R parameters (always keeping the assumption $\tau_R \ll \tau_D$).

In the case of white noise, meaning that the NPSD is constant (i.e. scaling as f^{-0}), then the NEP becomes:

$$\mathrm{NEP}_0(f) \propto \left[\frac{1}{\tau_D^2} + 4\pi^2 f^2 + 16\pi^4 f^4 \tau_R^2\right]^{\frac{1}{2}} \tag{B.9}$$

and the resolution is:

$$\sigma_0^2 \propto \frac{4}{\tau_D} \frac{1 + \tau_R/\tau_D}{(1 - \tau_R/\tau_D)^2} \rightarrow \frac{4}{\tau_D} \tag{B.10}$$

this entails that for white noise a long decay time gives a better SNR.

In the case of pink noise, meaning that the NPSD scales as f^{-1}, the NEP and the resolution are:

$$\mathrm{NEP}_1(f) \propto \left[\frac{1}{f\tau_D^2} + 4\pi^2 f + 16\pi^4 f^3 \tau_R^2\right]^{\frac{1}{2}} \tag{B.11}$$

$$\sigma_1^2 \propto \frac{4\pi^2}{\log(\tau_D/\tau_R)} \frac{1 + \tau_R/\tau_D}{1 - \tau_R/\tau_D} \rightarrow \frac{4\pi^2}{\log(\tau_D/\tau_R)} \tag{B.12}$$

this is a slightly more realistic noise scenario and, similarly to the previous case, shows that incrementing the gap between τ_R and τ_D is beneficial to the resolution.

The last type of noise analyzed is the case with brown noise, meaning that the NPSD scales as f^{-2}, the NEP and the resolution are:

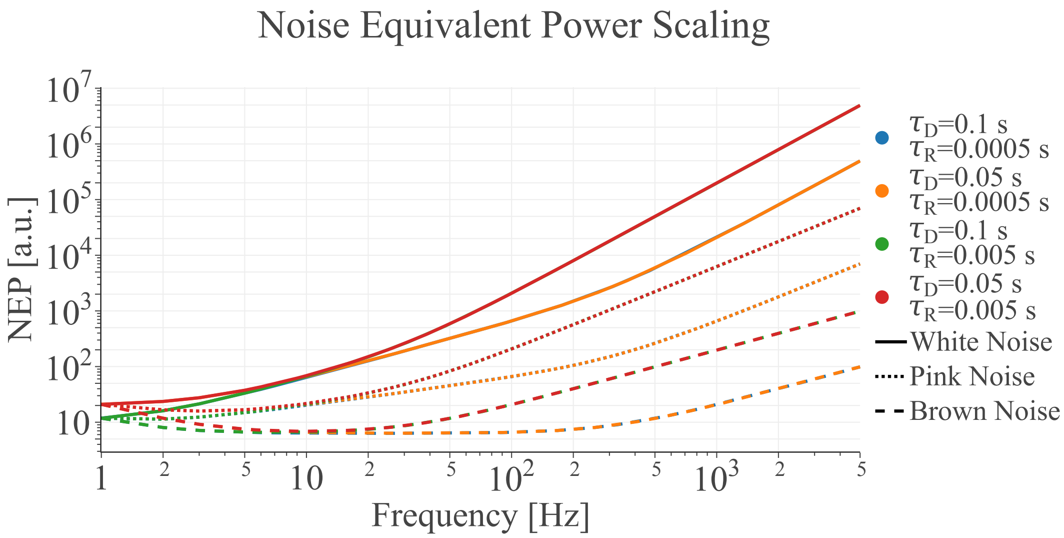

Figure B.2. NEP for the toy model, pulse shapes displayed in Figure B.1 (distinguished by color) in the three noise conditions analyzed (distinguished by the line-style).

$$\mathrm{NEP}_2(f) \propto \left[\frac{1}{f^2\tau_D^2} + 4\pi^2 + 16\pi^4 f^2\tau_R^2\right]^{\frac{1}{2}} \tag{B.13}$$

$$\sigma_2^2 \propto 16\pi^2\tau_R\frac{1+\tau_R/\tau_D}{(1-\tau_R/\tau_D)^2} \rightarrow 16\pi^2\tau_R \tag{B.14}$$

Differently from the previous scenarios, this one shows that the resolution is more impacted by having a lower τ_R. This can be understood by considering that if the NPSD decays quickly, it is more efficient to move the signal to a high frequency band than to have a low level of NEP at low frequencies.

The behavior of the NEP in the previous three noise cases are plotted in Figure B.2 while the scaling of the resolutions with respect to the rise and decay time constants of the pulses are respectively plotted in Figure B.4 and Figure B.3.

B.2 Remarks

In all this discussion, the assumption that the energy integration was instantaneous was made. Obviously, this is not the case, meaning that there is a lower limit to the reduction of τ_R after which not all the energy is integrated in the pulse amplitude increasing again the resolution, making the detector transition from being operated as a calorimeter to a bolometer. This is already partially taken into account by choosing to not normalize the signal toy model to 1, in this way the amplitude of the signal is dependent on the time constants.

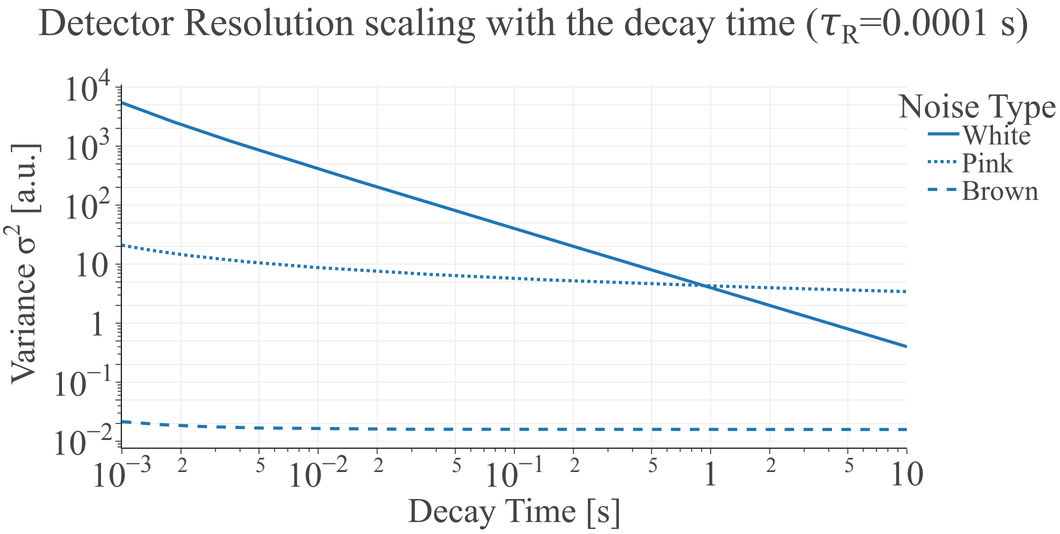

Figure B.3. Scaling of the detector resolution with respect to the decay time of the pulses. The scaling is plotted for the three noise conditions analyzed.

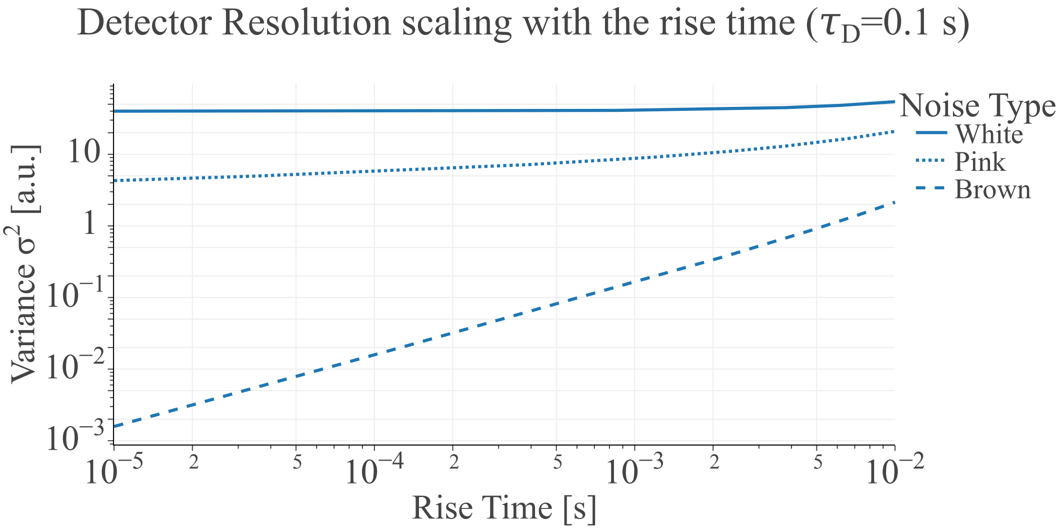

Figure B.4. Scaling of the detector resolution with respect to the rise time of the pulses. The scaling is plotted for the three noise conditions analyzed.

Appendix C

Linearization of $\chi_{L,R}$

In section 4.2.4 the matched filter based pulse shape parameters $\chi_{L,R}$ were presented. It was mentioned that they are only normally distributed around zero and with standard deviation 1 if the detector signals can be fully represented as:

$$v(t) = A \cdot s(t) + n(t) \tag{C.1}$$

where $v(t)$ is the detector signal. $s(t)$ is the signal template, A is the pulse amplitude and $n(t)$ is the noise of the system. If instead, the detector response is of the form:

$$v(t) = A \cdot s(t) + k(t, A) + n(t) \tag{C.2}$$

where $k(t, A)$ is a deviation from the signal template that can be dependent on the amplitude, then the $\chi_{L,R}$ parameters do not behave as expected.

The application of the matched filter is a linear operation, so if the signal is of the form presented in eq. (C.2) then its filtered equivalent is:

$$v^f(t) = A \cdot s^f(t) + k^f(t, A) + n^f(t) \tag{C.3}$$

where f indicates the filtering operation.

The definition of $\chi_{L,R}$ is:

$$\chi_{L,R} := \chi(t_{L,R}, t_0) = \frac{v^f(t_{L,R}) - \alpha(t_{L,R}) \cdot v^f_{max}}{\sigma_{eff}(t_{L,R}, t_0)} \tag{C.4}$$

where v^f_{max} with is the maximum of the filtered signal happening at the time t_0 and:

$$\sigma_{eff}(t_{L,R}, t_0) = \sqrt{\sigma_n^2 \cdot (1 + \alpha(t)^2) - 2\alpha(t) \cdot R(t - t_0)}$$

$$\alpha(t) = \frac{s^f(t)}{s^f_{max}}$$

where σ_n is the standard deviation of the filtered noise, $R(t-t_0)$ is the autocorrelation function of the filtered noise between the time t and the time t_0 and s^f_{max} is the maximum of the filtered signal template. Then by plugging eq. (C.3) in eq. (C.4), it becomes:

$$\chi_{L,R} = \frac{A \cdot s^f(t_{L,R}) + k^f(t_{L,R}, A) + n^f(t_{L,R}) - \alpha(t_{L,R}) \cdot v^f_{max}}{\sigma_{eff}} \tag{C.5}$$

To evaluate the parameters derived from the matched filtered signal, the maximum of the signal v^f_{max} is searched getting the position t_0, the template is then aligned to have maximum in t_0 and the amplitude A is set such that $v^f_{max} = A \cdot s^f_{max}$. Inserting this information in the previous equation, it becomes:

$$\begin{aligned}\chi_{L,R} &= \frac{A \cdot s^f(t_{L,R}) + k^f(t_{L,R}, A) + n^f(t_{L,R}) - \alpha(t_{L,R}) \cdot A \cdot s^f_{max}}{\sigma_{eff}} = \\ &= \frac{A \cdot s^f(t_{L,R}) + k^f(t_{L,R}, A) + n^f(t_{L,R}) - A \cdot s^f(t_{L,R})}{\sigma_{eff}} = \\ &= \frac{k^f(t_{L,R}, A) + n^f(t_{L,R})}{\sigma_{eff}}\end{aligned} \tag{C.6}$$

In absence of the signal deviation, the *linear* versions of $\chi_{L,R}$ are found:

$$\chi^{lin}_{L,R} := \frac{n^f(t_{L,R})}{\sigma_{eff}} \qquad \langle \chi^{lin}_{L,R} \rangle = \frac{\langle n^f(t_{L,R}) \rangle}{\sigma_{eff}} = 0 \qquad \sigma_{\chi^{lin}_{L,R}} = \frac{\sigma_{n^f(t_{L,R})}}{\sigma_{eff}} = 1 \tag{C.7}$$

It is then visible how the presence of a deviation from the signal template introduces an amplitude dependence of $\chi_{L,R}$.

If there are multiple control populations at different amplitudes A in the data, it is then possible to extrapolate an effective behavior of $k^f(t_{L,R}, A)$ by averaging the values of $\chi_{L,R}$ for the various populations, in fact the mean value of $\chi_{L,R}$ is:

$$\langle \chi_{L,R} \rangle = \frac{k^f(t_{L,R}, A) + \langle n^f(t_{L,R}) \rangle}{\sigma_{eff}} = \frac{k^f(t_{L,R}, A)}{\sigma_{eff}} \tag{C.8}$$

meaning that it is possible to extrapolate $\chi^{lin}_{L,R}$ from $\chi_{L,R}$ by doing:

$$\chi^{lin}_{L,R} = \chi_{L,R} - \langle \chi_{L,R} \rangle = \frac{n^f(t_{L,R})}{\sigma_{eff}} \tag{C.9}$$

which is then a variable well distributed over all the control populations.

This *linearization* of $\chi_{L,R}$ allows then to have a normally distributed pulse shape parameter over all the energy range and allows for energy independent quality cuts and efficiencies. A drawback of this procedure is that to accurately extract the pulse shape deviation from the data, a quite dense number of control populations are needed over the ROI of the measurement (this can be achieved by using LED induces pulses generated with the system in chapter 3).

Appendix D

PyDIANA

The ideal features for any analysis software are: robustness, speed, low memory usage, richness in ready to use algorithms, easy data handling and visualization. The classical Diana C++/ROOT [99] structure, which is used in the CUORE experiment [100], is not sufficient to ensure all the above criteria. While it does satisfy most of them, it does not allow for easy data handling and visualization and has a slow learning curve.

These are the reasons why *PyDiana* was created as a versatile python front-end to a robust C++/ROOT back-end. *PyDiana* is based on the new PyROOT [99] interface that allows to seamlessly integrate C++ code and ROOT classes into a python framework, ensuring a complete interoperability of both the data and the software. Moreover, via the use of the highly developed python based libraries, it is now possible to have a web interface to run the analysis on computing clusters.

A typical problem of python based data handling and visualization codes is the high memory consumption unless specific actions are taken to avoid it. *PyDiana* makes heavy use of the new *RDataframe* object available with ROOT to interface with the analyzed data with low memory usage and quick computation times thanks to the innate multicore computing of these objects.

In general, this newly developed python ecosystem has proven to be a winning choice, combing the best aspects of the C++ and python languages as shown in Figure D.1.

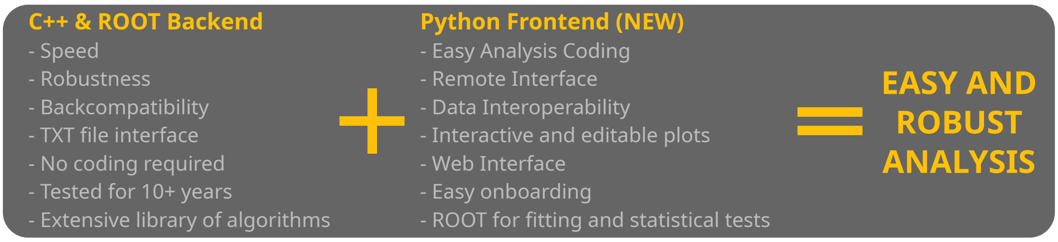

Figure D.1. Conceptual diagram of the new analysis framework, combining a C++ backend (*Diana*) and a python frontend (*PyDiana*).

Bibliography

[1] D. Akimov, J. B. Albert, P. An, and et al. Observation of coherent elastic neutrino-nucleus scattering. *Science*, 357(6356):1123–1126, 2017. doi: 10.1126/science.aao0990. URL `https://www.science.org/doi/abs/10.1126/science.aao0990`.

[2] F.J. Hasert, S. Kabe, W. Krenz, and et al. Observation of neutrino-like interactions without muon or electron in the Gargamelle neutrino experiment. *Physics Letters B*, 46(1):138–140, 1973. ISSN 0370-2693. doi: https://doi.org/10.1016/0370-2693(73)90499-1. URL `https://www.sciencedirect.com/science/article/pii/0370269373904991`.

[3] Daniel Z. Freedman. Coherent effects of a weak neutral current. *Phys. Rev. D*, 9:1389–1392, Mar 1974. doi: 10.1103/PhysRevD.9.1389. URL `https://link.aps.org/doi/10.1103/PhysRevD.9.1389`.

[4] Giorgio Del Castello. Development of energy calibration and data analysis systems for the NUCLEUS experiment, 2023. URL `https://arxiv.org/abs/2302.02843`.

[5] Manfred Lindner, Werner Rodejohann, and Xun-Jie Xu. Coherent neutrino-nucleus scattering and new neutrino interactions. *Journal of High Energy Physics*, 2017(3):97, Mar 2017. ISSN 1029-8479. doi: 10.1007/JHEP03(2017)097. URL `https://doi.org/10.1007/JHEP03(2017)097`.

[6] Particle Data Group, R L Workman, V D Burkert, and et al. Review of Particle Physics. *Progress of Theoretical and Experimental Physics*, 2022(8):083C01, 08 2022. ISSN 2050-3911. doi: 10.1093/ptep/ptac097. URL `https://doi.org/10.1093/ptep/ptac097`.

[7] Nicola Cargioli. *Standard model physics and beyond in low energy neutrino scattering and parity violating electron interactions with nuclei.* PhD thesis, Cagliari U., 2024.

[8] Giorgio Del Castello. Discovery of the neutrino nucleus coherent scattering. URL `https://www.researchgate.net/publication/353706711_Discovery_of_the_neutrino_nucleus_coherent_scattering`.

[9] Kelly Patton, Jonathan Engel, Gail C. McLaughlin, and Nicolas Schunck. Neutrino-nucleus coherent scattering as a probe of neutron density distributions.

Phys. Rev. C, 86:024612, Aug 2012. doi: 10.1103/PhysRevC.86.024612. URL `https://link.aps.org/doi/10.1103/PhysRevC.86.024612`.

[10] M. Atzori Corona, M. Cadeddu, N. Cargioli, and et al. Momentum dependent flavor radiative corrections to the coherent elastic neutrino-nucleus scattering for the neutrino charge-radius determination. *Journal of High Energy Physics*, 2024(5):271, May 2024. ISSN 1029-8479. doi: 10.1007/JHEP05(2024)271. URL `https://doi.org/10.1007/JHEP05(2024)271`.

[11] A. Konovalov and the COHERENT collaboration. COHERENT experiment: CsI detector. 2023. Contribution to Low Temperature Detectors ed. 20.

[12] M. Atzori Corona, M. Cadeddu, N. Cargioli, and et al. Nuclear neutron radius and weak mixing angle measurements from latest COHERENT CsI and atomic parity violation Cs data. *The European Physical Journal C*, 83(7): 683, Jul 2023. ISSN 1434-6052. doi: 10.1140/epjc/s10052-023-11849-5. URL `https://doi.org/10.1140/epjc/s10052-023-11849-5`.

[13] P. S. Barbeau, V. Belov, I. Bernardi, and et al. Accessing new physics with an undoped, cryogenic CsI CEvNS detector for COHERENT at the SNS. *Phys. Rev. D*, 109:092005, May 2024. doi: 10.1103/PhysRevD.109.092005. URL `https://link.aps.org/doi/10.1103/PhysRevD.109.092005`.

[14] B. Abi, T. Albahri, S. Al-Kilani, and et al. Measurement of the Positive Muon Anomalous Magnetic Moment to 0.46 ppm. *Phys. Rev. Lett.*, 126:141801, Apr 2021. doi: 10.1103/PhysRevLett.126.141801. URL `https://link.aps.org/doi/10.1103/PhysRevLett.126.141801`.

[15] M. Atzori Corona, M. Cadeddu, N. Cargioli, and et al. Probing light mediators and $(g-2)\mu$ through detection of coherent elastic neutrino nucleus scattering at COHERENT. *Journal of High Energy Physics*, 2022(5):109, May 2022. ISSN 1029-8479. doi: 10.1007/JHEP05(2022)109. URL `https://doi.org/10.1007/JHEP05(2022)109`.

[16] Carlo Giunti and Alexander Studenikin. Neutrino electromagnetic interactions: A window to new physics. *Rev. Mod. Phys.*, 87:531–591, Jun 2015. doi: 10.1103/RevModPhys.87.531. URL `https://link.aps.org/doi/10.1103/RevModPhys.87.531`.

[17] Valentina De Romeri, Víctor Martín Lozano, and G. Sanchez Garcia. Neutrino window to scalar leptoquarks: From low energy to colliders. *Phys. Rev. D*, 109:055014, Mar 2024. doi: 10.1103/PhysRevD.109.055014. URL `https://link.aps.org/doi/10.1103/PhysRevD.109.055014`.

[18] Julien Billard, Joseph Johnston, and Bradley J. Kavanagh. Prospects for exploring New Physics in Coherent Elastic Neutrino-Nucleus Scattering. *Journal of Cosmology and Astroparticle Physics*, 2018(11):016, nov 2018. doi: 10.1088/1475-7516/2018/11/016. URL `https://dx.doi.org/10.1088/1475-7516/2018/11/016`.

[19] Adam Bernstein, Nathaniel Bowden, Bethany L. Goldblum, Patrick Huber, Igor Jovanovic, and John Mattingly. Colloquium: Neutrino detectors as

tools for nuclear security. *Rev. Mod. Phys.*, 92:011003, Mar 2020. doi: 10.1103/RevModPhys.92.011003. URL `https://link.aps.org/doi/10.1103/RevModPhys.92.011003`.

[20] Caroline von Raesfeld and Patrick Huber. Use of CEvNS to monitor spent nuclear fuel. *Phys. Rev. D*, 105:056002, Mar 2022. doi: 10.1103/PhysRevD.105.056002. URL `https://link.aps.org/doi/10.1103/PhysRevD.105.056002`.

[21] M. Cadeddu, C. Giunti, Y. F. Li, and Y. Y. Zhang. Average CsI Neutron Density Distribution from COHERENT Data. *Phys. Rev. Lett.*, 120:072501, Feb 2018. doi: 10.1103/PhysRevLett.120.072501. URL `https://link.aps.org/doi/10.1103/PhysRevLett.120.072501`.

[22] I. Angeli and K.P. Marinova. Table of experimental nuclear ground state charge radii: An update. *Atomic Data and Nuclear Data Tables*, 99(1):69–95, 2013. ISSN 0092-640X. doi: https://doi.org/10.1016/j.adt.2011.12.006. URL `https://www.sciencedirect.com/science/article/pii/S0092640X12000265`.

[23] G. Fricke, C. Bernhardt, K. Heilig, and et al. Nuclear Ground State Charge Radii from Electromagnetic Interactions. *Atomic Data and Nuclear Data Tables*, 60(2):177–285, 1995. ISSN 0092-640X. doi: https://doi.org/10.1006/adnd.1995.1007. URL `https://www.sciencedirect.com/science/article/pii/S0092640X85710078`.

[24] Luca Pattavina, Nahuel Ferreiro Iachellini, and Irene Tamborra. Neutrino observatory based on archaeological lead. *Phys. Rev. D*, 102:063001, Sep 2020. doi: 10.1103/PhysRevD.102.063001. URL `https://link.aps.org/doi/10.1103/PhysRevD.102.063001`.

[25] H. Abele, A. Alekou, A. Algora, and et al. Particle physics at the European Spallation Source. *Physics Reports*, 1023:1–84, 2023. ISSN 0370-1573. doi: https://doi.org/10.1016/j.physrep.2023.06.001. URL `https://www.sciencedirect.com/science/article/pii/S0370157323001898`. Particle Physics at the European Spallation Source.

[26] Suzanne F. Nowicki, Stephen A. Wender, and Michael Mocko. The Los Alamos Neutron Science Center Spallation Neutron Sources. *Physics Procedia*, 90:374–380, 2017. ISSN 1875-3892. doi: https://doi.org/10.1016/j.phpro.2017.09.035. URL `https://www.sciencedirect.com/science/article/pii/S1875389217301943`. Conference on the Application of Accelerators in Research and Industry, CAARI 2016, 30 October – 4 November 2016, Ft. Worth, TX, USA.

[27] T.E. Mason, D. Abernathy, I. Anderson, and et al. The Spallation Neutron Source in Oak Ridge: A powerful tool for materials research. *Physica B: Condensed Matter*, 385-386:955–960, 2006. ISSN 0921-4526. doi: https://doi.org/10.1016/j.physb.2006.05.281. URL `https://www.sciencedirect.com/science/article/pii/S092145260601177X`.

[28] D. Akimov, P. An, C. Awe, and et al. Measurement of the Coherent Elastic Neutrino-Nucleus Scattering Cross Section on CsI by COHERENT. *Phys.*

Rev. Lett., 129:081801, Aug 2022. doi: 10.1103/PhysRevLett.129.081801. URL `https://link.aps.org/doi/10.1103/PhysRevLett.129.081801`.

[29] D. Akimov, P. An, C. Awe, and et al. Simulating the neutrino flux from the Spallation Neutron Source for the COHERENT experiment. *Phys. Rev. D*, 106:032003, Aug 2022. doi: 10.1103/PhysRevD.106.032003. URL `https://link.aps.org/doi/10.1103/PhysRevD.106.032003`.

[30] D. Akimov, J. B. Albert, P. An, and et al. First Measurement of Coherent Elastic Neutrino-Nucleus Scattering on Argon. *Phys. Rev. Lett.*, 126:012002, Jan 2021. doi: 10.1103/PhysRevLett.126.012002. URL `https://link.aps.org/doi/10.1103/PhysRevLett.126.012002`.

[31] R. Bouabid. First Measurement of CEνNS on Germanium by COHERENT. 2024. URL `https://indico.cern.ch/event/1342813/contributions/5913875/attachments/2875782/5036212/m7s_rbouabid_upload.pdf`. Contribution to Magnificent CEνNS.

[32] Spencer R. Klein and Joakim Nystrand. Exclusive vector meson production in relativistic heavy ion collisions. *Phys. Rev. C*, 60:014903, Jun 1999. doi: 10.1103/PhysRevC.60.014903. URL `https://link.aps.org/doi/10.1103/PhysRevC.60.014903`.

[33] D. Parno. he current status of the COHERENT experiment. 2024. URL `https://indico.cern.ch/event/1342813/contributions/5913905/attachments/2875468/5035531/Parno-COHERENT-Overview-M7s2024.pdf`. Contribution to Magnificent CEνNS.

[34] COHERENT collaboration, D. Akimov, P. An, and et al. A D2O detector for flux normalization of a pion decay-at-rest neutrino source. *Journal of Instrumentation*, 16(08):P08048, aug 2021. doi: 10.1088/1748-0221/16/08/P08048. URL `https://dx.doi.org/10.1088/1748-0221/16/08/P08048`.

[35] P. S. Barbeau, V. Belov, and et al. Accessing new physics with an undoped, cryogenic CsI CEvNS detector for COHERENT at the SNS. *Phys. Rev. D*, 109:092005, May 2024. doi: 10.1103/PhysRevD.109.092005. URL `https://link.aps.org/doi/10.1103/PhysRevD.109.092005`.

[36] T. Johnson. First Search for Neutrino-Induced Nuclear Fission. 2024. URL `https://indico.cern.ch/event/1342813/contributions/5913894/attachments/2877749/5040183/MagCEVNS_2024_TJohnson.pdf`. Contribution to Magnificent CEνNS.

[37] A. Schneider. Dark Sector Searches with Coherent CAPTAIN Mills. 2024. URL `https://indico.cern.ch/event/1342813/contributions/5913892/attachments/2877940/5040504/CCM%20Magnificent%20CEvNS%202024-06-14.pdf`. Contribution to Magnificent CEνNS.

[38] F. Monrabal. CEνNS at the ESS. 2024. URL `https://indico.cern.ch/event/1342813/contributions/5913877/attachments/2877548/5039702/Magnificent.pdf`. Contribution to Magnificent CEνNS.

[39] J. Lindhard and et al. INTEGRAL EQUATIONS GOVERNIN GRADIATION EFFECT . 1963. Mat. Fys. Medd. K. Dan. Vidensk. Selsk. 33, 1.

[40] N. Ackermann, H. Bonet, A. Bonhomme, and et al. Final CONUS results on coherent elastic neutrino nucleus scattering at the Brokdorf reactor. 2024. URL https://arxiv.org/abs/2401.07684.

[41] N. Ackermann, H. Bonet, A. Bonhomme, and et al. Final CONUS results on coherent elastic neutrino nucleus scattering at the Brokdorf reactor. 2024. URL https://arxiv.org/abs/2401.07684.

[42] Kaixiang Ni. Status of the CONUS+ experiment. 2024. URL https://indico.cern.ch/event/1342813/contributions/5913914/attachments/2876544/5037733/CONUS%20Magnificent2024.pdf. Contribution to Magnificent CEνNS.

[43] J. Colaresi, J. I. Collar, T. W. Hossbach, C. M. Lewis, and K. M. Yocum. Measurement of Coherent Elastic Neutrino-Nucleus Scattering from Reactor Antineutrinos. *Phys. Rev. Lett.*, 129:211802, Nov 2022. doi: 10.1103/PhysRevLett.129.211802. URL https://link.aps.org/doi/10.1103/PhysRevLett.129.211802.

[44] J. I. Collar, A. R. L. Kavner, and C. M. Lewis. Germanium response to sub-keV nuclear recoils: A multipronged experimental characterization. *Phys. Rev. D*, 103:122003, Jun 2021. doi: 10.1103/PhysRevD.103.122003. URL https://link.aps.org/doi/10.1103/PhysRevD.103.122003.

[45] E. Figueroa-Feliciano. The Magnificent CEνNS experimental summary. 2023. URL https://indico.cern.ch/event/1215362/contributions/5312783/attachments/2617634/4525516/Magificent_CEvNS_Figueroa.pdf. Contribution to Magnificent CEνNS.

[46] I. Alekseev, K. Balej, V. Belov, and et al. First results of the νGeN experiment on coherent elastic neutrino-nucleus scattering. *Phys. Rev. D*, 106:L051101, Sep 2022. doi: 10.1103/PhysRevD.106.L051101. URL https://link.aps.org/doi/10.1103/PhysRevD.106.L051101.

[47] A. Konovalov. Looking for CEνNS with the νGeN experiment. 2024. URL https://indico.cern.ch/event/1342813/contributions/5913887/attachments/2875525/5035786/nuGeN_M7.pdf. Contribution to Magnificent CEνNS.

[48] Henry Tsz-King Wong. Taiwan EXperiment On NeutrinO — History and Prospects. *The Universe*, 3(4):22–37, 2015. doi: 10.1142/S0217751X18300144.

[49] Henry T. Wong. TEXONO's νA_{el} KSNL : Results & Status. 2024. URL https://indico.cern.ch/event/1342813/contributions/5913890/attachments/2876526/5037703/nuA-M7-HT_Wong-June24.pdf. Contribution to Magnificent CEνNS.

[50] Javier Tiffenberg, Miguel Sofo-Haro, Alex Drlica-Wagner, Rouven Essig, Yann Guardincerri, Steve Holland, Tomer Volansky, and Tien-Tien Yu. Single-

Electron and Single-Photon Sensitivity with a Silicon Skipper CCD. *Phys. Rev. Lett.*, 119:131802, Sep 2017. doi: 10.1103/PhysRevLett.119.131802. URL `https://link.aps.org/doi/10.1103/PhysRevLett.119.131802`.

[51] Alexis A. Aguilar-Arevalo, Nicolas Avalos, Xavier Bertou, and et al. Searches for CEνNS and Physics beyond the Standard Model using Skipper-CCDs at CONNIE. 2024. URL `https://arxiv.org/abs/2403.15976`.

[52] I. Nasteva. Status of the CONNIE experiment using Skipper-CCDs. 2024. URL `https://indico.cern.ch/event/1342813/contributions/5913873/attachments/2876632/5037900/Nasteva_M7s.pdf`. Contribution to Magnificent CEνNS.

[53] E. Depaoli, D. Rodrigues, I. Sidelnik, and et al. Deployment and performance of a Low-Energy-Threshold Skipper-CCD inside a nuclear reactor. 2024. URL `https://arxiv.org/abs/2401.07885`.

[54] N. Martini. Current status of the RICOCHET experiment. 2024. URL `https://indico.cern.ch/event/1342813/contributions/5913912/attachments/2875656/5037087/Ricochet%20Status%20Mag7%202024%20-%20N.%20Martini.pdf`. Contribution to Magnificent CEνNS.

[55] W. Pontseele. Q-ARRAY: R&D TOWARDS SUPERCONDUCTING TARGETS FOR CEνNS. 2024. URL `https://indico.cern.ch/event/1342813/contributions/5913872/attachments/2875706/5036060/202406_M7s_qarray.pdf`. Contribution to Magnificent CEνNS.

[56] G. Agnolet, W. Baker, D. Barker, and et al. Background studies for the MINER Coherent Neutrino Scattering reactor experiment. *Nuclear Instruments and Methods in Physics Research Section A: Accelerators, Spectrometers, Detectors and Associated Equipment*, 853:53–60, 2017. ISSN 0168-9002. doi: https://doi.org/10.1016/j.nima.2017.02.024. URL `https://www.sciencedirect.com/science/article/pii/S0168900217302085`.

[57] R. Mahapatra. MIνER Experiment for CEν NS and ALP Searches. 2024. URL `https://indico.cern.ch/event/1342813/contributions/5913897/attachments/2875491/5036201/MINER_Magnificent_CENNS_2024.pptx`. Contribution to Magnificent CEνNS.

[58] E. Adams and et al. Search for inelastic dark matter-nucleus scattering with the PICO-60 CF3I and C3F8 bubble chambers. *Phys. Rev. D*, 108(6):062003, 2023. doi: 10.1103/PhysRevD.108.062003.

[59] E. V. Jàuregui. Measuring coherent elastic neutrino-nucleus scattering in argon with a scintillating bubble chamber. 2024. URL `https://indico.cern.ch/event/1342813/contributions/5913893/attachments/2876538/5037724/Magnificent_SBC_Eric_Vazquez_Jauregui.pdf`. Contribution to Magnificent CEνNS.

[60] J. J. Choi, E. J. Jeon, and N. E. O. N. Collaboration. Exploring coherent elastic neutrino-nucleus scattering using reactor electron antineutrinos in the NEON experiment. *The European Physical Journal C*, 83(3):226, Mar

2023. ISSN 1434-6052. doi: 10.1140/epjc/s10052-023-11352-x. URL https://doi.org/10.1140/epjc/s10052-023-11352-x.

[61] D.Y. Akimov, V.A. Belov, and et al. First ground-level laboratory test of the two-phase xenon emission detector RED-100. *Journal of Instrumentation*, 15 (02):P02020, feb 2020. doi: 10.1088/1748-0221/15/02/P02020. URL https://dx.doi.org/10.1088/1748-0221/15/02/P02020.

[62] Particle Data Group, P A Zyla, R M Barnett, and et al. Review of Particle Physics. *Progress of Theoretical and Experimental Physics*, 2020(8):083C01, 08 2020. ISSN 2050-3911. doi: 10.1093/ptep/ptaa104. URL https://doi.org/10.1093/ptep/ptaa104.

[63] M. Agostini and et al. Comprehensive measurement of pp-chain solar neutrinos. *Nature*, 562(7728):505–510, Oct 2018. ISSN 1476-4687. doi: 10.1038/s41586-018-0624-y. URL https://doi.org/10.1038/s41586-018-0624-y.

[64] Ciaran A. J. O'Hare. New Definition of the Neutrino Floor for Direct Dark Matter Searches. *Phys. Rev. Lett.*, 127:251802, Dec 2021. doi: 10.1103/PhysRevLett.127.251802. URL https://link.aps.org/doi/10.1103/PhysRevLett.127.251802.

[65] Wenbo Ma, Abdusalam Abdukerim, Chen Cheng, and et al. Search for Solar ^{8}B Neutrinos in the PandaX-4T Experiment Using Neutrino-Nucleus Coherent Scattering. *Phys. Rev. Lett.*, 130:021802, Jan 2023. doi: 10.1103/PhysRevLett.130.021802. URL https://link.aps.org/doi/10.1103/PhysRevLett.130.021802.

[66] E. Aprile, J. Aalbers, and et al. Projected WIMP sensitivity of the XENONnT dark matter experiment. *Journal of Cosmology and Astroparticle Physics*, 2020(11):031, nov 2020. doi: 10.1088/1475-7516/2020/11/031. URL https://dx.doi.org/10.1088/1475-7516/2020/11/031.

[67] E. Aprile, J. Aalbers, K. Abe, and et al. First Measurement of Solar ^{8}B Neutrinos via Coherent Elastic Neutrino-Nucleus Scattering with XENONnT, 2024. URL https://arxiv.org/abs/2408.02877.

[68] B. Aharmim, S. N. Ahmed, and et al. Combined analysis of all three phases of solar neutrino data from the Sudbury Neutrino Observatory. *Phys. Rev. C*, 88:025501, Aug 2013. doi: 10.1103/PhysRevC.88.025501. URL https://link.aps.org/doi/10.1103/PhysRevC.88.025501.

[69] M. Anderson, S. Andringa, S. Asahi, and et al. Measurement of the ^{8}B solar neutrino flux in SNO+ with very low backgrounds. *Phys. Rev. D*, 99:012012, Jan 2019. doi: 10.1103/PhysRevD.99.012012. URL https://link.aps.org/doi/10.1103/PhysRevD.99.012012.

[70] K. Abe, Y. Haga, Y. Hayato, and et al. Solar neutrino measurements in Super-Kamiokande-IV. *Phys. Rev. D*, 94:052010, Sep 2016. doi: 10.1103/PhysRevD.94.052010. URL https://link.aps.org/doi/10.1103/PhysRevD.94.052010.

[71] M. Agostini, K. Altenmüller, and et al. Improved measurement of ^{8}B solar neutrinos with 1.5 kt · y of Borexino exposure. *Phys. Rev. D*, 101:062001, Mar 2020. doi: 10.1103/PhysRevD.101.062001. URL `https://link.aps.org/doi/10.1103/PhysRevD.101.062001`.

[72] S. Abe, K. Furuno, A. Gando, and et al. Measurement of the ^{8}B solar neutrino flux with the KamLAND liquid scintillator detector. *Phys. Rev. C*, 84:035804, Sep 2011. doi: 10.1103/PhysRevC.84.035804. URL `https://link.aps.org/doi/10.1103/PhysRevC.84.035804`.

[73] Johannes Felix Martin Rothe. *Low-Threshold Cryogenic Detectors for Low-Mass Dark Matter Search and Coherent Neutrino Scattering*. PhD thesis, Munich, Tech. U., Munich, Tech. U., 2021.

[74] C. Goupy and NUCLEUS Collaboration. Comprehensive estimate of (particle) backgrounds at sub-keV energies for the NUCLEUS experiment. 2024. URL `https://indico.cern.ch/event/1342813/contributions/5913888/attachments/2876727/5054475/Mag7_NUCLEUS_Bckg_CGoupy.pdf`. Contribution to Magnificent CEνNS.

[75] A. Wex. Creation of a Vibration Free Environment in a Dry Dilution Refrigerator at Millikelvin Temperatures. 2015. Contribution to The 2nd International Conference on Particle Physics and Astrophysics.

[76] Tapani Ryhänen, Heikki Seppä, Risto Ilmoniemi, and Jukka Knuutila. SQUID magnetometers for low-frequency applications. *Journal of Low Temperature Physics*, 76(5):287–386, Sep 1989. ISSN 1573-7357. doi: 10.1007/BF00681735. URL `https://doi.org/10.1007/BF00681735`.

[77] C. Goupy. *Background mitigation strategy for the detection of coherent elastic scattering of reactor antineutrinos on nuclei with the NUCLEUS experiment*. Phd thesis, Service de Physique des Particules (SPP), Institut de Recherche sur les lois Fondamentales de l'Univers (IRFU), CEA - Saclay, France, 2024.

[78] P. Adari, A. Aguilar-Arevalo, D. Amidei, and et al. EXCESS workshop: Descriptions of rising low-energy spectra. *SciPost Phys. Proc.*, page 001, 2022. doi: 10.21468/SciPostPhysProc.9.001. URL `https://scipost.org/10.21468/SciPostPhysProc.9.001`.

[79] Delicato, D., Ahmad, A., Bandiera, L., Calvo, M., Cappelli, M., Del Castello, G., and et al. Low-energy spectrum of the BULLKID detector array operated on surface. *Eur. Phys. J. C*, 84(4):353, 2024. doi: 10.1140/epjc/s10052-024-12714-9. URL `https://doi.org/10.1140/epjc/s10052-024-12714-9`.

[80] G. Angloher, S. Banik, G. Benato, and et al. Latest observations on the low energy excess in CRESST-III. *SciPost Phys. Proc.*, page 013, 2023. doi: 10.21468/SciPostPhysProc.12.013. URL `https://scipost.org/10.21468/SciPostPhysProc.12.013`.

[81] M. Kaznacheeva and NUCLEUS Collaboration. New excess measurements from NUCLEUS. 2024. URL `https://agenda.infn.it/event/39007/`

contributions/235288/attachments/123168/180515/nucleus_excess24.pdf. Contribution to EXCESS workshop.

[82] G. Angloher, S. Banik, G. Benato, and et al. DoubleTES detectors to investigate the CRESST low energy background: results from above-ground prototypes. 2024. URL https://arxiv.org/abs/2404.02607.

[83] L. Cardani, N. Casali, A.Cruciani, and et al. Al/Ti/Al phonon-mediated KIDs for UV–vis light detection over large areas. *Supercond. Sci. Technol. 31 075002*, 2018. doi: 10.1088/1361-6668/aac1d4.

[84] *Low-Cost 64-Step Volatile Digital POT*. URL https://www.alldatasheet.com/datasheet-pdf/view/197234/MICROCHIP/MCP4011.html.

[85] *IC MULTIPLEXER 16X1 28TSSOP*, . URL https://www.micro-semiconductor.com/products/ADI(Analog-Devices,Inc.)/ADG1406BRUZ?gad_source=1&gclid=Cj0KCQjww5u2BhDeARIsALBuLnMucP55BSN1WAPYIYGaYIASM8RXdCKq1PbwN28VRCvcsfrjP_98ePMaApqPEALw_wcB.

[86] *PyLoN 100 Spectrometer*, . URL https://www.princetoninstruments.com/wp-content/uploads/2020/04/PyLoN_100_Datasheet.pdf.

[87] G. Del Castello. LANTERN: A multichannel light calibration system for cryogenic detectors. *Nuclear Instruments and Methods in Physics Research Section A: Accelerators, Spectrometers, Detectors and Associated Equipment*, 1068:169728, 2024. ISSN 0168-9002. doi: https://doi.org/10.1016/j.nima.2024.169728. URL https://www.sciencedirect.com/science/article/pii/S0168900224006545.

[88] L. Thulliez, D. Lhuillier, F. Cappella, and et al. Calibration of nuclear recoils at the 100 eV scale using neutron capture. *Journal of Instrumentation*, 16 (07):P07032, jul 2021. doi: 10.1088/1748-0221/16/07/P07032. URL https://dx.doi.org/10.1088/1748-0221/16/07/P07032.

[89] H. Abele, G. Angloher, A. Bento, and et al. Canonica. Observation of a Nuclear Recoil Peak at the 100 eV Scale Induced by Neutron Capture. *Phys. Rev. Lett.*, 130:211802, May 2023. doi: 10.1103/PhysRevLett.130.211802. URL https://link.aps.org/doi/10.1103/PhysRevLett.130.211802.

[90] S Di Domizio, F Orio, and M Vignati. Lowering the energy threshold of large-mass bolometric detectors. *Journal of Instrumentation*, 6(02):P02007, feb 2011. doi: 10.1088/1748-0221/6/02/P02007. URL https://dx.doi.org/10.1088/1748-0221/6/02/P02007.

[91] Giorgio Del Castello, H. Abele, G. Angloher, A. Bento, J. Burkhart, L. Canonica, F. Cappella, N. Casali, R. Cerulli, A. Cruciani, M. del Gallo Roccagiovine, A. Doblhammer, S. Dorer, A. Erhart, M. Friedl, A. Garai, V.M. Ghete, C. Goupy, D. Hauff, F. Jeanneau, E. Jericha, M. Kaznacheeva, A. Kinast, H. Kluck, A. Langenkämper, T. Lasserre, D. Lhuillier, M. Mancuso, R. Martin, A. Mazzolari, E. Mazzucato, H. Neyrial, C. Nones, L. Oberauer, T. Ortmann, L. Pattavina, L. Peters, Federica Petricca, W. Potzel, F. Pröbst, F. Pucci,

F. Reindl, M. Romagnoni, J. Rothe, N. Schermer, J. Schieck, S. Schönert, C. Schwertner, L. Scola, G. Soum-Sidikov, L. Stodolsky, R. Strauss, M. Tamisari, C. Tomei, M. Vignati, M. Vivier, V. Wagner, and A. Wex. Data analysis of the NUCLEUS experiment with the Diana framework. *PoS*, TAUP2023: 257, 2024. doi: 10.22323/1.441.0257.

[92] Sunil Ramanlal Golwala. *Exclusion limits on the WIMP-nucleon elastic-scattering cross-section from the Cryogenic Dark Matter Search*. University of California, Berkeley, 2000.

[93] G. Angloher, S. Banik, G. Benato, and et al. Observation of a low energy nuclear recoil peak in the neutron calibration data of the CRESST-III experiment. *Phys. Rev. D*, 108:022005, Jul 2023. doi: 10.1103/PhysRevD.108.022005. URL `https://link.aps.org/doi/10.1103/PhysRevD.108.022005`.

[94] A. Thompson, D. Attwood, and et al. 2009. URL `https://xdb.lbl.gov/xdb-new.pdf`.

[95] EXCESS Workshop. 2024. URL `https://agenda.infn.it/event/39007/`.

[96] Start Cryoelectronics. *Mr. SQUID User's Guide*. URL `https://starcryo.com/wp-content/themes/education-pro/manuals/MrSQm66.pdf`.

[97] B.D. Josephson. Possible new effects in superconductive tunnelling. *Physics Letters*, 1(7):251–253, 1962. ISSN 0031-9163. doi: https://doi.org/10.1016/0031-9163(62)91369-0. URL `https://www.sciencedirect.com/science/article/pii/0031916362913690`.

[98] Leon N. Cooper. Bound Electron Pairs in a Degenerate Fermi Gas. *Phys. Rev.*, 104:1189–1190, Nov 1956. doi: 10.1103/PhysRev.104.1189. URL `https://link.aps.org/doi/10.1103/PhysRev.104.1189`.

[99] *ROOT Analysis Framework*. URL `https://root.cern/manual/`.

[100] C Arnaboldi, F.T Avignone, J Beeman, and et al. Physics potential and prospects for the CUORICINO and CUORE experiments. *Astroparticle Physics*, 20(2):91–110, 2003. ISSN 0927-6505. doi: https://doi.org/10.1016/S0927-6505(03)00180-4. URL `https://www.sciencedirect.com/science/article/pii/S0927650503001804`.